Proceedings of the CEReS International Symposium on Remote Sensing of the Atmosphere and Validation of Satellite Data

February 22 - 23, 2001

Center for Environmental Remote Sensing
Chiba University, Japan

CEReS

Proceedings of the

CEReS International Symposium on Remote Sensing of the Atmosphere and Validation of Satellite Data

Nobuo Takeuchi
Hiroaki Kuze
Tamio Takamura (eds.)

February 22 - 23, 2001
Keyaki Hall, Chiba University

Center for Environmental Remote Sensing
Chiba University, Japan

The CEReS International Symposium on Remote Sensing of the Atmosphere and Validation of Satellite Data

February 22 - 23, 2001, Chiba University, Japan

CONTENTS

Derivation of fires from Space and their climatic effect

Robert Frouin

Scripps Institution of Oceanography
8605 La Jolla Shores Drive, La Jolla, California 92037

1. Introduction

Biomass burning, by releasing carbon dioxide to the atmosphere, is a potentially critical initiator of climate change. As much as 40% of the annual gross release of carbon dioxide through combustion may be due to biomass burning (Levine, 1991). In addition to carbon dioxide, biomass burning releases other greenhouse gases, particularly methane, carbon monoxide, and nitrous oxide. These gases also contribute to increase tropospheric ozone, another greehouse gas. Particulate matter emitted during fires (smoke), on the other hand, may cause a climate forcing comparable in magnitude yet opposite in sign to the greenhouse-gas forcing. Biomass-burning particles consist mostly of condensed organic species, but also contain black, elemental (soot) carbon. The black carbon may absorb sunlight and, like greenhouse gases, may exert a warming influence on the atmopshere.

On a global scale, about 9000 Tg of biomass (dry material) is consumed by annual burning, with the largest contribution from savanna grasslands (45%). The other components of biomass burning, i.e., agricultural waste, forests, and fuel wood, contribute approximately 25, 15, and 15% of the total biomass consumed. Biomass burning occurs not only in the tropics, but also in temperate and higher latitudes (e.g., boreal forests). Human activity is responsible for most biomass burning, and the scope and magnitude of this activity is thought to be increasing with time.

Until the 70's carbon emissions from the burning of fossil fuel were highly correlated with the increase in atmospheric carbon dioxide, but in the 80's the correlation became low as the fossil fuel source stopped to increase (e.g., IPCC, 1996). One wonders, therefore, whether the continued increase in atmospheric carbon dioxide may be due to an increase in biomass burning. This stresses the need for accurate inventories of biomass burning sources.

2. Fire Detection

Biomass-burning studies generally lack quantitative information on the spatio-temporal variability of fires at regional and global scales. Extending local results to large areas may give some idea of the global fire patterns (i.e., distribution of fires, amount of area burned, carbon emission rates), but errors may be large. Ground-based observations are inadequate to describe regional variability, making it

necessary to exploit the capabilities of Earth-observing satellites. Ground-based measurements are needed, however, to evaluate the performance of satellite techniques.

Fire-related studies using satellite data include acquiring pre-fire information (e.g., vegetation fuel content), detecting active fires and smoke plumes, and quantifying fire effects (burned areas, vegetation re-generation). Justice et al. (1993) have discussed the potential and limitations of various remote sensing systems and have outlined the current trends in fire studies. The choice of remote sensing system depends on the geographical extent and spectral characteristics of the fire signal. High spatial resolution sensors such as Thematic mapper (TM) and High Resolution Visible (HRV) radiometer, owing to the high cost and low time frequency of the data, are limited to local monitoring. Coarser resolution sensors such as the Advanced Very High Resolution radiometer (AVHRR) provide daily data that are adapted to regional studies. Local Area Coverage (LAC) data at 1-km resolution and sampled Global Area Coverage (GAC) data at 4-km resolution are available for this purpose. GAC data are more convenient to use on a global scale, but they are not recommended for quantitative studies related to fires (Kennedy et al., 1994; Belward et al., 1994).

2.1 Active fires

The detection of active fires is usually accomplished with infrared sensors. The technique is based on the sensitivity of the measured radiance in the short-wave infrared (3-5 μm) to fire radiative energy, and also on the sensitivity of the measured radiance in the thermal infrared (8-12 μm) to temperature. A review of fire detection using infrared remote sensing can be found in Robinson (1991). Various methods have been developed to enhance the detection capability in the infrared (Matson and Holben, 1987; Lee and Tag, 1990; Kaufman et al., 1990; Langaas, 1993a; etc.). Images at night can be used to detect active fires, but the results may not represent the actual burnings since the number of fires is often reduced at night due to nocturnal weather conditions (Langaas, 1993b). Nevertheless, studies such as those of Cahoon et al. (1992), who processed Defense mapping Satellite Program (DMSP) night time images of Africa, suggest that useful information on the distribution of fires can be obtained using available techniques.

2.2 Burn scars

While the detection of active fires has been studied expensively, less research has focused on the spectral characteristics of burn scars and the areas actually burned. Matson and Dozier 91981) described a method to deduce sub-pixel fire size and temperature using AVHRR data. The method is not applicable to saturated infrared pixels. Pereira et al. (1991) used AVHRR fire counts to estimate burned areas from active fires assuming that the fire occupies the entire pixel. their results, when

compared with those from higher resolution TM images, show an overestimate of the fire size by 43% on average and an underestimate of the fire size of long, continuously burning fires.

After a fire, the area burned is covered by ash, and ash is generally darker than the original background. This changes the top-of-atmosphere radiance in the visible and near-infrared and, therefore, the Normalized Difference Vegetation Index (NDVI), providing the basis of methods to detect burned areas from space. Studies have shown that burned areas can be identified using Multi Spectral Scanner (MSS) data (Tanaka et al., 1983) or TM data (Pereira and Setzer, 1993). Discrimination between burned and unburned areas, however, is difficult to make the presense of water (similar spectral signature) and, in the case of savanna ecosystems, is limited by the rapid regrowth of the vegetation just a few days after the fire (Fredericksen et al., 1990). For such ecosystems, data should be used with a higher frequency (e.g., once a day). Radiances in AVHRR visible and near-infrared bands and the derived NDVI have been used in Senegal (Fredericksen et al., 1990), Congo (Malingreau, 1990), and boreal forests (Kasischke et al., 1993), and have been found sensitive to fire-affected areas. In boreal forests, burned scars remain for a longer period of time (several months), making remote sensing easier.

The existing techniques to estimate burned areas, when applied to coarse spatial resolution sensors, generally assume that a pixel is either totally burned or totally unburned. The burned area is estimated by counting the number of pixels classified as burned or unburned. The procedure is adequate for fire extents larger than the sensor resolution, but becomes unreliable when a large number of partially burned pixels are present within a scene. In the savannas of West Africa, fires occupy typically a pixel or two in AVHRR LAC imagery. For such ecosystems and others with small fire size, Razafimpanilo et al. (1995) have established theoretical relationships between fraction of pixel burned and near-infrared reflectance (linear) and fraction of pixel burned and NDVI (non-linear). Their sensitivity analysis suggest that fraction inaccuracies of 0.2 and 0.1 may be obtained, respectively, in the case of uniform pixels.

3. Climate change

The greenhouse gases produced by biomass burning contribute 10 to 15% of the expected surface temperature increase due to all greenhouse gases emitted to the atmosphere from A. D. 1980 to 2030, as computed by a 1-dimensional climate model (Ramanathan et al., 1985). This contribution is smaller than fossil fuel combustion, but may dominate the total climate forcing in some regions. Uncertainties in emissions and the relative impact of the different gases are large, however, and the actual contribution of biomass burning may lie in the range 5-30%.

The climatic impact of biomass burning aerosols is not well understood. Organic carbon aerosols can reflect sunlight back to space and thus reduce the amount of heat received by the planet. Black carbon aerosols, on the contrary, may absorb sunlight and warm the atmosphere. The direct radiative forcing by condensed organic species is a loss of reflected flux of about -0.8 W/m^2 (Penner et al., 1992; Iacobellis et al., 1999), but because of uncertainties in emission factor, average lifetime of smoke, amount of biomass burned, and mass scattering efficiency, the actual value is probably between -2.2 and -0.3 W/m^2 (Penner et al., 1994). Penner et al. (1992) indicated that black carbon aerosols could reduce the amplitude of forcing by organic species by a few tenths of W/m^2, but uncertainties in the size-dependent optical properties of black-soot particles make the confidence level of any calculation very low.

The influence of biomass burning particles on the behavior of clouds (indirect climate forcing) is beyond current understanding, due to complex interactions such as the influence of cloud entrainment an mixing processes. In principle, the more aerosols, the more cloud condensation nuclei, therefore the more cloud droplets, and the smaller droplets. Clouds with smaller droplets reflect more solar radiation back to space, with the potential of affecting climate substantially.

Climate model simulations with only greenhouse gases predict a strong winter warming in high northern latitudes (IPCC, 1996), and a greater warming over land than over the ocean. The presence of biomass burning aerosols, mostly confined over land because of their relatively short life time, may reduce the warming and the land-ocean contrast (Taylor and Penner, 1994). In regions such as Southeast Asia, significant changes in atmospheric circulation and hydrology might occur. Improving our projections of future climate certainly requires a better knowledge of the geographic distribution of biomass-burning sources, including their seasonality. This can hardly be accomplished without satellite observations of fires and satellite estimates of burned areas and carbon stock available for burning before fires.

References

Belward, A. S., Kennedy, P. J., and Grégoire, J.-M., 1994: The limitations and potential of AVHRR GAC data for continental scale fire studies. Int. J. Rem. Sen., 15, 2215-2234.

Cahoon, D. R., Jr., Stocks, B. J., Levine, J. S., Cofer, W. R. , III, and O'Neill, K. P., 1992: Seasonal distribution of African Savanna fires. Nature, 359, 812-815.

Frederiksen, P., Langaas, S., and Mbaye, M., 1990: NOAA AVHRR and GIS-based monitoring of fire activity in Senegal - a provisional methodology and potential

applications. In Fire in the Tropical Biota, J. G. Goldammer, Ed., Ecological Studies 84, 400-417.

Justice, C. O., Malingreau, J. P., and Setzer, A. W., 1993: Remote sensing of fires: potential and limitations. In Fire in the Environment, P. J. Crutzen and J. G. Goldammer, Eds., 77-88.

Iacobellis, S. F., Frouin, R., and Somerville, R. C. J., 1999: Direct climate forcing by biomass-burning aerosols: Impact of correlations between controlling variables. J. Geophys. Res., 104, 12,031-12,045.

Intergovernmental Panel on Climate Change (IPCC), Climate Change 1995, the Science of Climate Change, J. T. Houghton, L. G. Meira Filho, B. A. Callander, N. Harris, A. Kattenberg, and K. Maskell, Eds., Cambridge Univ. Press, New York, 572 pp.

Kaufman, Y. J., Setzer, A., Justice, C., Tucker, C. J., Pereira, M. C., and Fung, I., 1990. Remote sensing of biomass burning in the tropics. In Fires in the Tropical Biota, , J. G. Goldammer, Ed., Ecological Studies 84, 371-399.

Kasischke, E. S., French, N. H. F., Harrell, P., Christensen, N. L., Ustin, S. L., and Barry, D., 1993: Monitoring of wild fires in boreal forests using large area AVHRR NDVI composite image data. Rem. Sen. Environ., 45, 61-71.

Langaas, S., 1993a: A parameterised bispectral model for savanna fire detection using AVHRR night images. Int. J. Rem. Sen., 14, 2245-2262.

Langaas, S., 1993b: Diurnal cycles in savanna fires. Nature, 363, 120.

Lee, T. F., and Tag, P. M., 1990: Improved detection of hotspots using the AVHRR 3.7 μm channel. Bull. Am. Meteor. Soc., 71, 1722-1730.

Levine, J. S., 1991: Global biomass burning: atmospheric, climatic, and biospheric implications. In Global Biomass Burning, J. S. Levine, Ed., MIT Press, Cambridge, MA, xxv-xxx.

Malingreau, J. P., 1990: The contribution of remote sensing to the global monitoring of fires in tropical and subtropical ecosystems. In Fires in the Tropical Biota, J. G. Goldammer, Ed., Ecological Studies 84, 337-370.

Matson, M., and Dozier, J., 1981: Identification of subresolution high temperature

sources using a thermal infrared sensor. Photogr. Eng. Rem. Sen., 47, 1311-1318.

Penner, J. E., Dickinson, R. F., and O'Neill, C. A., 1992: Effects of aerosols from biomass burning on the global radiation budget, Science, 256, 1432-1433.

Penner, J. E., et al., 1994: Quantifying and minimizing uncertainty in climate forcing by anthropogenic aerosols. Bull. Am. Meteor. Soc., 75, 375-400.

Pereira, M. C., Alfredo, C., Setzer, A. W., and Dos Santos, J. R., 1991: Fire estimates in savannas of central Brazil with thermal AVHRR/NOAA calibrated by TM/Landsat. In Proc. 24th Int. Sym. on Remote Sensing of the Environment, Rio de Janeiro, Brazil, 27-31 May.

Pereira, M. C., and Setzer, A. W., 1993: Spectral characteristics of fire scars in Landsat 5 TM images of Amazonia. Int. J. Rem. Sen., 14, 2061-2078.

Ramanathan, V., Cicerone, R. J., Singh, H. B., and Kiehl, J. T., 1985: Trace gas trends and their potential role in climate change. J. Geophys. Res., 90, 5547-5566.

Razafimpanilo, H., Frouin, R., Iacobellis, S. F., and Somerville, R. C. J., 1995: Methodology for estimating burned area from AVHRR data. Rem. Sen. Environ., 54, 273-289.

Robinson, J. M., 1991: Fire from Space: global fire evaluation using infrared remote sensing. Int. J. Rem. Sen., 12, 3-24.

Tanaka, S., Kimura, H., and Suga, Y., 1983: preparation of a 1:25,000 landsat map for assessment of burnt area on Etajima Island. Int. J. Rem. Sen., 4, 17-31.

Taylor, K. E., and Penner, J. E., 1994: Response of the climate system to atmospheric aerosols and greenhouse gases, Nature, 369, 734.

Observation of Asian dusts during 1997-2000 by NOAA/AVHRR

K.Kinoshita,[1] R.Iwasaki,[1] M.Koyamada,[1] N.Iino,[2] T.Yano,[2]
I.Uno,[3] H.Amano,[3] H.Yoshii [3] and T.Masumizu [4]

[1] Faculty of Education, Kagoshima University, Kagoshima 890-0065
[2] Faculty of Engineering, Kagoshima University, Kagoshima 890-0065
[3] Research Institute for Applied Mechanics, Kyushu University, Kasuga 816-8580
[4] Daiichi Institute of Technology, Kokubu 899-4332

Abstract: The NOAA/AVHRR images of the brightness temperature difference of 11 and 12 μm bands are utilized to detect Asian dust events during 1997-2000, and compared successfully for the events in 1998 and 2000 with the results of an on-line dust tracer model coupled with Regional Atmospheric Modeling System taking into account the surface wind, vegetation and snow coverage. The GMS-5/VISSR images of the same type are also useful to detect the dust events with its high frequency of observation and wide spatial coverage, though the sensitivity to diffused dust is inferior to the AVHRR.

1. Introduction

Asian dust(Kosa) events are gigantic phenomena affecting the atmospheric environment in East Asia and northern Pacific. Here we report recent results on the satellite imagery of their transport and diffusion from the Chinese continent toward Pacific Ocean.

The split-window method to take the difference of AVHRR-4 and 5 has been utilized to estimate vapor amount in the air to get the sea surface temperature. Because of the opposite emissivity difference of lithic aerosol in 11 and 12 μm bands against water vapor, this method has been applied to detect volcanic clouds and discriminate them from water/ice clouds [1]. The same method is found to be useful in detecting the extension of the Asian dust very effectively [2]. Here we present a brief summary of the events during 1997-2000, analyzing mainly the NOAA/AVHRR data received at the station in Kagoshima University, with supplementary data including GMS/VISSR provided by Japan Weather Association.

2. Procedure for analyzing satellite images

We adopt the following steps for the detection of the Kosa aerosol in NOAA/AVHRR images:

Step 1. The raw data of AVHRR are converted into calibrated ones, where a 10 bit value n_i of thermal infrared band i corresponds to the brightness temperature t_i in centigrade as $t_i = -50 + 0.1\, n_i$, for $i = 4, 5$.

Step 2. Geometrically corrected sub-scene data is obtained from a calibrated full-scene data. The form of sub-scene data is equi-distance description concerning the longitude and latitude. The reduction scale of a sub-scene is fixed for a series of the data.

Step 3. The brightness temperature difference of channels 4 and 5 is computed to obtain the Aerosol Vapor Index(AVI) defined as $AVI = n_5 - n_4 + 200$.

Step 4. The 10 bit data of AVI and the AVHRR chs. 1-4 in the daytime, or 3-4 in the nighttime, are converted into 16 bit without changing values.

Step 5. The JPEG or GIF images of AVI are obtained with a common gray scale for a sequence of the scenes in the date and time. Pair of output images within three hours are mosaicked into one for wider coverage.

Step 6. The AVI images with possible supplementary images are edited into a part of the quick report in http://www-sci.edu.kagoshima-u.ac.jp/sing/kosa/kosa-e.htm.

In the gray scale images, bright parts correspond to high AVI domains, i.e. $t_4 << t_5$, where the Kosa aerosol is expected to be dense. On the other hand, we follow the convention to assign bright parts to low values of t_4 in thermal images, so that clouds are white.

Dense aerosol in the daytime scenes may be seen in visible(AVHRR-1) and near-infrared (AVHRR-2) images as vague and relatively bright object in the gray scale corresponding to somewhat large values of n_1 and n_2. Comparative study of AVHRR-1, 2 and 4 with AVI may be useful to discriminate dense dust in the air from arid land without vegetation, which is also expected to be bright in AVI images.

3. Events during 1997-2000

(i) April 1997

Very dense dusts are seen in the AVI images around Ala Shan desert on 5 and 7 April, and diffused dusts toward east over Korea and the Sea of Japan in the following days up to 14 April [3]. They are consistent with Kosa records by the observatories of Japan Meteorological Agency in Kyushu and north-west side of Japanese peninsula, i.e., San-in and Hokuriku, and also with the back-trajectory analysis with ADEOSS/POLDER observation [4].

(ii) April 1998

An upraise of heavy dust in the northwest China is found in an AVI image on 15 April. In the images in the succeeding days, its slow transport southeastward is seen with the motion of a cut-off vortex over the Chinese continent, the Yellow Sea, Korean peninsula, Japanese Islands to the Pacific Ocean, extending and diffusing with the advance until 20 April [2]. This episode has been studied extensively by Asian Network Group of Lidar observation [5].

Another upraise of the dust is found in the NOAA images on 19 April around the Chinese-Mongolian border. Dense dust area extended on the next day toward the east covering the northeast part of China [6], and then moved quickly toward the east on 21 April over the Maritime Provinces and Sakhalin Island. Further transport of this dust domain in the northern Pacific can be traced by the NOAA images up to 23 April. Furthermore, trans-Pacific transport of aerosol reaching North America was seen in SeaWiFS images [7]. The satellite images of these dust events are well reproduced by an on-line dust tracer model coupled with Regional Atmospheric Modeling System taking into account the surface wind, vegetation and snow coverage [8].

(iii) January 1999

On 26 January, the first Kosa in 1999 was observed in western Japan including Ryukyu Islands,

with remarkable dust-falls along the Sea of Japan and snow-covered central mountains in Japan. In a series of AVI images of AVHRR [9], we see very dense and wide-spread dust around Ala Shan and Ordos deserts in northern China at 18 JST on 24 January. At 4:24 next day, very dense dust moved over Liaodong Peninsula, surrounded by diffused one over the northern and central parts of China. In the evening at 17:27, dense Kosa was covering Korean peninsula. In the daytime images on 26 January, diffused Kosa is covering northern China, Korea and Japan. At a few places in Korea, sharp peaks of total suspended particulate, about 800 $\mu g/m^3$ were recorded on 25 January, followed by mild peaks about 300-700 $\mu g/m^3$ next day[10], in accord with the AVI images. The upraise of Kosa on 24 January could be attributed to strong low-level wind over the desert area in China with high temperature and less precipitation [10].

(iv) April 1999

Strong wind by low-pressure system of the cut-off vortex type caused the upraise of Kosa dust in the Loess Plateau of China on 4 April, as clearly seen in an AVI image at 18:39. The advection and diffusion of this dust from northern China towards Japan passing over the East China Sea was brought by the slow advent of this cut-off vortex towards south-east, as seen in a series of NOAA AVI images [11].

(v) March 2000

The frequency and intensity of dust events in 2000, from the end of February until the middle of May, were remarkable during decades. We have displayed the AVI images of NOAA in our home page as fast as possible. Here we discuss only a few of remarkable events in March and April. In southwestern Japan, the first clear Kosa event was recorded on 7 March. This may be traced back to an AVI image of NOAA in the afternoon on 6 March shown in Fig. 1, where dense dust is seen north to Liaodong Peninsula in China. A cut-off vortex over the northeast part of China is seen near-by.

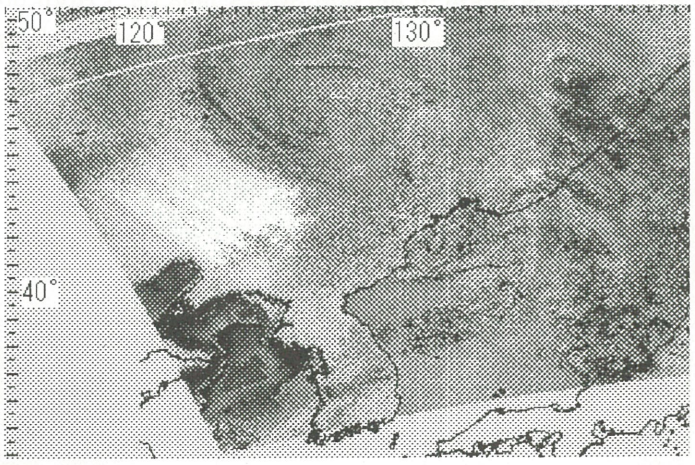

Fig. 1. NOAA AVI image at 16:43 JST on 6 March 2000.

At Chongwon, Korea, peaks of total suspended particulate exceeding 300 $\mu g/m^3$ were recorded on 3, 7 and 17, followed by 1400 $\mu g/m^3$ on 23 in March [12]. The episode of the dust, which brought extremely dense event in Korea on 23 March, started on 21 March by the low over Gobi and Ordos areas, as seen by comparing the GMS-5 satellite images and simulation results by 6-hour intervals. For this episode, we have utilized the AVI images obtained from IR1 and IR2 of GMS-5/VISSR, processed by Japan Weather

Association, as

$$AVI = N_2 - N_1 + 100,$$

where N_i is related to the brightness temperature of IRi in centigrade as $t_i = 0.5\ N_i - 85$, for i=1, 2. Fig. 2a illustrates an AVI image of GMS-5 at 21 JST on 23, and the corresponding column density distribution at the same time by the RAMS simulation. We see the dense dust trapped by the low in the cloud-free area near-by and in-between the clouds. This dust arrived at Kyushu in Japan next day, and also in Taiwan on subsequent days [13, 14].

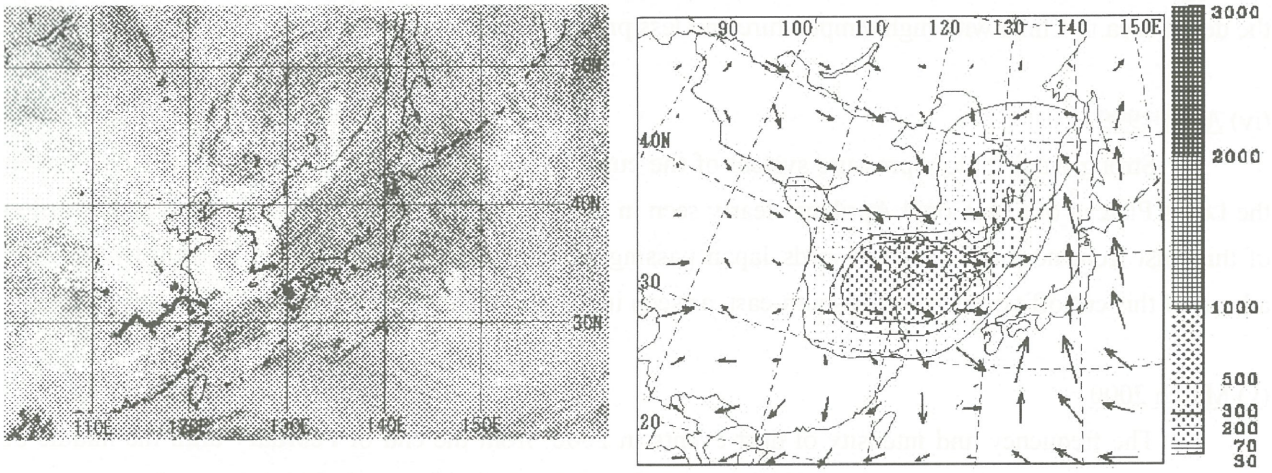

Fig. 2. A comparison of an AVI image of GMS-5(a) and the column density distribution ($\mu g\ /m^3$) by the RAMS simulation(b) at 21 JST on 23 March 2000.

(vi) April 2000

Dust storm in the northwest China on 5 April brought very dense dust over Beijing area next day [15]. Total suspended particulate at Chongwon, Korea on 7 April recorded 1200 which was the second peak in 2000[12]. A belt of dense dust across Korean peninsula is seen in an AVI image of NOAA/AVHRR in this afternoon as shown in Fig. 3. Remarkably dense dust was observed in Tokyo on 8 April with the maximum 600 per litter of the optical counter value of particles with the diameters greater than 5 μm, exceeding the corresponding value 233 at Nagasaki in western Japan [16].

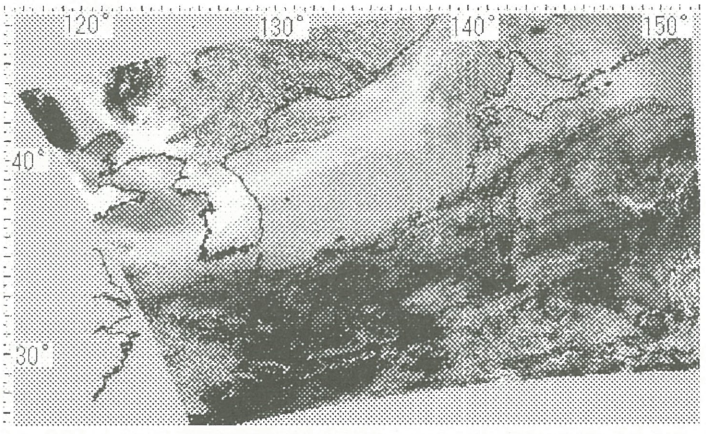

Fig. 3. NOAA-AVI image at 15:14 JST on 7 April 2000.

Many other dense dust events were seen in the AVI images of NOAA/AVHRR as well as GMS until the middle of May this year, successively starting from north-western China, travelling eastwards and covering Korean Peninsula and Japanese Islands. Especially, very dense dust was seen on 24 April over the Gobi and Ordos deserts, and transported almost southward along the east coast of the continent in the succeeding days. This episode brought high concentration events of particulate matter in various stations in Taiwan [14]. The backward trajectory analysis of this episode [14] agrees fairly well with the satellite images of the dust transport.

In the spring 2000, it was reported that the grasslands in Mongolia, especially around Dornogobi south of Ulan Bator, had been heavily damaged by field-mice abnormally increased [17]. This is compatible with the satellite observation of successive dense dust events in northern China, starting frequently from around the Gobi area.

4. Concluding remarks

The AVI images of NOAA/AVHRR and GMS/VISSR, exhibiting the brightness temperature difference in the thermal infrared bands, are very effective in detecting the rise, transport and diffusion of the Asian dusts over East Asia, as we have studied for the events from 1997 to 2000. Here, we make a few remarks on remaining problems.

Bright AVI signals are not limited to the dust in the air, but may possibly come from arid surfaces without vegetation especially in the desert areas in the central Asia. In the daytime, we may recognize the dust in visible and near-infrared images with relatively high resolution from the texture properties of them. Thermal images in day- and night-times are also helpful, as the temperature of the bare surface is quite different from one of the dust in the air. The time sequence of the AVI images and the weather patterns may also give clues to the recognition of the dust storm. In this respect, the simulation with enough weather information is useful. For instance, in comparing GMS AVI images with the simulated results during 21-27 March 2000, we found relatively bright domains of AVI in north-western China on 24 March images without corresponding dust storm. Such domains may be regarded as arid lands without much aerosol in the air.

We may hope to obtain quantitative estimate of diffused dust over the sea from the AVI values, if we could separate water vapor contribution. The latter may be computed as the column amount of precipitable water from the zonde data of upper air [19] and GPS retardation data [20].

The results on the events in 2000 presented here are rather preliminary. We have to compare the satellite data with the lidar observations, surface data and simulation results in more details.

Acknowledgements: We are grateful to Prof. T.Murayama and the members of LINK-J and Kosa Network for on-line information. One of the authors (K.K.) is indebted to the participants of International Workshop on Aerosol-Cloud-Radiation Interaction over Desert Area, Dunhuang, China, Aug. 2000 for stimulating discussions. Two of the authors (I.U. and K.K.) are thankful to the participants who provided new results on the transport of the Asian dust in 2000 at 7th Int. Conf. Atmospheric Sci. and Applications to Air Quality, Taipei, Oct.-Nov. 2000. We are grateful to Japan Science and Technology Corporation for supporting this work as a part of the ACT-JST project, Integration of Regional Meteorology and Chemical Transport Modeling over the East Asia, and also to the administration committee of the satellite data station in Kagoshima University for the on-line use of NOAA/AVHRR data.

References

[1] K.Kinoshita, S.Hosoyamada, A.Goto and S.Saitoh, NOAA-AVHRR imagery of volcanic clouds in Kyushu, Japan, Proc. 1993 Int. Geoscience and Remote Sensing Symposium, Tokyo, 1993, p.1824; N.Iino et al., these Proceedings, and papers cited therein.

[2] K.Kinoshita, M.Nishinosono, T.Yano, N.Iino, and I.Uno, Detection and analysis of Kosa using NOAA/AVHRR data, 26th Conf. Rem. Sens. Soc. Japan, 1999, p.253 (in Japanese), and references cited therein.

[3] N.Iino, R.Iwasaki, K.Kinoshita, T.Masumizu, and T.Yano, Time-series analysis of the dispersion of Kosa in April 1997 by the meteorological satellite NOAA, Kyushu Branch Conf. Met. Soc. Japan, 2000, p.1 (in Japanese).

[4] M.Kodama, N.Murata T.Inui and T.Kusaka, Estimation of the distribution of "Kosa" in satellite-leveled data using the long-range transport simulation, 26th Conf. Rem. Sens. Soc. Japan, 1999, p.257(in Japanese).

[5] T.Murayama, N.Sugimoto, I.Uno, K.Kinoshita, K.Aoki, N.Hagiwara, Z.Liu, I.Matsui, T. Sakai, T.Shibata, K.Arao, B.-J.Sohn, J.-G.Won, S.-C. Yoon, T.Li, J.Zhou, H.Hu, M.Abo, K.Iokibe, R.Koga, and Y.Iwasaka, Ground-based network observation of Asian dust events of April 1998 in East Asia, JGR, dust issue, 2001(in press).

[6] K.Kinoshita, R.Iwasaki, N.Iino, I.Uno and H.Amano, Wide area analysis of Asian dust events in April 1998 by NOAA data, 28th Conf. Rem. Sens. Soc. Japan, 2000, p.9 (in Japanese).

[7] See http://capita.wustl.edu/Asia-FarEast

[8] I.Uno, H.Amano, S.Emori, K.Kinoshita, I.Matsui and N.Sugimoto, Trans-Pacific Yellow Sand Transport observed in April 1998, - Numerical Simulation, JGR Dust Special Issue、2001 (in press).

[9] T.Masumizu, K.Kinoshita, N.Iino, T.Yano, R.Iwasaki and I.Uno, Analysis of advection and dispersion of Kosa in Jan. 1999 using NOAA satellite data, 27th Conf. Remote Sensing Soc. Japan, 1999, p.253 (in Japanese).

[10] B.-G.Kim and S.-U.Park, Transport and evolution of winter-time yellow sand observed in Korea, Atmos. Env., 2000 (in press).

[11] R.Iwasaki and K.Kinoshita, Optimization of the detection procedure of Kosa in NOAA satellite data, Kyushu Branch Meeting of Rem. Sens. Soc. Japan, Aug. 1999(in Japanese).

[12] Y.S.Chung, 2000, in www.kccar.re.kr

[13] M.T.Cheng, Y.C.Lin, C.P.Chio and C.E.Wang, Characterization of metallic elements in fine and course aerosols collected in central Taiwan during Asian dust-storm episodes, ASAAQ2000, 1D-3.

[14] T.-H.Lin, Long-range transport of yellow sand to Taiwan in spring 2000: observed evidence and simulation, ASAAQ2000, PD2-6.

[15] P.Wang, M.Duang and W.Zhang, The preliminary study of remote sensing of China dust aerosols, International Workshop on Aerosol-Cloud-Radiation Interaction over Desert Area, Dunhuang, China, Aug. 2000.

[16] T.Murayama and K.Arao, LINK-J communications, 2000.

[17] A news on 24 April 2000 by Kyodo-Tsushin, Japan.

[18] M.Nakamura, K.Kinoshita, N.Iino, J.Kohno and H.Kikukawa, NOAA/AVHRR data and the amount of precipitable water, Mem. Fach. Fish. Kagoshima Univ., **49**, 9, 2000.

[19] A.Kondoh et al., Construction of GPS vapor information system for interdisciplinary studies, Proc. Int. Symp. Atmospheric Correction of Satellite Data and Its Application to Global Environment, CEReS, p.65, 1998; CEReS GPS-Meteorology page, http://133.82.233.178/gpsmet/

Satellite imagery of ash clouds of the 2000 eruption of Miyake-jima Volcano

N. Iino[1], K. Kinoshita[2], M. Koyamada[2], S. Saitoh[3], K. Maeno[3] and C. Kanagaki[4]

[1] Faculty of Engineering, Kagoshima University, 1-21-40, Korimoto, Kagoshima 890-0065
[2] Faculty of Education, Kagoshima University, Kagoshima 890-0065
[3] Faculty of Fisheries, Hokkaido University, Hakodate 041-8611
[4] Hondo-higashi Junior High School, Hondo 863-0041
E-mail 1: iino@mech.kagoshima-u.ac.jp

Abstract

We analyze GMS/VISSR images for big eruptions in August 2000 and the NOAA/AVHRR images in August and September to detect the volcanic clouds from Miyake-jima. Furthermore, we discuss the dispersion of volcanic clouds corresponding to the SO_2 high concentration episodes in Main Island of Japan by comparing the satellite images with simulation results of a vertical shear model.

Keywords: GMS/VISSR, NOAA/AVHRR, vertical shear, plume, volcanic gas

1. Introduction

Miyake-jima volcano, about 160 km south from Tokyo, started eruptive activities at the summit Oyama (814 m) on 8 July 2000. Big eruptions were recorded on 10, 18 and 29 August with the altitudes of volcanic clouds about 8, 15 and 8 km, respectively. Since 28 August, volcanic clouds and gas toward Main Island of Japan caused high concentration events of SO_2 at many ground stations 100-400 km leeward from Miyake-jima. Although big eruptions were not recorded since September, and plume heights were less than 3000 m above the sea level, the estimated emission of SO_2 increased to 20-30 kt/day since the middle of September. Southern and south-westerly winds brought the volcanic gas to the Main Island of Japan, where the smells of sulfur and/or H_2S were reported in various places. Since October, gray ash clouds are hardly seen, and the plumes turned out to be white with the heights less than 1500 m above the sea level after the middle of that month. However, very high level of gas emission has continued.

In this study, we analyze GMS/VISSR images for three big eruptions in August, and 29 scenes of NOAA/AVHRR images during August 28 – September 27 to detect the volcanic clouds from Miyake-jima, and also compare with other satellite images found in the Internet. Furthermore, we discuss the satellite images of volcanic clouds corresponding to the SO_2 high concentration episodes recorded in central part of Japan, August 28 in Kanto area and September 13-15 in Chubu district, by comparing the dispersion of volcanic clouds in the satellite images and gas informations at the surface with the simulation result of a vertical shear model based on the upper wind data.

2. Informations on volcanic ejecta and methods of analyses

Many detailed informations on the activities of Miyake-jima volcano are publicized in various web-sites in the Internet with almost real-time and mostly in Japanese. Some of them are well archived. These informations are very helpful in our analysis of the dispersion of volcanic ejecta in addition to the satellite images and meteorological data.

2-1. Satellite data and their analysis

GMS-5/VISSR data with visible (VIS) and thermal infrared (IR1 and IR2) bands provided by Japan Weather Association (JWA) are analyzed concerning three big eruptions in August. GMS images at one-hour intervals are suited to see the time developments of big eruptions.

NOAA/AVHRR and other satellite data of the volcanic clouds at Miyake-jima are listed in Table 1, together with observation results of volcanic clouds from helicopters in Geological Survey of Japan (GSJ) home page: http://www.gsj.go.jp/~yagi/miyake/heliobs.html. Volcanic clouds from Miyake-jima were recognized as bright objects in visible and near infrared images. Although it is difficult to discriminate between the volcanic clouds and meteorological ones by these grayscale images, their advection shapes from the crater may be taken as clues for our understanding. Satellite imagery characteristics of volcanic clouds for various bands are described in detail in the references [1, 2]. As for the daytime NOAA/AVHRR data, the false color composite images by assigning n(4), n(2) and n(1) to blue, green and red colors are useful to

detect the volcanic clouds and discriminate them from meteorological ones.

In our previous studies, the split-window method taking the difference of AVHRR-4 and 5 (dT = T(4) – T(5)) was very useful for the discrimination of volcanic clouds of Mt. Sakurajima and Mt. Aso from meteorological ones [1-3]. This is due to the ash components with emissivity at 12 μm higher than at 11 μm, and similar response to dT is expected from the sulfuric acid aerosol in the downstream [4]. This method can be applied in monitoring large volcanic eruption by GMS-5/VISSR [5].

NOAA/AVHRR images received at Kagoshima University (K-N) are provided as a 10-bit data. The original data are converted into 16-bit data where the value n(i) of thermal infrared band i corresponds to the brightness temperature T(i) in degrees centigrade as $T(i) = -50 + 0.1 \times n(i)$, i = 4, 5. On the other hand, the data provided by Hokkaido University (H-N) is an 8-bit format, thus $T(i) = - X + Y \times n(i)$, i = 4, 5, where X = 10 and Y=0.2, except for the * marked data, where X = 30 and Y = 0.3.

In this study, as an expression of the brightness temperature difference, we define the Aerosol Vapor Index (AVI) as

AVI = n(5) - n(4) + Z, for NOAA/AVHRR with Z = 200 (K-N) or 100 (H-N)

AVI = IR2 – IR1 + 100, for GMS/VISSR

Table 1 Satellite data of volcanic clouds from Miyake-jima. Dir. and L denote the direction and length of a volcanic cloud, respectively. The data sources are denoted as K, H and I for Kagoshima University, Hokkaido University and Internet web-sites, respectively. The mark + denotes the case that plume flow exceeded the image scene. The mark – denotes the cases without signal and no comment. The observation results of volcanic clouds from helicopters are also listed from GSJ home page.

2000	JST	Sat.	Dir.	L(km)	Source	Observation of volcanic clouds from a helicopter			
						height (m) above sea level	color	advection dir.	comment
8/28	4:39	NOAA-14	–	–	H				
	5:51	NOAA-12	NW	49	K				
	9:54	Landsat-5	NW-N	188	I				
	12:00	SeaWiFS	NNW-NE	312	I				
	17:07	NOAA-12	N-NE	179	K				
8/29	4:27	NOAA-14	Erupt.	–	H				
	5:28	NOAA-12	NE	18	H*				
	7:59	NOAA-15	NE	46	K				
	10:42	ASTER	N-NE	54	I				
	12:00	SeaWiFS	N-NE	300+	I				
	15:51	NOAA-14	N-E	280	H*				
	16:46	NOAA-12	N-E	218	K				
9/3	11:01	ASTER	W	38+	I				
9/6	17:03	NOAA-12	NE	58	K				
9/7	16:40	NOAA-12	NNE	19	K				
9/9	3:59	NOAA-14	N	62	H				
	15:23	NOAA-14	N-NNE	215	H	2200	dark gray	N	–
	15:56	NOAA-12	NNE	115+	K				
9/10	15:11	NOAA-14	N-NNE	152	H				
	17:12	NOAA-12	NNE	77	K	2200	dark gray	N	–
9/12	5:09	NOAA-12	NNE	31	H	1700	white	N-NNE	Ash
	16:27	NOAA-12	NE	58	K				
9/13	4:53	NOAA-14	NNW	32	H	1900	white	–	–
	9:54	Landsat-5	W-NW	88	I				
9/14	4:42	NOAA-14	NW	25	H				
	6:05	NOAA-12	NW	62	K				
	16:05	NOAA-14	NW	165	H				
9/15	4:30	NOAA-14	–	–	H				
	5:42	NOAA-12	WNW	11	K	2500	white	W-WNW	–
	15:53	NOAA-14	N-W	239	H				
9/18	6:35	NOAA-12	NNE	77+	K	1500	white – white gray	E	Ash
	10:28	SPOT-1	NE	17+	I				
9/21	16:51	NOAA-12	SSW	192	K	2000	white	SE	–
9/22	10:20	SPOT-2	W	10+	I				
9/24	16:53	NOAA-12	ESS	19	K				
9/25	5:14	NOAA-12	E	65	K	1800	white	E-ESE	–
9/26	16:08	NOAA-12	SE	115	K				
9/27	10:24	SPOT-2	E	10+	I	2500	white – white gray	upper layer: SW lower layer:SE	Ash

LANDSAT and SPOT images on Miyake-jima are found in NASDA-EOC home page: http://www.eoc.nasda.go.jp/guide/topics/news/miyake/miyake_iland_j.html. ASTER images are displayed in ERSDAC home page at http://www.gds.aster.ersdac.or.jp/gds_www2000/gallery_e/image_miyake_e/set_image_miyake_e.html. SeaWiFS images can be seen in NASA home page at http://visibleearth.nasa.gov/Sensors/OrbView-2/SeaWiFS.html.

2-2. Meteorological data and vertical shear model

Upper air data by means of radio-sonde measurements are obtained at observation points illustrated in Fig.1. In addition, surface weather charts are also considered.

To investigate the advection and dispersion of volcanic clouds and gas corresponding to SO_2 high concentration episodes in Kanto area and Chubu district in conjunction with satellite images, we simulate the dispersion of volcanic clouds based on a simple vertical shear model (VSM) using upper wind data [2]. In this study, we assume that the volcanic gas behaves almost together with volcanic clouds, on the bases of previous analysis of Sakurajima volcano [1].

As shown in Fig. 1, the nearest station of upper air observation is Hachijojima. We confirmed that the wind field around Miyake-jima is well approximated by the Hachijojima-winds in most cases, based on the advection of volcanic clouds seen in the satellite images and ground-observation informations. For simplicity, we assume that the wind field is uniform at certain height and time, and we use only the wind data of Hachijojima observed at six-hour intervals at standard pressure levels, 925, 900, 850, 800 and 700 hPa which correspond to the altitudes about 790, 1000, 1500, 2000 and 3100 m, respectively. We first get the upper-wind data set in height and time at intervals of 10 hPa and one hour, respectively by the linear interpolation for wind speeds and directions. In the interpolation, we choose the wind directions so that the variations never exceed 180 degrees.

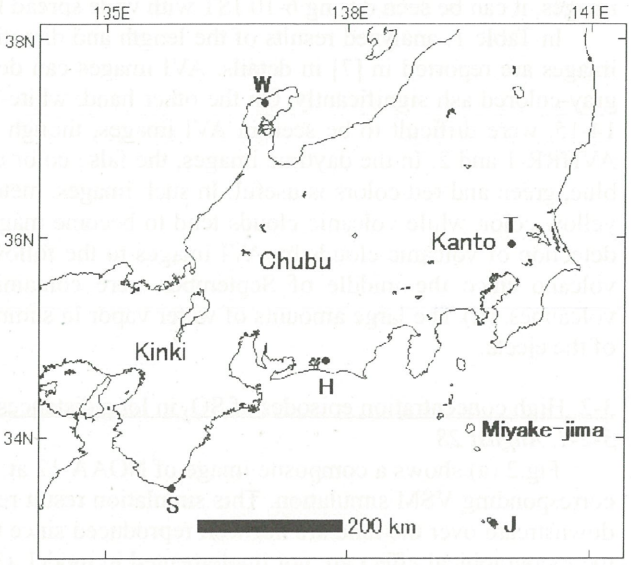

Fig. 1 Observation points of upper air in central part of Japan, denoted as H: Hamamatsu, J: Hachijojima, S: Sionomisaki, T: Tateno and W: Wajima.

We calculate the locations of dimensionless, weightless particles at 1-hour increments after they are released into the atmosphere at specified pressure-altitudes above the volcano. The model's ideal particles remain at the initial pressure-altitudes which are released. Emission rate of particles is assumed to be constant for a certain time interval, and the positions of them at a certain time are displayed corresponding to the satellite images of volcanic clouds.

2-3. SO_2 concentration and other informations

The estimates of total SO_2 emission by the correlation spectrometer (COSPEC) data are shown in the home pages of GSJ and Japan Meteorological Agency: http://www.gsj.go.jp/~imiyagi/Works/Event/Miyake2000/geol/000916cospec/ and http://www.kishou.go.jp/miyake/jyoukyo/1116.pdf, respectively.

The one-hour values of SO2 concentration in Tokyo were provided by Tokyo Metropolitan Government, as analyzed in details in [6].

Other informations, such as volcanic activities and plume photos are collected from Internet news and related home pages. Especially, the reports of habitants about the smells of H_2S and/or SO_2 are obtained via Internet BBS: http://www.jah.ne.jp/%7Echili/camp/nagaya.cgi?room=005.

3. Results and discussions

3-1. Satellite imagery of volcanic clouds

GMS/VISSR images for three big eruptions in August were analyzed. Although spatial distributions of them are rather limited, they can be seen in AVI images. We will discuss the observation time of each scene based on the filename time according to JWA. As for the eruption at 6:30 on August 10, the eruption clouds

are seen as small but bright clear objects with linear shape in 9 and 10 JST images. The dispersion of time-series of the eruption cloud after the eruption at 17:02 on August 18 can be seen during 18-24 JST image, though the volcanic clouds were merged with meteorological ones. In these images, two directional flows toward NW and SE are recognized, and this behavior is explained well by the PUFF Model simulation result in http://www.geo.tsukuba.ac.jp/~tanaka/tanaka/m0818b.html. After the eruption at 4:35 on August 29, the ejected clouds were detected with both AVI images of the GMS/VISSR and NOAA/AVHRR. In the GMS images, it can be seen during 6-10 JST with wide spread form.

In Table 1, analyzed results of the length and direction of volcanic plumes are also listed. A part of the images are reported in [7] in details. AVI images can detect the eruption clouds and the plumes containing gray-colored ash significantly. On the other hand, white-colored volcanic clouds, for instance on September 14-15, were difficult to be seen in AVI images, though it can be detected easily by single band images of AVHRR-1 and 2. In the daytime images, the false color composite image by assigning n(4), n(2) and n(1) to blue, green and red colors is useful. In such images, meteorological clouds at high altitudes are displayed in yellow color, while volcanic clouds tend to become magenta colored. We may attribute the difficulty of the detection of volcanic clouds by AVI images to the following reasons: (i) Plumes ejected from Miyake-jima volcano since the middle of September were containing less silicates than from Sakurajima and Aso volcanoes. (ii) The large amounts of water vapor in summer above the volcanic clouds cancel the AVI signal of the ejecta.

3-2. High concentration episodes of SO_2 in long distances

3-2-1. August 28

Fig.2 (a) shows a composite image of NOAA-12 at 17:07 on 28 August 2000, and Fig.2 (b) illustrates a corresponding VSM simulation. This simulation result reproduces well the upstream of the plume, while the downstream over the land are not well reproduced since the advection near the surface by the sea breeze and the topographical effect are not implemented in model. On this day, the SO_2 high concentration values at the surface were reported all over Kanto area such as Tokyo, Kanagawa, Shizuoka, Saitama and Gunma in the daytime, as shown in Atmospheric Environmental Regional Observation System (AEROS). The maximum values were recorded during 12:00-14:00. This may be due to the convection mixing developed in the daytime to pull down the gas in the plume in the upper air to the surface. The distribution of these high concentration points corresponds well to the dispersion of volcanic clouds demonstrated in the satellite images and to the detailed simulation of the convection mixing by the SPEEDI of Japan Atomic Energy Research Institute: http://www.jaeri.go.jp/genken/press/000907kan/index.html.

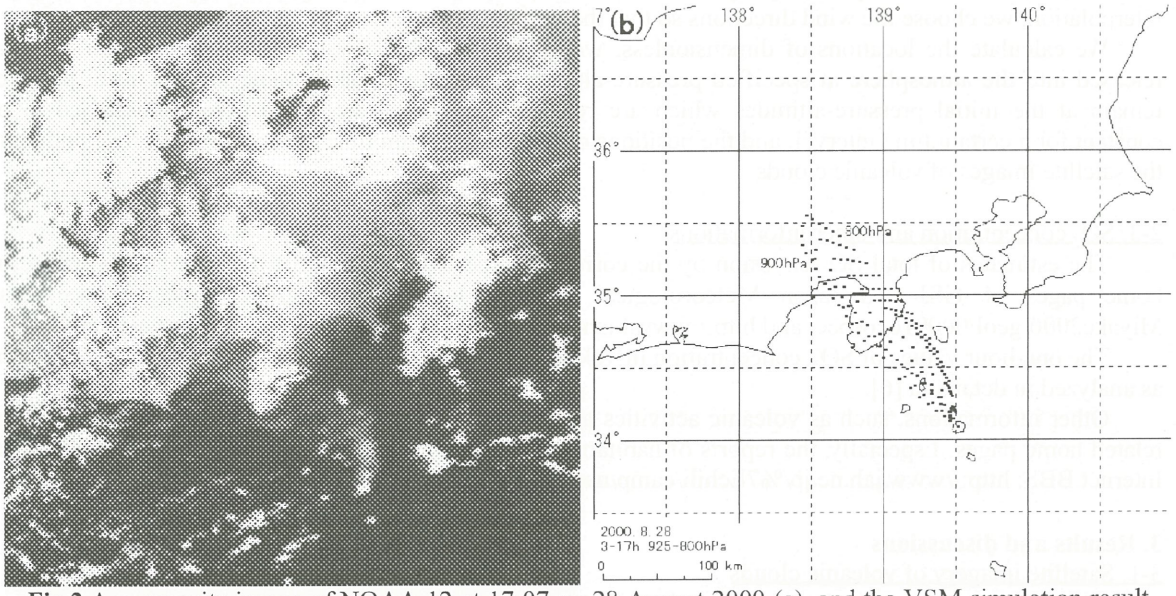

Fig.2 A composite image of NOAA-12 at 17:07 on 28 August 2000 (a), and the VSM simulation result at 925-800 hPa for the ejection during 3-17 JST (b).

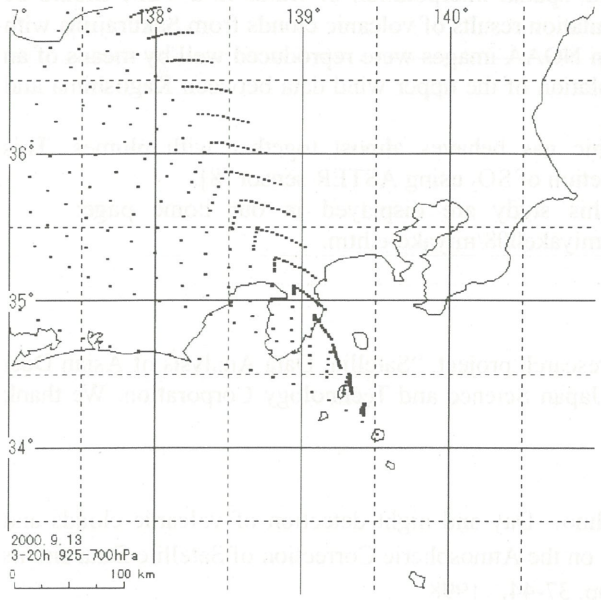

Fig. 3 Simulation result at 925-700 hPa for the ejection during 3-20 JST on 13 September 2000

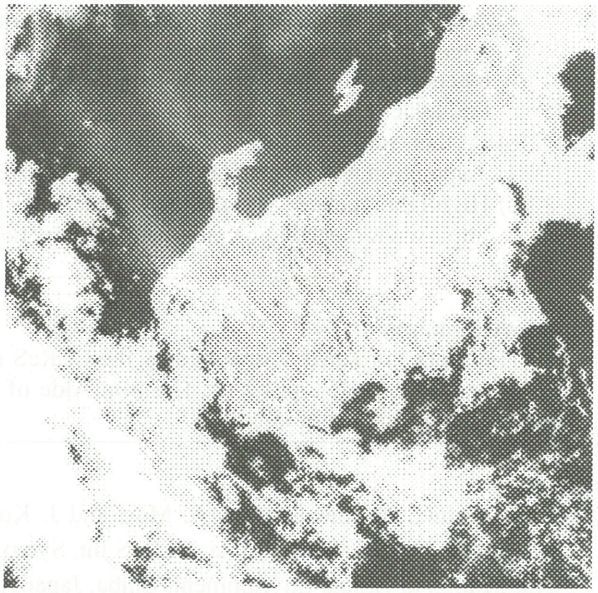

Fig. 4 A composite image of NOAA-14 at 15:53 on 15 September 2000

3-2-2. September 13-15

In these days, SO_2 high concentration records from various stations were reported in Chubu district. Volcanic clouds flowing toward NW due to the wind around typhoon stagnating in south-western direction are seen in satellite images. Fig. 3 illustrates the simulation result at 925-700 hPa for the ejection during 3-20 h, on September 13 which is similar to the PUFF Model simulation at the University of Tsukuba: http://www.geo.tsukuba.ac.jp/~tanaka/tanaka/m0913a.html. We may infer that the high concentration events at Nagano caused by the plume flowed at the altitude of 2000-3000 m with collimated winds, and it is understood that the smells of sulfur and/or H_2S in the northern-part of Kinki and the high concentration values observed at night in Kyoto were due to the dispersion owing to the large vertical wind shear at the altitudes less than 2000 m. Similar results of the simulation and satellite images are obtained the next day.

On the other hand, a composite AVHRR image at 15:53 on September 15 shown in Fig.4 indicates the long-range advection of volcanic cloud reached to the Sea of Japan, which is in accord with the high concentration values observed at the both sides of central mountains in Main Island, i. e., Gifu and Fukui, and also with the simulation result.

4. Concluding remarks

We have analyzed GMS/VISSR images for three big eruptions in August and 29 scenes of NOAA/AVHRR images during August 28 - September 27 to detect the volcanic clouds from Miyake-jima. Furthermore, we have discussed the satellite images of volcanic clouds corresponding to the SO_2 high concentration events recorded in central parts of Japan, August 28 in Kanto area and September 13-15 in Chubu district, and these VSM simulations to describe the dispersion of them. The results are summarized as follows:

(1) The eruption clouds and ash plumes from Miyake-jima volcano were detected in AVI images.

(2) As for the white plumes, the false color composite image by assigning n(4), n(2) and n(1) to blue, green and red colors is very useful. It is possible to discriminate between the volcanic clouds and the meteorological ones by color tones.

(3) The dispersion of volcanic clouds corresponding to the distribution of the SO_2 high concentration points are understood by means of a simple vertical shear model based on the upper wind data of Hachijojima.

Here let us make a few remarks on remaining problems.

(a) Instead of the uniformity of upper wind field, spatial interpolation of winds in a VSM should be considered. In our previous study [2], the simulation results of volcanic clouds from Sakurajima with a long-range advection toward north shown in NOAA images were reproduced well by means of an extended VSM that performed spatial interpolation of the upper wind data between Kagoshima and Fukuoka.

(b) In this study, we assumed that the volcanic gas behaves almost together with plumes. This assumption will be clarified by the direct detection of SO_2 using ASTER sensor [8].

(c) Highlight scenes of satellite images of this study are displayed in our home page: http://www.mech.kagoshima-u.ac.jp/lab/netu/miyake008/miyake-e.htm.

Acknowledgments

This work is partially supported by the CEReS research project, "Satellite Data Analysis of Asian Dust and Volcanic Aerosol" and by the Grant-in-Aide of Japan Science and Technology Corporation. We thank very much to these institutions.

References

[1] K. Kinoshita, N. Iino, I. Uno, A. Mori and J. Kohno, Day and night detection of volcanic clouds and aerosol by NOAA/AVHRR data, CEReS Int. Symp. on the Atmospheric Correction of Satellite Data and its Application to Global Environment, Chiba, Japan, pp. 37-44, 1998.

[2] N. Iino, K. Kinoshita, T. Yano and S. Torii, Detection and morphology of volcanic ash clouds from Mt. Sakurajima in satellite images, The 3rd Pacific Symp. on Flow Visualization and Image Processing, Maui, Hawaii, U.S.A., 2001, in press.

[3] K. Kinoshita, S. Hosoyamada, A. Goto and S. Saitoh, NOAA-AVHRR imagery of volcanic clouds in Kyushu, Japan, Proc. Int. Geosci. and Rem. Sen. Symp., Tokyo, Japan, pp. 1824-1826. 1993,

[4] A. J. Prata, Observations of volcanic ash clouds in the 10-12 μm window using AVHRR/2 data, Int. J. Rem. Sens., Vol. 10, pp. 751-761, 1989.

[5] M. Tokuno, Satellite observation of volcanic ash clouds, Meteor. Sat. Center Tech. Note, Vol. 33, pp. 29-48, 1997.

[6] K. Kinoshita, C. Kanagaki, M. Koyamada and N. Iino, Behavior of volcanic gas at Miyake-jima and meteorological conditions, Western Regional Div. Rep. of Japan Group for the Study of Natural Disaster, No.25, 2001, in press (in Japanese).

[7] M. Koyamada, K. Kinoshita, N. Iino and C. Kanagaki, Flow of volcanic clouds and gas from Miyake-jima and satellite images analysis, Proc. 29th Japanese Conf. Rem. Sens., pp.37-40, 2000 (in Japanese with English abstract).

[8] M. Urai, K. Fukui, Y. Yamaguchi and D. C. Pieri, Volcano observation potential and global volcano monitoring plan with ASTER, Bull. Volcanological Soc. of Japan, Vol. 44, No.3, pp. 131-141, 1999 (in Japanese with English abstract).

A New Model on Surface-Atmospheric Coupled Radiation for Satellite Remote Sensing Application

Qiu Jinhuan

Institute of Atmospheric Physics, Chinese Academy o Sciences, Beijing 100029, China

Abstract

Based on the physical process of interaction of solar radiation with the surface and the atmosphere, a new model of on bidirectional reflectance surface—atmospheric coupled radiation is developed. In this model, the contribution of the bidirectional reflectance surface to the upwelling radiance at the top of the atmosphere is decomposed as the sum of three terms (or physically two term). The first two term is radiation contribution of total (dirrect+ diffussion) radiation arrived at surface, first reflected by the surface and then directly transmitted to the sensor.; while the third term is radiation contribution of the total radiation arrived at surface, first reflected by the surface and then diffused to the sensor. As shown in numerical simulation, this model is better than the 6S model. The standard error among 110112 sets of upward radiance data calculated by this model is 0.49%, which is about one fourth of the one by 6S. In the condition of the solar zenith angle $\theta_s \leq 75°$ and the viewing angle $\theta_v \leq 60°$, the error by the new model is usually smaller than 2.5%.

1. Introduction

A exact and available model on bidirectional reflectance surface- atmospheric coupled radiation is important for spaceborne remote sensing of the surface and the atmospheric aerosol parameter and so on. Spaceborne remote measurement of Earth's futures such as the surface reflectance, vegetation index, agricultural amount is affected by the surface-atmospheric radiative interaction. Therefore, a so-called atmospheric correction using the interaction model is needed to limit this effect, which is one of key techniques for quantitative application of spaceborne remote sensing. For a Lambertian surface, the upward radiance can be explicitly expressed as a function of surface reflectance. But the error resulting from the Lambertian assumption can be large for the bidirectional reflectance. Therefore, recently some efforts have been devoted to developing the bidirectional reflectance surface- atmospheric coupled radiation model. The 6S model (Vermote et al, 1997) is one of most famous models. In the model, the contribution of the target to the signal at the top of the atmosphere is decomposed as the sum of four terms. The radiance calculated by 6S can be evidently underestimed when the solar zenith angle is larger (Qiu, 2001). Based on the physical understanding of radiation interaction between

the atmosphere and surface, this paper develops a more exact bidirectional reflectance surface- atmospheric coupled radiation model

2. Surface-atmospheric Coupled Radiation Model

In the present model, the radiation reflectance at the top of the atmosphere, ρ_{TOA}, is decomposed as the sum of three terms, i.e.

$$\rho_{TOA}(\tau, \mu_s, \mu_v, \phi_s - \phi_v) = \rho_{Path} + \rho^{(1)} + \rho^{(2)} + \rho^{(3)}, \tag{1}$$

$$\rho^{(1)} = \exp(-\tau/\mu_v - \tau/\mu_s)\rho_s(\mu_s, \mu_v, \phi_s - \phi_v), \tag{2}$$

$$\rho^{(2)} = \exp(-\tau/\mu_v)t_d(\mu_s)\bar{\rho}/(1 - S\bar{\rho}), \tag{3}$$

$$\bar{\rho}(\mu_s, \mu_v, \phi) = \frac{\int_0^{2\pi}\int_0^1 \mu L^{\downarrow}_{Path}(\tau, \mu_s, \mu, \phi')\rho_s(\mu, \mu_v, \phi' - \phi)d\mu d\phi'}{\int_0^{2\pi}\int_0^1 \mu L^{\downarrow}_{Path}(\tau, \mu_s, \mu, \phi')d\mu d\phi'}, \tag{4}$$

$$\bar{\bar{\rho}} = \overline{\bar{\rho}(\mu_s, \mu_v, \phi)}, \tag{5}$$

In Eqs.1-5 ρ_{Path} is the path reflectance without being reflected by the surface; μ_v and μ_s are cosines of viewing and solar zenith angles; ϕ is the azimuth angle; S is the spherical atmospheric reflectance integrated over both zenith and azimuth directions, ρ_s is the surface pixel reflectance; t_d is the diffuse transmission of the atmosphere; τ is the total optical depth; $L^{\downarrow}_{Path}$ is the downward path radiance. First term, $\rho^{(1)}$, represents the radiation directly transmitted from the Sun to the surface, and then directly reflected back to the spaceborne sensor. The second term, $\rho^{(2)}$, is the radiation scattered by the atmosphere, then reflected by the surface and transmitted to the sensor. Therefore, the first two terms are radiation contribution of total (dirrect+ diffussion) radiation arrived at surface, first reflected by the surface and then directly transmitted to the sensor. The third term, $\rho^{(3)}$, is radiation contribution of the total radiation arrived at surface, first reflected by the surface and then diffused to the sensor. The third term must meet following flux equation:

$$F_{uTOA}(\mu_s, \rho_s) = F_{uPATH}(\mu_s) + F^{(1)} + F^{(2)} + F^{(3)}, \tag{6}$$

where F_{uTOA} and F_{uPATH} are the exact upward flux for the reflectance ρ_s and the path flux, respectively. Here $F^{(1)}$, $F^{(2)}$ and $F^{(3)}$ are three flux components, corresponding with three radiance components as shown in Eq.1, respectively. Then the third term is derived, by using Eq.6.

3. Numerical Simulation Tests

Considering that the Gauss-Seidel iterative algorithm (Herman and Browning, 1965; Qiu, 2001) is available for usually bidirectional surface, this paper uses it to solve radiative transfer equation. In order to improve accuracy, Gaussian integration over μ with 120 quadratic points, Sinpson integration over φ with a step of 5°, and the optical depth step of 0.005 are taken. The radiance is regarded as the "true" radiance in the error analysis later.

The semiempirical reflectance model presented by Rahman et al (1993) is used in the present simulations. Four kinds of surface BRDF are selected, which are soybean, plowed field, hard wheat and lawn.

Figs.1, 2 and 3 compare percent relative radiance errors by 6S and the present New Model (N-M) when θ_s=0°, 60° and 75°, respectively. Here other input parameters are: the hard wheat cover, the infrared channel, the Junge-type aerosol and τ=0.3.

For the case of θ_s=0° as shown in Fig.1, both 6S and N-M have a very good accuracy, and their maximum errors are 3.7% and 1.5%, standard errors are 0.0042% and 0.0065%, respectively, when θ_v is within ±60°. In an average sense, the accuracy of N-M is a little better. But when $-55° < \theta_v < 15°$, 6S has a little better accuracy than N-M.

For two cases of θ_s=60° and 75°, as shown in Fig.2 and Fig.3, the upward radiance solution by 6S is systematically underestimated as θ_v is within ±60°. The maximum error is 6.7%. But the maximum error by N-M is only 1.7%. N-M is evidently better than 6S.

By selecting the four surfaces of soybean, plowed field, hard wheat and lawn, a total 110112 sets of comparative radiance data are further simulated. The results show that the standard error among the all radiance data calculated by this new model is 0.49%, which is about one fourth of the one by 6S. In the condition of the solar zenith angle $\theta_s \leq 75°$ and the viewing angle $\theta_v \leq 60°$, the error by the present model is usually smaller than 2.5%.

References

Herman B M and Browning S R, 1965, A numerical solution to the equation of radiative transfer. *J. Atmos. Sci.*, 22: 559-566.

Qiu Jinhuan, 2001, An improved of surface BRDF- atmospheric coupled radiantion, IEEE Trans. Geosci. Remote Sens., Vol. 39, No.1.

Rahman H, Pinty B, Verstraete M M. 1993, Coupled surface-atmosphere reflectance (CSAR) model, 2. Semiempirical surface model usable with NOAA Advanced Very High Resolution Radiometer data. J. Geophys. Res., 98: 20791-20801.

Vermote E F, Tanre D, Deuze J L, et al, 1997, Second simulation of the satellite signal in the solar spectrum, 6S: an overview. IEEE Trans. Geosci. Remote Sens., 35: 675-686.

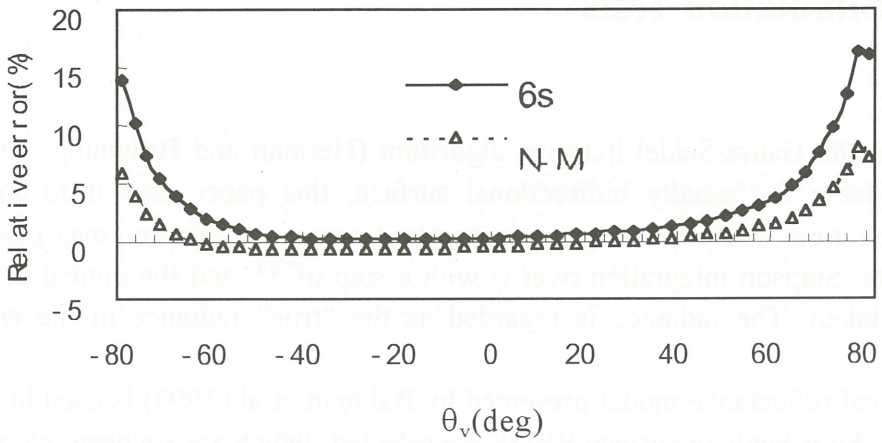

Fig.1 Relative upward radiance errors by 6S and N-M in the case of the wheat infrared channel and θ_s=0°.

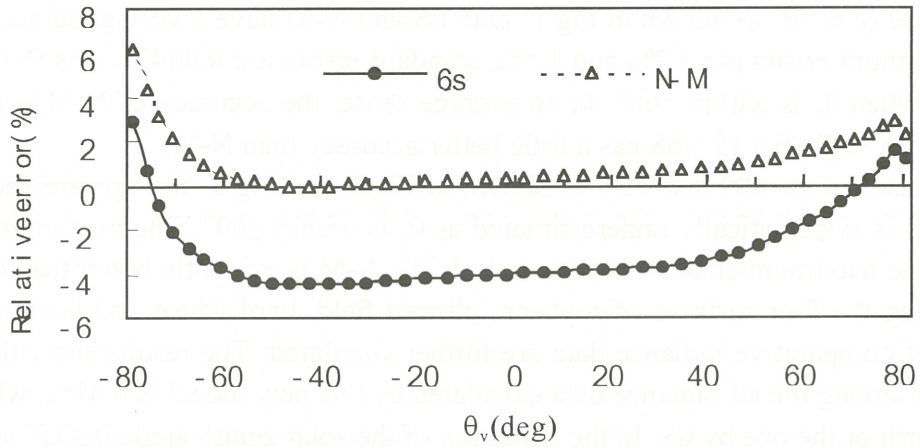

Fig.2 Same as in Fig.1 except for θ_s=60°.

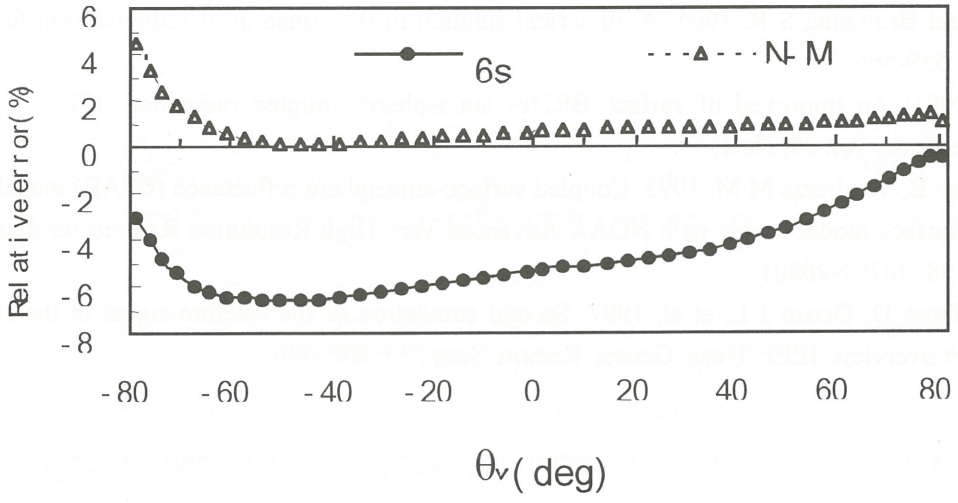

Fig.3 Same as in Fig.2 except for θ_s=75°.

AEROSOL OPTICAL PARAMETER RETRIEVAL FROM SATELLITE DATA

Yasuyuki Kimura, Toshiaki Izumiya and Yoshiyuki Kawata

Environ. Infor. Research Lab.,Kanazawa Institute of Technology,
Ogigaoka 7-1, Nonoichi, Ishikawa 921-8501, Japan

ABSTRACT

The satellite image data, measured by ADEOS/POLDER, ADEOS/OCTS and NOAA/AVHRR, were used to retrieve aerosol optical parameters. We examined two methods for retrieving local aerosol optical parameters using the ADEOS/POLDER data by comparing with the validation data. The first method is based on a R-P(Reflectance-Polarization) algorithm using both multi-directional reflectance and multi-directional polarization information in 865nm band. The second method is based on a R-R(Reflectance-Reflectance) algorithm using only multidirectional reflectance information in two infrared bands(670nm and 865nm). We found that the former gives better agreement with the measured sky validation data than the latter. Furthermore, the retrieval results by the R-R algorithm using the mono-directional reflectance data of ADEOS/OCTS and NOAA/AVHRR were compared with those of ADEOS/POLDER, based on the R-P algorithm. Although we had a relatively good agreement in the aerosol optical thickness among these algorithms, we found that the retrieval results of Ångström exponent are not reliable in the cases of the R-R algorithm using the reflectance data alone.

1. INTRODUCTION

The POLDER and OCTS were on board of the same ADEOS and they have nearly six identical spectral bands. POLDER was an imaging sensor with nadir ground resolusion of 7 km, whereas OCTS was a scanning sensor with that of 0.7 km. They had collected global data sets for about 8 months during the ADEOS's operational period (launched in August 1996 - ended in June 1997). Since the POLDER had unique capabilities of measuring both multi-directional radiance in 8 wavelength bands(443, 490, 565, 670, 763, 765, 865, and 910[nm]) and linear polarization in 3 bands(443, 670, and 865[nm]) reflected by the Earth's atmosphere-surface system, the retrieval of aerosol's three optical parameters(i.e., real part of refractive index, optical thickness, and Ångström exponent) may be possible. by using POLDER's mult-directional information. However, it is difficult to retrieve aerosol's real part of refractive index from the reflectance data by OCTS and NOAA/AVHRR, because they collects the radiance reflected by the target from only a mono-direction.

2. BASIC BACKGROUNDS

The incident solar flux vector in Stokes vector representation is given by Eq.(1).

$$\pi\mathbf{F}=\pi[f\ 0\ 0\ 0]^t \qquad (1)$$

where a superscript represents the matrix transposition. In this notation we assume an incident solar flux vector $\pi\mathbf{F}$ illuminates a zenith angle θ_0 and the solar azimuth angle ϕ_0, respectively. In the right side πf equals to the extraterrestrial irradiance per unit area

normal to the direction of solar rays, E_s[W/m^2]. Then, the upwelling Stokes vector at the top of the atmosphere (TOA) in the direction of (μ, ϕ), $\mathbf{I}(\tau_{at}, \mu, \mu_0, \phi - \phi_0) = [I\ Q\ U\ V]^t$ can be expressed by Eq.(2) in terms of the reflection matrix of the atmosphere-ocean system $\mathbf{R}_{at+sf}$.

$$\mathbf{I}(\tau_{at}, \mu, \mu_0, \phi - \phi_0) = \mu_0 \mathbf{R}_{at+sf}(\tau_{at}, \mu, \mu_0, \phi - \phi_0)\mathbf{F} \tag{2}$$

As for the components of Stokes vector, I is the radiance, Q and U are related to the degree of linear polarization and angle of polarization, and V to the circular polarization. In the Earth's atmosphere the circular polarization can be ignored. By using the adding method[1], $\mathbf{R}_{at+sf}$ can be expressed in terms of the reflection matrix, the transmission matrix, of the atmosphere and the reflection matrix of the sea surface, $\mathbf{R}_{at}$, $\mathbf{T}_{at}$, and $\mathbf{R}_{sf}$, respectively. For the basic formulations of these matrices for a single atmospheric layer with a Gaussian type ocean surface (Cox-Munk model [2]), refer to our previous paper [3].
The reflectance R and degree of linear polarization P in the reflected radiation at the top of the atmosphere are given by Eq.(3) and Eq.(4), respectively.

$$R = \pi I / \mu_0 E_s \tag{3}$$

$$P = (Q^2 + U^2)^{1/2} / I \tag{4}$$

For simplicity, we shall call the degree of linear polarization the polarization in this paper.

3. SIZE DISTRIBUTION MODEL OF AEROSOL

As for aerosol size distribution models, Junge type power law model was only considered as a base-line and it is given by Eq.(5).

$$n(r) = \begin{cases} C \cdot 10^{\nu+1} & 0.02\mu m \le r \le 0.1\mu m \\ C \cdot 10^{-(\nu+1)} & 0.1\mu m \le r \le 10\mu m \\ 0 & r < 0.02\mu m, r > 10\mu m \end{cases} \tag{5}$$

where n(r) is the number density whose particle size is between r and r+dr. C is a constant which is determined to satisy $\int_{r_{min}}^{r_{max}} n(r)dr = 1$, where r_{min}=0.02 [mm]and r_{max}=10.0[mm]. The index n in Eq.(5) can be used as a measure of the size of aerosol particles. As a measure of aerosol optical thickness, we shall use the aerosol optical thickness τ_{500} at 500[nm] in this study. The aerosol optical thickness τ_λ at any wavelength λ[nm] can be expressed by Eq. (6) interms of τ_{500}.

$$\tau_\lambda = \tau_{500}\left(\frac{\lambda}{500}\right)^{-\alpha} \tag{6}$$

where α is Ångström exponent and it is approximately related to Junge's index n as follows: $\alpha = \nu - 2$. Since Ångström exponent is commonly used, we shall use a as a measure of the size of aerosol particles, hereinafter, instead of n. In other words, we considered here 5 different cases of α, namely, α = 0.5, 1.0, 1.5, 2.0 and 2.5. The small and large values of a correspond to large and small aerosol particle size cases, respectively. As for aerosol refractive index, we considered 8 cases of refractive index, i.e., m=1.30 -i0.0, 1.33 -i0.01.35 -i0.0, 1.40 -i0.0, 1.45 -i0.0, 1.5 -i0.0, 1.55 -i0.0 and 1.60 -i0.0, where we ignored absorbing aerosol cases. In addition,

we used the optical thicknesses of Rayleigh molecules, computed by the formulae in Hansen and Travis's paper[1]. We computed Look Up Tables (LUTs) of the space reflectance and polarization for a given aerosol model with 11 different parameterized aerosol optical thicknesses of τ_{500} from τ_{500} = 0.0 to 1.0 with an increment of $\Delta\tau_{500}$ = 0.1, for 33 different zenith angles of the incident and viewing direction and 72 different azimuthal angles of $\phi-\phi_0$. The LUTs were computed at 670 and 865[nm] by the adding and doubling radiative transfer code, including polarization, for 40 aerosol models (5 cases of a x 8 cases of m). In the computation, we assumed a homogeneous atmosphere(mixture of aerosol and Rayleigh particles) bounded by an isotropic Gaussian type ocean surface with a wind speed of V=5.0 [m/s].

As for the validation of aerosol optical parameter retrieval, the simultaneous solar attenuation measurements were made by the skyradiometer (POM-01: PREDE made) with 4 wavelength channels of 400, 500, 870, and 1040[nm] at Uchinada Agricultural Experiment Center in Ishikawa Prefecture in Japan, very close to the study site A in Fig.1.

4. MULTI-DIRECTIONAL R-P ALGORITHM

The use of multi-directional R-P(Reflectance-Polarization) diagram in a single infrared band was originally proposed by our previous study[4] . We presented a parametrized R-P diagram in 865[nm] at a viewing condition of (Scene 35:θ_0 =29.14, θ =55.87, $\phi-\phi_0$=88.25; scattering angle Θ=118.5) for m=1.45-i0.0 in Fig.2. From the diagram in Fig.2, we can find easily an appropriate parameter solution, i.e., (τ_{500} =0.241, α =1.77) from a location of X in the case of m=1.45-i0.0, where X satisfies both observed reflectance and polarization values by POLDER. These estimated values agree very well with the measured values of τ_{500} (obs) =0.248, α(obs) =1.63) by sky observation near the target A on April 26, 1997. We found parameter solutions with slightly different values for other viewing conditions for m = 1.45-i0.0. Appropriate aerosol parameters at the target A should be computed by taking an average over multi-angle conditions. Since we found no appropriate parameter solution for m=1.30-i0.0, m=1.35-i0.0, and m= 1.60-i0.0 , we can reject these three cases of m. There existed an appropriate paremeter solution for m = 1.40-i0.0, 1.45-i0.0, 1.50-i0.0 and 1.55-i0.0. Because the sum of relative difference $S(m_j)$ between the model and observation in the case of m = 1.40-i0.0 is the smallest among four possible cases of m, we can adopt the case of m=1.40-i0.0 as the best case. The definition of $S(m_j)$ is given by Eq.(9). Finally, an appropriate set of aerosol parameters at the target site A, based on the above arguments, was found to be (τ_{500} =0.245, α=1.20, m=1.40-i0.0) which was close to the measured ones (τ_{500} [obs]=0.248, α [obs]=1.63).

Our new algorithm for retrieving aerosol's real part of refractive index, τ_{500} and α, is as follows:

(a) Find a solution of ($\tau(i,m_j)_{500}$, $\alpha(i,m_j)$) using the R-P diagram at the first pixel in POLDER scene under consideration at a given viewing condition, Θ_i, for fixed m=m_j, where i=1- 5 and j=1-8. As for Θ_i, we consider 6 cases of scattering angles Θ_i, namely, Θ_i:(i=1-5)=$123.5^\circ, 136.4^\circ, 150.8^\circ, 162.7^\circ, 163.0^\circ$ *and* 154.7° selected among POLDER'S 12-14 viewing conditions at each pixel. As for m_j, we consider 8 cases of real part of refractive index, namely, m_j=1.30 -i0.0, 1.33 -i0.0,1.35 -i0.0, 1.40 -i0.0, 1.45 -i0.0, 1.5 -i0.0, 1.55 -i0.0 and 1.60 -i0.0.

(b) Compute an average optical thickness $\tau_{av}(m_j)_{500}$ and Angstrom exponent $\alpha_{av}(m_j)$ for fixed m_j, as follows:

$$\tau_{av}(m_j)_{500} = \frac{1}{n_j}\sum_i \tau(i,m_j)_{500} \tag{7}$$

$$\alpha_{av}(m_j) = \frac{1}{n_j}\sum_i \alpha(i,m_j) \tag{8}$$

where n_j is the total number of existing solutions for fixed m_j. We reject the case of m_j as an inappropriate case, if no possible solution is found in the P-R diagram.

(c) Compute theoreatical reflectance $R_t(i)$ and polarization $P_t(i)$ at each pixel for Θ_i, using the values of $\tau_{av}(m_j)_{500}$ and $\alpha_{av}(m_j)$. Then, compute a sum of relative differences $S(m_j)$ between the model (m=m_j) and observation, according to Eq.(9).

$$S(m_j) = \frac{1}{2}\sum_i [\frac{|R_{ob}(i) - R_t(i)|}{R_{ob}(i)} + \frac{|P_{ob}(i) - P_t(i)|}{P_{ob}(i)}] \quad (9)$$

where $R_{ob}(i)$ and $P_{ob}(i)$ are the observed reflectance and polarization values for Θ_i.

(d) Assign m=m_k as an appropriate real part of refractive index at the pixel, where m_k satisfies Eq.(10).

$$S(m_k) = Min\{S(m_j): j = 1,2,..,8\} \quad (10)$$

Three values of m_k, $\tau_{av}(m_k)_{500}$ and $\alpha_{av}(m_k)$ are appropriate aerosol optical parameters at the pixel.

(e) Repeat steps (a) to (d) for all pixels in a series of POLDERscenes.

5. MULTI- AND MONO- DIRECTIONAL R-R ALGORITHMS

This is a method for retrieving aerosol optical parameters, using two band reflectance values alone. This method was originally used in the retrieval analysis of NOAA/ AVHRR data by Stowe et al.[5]. By using a parameterized diagram of theoretical reflectances in 670 and 865[nm] bands at a given angular condition, we can also estimate an appropriate set of (τ_{500}, α) which satisfies the observed reflectances at 670 and 865[nm]. The R-R (Reflectance-Reflectance) algorithm in two bands is applicable to POLDER's multi-directional reflectance data and the mono-directional reflectance data of OCTS and NOAA/AVHRR. We can retieve aerosol's three optical parameters from POLDER's reflectance data using the similar algorithm in the previous section, except using multi-directional R-R diagrams and the different definition of S(m_j) given below.

$$S(m_j) = \frac{1}{2}\sum_i [\frac{|R_{obs}^{670}(i) - R_t^{670}(i)|}{R_{obs}^{670}(i)} + \frac{|R_{obs}^{865}(i) - R_t^{865}(i)|}{R_{obs}^{865}(i)}] \quad (11)$$

However, it is difficult to retrieve aerosol's real part of refractive index by the R-R diagram from the mono-directional reflectance data by OCTS and NOAA/AVHRR, because they collects the radiance reflected by the target from a mono-direction. In other words, we can retrieve only values of τ_{500} and α by using a mono-directional R-R algorithm.

6. COMPARISON OF RETRIEVED RESULTS

Retrieved distribution maps of aerosol parameters, namely, m=Nr-i0.0, τ_{500}, and α, from POLDER, OCTS, and NOAA/AVHRR aquired on April 26, 1997 were presented in Fig.3, Fig.4, and Fig.5, respectively. Here, Nr is the real part of refractive index. In these figures (a) and (b) represent retrieved results from POLDER data by the multi-directional R-P algorithm and multi-directional R-R algorithm, respectively. In addition, (c), (d) , and (e) represent those from the reflectance data of OCTS, AVHRR with 1.5 hours time-lag and AVHRR with 4 hours time-lag by the mono-directional R-R algorithm. The retrieved results at the validation site A are shown in Table 1. We can find that the multi-directional R-P algorithm gives the best agreement with the observation data among different algorithms. The retrieved map of the real part of refractive index cannot be made from OCTS and AVHRR data, because of their mono-directionality limitation. Fig.3-(a) shows that we have a large extended region of aerosols with Nr in a range of 1.40 to 1.45 from Asian Continent to Japanese islands, whereas we have regions of aerosols with that in a range of 1.30 -1.35 in the Pacific Ocean. Fig.4-(a) shows that the aerosol optical thickness (τ_{500} =0.0- 0.2) is much smaller in the Pacific Ocean than that (τ_{500} =0.4-0.5) in the Japan Sea. As for α, we have aerosol regions with α=0.5 (corresponds to large size particles: Oceanic Particles) in the Pacific Ocean, whereas we have a very large region with a =2.0-2.5 (corresponds to small size particles: Land Particles), which

extends from Asian Continent toward the Pacific Ocean, as is seen in Fig.5-(a). All features by the mult-directional P-R algorithm were consistent and they agreed well with our general knowledge about the local atmospheric movement. We have strong Yellow dusts from Asian Continent (China) in spring and they are extending over Japan and the western part of the Pacific Ocean. Since most features in Fig.4-(b) , -(c), -(d) and-(e) are similar to those in Fig.4-(a), we can judge that retrieved results of τ_{500} from the reflectance data are qualitatively reliable, but not quantitatively. We should note that the retrieved results of τ_{500} and α from POLDER and OCTS data, based on either multi- or mono- directional R-R algorithms, are very close to each other, whereas they are very different in the case of AVHRR data. The reasons are not clear at present. There are many factors which were not taking into account in our dealing with the AVHRR data, such as the effect of water vapor absorption in wider band-width of AVHRR, the observation time-lag between ADEOS and NOAA, and others. As for α and m=Nr-i0.0, we can judge that results from the reflectance data may not be trusted, because we found that the computed polarization values, assuming the optical parameters based on the R-R algorithm, failed to satisfy the observed polarization values.

7. CONCLUSIONS

Conclusions of this study can be summarized as follows:

(1) For the first time, we showed that aerosol's real part of refractive index, together with aerosol optical thickness and Ångström exponent, can be retrieved systematically by the multi-directional R-P algorithm using POLDER's reflectance and polarization data.

(2)We found a good agreement between the retrieved and measured aerosol optical parameter values at the validation site.

(3)Retrieved maps of aerosol's toptical parameters by the proposed algorithm were compared with those by the multi-directional R-R algorithm and by the mon-directional R-R algorithm using the reflectance data of POLDER, OCTS and AVHRR.

(4)We found retrieved results from reflectance data seemed to be qualitatively correct in the estimation of τ_{500} , but not reliable in the estimation of m=Nr-i0.0 and α.

ACKNOWLEDGMENTS

We thank very much Dr. A. Yamazaki at MRI (Meteorological Research Institute of Japan)for helpful discussions and suggestions. This study was partially supported by CERes, Chiba Univ. Joint Project Research 12-1, Ministry of Education under Grant in aid No. 12680533 and NASDA Research Contract, NASDA-PSPC-21409. The results were obtained from CNES's POLDER and NASDA's OCTS on board NASDA's ADEOS.

REFERENCES

[1] Hansen,J.E. and Travis,L.D., 1974. Light scattering in planetary atmospheres. Space Sci. Rev., 13, pp. 527-610.

[2] Cox,C. and Munk,W., 1954. Measurement of the roughness of the sea surface from photographs of the sunÕs glitter. J. Opt. Soc. Amer. 44, No.11, pp. 838-850.

[3] Kawata,Y. and Yamazaki,A., 1998. Multiple scattering analysis of airborne POLDER image data over the sea. IEEE Trans. GRS., vol.36, No.1, pp.51-60.

[4] Kawata,Y. , Izumiya, T. and Yamazaki,A., 1999. Retrieval algorithm for aerosol optical parameters from POLDER's directional reflectance and polarization data. Proc. of SPIE, Vol. 3759, pp. 40-48.

Table 1. Retrieved aerosol optical parameters by different algorithms at validation site A.

Satellite Data	Algorithm	τ	α
NOAA/AVHRR(1.5 hours later)	R-R Mono-angle	0.279	0.50
NOAA/AVHRR(4 hours later)	R-R Mono-angle	0.281	0.23
ADEOS/POLDER	R-R Multi-Angles	0.233	0.95
ADEOS/POLDER	R-P Multi-Angles	0.245	1.20
ADEOS/OCTS	R-R Mono-angle	0.219	0.93
Observed Data		0.248	1.63

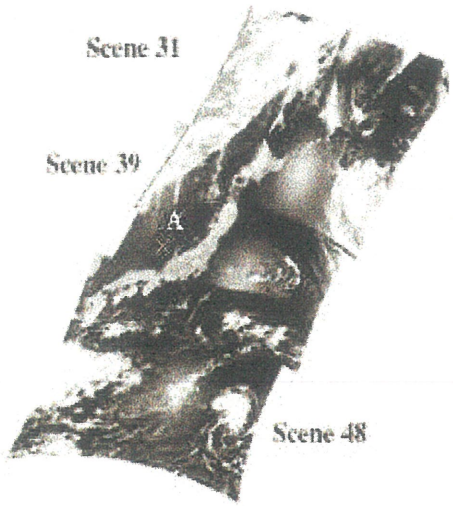

Fig.1. Sequential POLDER scenes on April 26,1997.

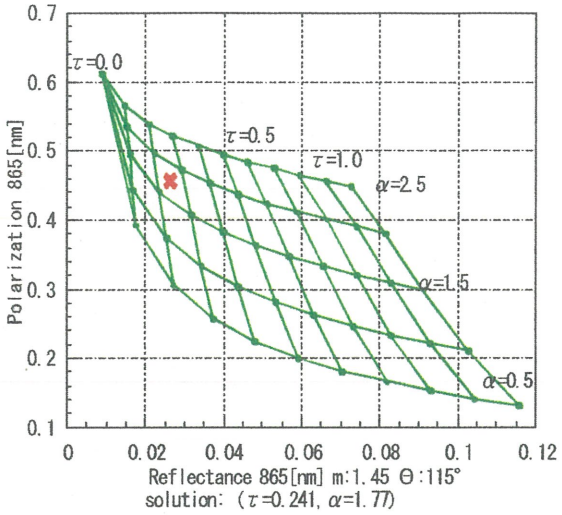

Fig.2. Directional P-R diagram . X represents a point satisfying observation values by POLDER

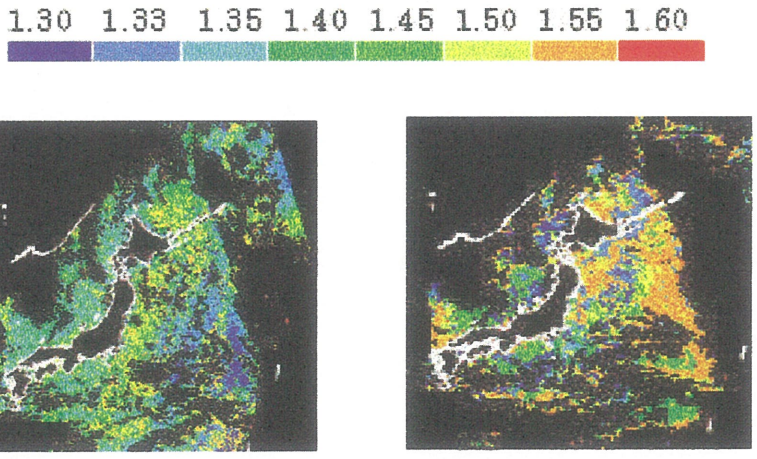

(a) Nr (POLDER: R-P)

(b) Nr (POLDER: R-R)

Fig.3. Retrieved distribution maps of aerosol's real part of refractive index

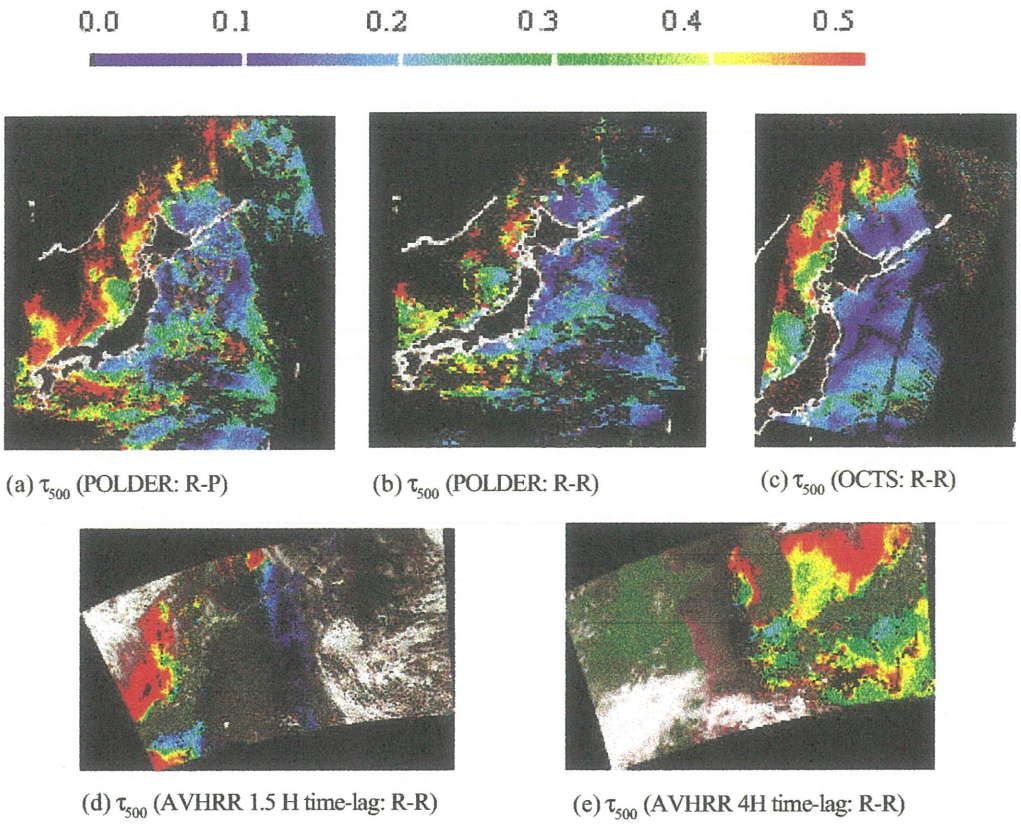

(a) τ_{500} (POLDER: R-P)　(b) τ_{500} (POLDER: R-R)　(c) τ_{500} (OCTS: R-R)

(d) τ_{500} (AVHRR 1.5 H time-lag: R-R)　(e) τ_{500} (AVHRR 4H time-lag: R-R)

Fig4. Retrieved distribution maps of aerosol's optical thickness

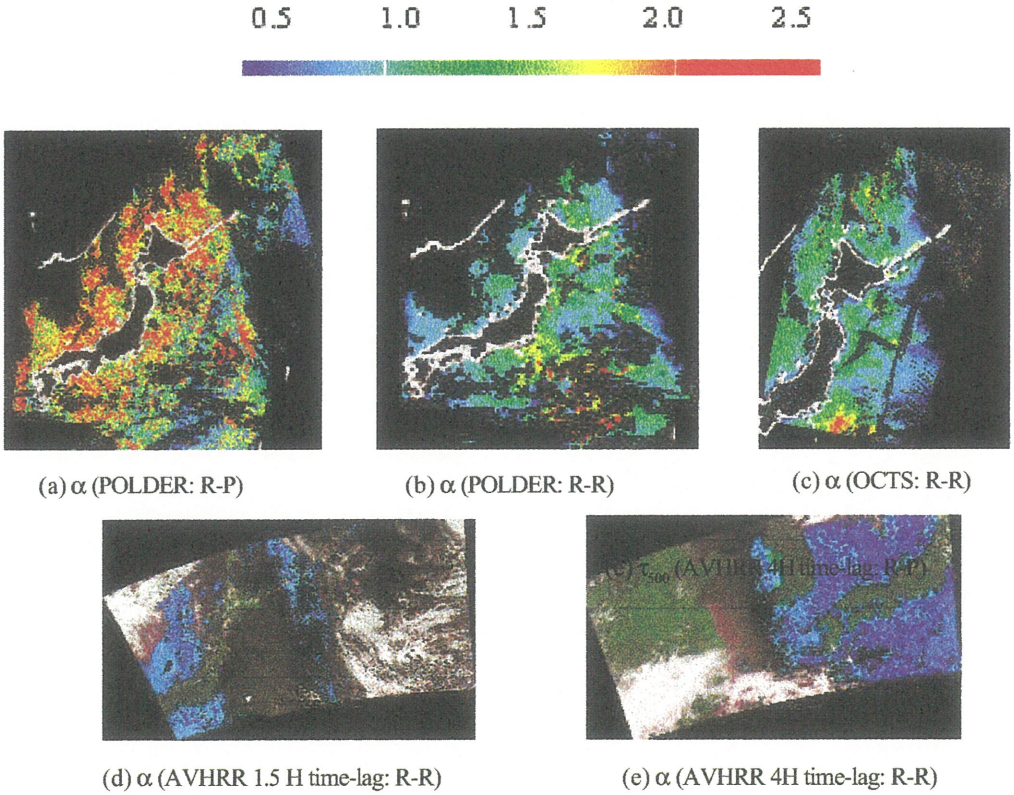

(a) α (POLDER: R-P)　(b) α (POLDER: R-R)　(c) α (OCTS: R-R)

(d) α (AVHRR 1.5 H time-lag: R-R)　(e) α (AVHRR 4H time-lag: R-R)

Fig.5. Retrieved distribution maps of aerosol's ÅngstrÕm exponent

Atmospheric correction for satellite-borne and airborne spectrometry —effects of aerosol type and pixel size

Daren LU and Minzheng DUAN
LAGEO, Institute of Atmospheric physics,
CAS, Beijing 100029 CHINA
ludr@public2.east.cn.net

Atmospheric correction plays very important role in quantitative remote sensing of the earth surface, in particular to dark surface such as ocean, as well as land surface with strong inhomogeneous reflectance. To develop appropriate method we need to consider various real situation, including sensor position such as satellite borne or airborne, aerosol type, pixel size, as well as the inhomogeneity of the surface. It is well known that atmospheric correction is consisted of the deduction of atmosphere path radiance as well as the correction of adjacency effect. The former will be solved by radiation transfer model calculation when the atmospheric aerosol loading is known and assuming surface reflectance as zero. The latter part will be solved with an atmospheric spread function and also related pixel size. In this paper at first we reviewed the present situation of the atmospheric correction. Then we derived a new expression of the atmospheric spread function which is based on the physical analysis of the adjacency effect and numerical R-T simulation. This expression is adaptive to the sensor height, pixel size, and aerosol distribution.

Based on R-T model computation and the expression of atmospheric spread function, we made a series of calculation showing the effect of aerosol type, sensor height, and pixel size. After this discussion, we suggested a procedure of atmospheric correction for satellite image such as TM. Some case study will be shown.

Atmospheric and Topographic Effects Observed in Shadowed Pixels of Satellite Imagery

Yoshikazu Iikura

Faculty of Science and Technology, Hirosaki University
3 Bunkyo-cho, Hirosaki 036-8561 Japan
E-Mail : iikura@cc.hirosaki-u.ac.jp

ABSTRACT: With high sun elevation, the cosine law of solar incidence angle can be validated after the subtraction of offset component from satellite images. The offset component is mainly consisted of path radiance, which depends on target surface altitude in visible bands, in particular. With low sun elevaton, the irradiance from diffuse sky or adjacent slope might have significant effect. In this paper, these effects are quantitatively evaluated using shadowed pixels in actual satellite images (LANDSAT/TM).

1.Introduction

In satellite images over ruuged terrain, we can find several atmospheric and topographic effects which vary from one pixel to another. Though the solar incidence angle is the most significant topographical factor, there are some other minor factors such as[1),2),3)]

(1) the path radiance which depend on the altitude of the target pixels,
(2) the reduction of diffuse sky irradiation on the target pixels because the topography hides a part of sky hemisphere,
(3) the irradiation on the target pixel reflected by the adjacent slope.

When we deal with the satellite images with low sun elevation or hazy atmospheric conditions, careful attention should be paid to these effects though the precise correction seems difficult.

In this paper, we will evaluate these minor effects by using shadowed pixels of an actual satellite image (LANDSAT/TM). For this purpose, we prepare a digital elvation model which is consistent to the satellite image, and calculate some topographic parameters such as horizon[4)] and viewshed[5)] for each pixel as well as solar incidence angle. The satellite image is geometrically corrected to overlay these parameters.

2. Theoretical background

2.1 Modelling of satellite level radiance

Satellite level radiance(Ls) of target pixel (x,y) mainly consisits of reflected target irradiance(Io) and path radiance(Lp) as [2)]

$$Ls = Ts(z)R(x,y)Io + Lp(z) \quad (1)$$

where z is altitude, R is target reflectance, s is sensor scan angle, T s is transmittance from target to satellite.

Target irradiance (Io) is broken down into direct solar beam, diffuse sky irradiation Ed and irradiation from adjacent slope Ee as [1),3)]

$$Io = E_0 T_\theta(z)\cos\beta + Ed + Ee \quad (2)$$

where T_θ is transmittance from sun to target, θ is solar elevation angle, and β (solar incidence angle) is the angle between surface normal and the solar beam.

In the case of flat plane, there is no Ee and most parameters can be assumed constant. In the rugged terrain, however, not only solar incidence angle β but also path radiance and transmittance vary pixel by pixel. Irradiance from the diffuse sky and adjacent slope also depend on the local topography.

2.2 Correction of high sun elevation images

As Ed and Ee can be ignored for the satellite images with high sun elevation, topographical effects can be corrected using the cosine law of solar incident angle after the subtraction of offset component as

$$R(x,y)=(Ls-Lp)/EoTsT\theta\cos\beta \quad (3)$$

The parameters in eq.(3) are usually estimated by using radiative transfer code such as 6S[2] or Modtran[6]. However, there always remain some uncertainity in atmospheric conditions, in particular, aerosol concentration and characteristics. Conversion of the digital numbers into radiance is another error source.

In order to avoid these difficulties, Iikura et al.[7] have proposed the digital number based relative correction as

$$R(x,y) \sim (DN-a-b*z)/\cos\beta \quad (4)$$

where the dependence of path radiance is approximated by a linear function. This correction was based on the analysis of simulated data using 6S, which showed that the offset component decreases significantly in visible bands as the target altitude becomes higher, while it can be assumed constant in infrared bands. The analysis of shadowed pixels also supported the offset decrease in visible bands. In infrared bands, however, the DN in infrared bands have larger deviance than those expected from 6S simulation which assumes flat plane.

It is reasonable to think that the deviation of infrared bands is mainly caused by the irradiance of adjacent slope, because the used image was mainly occupied by the deciduous forest with high reflectance in infrared bands compared to visible bands.

3.Study Area and Data Base

In ordet to make our analysis clear, the Sirakami mountaneous region was selected as the study area, which is famous for its well preserved beech forest and covers 24 km by 21 km. From the vegetation map, the beech forest occupy about 70 % of the area as shown in Fig.1.

The Landsat TM image used for this study was aquired on November 2, 1998 (Path 108/ Row32). The study area is extracted and orthorectified to the UTM coordinate system (Zone 54) by using the carfully selected ground control points. The size of the image is 800 lines and 700 pixels with 30m resolution. Sun elevation angle (θ) is 32 degree and its azimuth angle (A) is 127 degree from the north. Figure 2 shows Band 5 image, which is used for the analysiis of adjacent slope effect.

Japan Geographycal Survey has published digital elevation model with latitude and longitude coordinate system with about 50m spatial resolution. We have transformed the DEM into UTM coordinate system as the satellite image. The bilinear interpolation is used for resampling.

4. Direct solar radiation

The direct solar radiation is propotional to the cosine of solar incidence angle β given as

$$\cos\beta = \sin\theta\cos e + \cos\theta\sin e\cos(\phi - A) \quad (5)$$

Fig.1 Beech forest area in Sirakami mountaneous region

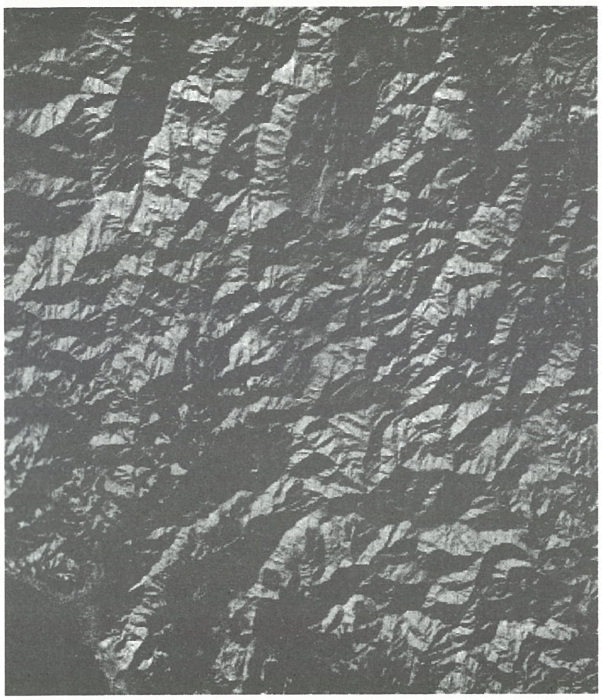

Fig.2 Landsat TM image (Band 5) used in this study

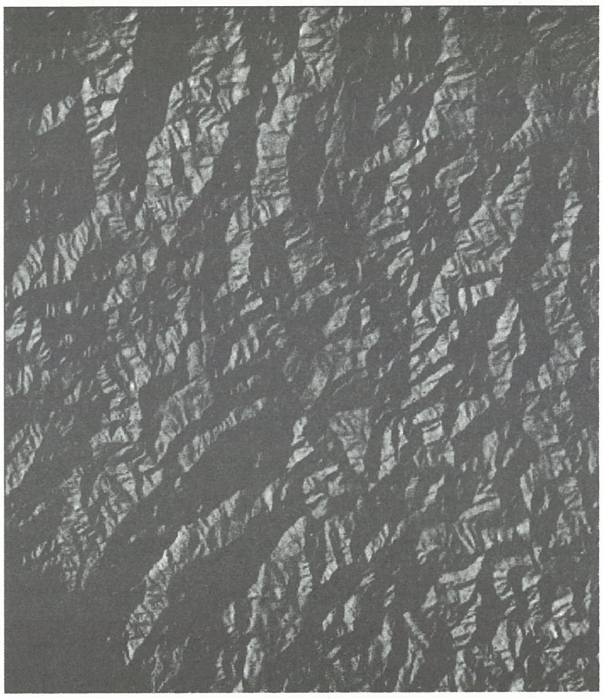

Fig.3 Direct solar radiation image calculated from the DEM

where e is slope angle and A is slope azimuth, which are calculated from the DEM. The cosβ is shown in Fig.3.

We can note the similarity between the satellite image and cosβ image. Their spatial correlation without displacement (δ =0)[8] is 0.74 as shown in Table 1. As the correlation for displaced satellite images, the accuracy of the geometrical correction is considered as within one pixel. It is also noted that Band 5 has higher correlation than visible bands because it is less atmosphecally influenced.

5. Extraction of shadowed region

There are two type of shadowed pixels, the one is self shadowed and the other is cast shadowed. The self shadowed pixel has negative cosβ, while the cast shadowed pixel has the higher horizon angle to the sun direction than theelevation angle of the sun.

Table 1 Change of correlation with displacement of the satellite image

δ	-2	-1	0	1	2
-2	0.34	0.46	0.58	0.66	0.68
-1	0.46	0.58	0.68	0.72	0.70
0	0.57	0.67	0.74	0.72	0.64
1	0.63	0.70	0.71	0.65	0.54
2	0.64	0.67	0.63	0.54	0.43

In one dimentional case, Dozier et al.[4] developed an efficient algorithm for the horizon computation. This algorithm has been extended to the two dimensional case by use of rotation and interpolation of the DEM[9].

Taking the ambiguity in the DEM and these calculation into consideration, we selected the the pixels of which cos β is less than -0.2 and of which horizon angle is less than 35degree. In Fig.4, the relationship between target altitude and digital number of the selected pixels are drawn. The DN of Band 1 decrease as the altitude becomes higher. On the other hand, there is no clear trend in Band 5 and it has large deviation.

6. Irradiance from the adjacent slope

The radiance recieved by the point M and coming from point P as shown in Fig.5 can be written as[1]

$$L_{MP}=(L_P\, dS_M \cos T_M\, dS_P \cos T_P)/r_{MP}^2 \qquad 6)$$

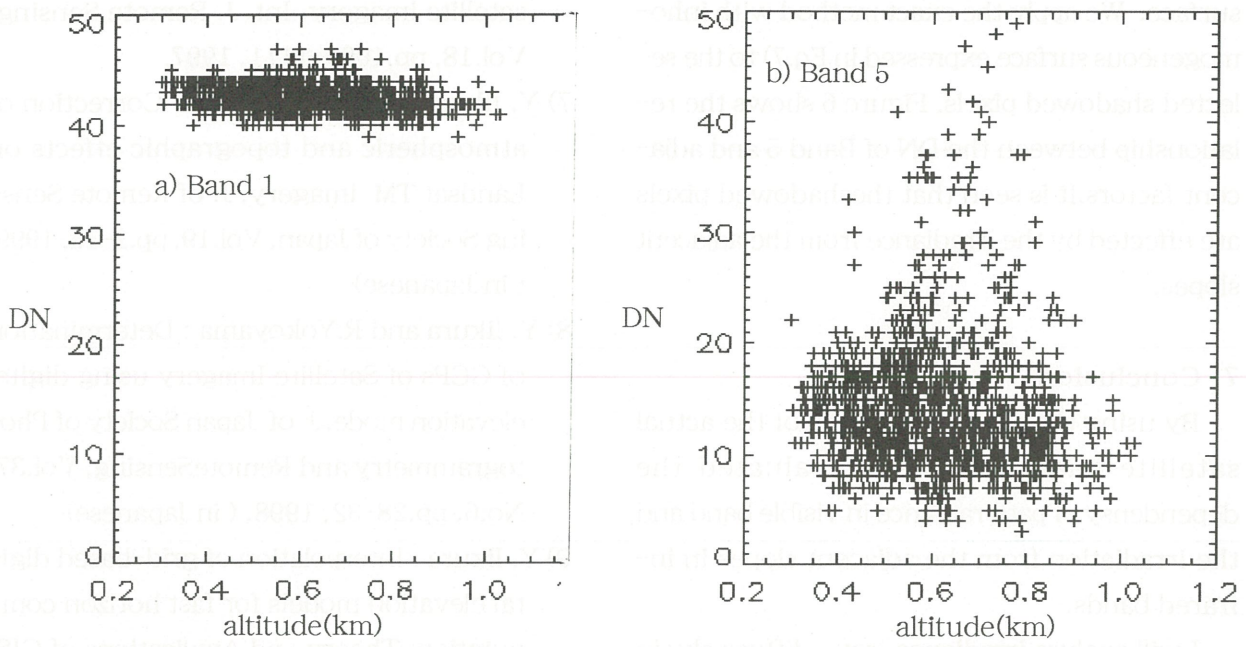

Fig.4 Relationship between DN and target altitude of shadowed pixels

where dS_M and dS_P are the areas of pixels M and P respectively, T_M and T_P are the angles between the normal to the ground and the line MP, L_P is the luminance of P, r_{MP} is the distance between M and P.

Though absolute value of Lp is not determined, it is natural to assume that Lp is propotional to the DN of pixel M. Then the total irradiance recieved by point M is relatively expressed as

$$E_M \sim \sum_P DN_P \cos T_M \, dS_P \cos T_P)/r_{MP}^2 \quad 7)$$

We call this adjacent slope factor. The sum must include the pixels which are oriented towards M and not hidden from pixel M, that is , the calculation of viewshed for each pixels is required.

As the viewshed calculation is time expensive, the approximate method has been usually applied to the actual satellite images[2),6),13)], which ignore the distance and radiation of adjacent slope.

Recently, fast algorithms for viewshed generation have been presented[10),11),12)]. Wang et al. applied their algorithm to the actual satellite images[3)], but they assumedthe homogenius

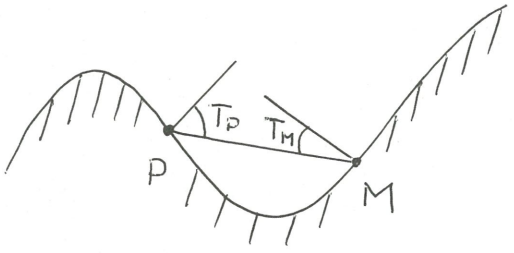

Fig.5 Geometrical consideration of the possible reflections from adjacent slopes

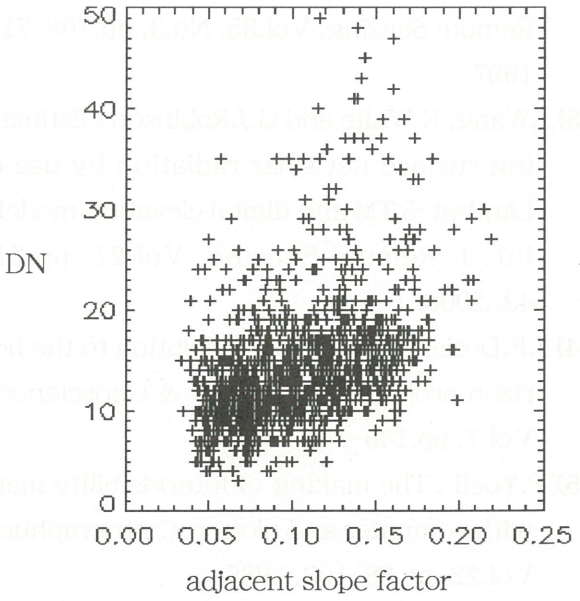

Fig.6 Relationship between adjacent effect factors and DN of shadowed pixels

surface. We apply the exact method with inhomogeneous surface expressed in Eq.7) to the selected shadowed pixels. Figure 6 shows the relationship between the DN of Band 5 and adjacent factors.It is seen that theshadowed pixels are effected by the irradiance from the adjacent slopes.

7. Conclusion

By using the shadowed pixels of the actual satellite image, we have evaluated the dependensy of path radiance in visible band and the irradiation from the adjacent slopes in infrared bands.

I will analyze irradiance from diffuse sky in visible band. Inaddition, these results should be analyzed statistically to develop the effective correction algorithm for the satellite image even with low solar elevation.

References

1) C.Proy, D.Tanre and Y.Deschamps : Evaluation of topographic effects in remotely sensed data, Remote Sensing of Environment, Vol.30, pp.21-32.,1989.

2) S.Sandmeier and K.Itten : A physically-based model to correct atmospheric and illumination effects in optical satellite data of rugged terrain, IEEE Trans. on Geoscience and Remote Sensing, Vol.35, No.3, pp.708-717, 1997.

3) J.Wang, K.White and G.J.Robinson : Estimating surface net solar radiation by use of Landsat-5 TM and digital elevation models, Int. J. Remote Sensing, Vol.21, pp.31-43.,2000.

4) J.F.Dozier et al. : A faster solution to the horizon problems, Computer & Geosciences, Vol.7, pp.145-151, 1981

5) P.Yoeli : The making of intervisibility maps with computer and plotter, Cartographuca, Vol.22, pp.88-103, 1985

6) R. Richter,Correction of atmospheric and topographic effects for high spatial resolution satellite imagery, Int. J. Remote Sensing, Vol.18, pp.1099-1111, 1997.

7) Y. Iikura and R.Yokoyama : Correction of atmospheric and topographic effects on Landsat TM imagery, J. of Remote Sensing Society of Japan, Vol.19, pp.2-16, 1999. (in Japanese)

8) Y. Iikura and R.Yokoyama : Determination of GCPs of Satellite Imagery using digital elevation mode, J. of Japan Society of Photogrammetry and RemoteSensing, Vol.37, No.6, pp.28-32, 1998. (in Japanese)

9) Y. Iikura : Interpolation of grid-based digital elevation models for fast horizon computation, Theory and Applications of GIS, Vol.8,No.2, pp.1-8, 2000.(in Japanese)

10) J.Wang, G.J.Robinson, K.White: A fast solution for computation local viewshed from gridded digital elevation models, Photogrammetric Engineering and Remote Sensing, 62, pp.1157-1164, 1996

11) J.Wang, G.J.Robinson, K.White: Generating viewsheds without using sightlines, Photogrammetric Engineering and Remote Sensing, 66, pp.87-90,2000

12) Y. Iikura : Systematic determination of invisible area using covering plane, Theory and Applications of GIS, Vol.8,No1, pp.39-46, 2000.(in Japanese)

13) J.F.Dozier, J.Frew : Rapid calculation of terrain parameters for radiation modelling from digital elevation data, IEEE Trans. on Geosciences and Remote Sensing, GE-28, pp.963-969,1990

Atmospheric correction algorithm of visible and near-infrared satellite data using radiance components: pixel-by-pixel calculation of the adjacency effect

Mitsuo Minomura, Hiroaki Kuze, and Nobuo Takeuchi
Center for Environmental Remote Sensing (CEReS),
Chiba University, 1-33, Yayoi-cho, Inage-ku, Chiba, 263-8522, Japan
mino@ceres.cr.chiba-u.ac.jp

Key words: atmospheric crrection, radiance components, adjacency effect, aerosol extinction profile, single scattering, optical thickness, radiative transfer

1. Introduction

In this paper we describe the framework of an atmospheric correction algorithm which we have developed recently. The algorithm is for the correction of visible and near-infrared satellite images, with ancillary information on atmospheric parameters obtained with a sun photometer and a multi-wavelength lidar. The ground observations synchronized with the satellite overpass provide the aerosol optical thickness τ_a, its wavelength dependence, and the vertical profile of the aerosol extinction coefficient. In the algorithm, first the pixel reflectance is analytically expressed in terms of radiance components detected by a satellite sensor. This scheme enables us to calculate the influence of the atmospheric extinction using a general radiative transfer code such as the MODTRAN3. The second part of the algorithm deals with the range ($N \times N$ pixels around the target) in which the adjacency effect should be incorporated. We assume that the optical thickness τ_a is relatively small, hence the scattering process is reasonably handled by the single scattering approximation. Simulation results indicate that both τ_a and aerosol vertical distribution play significant role in the determination of τ_a.

In Sec. 2, we describe the essential aspects of the present algorithm for the atmospheric correction. The accuracy of the retrieval of ground reflectance is also discussed. In Sec. 3, the basic concept of the single scattering treatment of the adjacency effect evaluation is presented along with simulation results.

2. Atmosphric correction

2.1 Algorithm

Our algorithm[1] is based on Richter's two-step algorithm[2]. If we assume in his algorithm that a responce function takes a constant value within the sensor bandwidth, the equation of the first-order reflectance, $\rho^{(1)}$, can be simplified as follows

$$\rho^{(1)} = \rho_{\mathrm{MOD}} \frac{L_{\mathrm{pix}} - L_0}{L_{\mathrm{total}} - L_0} \qquad (1)$$

Here, ρ_{MOD} is the surface reflectance used in the MODTRAN calculation, L_{pix} is the pixel radiance observed by the sensor, and L_{total} and L_0, respectively, are the total and path radiances at the TOA obtained from the MODTRAN calculation. Figure 1(a) shows the dependence of MODTRAN radiance components on the surface reflectance. As can be seen from this figure, the value of $L_{\mathrm{total}} - L_0$ is proportional to the surface reflectance to a good approximation. This indicates that in Eq. (1) the ratio of $\rho_{\mathrm{MOD}}/(L_{\mathrm{total}} - L_0)$ does not depend on the value of ρ_{MOD} assumed in the MODTRAN calculation: in the present simulation, we use $\rho_{\mathrm{MOD}} = 0.2$.

The second-order expression of the adjacency effect correction becomes

$$\rho^{(2)} = \rho^{(1)} + \frac{L_{\mathrm{p}} - L_0}{L_{\mathrm{g}}} \left(\rho^{(1)} - \bar{\rho}^{(1)} \right) \qquad (2)$$

where $\bar{\rho}^{(1)} = \sum_{j=1}^{N^2} \rho_j^{(1)} / N^2$, L_{g} is the TOA radiance due to the ground reflection, and L_{p} is the path radiance: these are also obtainable through

the usual MODTRAN calculation, as given in Fig. 1(a).

Now, we consider improvement of the correction of the adjacency effect. In order to consider this effect, here we use the following expression, similar to Eq. (2), to define $\rho^{(3)}$:

$$\rho^{(3)} = \rho^{(2)} + \frac{L_\mathrm{p} - L_0}{L_\mathrm{g}} \left(\bar{\rho}^{(1)} - \bar{\rho}^{(2)} \right) \qquad (3)$$

Repeated application of similar procedure leads to an expression for k-th order correction of the adjacency effect:

$$\rho^{(k)} = \rho^{(k-1)} + \frac{L_\mathrm{p} - L_0}{L_\mathrm{g}} \left(\bar{\rho}^{(k-2)} - \bar{\rho}^{(k-1)} \right) \qquad (4)$$
$$k = 3, 4, \cdots$$

Tests have shown that usually the progression of $\rho^{(k)}$ converges for $k \geq 3$, and $k = 3$ gives sufficient accuracy. Here we use $\rho^{(3)}$ as the final form of the atmospheric correction. Thus, we have derived a three-step algorithm based on Eqs. (1), (2), and (3).

2.2 Validation method of the three-step algorithm

The MODTRAN code gives the TOA total radiance in a form of

$$L_\mathrm{total} = L_\mathrm{gd} + L_{\mathrm{gi}_1} + L_{\mathrm{gi}_2} + L_\mathrm{ps} + L_{\mathrm{pm}_1} + L_{\mathrm{pm}_2} \qquad (5)$$

where L_gd is the directly ground-reflected radiance, L_{gi_i} the indirectly ground-reflected radiance, L_ps the path radiance due to single scattering, and L_{pm_i} the path radiance due to multiple scattering. A detailed analysis shows that among these components, L_{pm_2} is proportional to the ground reflectance and L_{gi_2} is proportional to the square of the surface reflectance (Fig. 1(b)). Thus the total radiance that would be observed by a satellite sensor for a target pixel, then, can be expressed as

$$L_\mathrm{pix} = L_\mathrm{gd}(\rho) + L_{\mathrm{gi}_1}(\rho) + L_{\mathrm{gi}_2}(\rho, \bar{\rho}) + L_\mathrm{ps} + L_{\mathrm{pm}_1} + L_{\mathrm{pm}_2}(\bar{\rho}) \qquad (6)$$

Here ρ is the target reflectance and $\bar{\rho}$ is the average reflectance. In the calculation of L_pix using Eq. (6), the reflectance dependence of each radiance component is determined by atmospheric conditions, the optical thickness at 550 nm, τ_{550},

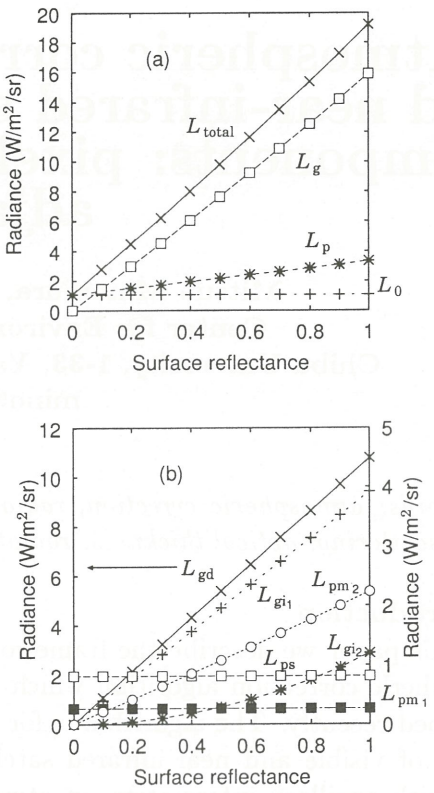

Figure 1: Surface reflectance dependence of the radiance components calculated for an aerosol optical thickness of 0.198. (a) Four radiance components in the MODTRAN code. (b) Each of L_pm and L_gi are separated into two components. The left ordinate is for L_gd, and the right ordinate is for the other five components.

and the aerosol model specified for the MODTRAN calculation (The aerosol model determines the wavelength dependence of the aerosol extinction). In the present simulation, we use the urban aerosol model.

The process of the present simulation is schematically shown in Fig. 2. The result is evaluated for the second- and third-step reflectances, $\rho^{(j)}$ $(j = 2, 3)$, by means of relative errors defined as $r^{(j)} = (\rho^{(j)} - \rho_\mathrm{t})/\rho_\mathrm{t}$.

Since for each pixel, the relative importance of the adjacency effect differs in accordance with the pixel reflectance, we make a statistical consideration for each pixel group that consists of pixels characterized by the same reflectance. We define

Table 1: NOAA AVHRR data and related parameters. τ_{550} is the aerosol optical thickness at 550 nm derived from the simultaneous observation using a sunphotometer. S_j and I_j are the calibration (slope and intercept) constants for the channel j(=1,2) NOAA data.

No.	Date	Time	τ_{550}	S_1	I_1	S_2	I_2
1	1997/12/05	13:51	0.198	0.1338	-5.4876	0.1690	-6.9267
2	1998/12/28	14:22	0.317	0.1304	-5.3464	0.1531	-6.2776
3	1999/04/14	14:32	0.357	0.1321	-5.4172	0.1548	-6.3474
4	1999/07/29	14:46	0.150	0.1336	-5.4762	0.1562	-6.4055

the average value of the relative error $r^{(j)}$ as

$$\bar{r}^{(j)}(\rho_t) = \sum_{\rho_t} r_i^{(j)} / m(\rho_t) \qquad (7)$$

where the summation is carried out for $m(\rho_t)$ pixels which has the original reflectance of ρ_t. Similarly, we define the standard deviation of $r^{(j)}$ as

$$\sigma^{(j)}(\rho_t) = \left[\frac{1}{m(\rho_t) - 1} \sum_{\rho_t} \left(r_i^{(j)} - \bar{r}^{(j)}(\rho_t) \right)^2 \right]^{1/2} \qquad (8)$$

If the atmospheric correction of the $L_{\rm pix}$ image were carried out in a perfect way, both $\bar{r}^{(j)}(\rho_t)$ and $\sigma^{(j)}(\rho_t)$ become zero.

2.3 Sensitivity analysis using the AVHRR data

2.3.1 AVHRR data

Table 1 shows the NOAA14 AVHRR data used in the present simulation and analysis. The satellite overflight took place between 1:30 and 3:00 p.m. over the Chiba area: each image (190×190 pixels) was taken at the near nadir angle centered at the area. Both channel 1 and channel 2 images are employed here.

For each satellite data in Table 1, we use the aerosol optical thickness obtained using a sunphotometer at the time of the NOAA14 overflight. The value at 550 nm, τ_{550}, which is required as an input parameter in the MODTRAN calculation, is determined by the interpolation of the eight-wavelength sunphotometer data. The values are listed in the fourth column of the table.

For the other parameters given to the MODTRAN code, we employ the standard atmosphere (midlatitude) and the urban aerosol model for the wavelength dependence of the aerosol extinction.

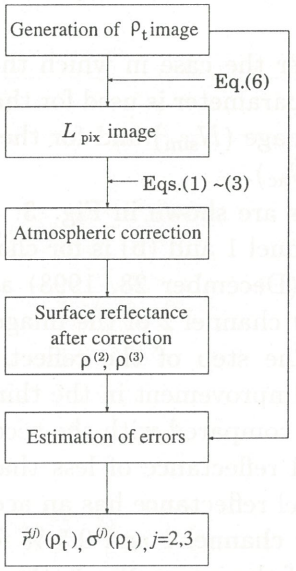

Figure 2: Flow chart of the sensitivity analysis of the present three-step atmospheric correction algorithm.

The wavenumber region is 14184 ~ 17467 cm^{-1} for channel 1 and 9975 ~ 13840 cm^{-1} for channel 2. Both the bin width and the width of the triangular function are taken to be 40 cm^{-1}. This corresponds to the assumption of the uniform sensitivity over the sensor bandwidth in the calculation of the radiance components.

2.3.2 Images for simulation

For the implementation of the method described in Sec. 2.2, we prepare images around the Chiba area based on the real satellite data after the atmospheric correction. The pixels with $\rho_t > 0.5$ are regarded as having $\rho_t = 0.5$. The size of the Chiba images is 186 × 186. We choose im-

ages No.2 and No.3 with relatively large values of the optical thickness to construct the test images.

In the MODTRAN calculation using eq. (6), we use the optical thickness at 550 nm (τ_{550}) in Table 1. For the calculation of the average reflectance $\bar{\rho}$, we study two cases of $N = 15$. It is noted that in the practical application of atmospheric correction, the choice of the range parameter N is crucial for the exact removal of the adjacency effect[3,4].

2.3 Retrieval with the same range parameter

We consider the case in which the same value of the range parameter is used for the preparation of the test image (N_{sim}) and for the atmospheric correction (N_{ac}).

The results are shown in Fig. 3: (a) is for the AVHRR channel 1 and (b) is for channel 2 of the image No.2 (December 28, 1998) and (c) channel 1 and (d) channel 2 of the image No.3 (April 14,1999). The step of the reflectivity, $\Delta\rho_{\mathrm{t}}$, is about 0.01. Improvement in the third-step result is evident as compared with the second-step one. For the pixel reflectance of less than ~ 0.2, the retrieved pixel reflectance has an accuracy better than 1 % for channel 1 and 0.5 % for channel 2. In the case of the image No. 3, the relative error increases with ρ_{t}. This is ascribed to the cloud pixels which are relatively small in number (less than 20 pixel for each reflectivity) yet quite influential to the neighboring pixels.

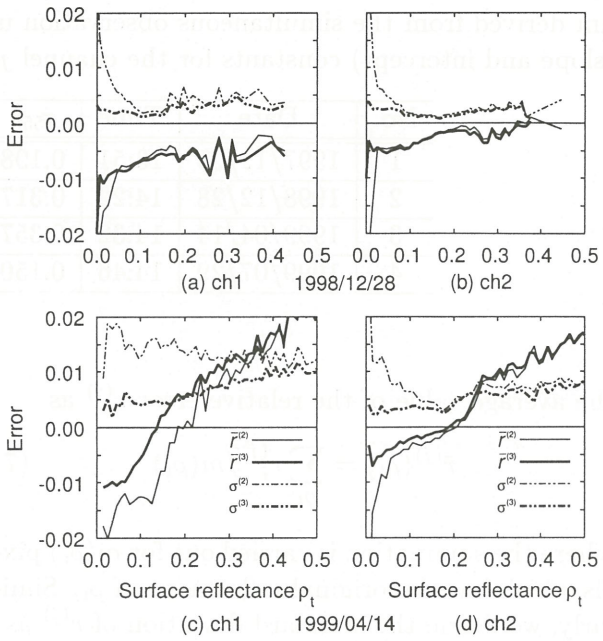

Figure 3: Retrieval errors for the Chiba images. (a) (AVHRR channel 1) and (b) (channel 2) are for the image No.2 (December 28, 1998), and (c) (channel 1) and (d) (channel 2) are for the image No.3 (April 14,1999). Pixel reflectances are retrieved with an accuracy of about 1 % (channel 1) and 0.5 % (channel 2) for pixels with relatively low reflectance of less than 0.2. Range parameter $N = 15$ is used for all cases.

3 Adjacency effect

3.1 Radiation component relevant to the adjacency effect

In the visible and near-infrared region of the solar spectrum, the purpose of the atmospheric correction is to extract the directly ground-reflected component L_{gd} from the six components depicted in Fig. 4. In the following, we evaluate the magnitude of the adjacency component corresponding to L_{pm_2} in Fig. 4. As compared with this term, other adjacency component, L_{gi_2}, exhibits smaller contribution due to increase in the number of scattering processes involved.

Figure 5 illustrates the present configuration used to calculate the irradiance related to the adjacency effect. We assume that the atmosphere is horizontally layered, with a uniform extinction coefficient in each layer. The ground surface is planar and shows Lambertian reflection, with the reflectivity changing on a pixel by pixel basis. The photon relevant to L_{pm_2} is first reflected by an adjacent pixel, then scattered only once in the instantaneous FOV of the sensor element. In the following, for simplicity, μ stands for $\cos\theta$, with subscripts s, r, and v indicating the solar zenith angle, reflection angle, and observation angle, respectively. When the solar irradiance at the TOA is written as E_{ext}, and the optical thickness from the ground to the TOA as τ_{TOA}, the downward solar irradiance at the ground is given as $E_{\mathrm{g}} = \mu_{\mathrm{s}} E_{\mathrm{ext}} e^{-\tau_{\mathrm{TOA}}/\mu_{\mathrm{s}}}$. It should be noted that for E_{g}, we consider only the directly transmitted light. The scatterer (aerosol or molecule) is located at an altitude of z. The energy incident on the cross section σ of the scatterer per unit time

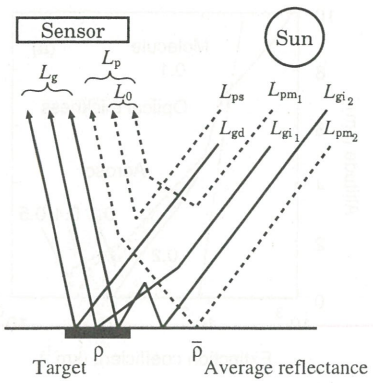

Figure 4: Radiance components detected by a satellite sensor. L_{gd}: ground-reflected radiance, L_{p}: path radiance, and L_0: dark target radiance.

is given by

$$\sigma E_{\mathrm{in}}(z,\mu_{\mathrm{r}}) = \mu_{\mathrm{r}} \frac{\rho\sigma E_{\mathrm{g}} A}{\pi r^2} e^{-\tau(z)/\mu_{\mathrm{r}}}. \qquad (9)$$

Here, A is the surface area of a pixel, ρ its reflectance, r the length of a vector connecting the reflecting pixel to the scatterer, θ_{r} the zenith angle of $\mathbf{r}$, and $\tau(z)$ the optical thickness at the altitude z.

Next we consider the radiation flux $d\Phi_{\mathrm{sp}}(z)$ that is received by a single element (area dS_1) of the sensor located at a distance of R:

$$\frac{d\Phi_{\mathrm{sp}}(z)}{dS_1} = E_{\mathrm{in}}(z,\mu_{\mathrm{r}}) \frac{\sigma}{R^2} p(\cos\Theta) e^{-\tau'(z)/\mu_{\mathrm{v}}}. \qquad (10)$$

Here Θ is the scattering angle, $p(\cos\Theta)$ is the phase function, and $\tau'(z)$ is the optical thickness from the particle to the sensor. Thus, eq. (10) describes the irradiance into the sensor element originating from the light that has reflected from the surface and then scattered by a single scatterer. It is also noted that the sensor element is the one relevant to the target pixel in the instantaneous FOV of the sensor.

The number of scattering particles $N(z)$ in an volume element dV is given by $N(z) = n(z)dV$, where $n(z)$ is the number density of scattering particles. The volume element can also be expressed as $dS(z)dz$, where $dS(z)$ is the base area of the volume element (see Fig. 5). Using the single scattering albedo ω_0 and the extinction coefficient $\alpha(z)$, the total scattering cross section

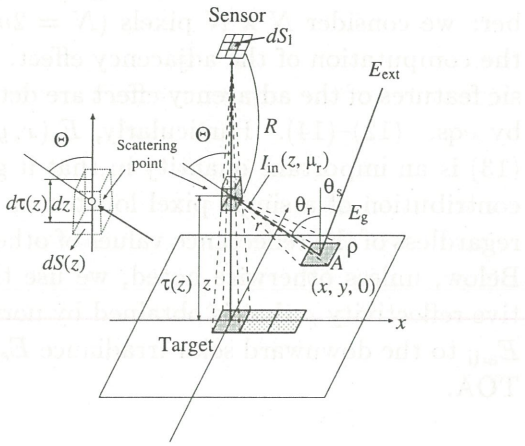

Figure 5: Calculation of the irradiance E_{adj} due to the adjacency effect. After reflected from an adjacent pixel located at $(x, y, 0)$, the light ungdergoes a single scattering at $(0, 0, z)$.

due to the particles inside dV is given as

$$\begin{aligned} \sigma N(z) &= \sigma n(z) dV \\ &= \omega_0 \alpha(z) dS(z) dz. \end{aligned} \qquad (11)$$

Under this situation, the radiation flux to the sensor element from the volume element dV becomes

$$\frac{d\Phi_{\mathrm{s}}(z)}{dS_1} = E_{\mathrm{in}}(z,\mu_{\mathrm{r}}) \frac{\omega_0 \alpha(z) dS(z) dz}{R^2} \cdot p(\cos\Theta) e^{-\tau'(z)/\mu_{\mathrm{v}}}. \qquad (12)$$

In the actual evaluation, one has to consider contributions from both aerosol particles and molecules.

We take the origin of the coordinate system at the location of the target pixel. The total contribution from the light reflected at a pixel at $(x, y, 0)$ is calculated by summing up contributions from all the atmospheric layers. Therefore, when l-fold layers are assumed, the irradiance due to the adjacency effect from that pixel is given by

$$E_{\mathrm{s}}(x,y) = \sum_{i=1}^{l} \frac{d\Phi_{\mathrm{s}}(z_i)|_{(x,y)}}{dS_1}. \qquad (13)$$

Since the total irradiance E_{adj} is obtained from a summation of $E_{\mathrm{s}}(x, y)$ over a sufficient number of pixels around the target, we have

$$E_{\mathrm{adj}} = \sum_{y=-n}^{n} \sum_{x=-n}^{n} E_{\mathrm{s}}(x,y), \qquad (14)$$

where n denotes a sufficiently large positive number: we consider $N \times N$ pixels ($N = 2n + 1$) in the computation of the adjacency effect. The basic features of the adjacency effect are determined by eqs. (12)-(14). Particularly, $E_s(x, y)$ in eq. (13) is an important quantity in that it gives the contribution of a single pixel located at $(x, y, 0)$, regardless of the reflectance values of other pixels. Below, unless otherwise noted, we use the effective reflectivity ρ that is obtained by normalizing E_{adj} to the downward solar irradiance E_{ext} at the TOA.

3.2 Optical Parameters

The composite values of the extinction coefficient $\alpha(z)$, phase function $p(\cos\Theta)$, and single scattering albedo ω_0, are given, respectively, as

$$\alpha(z) = \alpha_m(z) + \alpha_a(z), \tag{15}$$

$$p(\cos\Theta) = \frac{p_m(\cos\Theta)d\tau_m + p_a(\cos\Theta)d\tau_a}{d\tau_m + d\tau_a}, \tag{16}$$

$$\omega_0 = \frac{\omega_{0_m} d\tau_m + \omega_{0_a} d\tau_a}{d\tau_m + d\tau_a}. \tag{17}$$

Here $d\tau$ is the atmospheric optical thickness for an altitude element form z to $z + dz$.

3.3 Simulation and analysis

In the present simulation, we assume the following parameters: the solar zenith angle 37.75°, satellite observation zenith angle 0° (nadir looking), satellite altitude 850 km, satellite bandwidth 18100-18260 cm^{-1} (in wavelength, 0.5476-0.5525 μm), and solar irradiance 9.062 W/m^2. These values are in accordance with the parameters for NOAA AVHRR channel 1. The urban aerosol model is assumed for all the layers, with the single scattering albedo $\omega_{0a} = 0.9$ and the asymmetry parameter $g = 0.65$. The pixel size in the satellite image is 1 km × 1 km. For the maximum range of the adjacency effect calculation, we take $n = 15$ ($N = 31$) in eq. (14). For the vertical division of the atmosphere, we assume 51 layers in the altitude between 0 and 5 km, and 27 layers between 5 and 100 km. Details on the most essential parameters, namely the aerosol extinction profiles and the reflectance distribution of the ground surface, are explained below.

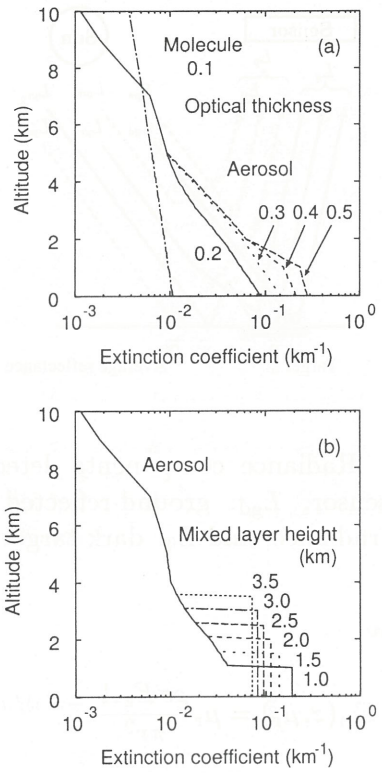

Figure 6: Aerosol and molecular extinction profiles used in the simulation. (a) Profiles based on the MODTRAN code. Here profiles with the aerosol optical thickness of 0.2 ~ 0.5 are shown. (b) Profiles with variable mixed layer height. In this figure, the aerosol optical thickness is fixed at 0.3.

3.3.1 Aerosol extinction profile

A range of the aerosol optical thickness of τ_a = 0.18 to 0.50 (from the ground to the TOA) is considered here. Two kinds of extinction profiles are postulated as depicted in Fig. 6. The first type is model profiles used in the MODTRAN code. Figure 6 (a) shows such profiles for τ_a = 0.2, 0.3, 0.4, and 0.5. The other type is profiles in which a mixed layer with constant aerosol extinction exists up to a certain altitude, as illustrated in Fig. 6(b). In these profiles, the aerosol optical thickness is kept constant ($\tau_a = 0.3$ for the case of Fig. 6(b)) while the mixed layer height is varied as h_{ML} = 1.0, 1.5, ···, 3.0, and 3.5 km.

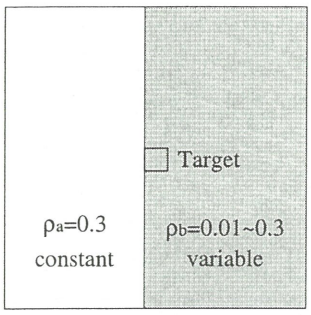

Two-reflectance surface

Figure 7: Flat and Lambertian surfaces with two reflectance values. ρ_a is fixed at 0.3, while ρ_b is varied between 0.01 and 0.3. The target area is placed on the border of the two surfaces, on the side of the surface with the variable reflectance.

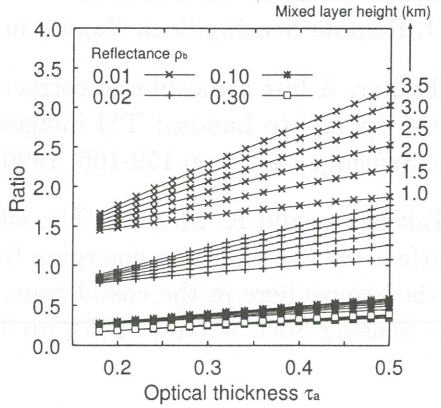

Figure 8: Adjacency effect relative to the ground-reflected irradiance. The curves show $r = E_{adj}/E_{gd}$ for various values of ρ_b and the mixed layer height h_{ML}.

3.3.2 Surface reflectance

In the present simulation, we adopt a situation with which the effect can be studied with the utmost clarity; namely we assume two (flat and Lambertian) surfaces with different reflectances (Fig. 7). As indicated in Fig. 7, the reflectance at the left side is fixed at $\rho_a = 0.3$, and that on the right side (ρ_b) is varied between 0.01 and 0.3. A target pixel is defined on the border of the two surfaces, on the side of the surface with the variable reflectance. We study the adjacency effect exerted on the "satellite image" of this target by changing the atmospheric as well as reflectivity conditions.

3.4 Results: Dependence on the surface reflectance

The influence of the surface reflectance is studied. Practically, it would be useful to give information on the ratio between the irradiances due to the adjacency effect and the direct ground reflection. Figure 8 shows the ratio $r = E_{adj}/E_{gd}$ as a function of the total aerosol optical thickness τ_a for various values of the surface reflectance ρ_b and mixed layer height h_{ML}. For the case of $\rho_b = 0.01$, the ratio is straightforwardly calculated from the E_{adj} and E_{gd}. It is found that the ratio r is larger for larger τ_a and larger h_{ML}. As the surface reflectance increases, r values are found to decrease, but exhibiting similar dependence on τ_a and h_{ML}. It is noteworthy that when ρ_b is small, even a small change of this value (*e.g.* from ρ_b =0.01 to 0.02) results in notable difference in the r values. When the surface reflectance is uniform (ρ_b = 0.3), the dependence on h_{ML} becomes minimal.

4. Conclusions

We have presented an algorithm in which only radiance components at the top of atmosphere are needed to calculate the reflectance of each pixel in satellite images. It has been shown that when the same atmospheric conditions are assumed for the construction of the test image and for the retrieval procedure, an accuracy of 1% is attained in the case of a visible image. The adjacency effect can easily be calculated on a pixel-by-pixel basis by means of our single scattering approximation. This calculation makes it possible to determine the range parameter N for each pixel. So far we have used aerosol models (i.e. wavelength dependence of the extinction) and aerosol vertical profiles provided in the MODTRAN source code. In this context, the data obtained with our multi-wavelength lidar will be quite beneficial to improve the actual atmospheric correction of the satellite images including Chiba area.

References

1) M. Minomura, H Kuze, and N. Takeuchi, Atmospheric correction of visible and near-infrared satellite data using radiance

components: an inproved treatment of adjacency effect, J. Remote Sensing Soci. Japan, in press.

2) R. Richter, A fast atmospheric correction algorithm applied to Landsat TM images, Int. J. Remote Sensing, **11**(1), pp.159-166, 1990.

3) T. Takashima and K. Masuda, The effect of land surface on the radiation emerging from the top of the atmosphere in the costal zone, J. Remote Sensing Soci. Japan, **18**(5), pp.3-13, 1997.

4) K. Thome, F. Palluconi, T. Takashima, and K. Masuda, Atmospheric correction of ASTER, IEEE Trans. Geosci. Remote Sensing, **36**(4), pp.1199-1211, 1998.

Retrieval of aerosol optical thickness from NOAA/AVHRR data on the sea and land areas

○ K. Asakuma, S. Otsutsumi, M. Yabuki, T. Kubota, H. Kuze, and N. Takeuchi
Center for Environmental Remote Sensing, Chiba University
1-33 Yayoi-cho, Inage-ku, Chiba, 263-8522, Japan
asakuma@ceres.cr.chiba-u.ac.jp

Abstract:
We present a retrieval algorithm of aerosol optical thickness over the land area. This algorithm is based on the dark-target approach combined with the texture analysis. In the first part of the algorithm, we employ the 6S code to calculate the relevant radiance components. The aerosol optical thickness is retrieved over the sea surface assuming a surface reflectance of 2 % with typical aerosol models in the 6S code (e.g. Maritime, Urban and Continental). In addition, we present a "Kanto" aerosol model on the basis of the ground measurements conducted at 11 sites on the Kanto plain during December 22-24, 1997. In this model, chemical composition data are used to derive the single scattering albedo and the asymmetry parameter. These optical parameters are useful to improve the accuracy of the radiation calculation with the 6S code. This method is applied to several sites arbitrary chosen on the sea area, and by two-dimensional linear interpolation, we obtain a "τ-image" over the land area. In the second part, a difference image is calculated between an actual satellite image (turbid image, NOAA AVHRR channel 1 on December 1, 1997) and a clear image that is obtained by applying the atmospheric correction to a satellite image (December 15, 1997). In the last part, the atmospheric features included in the difference image are analyzed by the texture analysis. For each area that includes both land and sea surfaces, and is categorized into a texel (i.e. its atmospheric feature is considered to be uniform), the optical thickness of the land area is assumed to be the same as that over the sea area. As a whole, the present method makes it possible to extend the method of analyzing atmospheric conditions from satellite data to the land surfaces that are surrounded by water areas.

1. Introduction

In order to derive precise surface reflectance from satellite image data in the visible and near-infrared bands, it is required to conduct the atmospheric correction which serves to remove the effects of molecular and aerosol scattering [1]. Generally the parameters needed in this type of calculation are the values of the optical thickness for molecules and aerosol particles. Thus far, we have studied the atmospheric correction based on a modification of the Richter's two-step algorithm [2, 3]. Since the chemical composition and size distribution of aerosol are quite variable, it is desired to devise some operational techniques to determine the aerosol optical thickness from satellite images themselves. A τ-map that describes the horizontal distribution of aerosol optical thickness could possibly be obtained by interpolating the aerosol optical properties observed at several sites using ground sampling and ground observations by means of instruments such as a sun-photometer and a lidar[4, 5]. Obviously this method could become laborious since it requires simultaneous observations at sufficient number of sites. In contrast, satellite images themselves can provide the instantaneous distribution of aerosol optical thickness in a broad area, once the ground reflectance is given. This approach, however, is hardly applicable to land surfaces because of a wide variety of surface conditions such as urban area, forest area, etc. In contrast, the sea surface and vegetation canopy exhibit more or less uniform reflectance, and over such surfaces, it becomes possible to retrieve the aerosol optical thickness by means of radiation transfer calculations. Recently the development of radiation transfer codes such as the 6S [6] has improved the situation, since they are equipped with standardized atmospheric conditions such as typical aerosol models. Moreover, the 6S code allows the user also to define the aerosol size distribution.

In this paper we present an algorithm for deriving the aerosol optical thickness over land areas surrounded by sea (or dark target) areas. Radiation transfer calculations and image processing techniques are combined to analyze the NOAA AVHRR images over the Chiba area. In the demonstration of our algorithm, we make use of the 6S code with its standardized aerosol models. In addition, we describe a method to determine aerosol optical quantities from their chemical properties acquired by ground sampling.

2. Algorithms

2.1 Radiance components detected by a satellite sensor

In the visible and near-infrared bands, a satellite sensor detects the radiance that is affected by the atmospheric absorption and scattering. The radiance received by a sensor is expressed as :

$$L_{\mathrm{total}}^{\mathrm{SAT}} = (DN \cdot S + I)\frac{E_s}{100\pi W} \qquad (1)$$

where DN stands for the digital number at each pixel in the satellite image, E_s is the solar irradiance at the top of the atmosphere, W is the band width, and S and I are the calibration constants of the satellite sensor. Figure 1 shows the radiance components detected by a satellite sensor. The 6S code computes the following six components : 1) L_{tar} : The radiance due to the target pixel L_{tar} includes the three components of L_{gd}, L_{gi}, and L'_{gi}. 2) L_{env} : The "environmental" radiance arising from the contigu-

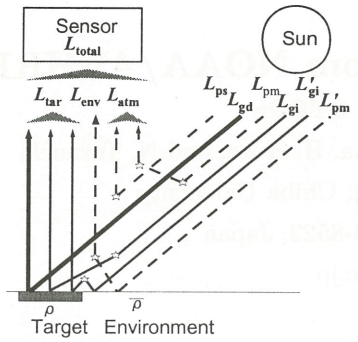

Fig. 1: Radiance components detected by a satellite sensor.

ous pixels. 3) $L_{\rm atm}$: The path radiance originating from the single and multiple atmospheric scattering.

The 6S code does not provide the directly ground reflected component, $L_{\rm gd}$. Alternatively, we use the following equation to obtain this component, which is denoted as $L_{\rm gd}^{\rm RTC}$:

$$L_{\rm gd}^{\rm RTC} = \frac{1}{\pi}\int E_s(\lambda)T_g^{\lambda}(\theta_s)\mu_s e^{-\tau/\mu_s}\rho e^{-\tau/\mu_v}d\lambda. \quad (2)$$

Here τ_{550} stands for the aerosol optical thickness at 550nm, used as an input parameter in the 6S code. Now the directly ground-reflected radiance observed by the satellite sensor, $L_{\rm gd}^{\rm SAT}$, is expressed as a function of τ_{550}:

$$L_{\rm gd}^{\rm SAT} = L_{\rm total}^{\rm SAT} - L^{'}(\tau_{550}), \quad (3)$$

$$L^{'}(\tau_{550}) = L_{\rm total} - L_{\rm gd}^{\rm RTC}, \quad (4)$$

$$L_{\rm total} = L_{\rm atm} + L_{\rm env} + L_{\rm tar} \quad (5)$$

where $L_{\rm total}^{\rm SAT}$ is the radiance received by the AVHRR sensor (channel 1) obtained with Eq.(1), and $L^{'}(\tau_{550})$ the total path radiance at 550 nm: this path radiance is a function of τ_{550} alone when the ground reflectance ρ is assumed to be 0.

2.2 Construction of Kanto aerosol models from the chemical properties

Aerosol particles are emitted from diverse origins and suspended in the air incessantly changing their size and composition[7]. Although there exist numerous ways to classify the aerosol composition, primary components are soil and sea salt from natural origin, carbon and heavy metal from artificial sources, and water-solubles such as sulfates and nitrates. In the visible wavelength, particularly important components are elementary carbon and water-soluble particle, both of which effectively absorb visible photons. Moreover, water-soluble particles promote the cloud condensation working as nuclei in the process. In the simple treatment of the global radiative forcing, it is customary to use the ratio between elementary carbon and water-solubles[8]. Also in the 6S code, aerosol optical properties are calculated using this ratio as well as the parameters describing the soil and maritime components.

In the present work, we adopt the method developed by Ota[9]. Namely, it is assumed that in the troposphere aerosol particles consist of six species, *i.e.* elementary carbon (EC), organic carbon (Org), ammonium sulfate ($(NH_4)_2SO_4$), ammonium nitrate (NH_4NO_3), sea salt cation, and soil. The effect of humidity on the particle radius and density of water-soluble particles are incorporated by the Tang's theory. For non water-soluble particles, values of density, radius, and refractive index are assumed to be constant irrespective of the relative humidity.

In the sampling, a low-volume Andersen sampler is used with quartz fiber and poly-flon filters, giving classification of the particle radius in nine classes. Ion and carbonic components are detected by analyzing particles clinging to each filter. These components are divided into the above six species, and for each, the size distribution is determined by fitting the result to a bimodal, lognormal distribution. Since the refractive index of each constituent is available[12], the Mie-calculation gives the extinction coefficient $\sigma_{\rm ext}$, scattering coefficient $\sigma_{\rm sca}$, and scattering phase function $P_i(\theta)$ for each component:

$$\sigma_{\rm ext}^{i} = \int Q_{\rm ext}^{i}(r,\widetilde{n})\cdot n_i(r)dr, \quad (6)$$

$$\sigma_{\rm sca}^{i} = \int Q_{\rm sca}^{i}(r,\widetilde{n})\cdot n_i(r)dr, \quad (7)$$

$$\int P_i(\theta)d\Omega = 4\pi, \quad (8)$$

where $Q_{\rm ext}$ and $Q_{\rm sca}$ are the extinction and scattering cross section, and the suffix $i = [1, 2, \cdots, 6]$ refers to the aerosol species. For the mixture of the six components, the single scattering albedo ω_0 and the asymmetry factors g are calculated using the sum of $\sigma_{\rm ext}$, $\sigma_{\rm sca}$ and $P_i(\theta)$.

2.3 Determination of τ and construction of τ-MAP

In this paper, we derive the optical thickness from images of AVHRR channel 1 (centered at 630nm). The reflectance of the sea surface is assumed to take a constant value of ρ =0.02. In addition to the radiance components mentioned above, the code yields the aerosol optical thickness which corresponds to the center wavelength of 630 nm, $\tau_{630}^{\rm RTC}$. If the target exhibits the Lambertian reflection, the same optical thickness at 630 nm that the satellite sensor observes can also be calculated from the direct component $L_{\rm gd}^{\rm SAT}$ as

$$\tau_{630}^{\rm SAT} = \frac{-1}{\sec\theta_s + \sec\theta_v}\ln\left(\frac{\pi L_{\rm gd}^{\rm SAT}}{E_s\rho\mu_s\mu_v}\right). \quad (9)$$

Thus, we can determine the "best fit" value of the optical thickness from the condition of $L_{\rm gd}^{\rm SAT} = L_{\rm gd}^{\rm RTC}$.

The calculation is carried out at about 30 pixels in Fig.2, arbitrarily chosen on the sea area around the Chiba prefecture (Boso peninsula surrounded by the Tokyo Bay and the Pacific Ocean). By interpolating the τ_{630} values from the sampling points, we

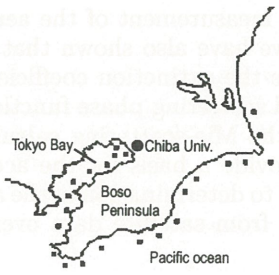

Fig. 2: Sampling points around Boso peninsula.

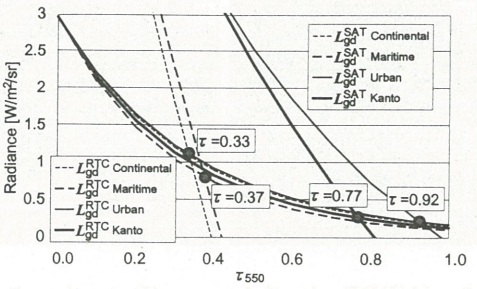

Fig. 3: Relationship between τ_{550}, $L_{\rm gd}^{\rm SAT}$ and $L_{\rm gd}^{\rm RTC}$ over Tokyo-bay (December 5, 1997).

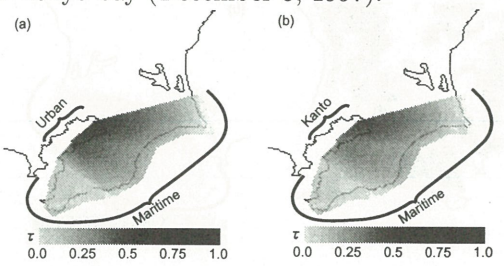

Fig. 4: τ-maps around Chiba (December 5, 1997).

obtain a τ-map. The two-dimensional interpolation is performed by combining three sampling points ($\triangle$ ABC), linearly interpolating the value on an arbitrary side (e.g. $\overline{\rm BC}$), and linearly interpolating along the lines which connect each sampling point on the chosen side ($\overline{\rm BC}$) with the residual point of the triangle (A).

For modification of the τ-map, we make use of a classification technique based on the texture analysis. The method is applied to an image obtained by subtracting a "clear" image from an actual "turbid" satellite image. This difference image is thought to involve the main feature of the atmosphere involved in the test image. The actual calculation of the difference image is conducted by converting the radiance values of AVHRR channel 1 into the reflectance values. The difference between the test image reflectance $\rho_{\rm t}^*$ and the reference image reflectance $\rho_{\rm c}^*$ is evaluated by means of the following parameter dif:

$$dif = (\rho_{\rm t}^* - \rho_{\rm c}^*)/(\rho_{\rm t}^* + \rho_{\rm c}^*). \qquad (10)$$

The texture analysis is carried out to look for regions that are characterized by uniform conditions of the atmosphere [10]. Texture stands for a pattern of radiances which a region exhibits in an image. The actual implementation of the texture analysis generally relies on the co-occurrence probability matrix, $P_{\rm c}(k,l)_{r\theta}$. This describes the probability that when the distance r and the angle θ between two pixels are specified, the combination of their radiance values becomes (k,l).

In order to simplify the calculation, however, here we adopt the gray level difference vector (GLDV) method, in which the difference in the radiance, $n = |k-l|$, is employed rather than the pair of radiance values [11]. As for the textural feature value, we make use of the following normalized parameter derived from the GLDV, $P_{\rm g}(n)_{r\theta}$:

$$f_{\rm m}(r,\theta) = \sum_{n=0}^{N_g-1} nP_{\rm g}(n)_{r\theta}/(N_g-1). \qquad (11)$$

Here N_g denotes the bin number used in the radiance classification, and the function $f_{\rm m}(r,\theta)$ takes a value between 0 and 1. This function describes the extent of the difference in the maximum and minimum densities in a image: when high similarity is present among neighboring pixels, $f_{\rm m}(r,\theta)$ approaches 0.

Using the result of the texture analysis, the interpolation of the τ-map is conducted again. This time, when some land and sea areas are included in a region with a uniform condition of the atmosphere (*i.e.* in a texel), the aerosol optical thickness on the sea surface is extended to the land area as well.

3. Results and Conclusions

Figure 3 shows relationship between τ_{550}, $L_{\rm gd}^{\rm SAT}$ and $L_{\rm gd}^{\rm RTC}$ over Tokyo-bay on December 5, 1997. The typical aerosol models, such as Maritime, Urban and Continental model, and the Kanto model explained in Sec.2.2 are employed with the provided models in 6S code. For each model, the value of τ_{550} is obtained from the condition of $L_{\rm gd}^{\rm SAT} = L_{\rm gd}^{\rm RTC}$. For acquiring the Kanto aerosol model, simultaneous observations were made at eleven sites to observe chemical properties of aerosol particles during December 22 to December 26, 1997. From this data, we calculate the following four optical parameters that are used as input parameters in the 6S code: the extinction coefficient, single scattering albedo, asymmetry factor, and scattering phase function. We can recognize that result from the Kanto model is close to that from the urban model.

Figure 4 shows τ-maps with combined aerosol model on December 5, 1997. (a) is obtained with the urban aerosol model on the Tokyo-bay side, (b) with Kanto aerosol model. Although the values of τ are different between Fig.4 (a) and (b), the resulting distributions have some characteristics in common: τ is relatively large around the Tokyo Bay, and it tends to decrease toward the east and south directions.

Figure 5 (b) shows the difference image between NOAA AVHRR ch.1 raw image on December 5, 1997 in Fig.5 (a) and its atmospherically corrected image. The correction is made using the Richter's two-step algorithm with the optical thickness values measured

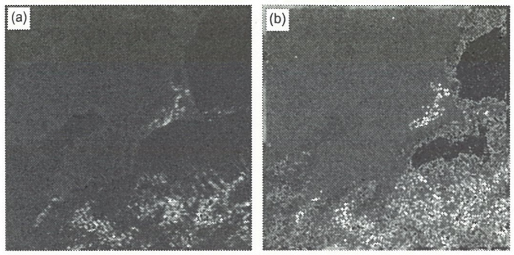

Fig. 5: AVHRR ch. 1 images (December 5, 1997). (a) Raw image and (b) Difference image between the raw image and the atmospherically corrreced image.

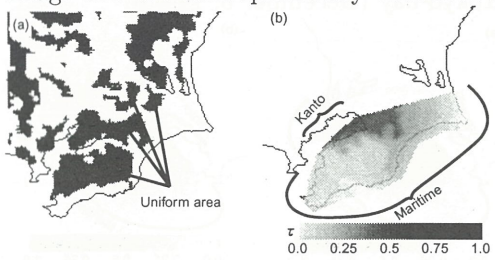

Fig. 6: Result of texture analysis. (a) Uniform atmospheric condition areas obtained from Fig.5 (b) and (b) Modified τ-map with Fig.6 (a).

at Chiba University. Because of the adjacency-effect correction, a trace of the seashore is recognizable in Fig.5 (b). Nevertheless, in this figure as a whole, the influence of the ground reflection has been removed satisfactorily, and the image is mostly contributed from the atmosphere.

The texture analysis is implemented to the difference pixel radiance defined in Eq.(10). and the result is shown in Fig.6 (a). In this figure, black regions indicate that in them, the optical thickness is considered to be uniform. This result is obtained by assuming a texture size of 9×9, $r = 1$, $\theta = 0°$ and $\theta = 90°$. Moreover, we make a logical product of the image with $\theta = 0°$ and $\theta = 90°$, both being converted to binary images with a threshold of $f_{\mathrm{m}}(r, \theta) = 0.3$. In this figure, two regions are discerned that have uniform atmospheric conditions beyond the land/sea borders over the southern part of the Boso peninsula, and three uniform regions are found the northern part of the Boso peninsula.

By supplementing the τ-map in Fig.4 by the texture information in Fig.6 (a), we obtain an improved τ-map as shown in Fig.6 (b). Comparing this figure with Fig.4, it is seen that the region of relatively large τ becomes more limited around the city area. At the same time, the region with smaller τ near the entrance of the bay becomes more extended toward the inland.

In this work, it has been shown that for a land surface surrounded by water areas (or more generally, dark areas), the combination of dark target method and the texture analysis provides a possibility to derive the distribution of aerosol optical thickness from satellite data. A set of reference (atmosphercally corrected) images and aerosol database with the information on the seasonal variations would be particularly beneficial for this purpose. On the basis of a campaign measurement of the aerosol chemical composition, we have also shown that optical information such as the extinction coefficient, scattering coefficient, and scattering phase function are obtainable through the Mie-scattering calculation. These parameters provide a basis for the accurate aerosol model, leading to determination of the aerosol optical thickness map from satellite data over the relevant area.

References

[1] Y. J. Kaufman and C. Sendra : Algorithm for automatic atmosperic corrections to visible and near-IR satellite imagery, Int. J. Remotesensing, 9, 1,357-1,381, 1998

[2] R. Richter : A fast atmospheric correction algorithm applied to Landsat TM image, Int. J. Remotesensing, 11, 159-166, 1990

[3] M. Minomura, J. Ru, H. Kuze and N. Takeuchi : Atomospheric correction of satellile data using Multi-Wavelemgth Lidar data with MODTRAN 3 Code, Adv. Spase Res., 25, 1,033-1,036, 2000

[4] H. Ouaidrari and E. F. Vermote : Operational atomospheric correction of Landsat TM Data, Remote Sens. Env., 70, 4-15, 1999

[5] M. Yabuki : Optical properties of the atmospheric aerosols derived from the lidar measurement and aerosol sampling, Master thesis (in Japanese), Chiba Univ., 2000

[6] E. F. Vermote, D. Tanre, J. Deuze, M. Herman and J. Morcrette : Second simulation of the satellite signal in the solar spectrum, 6S ; An overview, IEEE Trans. on Geosc. and Remote Sens., 35, 675-686, 1997

[7] G. Hanel : Single scattering albedo, asymmetry parameter, apparent refractive index, and apparent soot content of dry particles Appl. Opt., 27, 2,287-2,295, 1988

[8] I. Schult, J. Feichter and W. F. Cooke : Effect of black carbon and sulfate aerosols on the global radiation budget J. Geoph. Res., 102, 30,107-30,117, 1997

[9] S. Ohta, M. Hori, N. Murao, S. Yamagata and K. Gast : Chemical and optical properties of lower tropospheric aerosols measured at Mt. Lemmon in Arizona, J. Global Environ. Engineer., 2, 66-78, 1996

[10] K. S. Kuo and R. M. Welch : Structural and textural characteristics of cirrus clouds observed using high spatial resolution LANDSAT imagery, J. Appl. Meteorol, 27, 1,242-1,260 1988

[11] S. Christopher, D. Kliche, C. Joyce and R. M. Welch : First estimates of the radiative forcing of areosols generated from biomass burning using satellite data, J. Geoph. Res., 101, 21,265-21,273, 1996

[12] A preliminary cloudless standard atmosphere for radiation computation, World Climate Programme; WCP-112, World Meteorological Organization, 1986

SeaWiFS-derived Ocean Color and Aerosol in the Western Equatorial Pacific Ocean :Validation and Comparison

K.Kozai[1], K.Ishida[2], M.Kusakari[1], M.Sasaki[3] and K.Nojima[4]
1 Kobe Univ. Mercantile Marine, 5-1-1, Fukaeminami, Higashinada, Kobe 658-0022,
2 Toba National College of Maritime Technology, 1-1, Ikegami, Toba 517-8501,
3 Meteorological Satellite Center, Japan Meteorological Agency, 235, Nakakiyoto 3, Kiyose,
4 Kinki University, 3-4-1, Kowakae, Higashiosaka 577-8502

Abstract

Observation of aerosol optical thickness and spectral water-leaving radiance are carried out onboard R/V MIRAI in the western equatorial Pacific Ocean during the international observation project of Nauru99 (MR99-K03 cruise) and the continuing MR00-K04 cruise. In situ data are taken with synchronized SeaWiFS overpasses and the SeaWiFS-derived aerosol optical thickness and normalized water-leaving radiance products are validated against the in situ data. By using the archived NOAA and SeaWiFS-derived aerosol optical thickness and other products in the western equatorial Pacific Ocean in situ aerosol optical thickness data for two cruises are compared with not only each other but also temporal and spatial variability of archived satellite-derived datasets. Based on these comparisons it was found out that the in situ aerosol optical thickness data are corresponded to the low values of aerosol optical thickness in the seasonal variability.

1. Introduction

The western equatorial Pacific Ocean is known as "warm pool"[1)] where the most active air-sea interaction is taken place in the world. During the last two years R/V MIRAI of Japan Marine Science and Technology Center (hereafter called JAMSTEC) extensively surveyed this region in order to clarify the mechanism of various air-sea interactions[2)]. We joined these cruises for observing aerosol optical thickness and spectral water-leaving radiance onboard R/V MIRAI synchronized with SeaWiFS overpasses in order to make it clear how aerosol optical thickness affects spectral water-leaving radiance which is known as ocean color. In this study in situ aerosol optical thickness and spectral water-leaving radiance are not only validated against the SeaWiFS-derived products but also compared with NOAA-derived aerosol optical thickness for annual and seasonal variability.

2. Method

The study area is shown in Fig.1. MR99-K03 cruise is carried out around Nauru Island as an international cooperation project called Nauru99 during the period from June 17 to July 17, 1999. MR00-K04 cruise is conducted north of New Guinea Island during the period from June 12 to July 6, 2000. During these cruises radiation observation onboard R/V MIRAI synchronized with SeaWiFS overpasses are carried out to characterize aerosol optical properties and their impacts on SeaWiFS-derived ocean color in the western equatorial Pacific Ocean. SeaWiFS is an abbreviation of Sea-viewing Wide Field-of-view Sensor onboard the SeaStar launched in 1998. The sensor has eight bands in the visible and near infrared wavelength and the tilt mechanism to avoid sun glitter as shown in Table 1[3)].

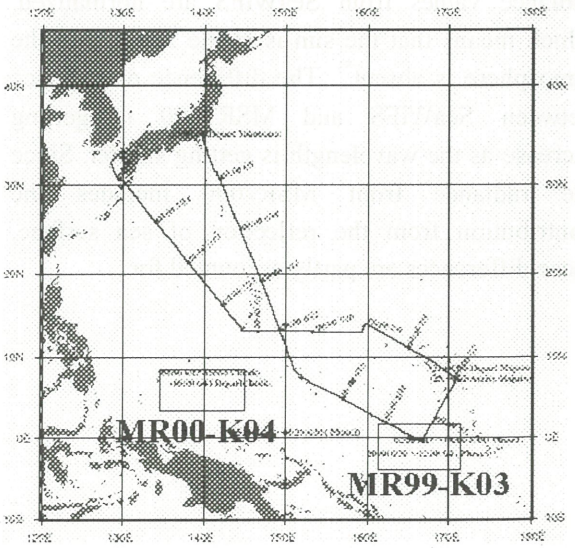

Fig.1 Study area with two R/V MIRAI cruises.
(Solid line shows the observation line of MR00-K03.)

Table 1. Specification of SeaWiFS

Band No.	wavelength(nm)
1	402-422
2	433-453
3	480-500
4	500-520
5	545-565
6	660-680
7	745-785
8	845-885
Equator Crossing	Local Noon(±20min), descending
Orbit type	Sun Synchronous at 705km
Spatial resolution	1.13km(LAC), 4.5km(GAC)
Swath width	2801km(LAC), 1502km(GAC)
Scan Plane Tilt	+20° ,0° , -20°

Table 2. Specifications of MSR7000,FPR5000,PSR1000

MSR7000	
Wavelength	400-1000nm
Wavelength resolution	1nm
Field of view	2 deg.
Detector	Silicon photo diode, photo multiplier

FPR5000, PSR1000	
Channel	Wavelength (band width)
0	443nm (20nm)
1	490nm (20nm)
2	565nm (20nm)
3	670nm (20nm)
4	765nm (40nm)
5	865nm (40nm)
Detector	Silicon photo diode
Polarizer	Glan Thompson prism
Field of view	2 deg.

Spectral water-leaving radiance is observed by a spectroradiometer MSR7000 and solar irradiance is measured by multi-polarimeter FPR5000 and PSR1000. Specifications of these radiometers are shown in Table2. Raw data derived from FPR5000 is converted to aerosol optical thickness using the algorithm developed by Masuda et al[4].

3. Validation and comparison

3.1 Spectral water-leaving radiance

An example of spectral water-leaving radiance derived from SeaWiFS and MSR7000 during the MR00-K04 cruise is shown in Fig.2. Spectral radiance values from SeaWiFS are normalized, which means that the sun is at the zenith and the atmosphere is absent[5]. The difference of radiance between SeaWiFS and MSR7000 is getting increase as the wavelength is getting shorter. Since the radiance from MSR7000 includes the contribution from the reflection of sea surface, these differences are partly accounted for.

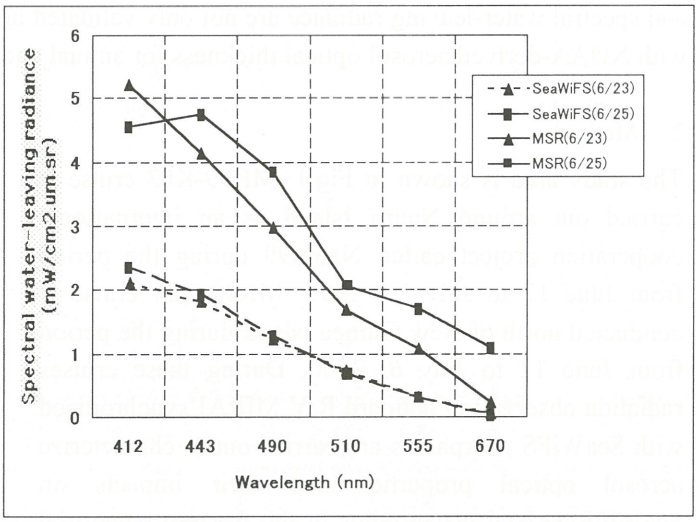

Fig.2 Spectral water-leaving radiance from SeaWiFS and MSR7000 at June 23 and 25, 2000 during the MR00-K04 Cruise.

3.2 Aerosol optical thickness

Aerosol optical thickness is observed by FPR5000 in 1999 and by PSR1000 in 2000. Since the number of matched observation between the in situ and synchronized SeaWiFS is small especially during the MR00-K04 cruise, an attempt is made to compare with archived aerosol optical thickness derived from NOAA/AVHRR[6]. More detailed discussion on operational aerosol products using NOAA/AVHRR is found in Stowe et al[7]. Fig.3 shows the comparison of aerosol optical thickness derived from satellites (NOAA/AVHRR and SeaWiFS) and in situ sensors (FPR5000 and PSR1000). Aerosol optical thickness from NOAA/AVHRR (indicated as average) is the mean value from 5 degrees south to 10 degrees north latitude at 150 degrees east longitude. During the period of two years aerosol optical thickness from NOAA/AVHRR clearly indicates the seasonal variability in which the low values dominates from June to October and high values from December to April. It is found out that SeaWiFS and in situ aerosol optical thickness values during the two cruises correspond to the low values in the seasonal variability.

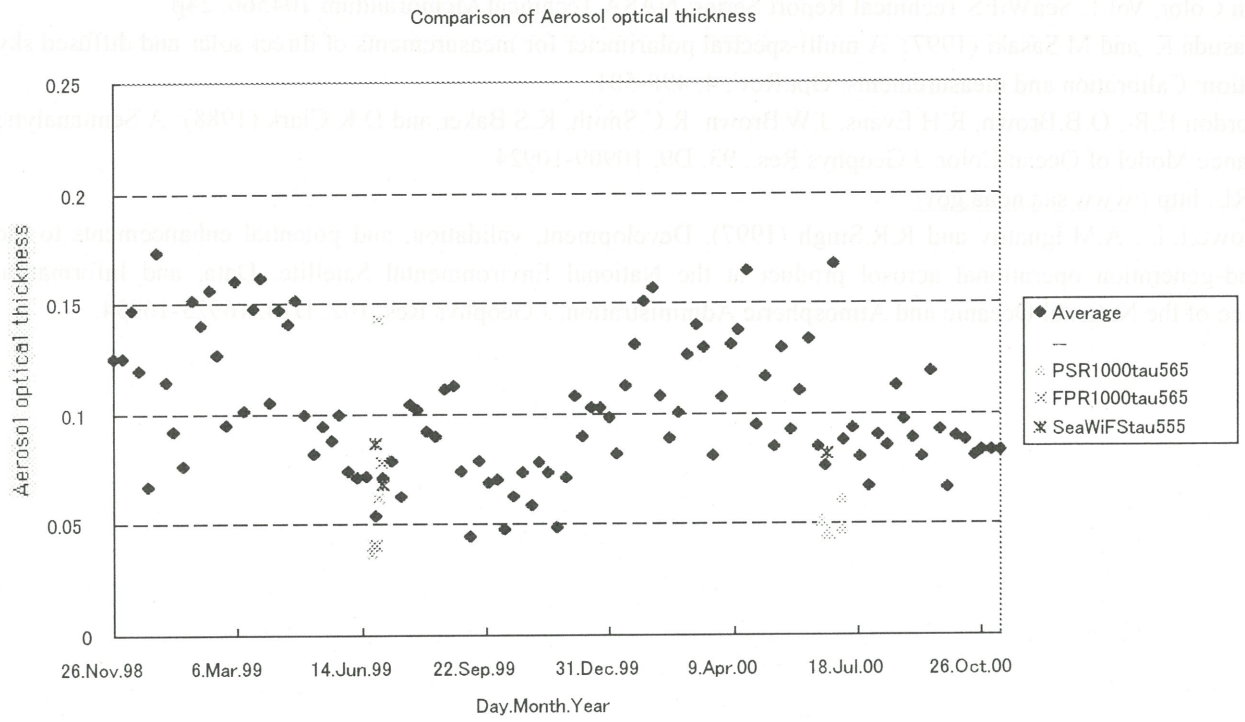

Fig.3 Comparison of aerosol optical thickness derived from satellites (NOAA/AVHRR indicated as average, SeaWiFS) and from in situ sensors (FPR5000 and PSR1000).

4. Summary

Based on the results and discussion above, the summary is described as follows.

(1) The difference of radiance between SeaWiFS and MSR7000 is getting increase as the wavelength is getting shorter. It is probably due to the fact that the radiance from MSR7000 includes the contribution from the reflection of sea surface.

(2) It is found out that SeaWiFS and in situ aerosol optical thickness values during the two cruises correspond to the low values in the seasonal variability derived from NOAA/AVHRR.

Acknowledgements
The authors would like to express their gratitude to the captain and crews of R/V MIRAI for conducting the international observation project of Nauru99(MR99-K03 cruise) and MR00-K04 cruise. They also acknowledge Dr.Asanuma of JAMSTEC for providing SeaWiFS LAC data (The first author (K.K) is the SeaWiFS authorized user). All SeaWiFS data are processed by SeaDAS version 4.0 provided by NASA GSFC.

References

1) Soloviev,A. and R.Lukas (1997): Observation of large diurnal warming events in the near-surface layer of the western equatorial Pacific warm pool. Deep-Sea Research I, 44, 6, 1055-1076.
2) Yoneyama,K. and M.Katsumata (2000): Overview of the R/V MIRAI Nauru99 Cruise. UMI TO SORA (J. of the Marine Meteorological Society) 76, 2, 59-63.
3) Hooker,S.B., W.E.Esaias, G.C.Feldman, W.W.Gregg and C.R.McClain (1992): An Overview of SeaWiFS and Ocean Color, Vol.1, SeaWiFS Technical Report Series, NASA Technical Memorandum 104566, 24p.
4) Masuda,K. and M.Sasaki (1997): A multi-spectral polarimeter for measurements of direct solar and diffused sky radiation: Calibration and measurements. Opt.Rev., 4, 498-501.
5) Gordon,H.R., O.B.Brown, R.H.Evans, J.W.Brown, R.C.Smith, K.S.Baker and D.K.Clark (1988): A Semianalytic Radiance Model of Ocean Color. J.Geophys.Res., 93, D9, 10909-10924.
6) URL: http://www.saa.noaa.gov/
7) Stowe,L.L., A.M.Ignatov and R.R.Singh (1997): Development, validation, and potential enhancements to the second-generation operational aerosol product at the National Environmental Satellite, Data, and Information Service of the National Oceanic and Atmospheric Administration. J.Geophys.Res.,102, D14, 16923-16934.

Detection of Asian dust aerosol over land using SeaWiFS data

Hajime Fukushima,[1] Masahiro Miura,[1] Tomohiro Takaoka,[1] Mitsuhiro Toratani,[1] and I. Uno [2]

[1] School of High-technology for Human Welfare, Tokai University
[2] Research Institute for Applied Mechanics, Kyushu University

Abstract

We propose a simple method of detecting dust-loaded airmass over the land area, which is based on the difference between Rayleigh-corrected reflectances at 412 nm and 443 nm bands of SeaWiFS data. The method, together with multi-band based cloud masking algorithm, is applied to '98 April SeaWiFS images of continental China, when a major dust event occurred. The resulted "dust aerosol index" imageries are compared with dust amount distribution predicted by a dust transport model, showing good general agreement. The correlation of the satellite-derived index and the predicted dust amount is discussed from the viewpoint of difference in the land cover.

Introduction

Mineral dust-rich aerosol, such as with Saharan dust or Asian dust particles, is important in terms of its effect on radiation budget as well as its role as a source of micro-nutrient in the oceanic phytoplankton ecosystem. To know the spatial distribution and its temporal variability, satellite observation of dust aerosol is of great importance.

There have been many works in satellite remote sensing of aerosol (King *et al.*, 1999, for example), where typical observation bands are mid-visible to near-infrared or short wave infrared. An exceptional case is Herman *et al.* (1997) who used UV observation data of Total Ozone Mapping System (TOMS) to derive Aerosol Index (AI), but there seems to be no attempt to use short wavelength visible band data, which may be useful in observing absorptive aerosol.

In this paper we study the possibility of using "blue" bands of Sea Wide Field-of-View Scanner (SeaWiFS) to detect the Asian dust-loaded aerosol over the land area. One of the differences between ocean and land in terms of satellite remote sensing of aerosol is the variability in the spectral reflectance of the surface. While the oceanic water is almost black at near infrared bands where most of the signal comes from aerosol, the land surface changes its spectral response over wide range of visible through near-infrared region, largely depending on its land cover category. Hence, we should take the difference in land cover into consideration although the analysis was not made at full strength in the present study.

In this paper, we define a simple empirical formula of "dust veil index over land (LDVI)" which is derived from the 412 and the 443 nm band data of SeaWiFS. Then, a series of "one day composite" imagery of the dust veil index over 11 days in April, 1998 is compared with the columnar mass of dust particles predicted by a dust transport model calculation developed by one of the authors. Comparison is also made with the contemporaneous TOMS Aerosol Index (AI) images. We also discuss the effect of different land cover category, using an existing land cover data base (Tateishi *et al.*, 1999).

Dust veil index over land (LDVI) for SeaWiFS data

Definition of LDVI

We first define the elevation-corrected Rayleigh radiance L_{CR} as the radiance that the satellite would observe at the pixel location when the atmosphere consists of air molecules only. In calculating this, we assume that the Rayleigh radiance is proportional to the surface pressure which, in tern, is a simple function of the elevation at the location.

Then, the empirical dust veil index over land LDVI is defined as

$$LDVI = \left\{L_T(443) - L_{CR}(443)\right\} - \left\{L_T(412) - L_{CR}(412)\right\}$$

where $L_T(\lambda)$ stands for the total radiance observed by SeaWiFS in λ [nm] band.

The rationale for this is formula as follows. Firstly, $L_T - L_{CR}$ is modeled as the sum of the radiance due to aerosol and the radiance due to the ground. Since the pair of the selected bands (412nm and 443nm) is located so close that we can anticipate minimum difference in the surface reflectance. Meanwhile, when we have dust aerosol, the aerosol radiance in 412nm band will be more diminished than in 443nm band due to the enhanced absorption effect that arises from larger value of imaginary part of refractive index of dust particles. This effect is also enhanced from the larger interaction between dust particles and air molecules due to the thicker Rayleigh optical thickness. Hence, we anticipate larger LDVI value when aerosol is more absorptive.

SeaWiFS data processing

SeaWiFS Level–1 GAC data that covers 80 – 150°E range were collected to form daily composites of LDVI images over the period of April 15 – 25 in 1998. The "cloud" pixel is masked when the following criteria were met at the same time.

$L_T(412) - L_{CR}(412) \geqq 8$,
$L_T(443) - L_{CR}(443) \geqq 10$, and
$L_T(670) - L_{CR}(670) \geqq 10$ ($\mu W/cm^2/nm/sr$).

Comparisons with other dust indices

Image comparisons

The resulted dust veil index images are shown in figure 1, together with ONLT model–predicted columnar amount (center) and TOMS Aerosol Index images (right). On–line dust transport (ONLT) model was implemented into Regional Atmospheric Modeling System (RAMS), to simulate the transportation of dust particles which originate desert areas in China (Uno *et. al.*, in press). The original data of TOMS AI are taken from the TOMS home page (http://toms.gsfc.nasa.gov/TOMSmain.html). Looking the dust images in a day by day basis, there is general agreement in "dust distribution" pattern among the three different imageries. The LDVI images show good correlation with the ONLT–predicted dust distribution, although it seems to fail in depicting "extreme dust load" in dust source area. In comparison with the LDVI and ONLT images, TOMS AI imagery shows significant difference in the magnitude of the index. It is not so sensitive for heavy dust load in the source areas whereas it shows high sensitivity in the areas far from the sources where the dust concentration is much lowered. This may indicate relative insensitivity to the near–surface dust events.

Consideration on different land cover

Although we assumed that the spectral reflectance of the surface observed in 412 and 443 nm bands are close and the effect of the variability in land surface reflectance is minimum, the LDVI values may be affected by different land cover. To see the variability due to that aspect, we used AARS Asian land cover data set (Tateishi *et al.*, 1999) to compare with the imageries. We show a part of our analysis below.

Figure 2 shows a scatter diagram of the sub-sampled LDVI and ONLT dust amount for April 20, 1998. At each sample location, the land cover is checked and, for this figure, the sample point is masked if the land cover is one of "water" categories or urban area. Hence, the points in the figure covers wide range of land cover classes, including vegetation, forests, grasslands, paddy/wheat fields, and even those non-vegetative areas such as bare ground, sand or rock. Although the scatter in figure 2 is not small, we see positive correlation of the index with the model-predicted dust amount.

We also conducted similar analysis on TOMS data whose result is shown in figure 3. Note that the diagram has more variability than the one in the previous figure, reflecting different response of TOMS AI over "source area" and "far area".

Figures 4 and 5 show examples of LDVI-ONLT relationship over different classes of land cover. In figure 4, we restricted samples to those with categories 10 through 132 of the land cover data set that corresponds to general vegetation area. This clearly shows better correlation in contrast to the result in figure 5 where the samples were taken from a set of categories which consists of paddy/wheat fields and other typical desert-type land cover such as sand, rock or bare ground.

Conclusion

We have introduced a simple index for dust-loaded aerosol based on the SeaWiFS short wavelength visible band data and conducted initial evaluation using a model-predicted dust amount and TOMS Aerosol Index over 11 day period in April, 1998 when major series of dust events occurred. From the results, our dust veil index (LDVI) shows significantly high correlation with ONLT model-predicted dust amount, which seems to be better than TOMS AI. At the same time, LDVI obviously has dependency on land cover, which necessitates further investigation.

Acknowledgement

This work was supported by the Ministry of Education, Science and Culture. The part of this work was also supported by National Space Development Agency of Japan.

References

Fukushima, H., M. Schmidt, B. J. Sohn, M. Toratani, and I. Uno (1999): Detection of dust loaded airmass in SeaWiFS imagery: an empirical dust index in comparison with model-predicted dust distribution over the Pacific in April 1998, Proc. 15th fall symposium, Korean Soc. Remote Sens. (KSRS).

Herman, J., P. K. Bhartia, O. Torres, C. Hsu, C. Seftor, and E. Celarier (1997): Global distribution of UV-absorbing aerosols from Nimbus-7/TOMS data, JGR, 102, 16,911-16,922.

King, M, Y. Kaufman, D. Tanre, and T. Nakajima (1999): Remote sensing of tropospheric aerosols from space: past, present, and future, Bull. American Meteor. Soc., 80, 11, 2229-2259.

Tateishi, R. and the Land Cover Working Group of the Asian Assoc. on Remote Sens. (1999): AARS Asia 30-second land cover data set, a CD-ROM publication, CeRES, Chiba Univ.

Uno, I., H. Amano, S. Emori, K. Kinoshita, I. Matsui, and N. Sugimoto (in press): Trans-Pacific yellow sand transport observed in April 1998: numerical simulation, JGR.

USGS EROS Data Center, GTOPO30, http://edcdaac.usgs.gov/gtopo30/gtopo30.html.

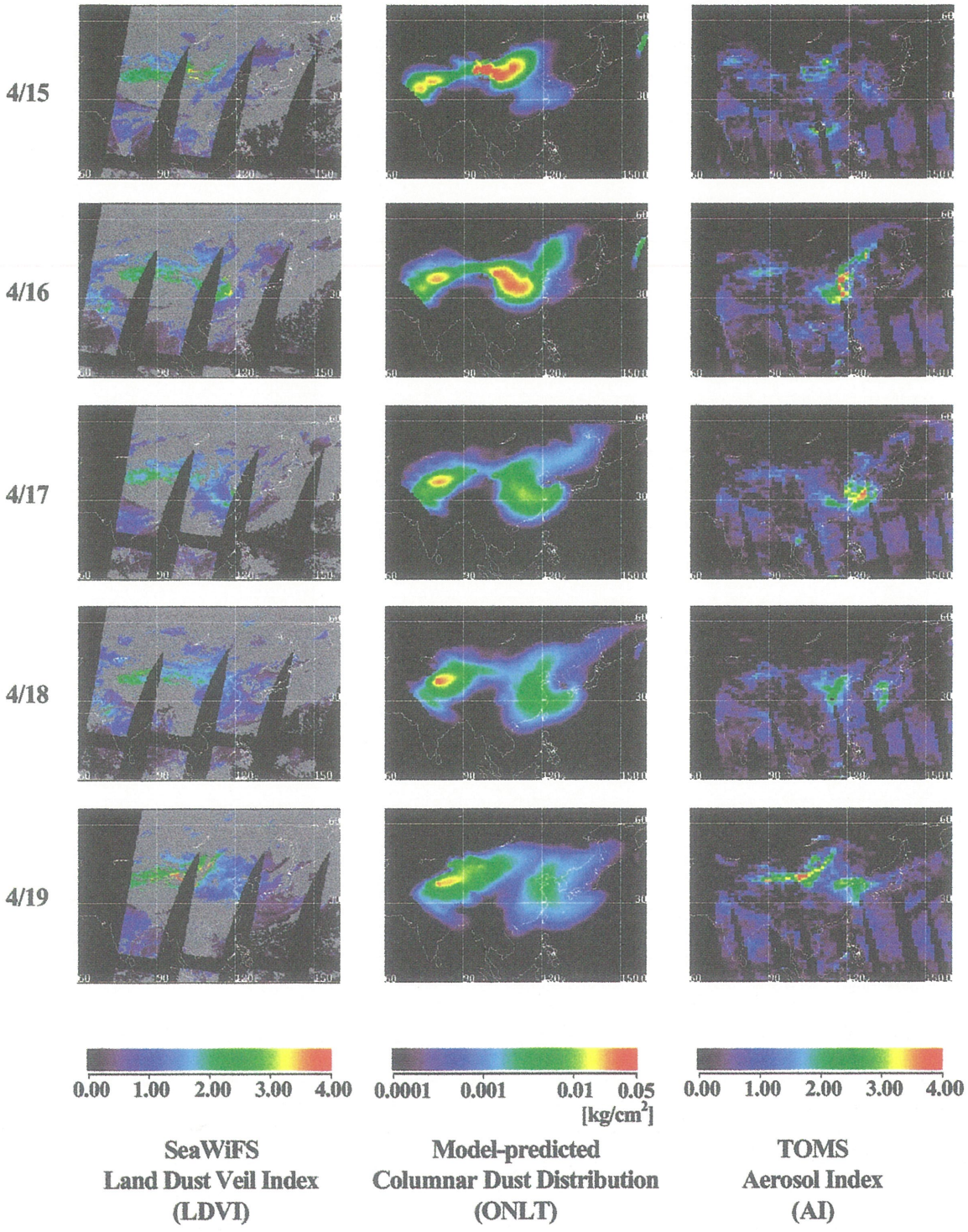

Figure 1. Comparisons of dust imageries over April 15 – 19, 1998. SeaWiFS-derived dust veil index for land (LDVI) proposed in this study, ONLT model-predicted columnar dust amount, and TOMS Aerosol Index taken from the TOMS home page.

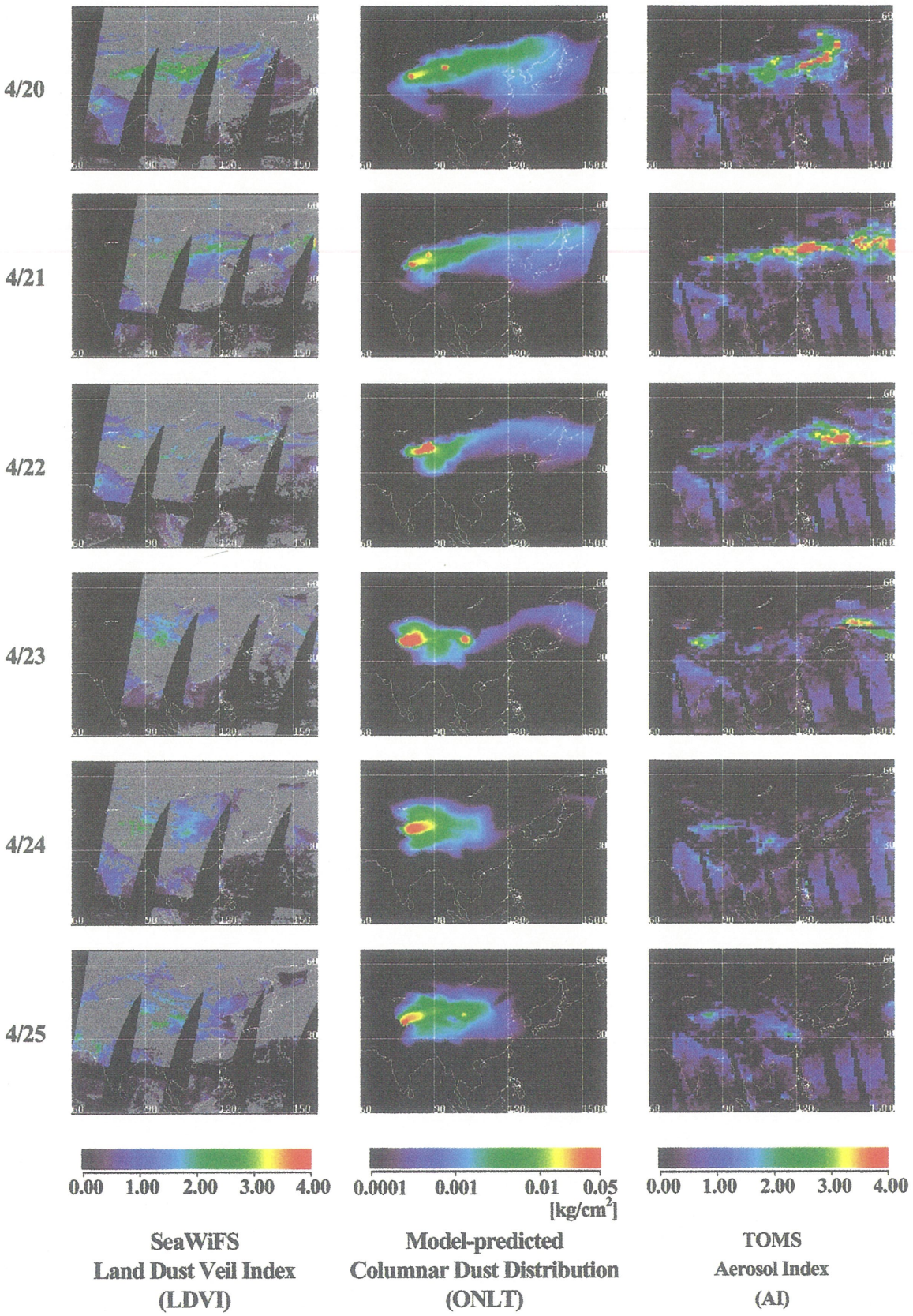

Figure 1. (continued) Comparisons of dust imageries over April 20 – 25, 1998.

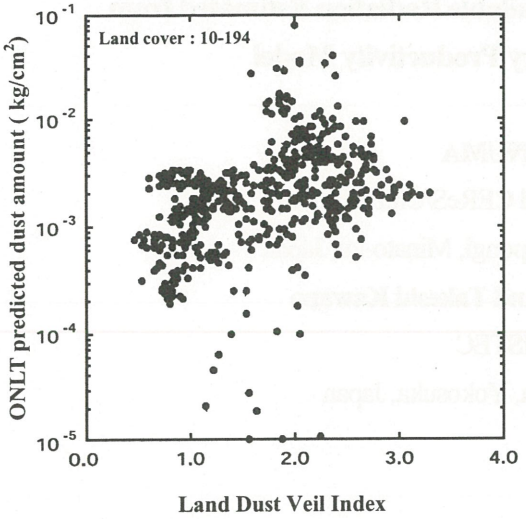

Figure 2. Scatter diagram of the SeaWiFS-derived dust veil index for land (LDVI) and the ONLT model-predicted columnar mass of the dust particles on April 20, 1998. Points are sampled with about 1-degree grid spacing over 30°-50°N and 75°-135° E areas. Land cover categories of 10-194 are considered.

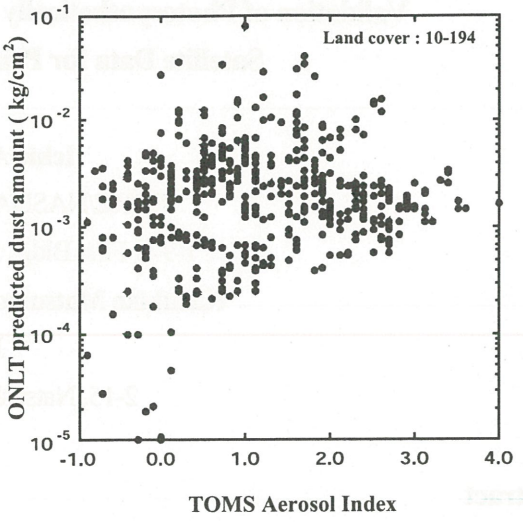

Figure 3. Scatter diagram of TOMS Aerosol Index and the ONLT model-predicted columnar mass of the dust particles on April 20, 1998. Points were sampled in the same way as Figure 2.

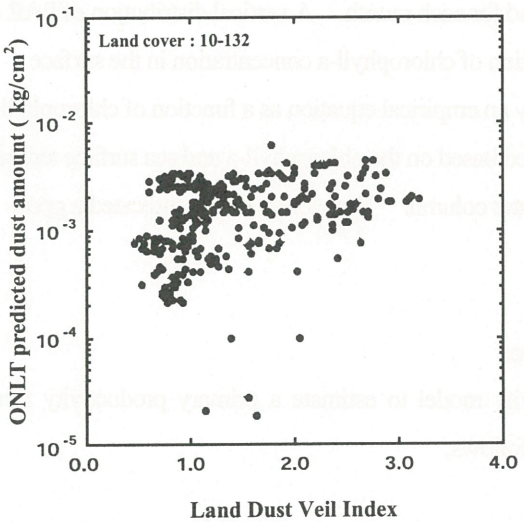

Figure 4. Same as Figure 2 but samples are limited to the land cover categories 10-132, which are mostly vegetation and grassland.

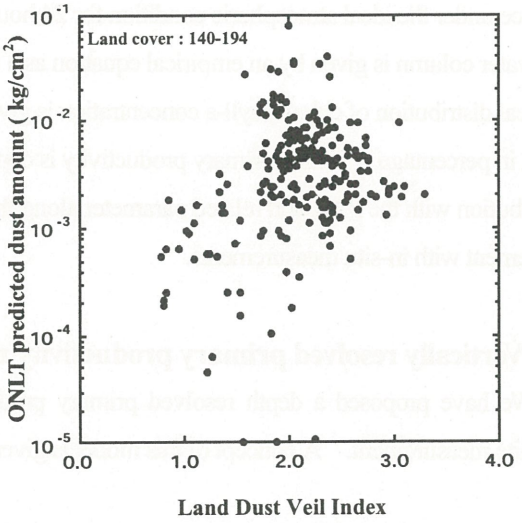

Figure 5. Same as Figure 2 but samples are limited to the land cover categories 140-194, which include paddy, wheat, bare ground and rock.

Validation of Photosynthetically Available Radiation Estimated from Satellite Data for Primary Productivity Model

Ichio ASANUMA
EORC/NASDA and CEReS/Chiba Univ.
1-9-9, First Bldg., Roppongi, Minato-ku, Japan
Kazuhiko Matsumoto and Takeshi Kawano
JAMSTEC
2-15, Natsushima, Yokosuka, Japan

Abstract

A vertically resolved primary productivity model was proposed for a satellite remote sensing using a ocean color sensor and an infrared thermal sensor. A photosynthetically available radiation (PAR) was estimated from a satellite data and a radiative transfer model. A basic function for the PAR is given as a function of cloud distribution from satellite observations. A weekly composite of chlorophyll-a distribution by SeaWiFS was used to estimate a cloud distribution. The radiative transfer model, MODTRAN 4.3, was operated to compute the solar irradiation on the sea surface under the ideal atmospheric condition for 24 hours and for each month. A vertical distribution of PAR along the water column is given by an empirical equation as a function of chlorophyll-a concentration in the surface. A vertical distribution of chlorophyll-a concentration is given by an empirical equation as a function of chlorophyll-a and PAR in percentage. Then a primary productivity is computed based on the chlorophyll-a and sea surface temperature distribution with the PAR and related parameter along the water column. The current model indicated a good agreement with in-situ measurements.

1. Vertically resolved primary productivity model

We have proposed a depth resolved primary productivity model to estimate a primary productivity from a satellite measurement. A concept of this model is given as follows;

$$PP_{eu}=\int\int_z P_b(z,PAR(z,t),T)C(z,E\%(z))dz\,dt \quad \text{.....(1)}$$

,where PP_{eu} is the primary productivity (mgC.m^{-2}.day^{-1}), P_b *is the* carbon fixation rate (mgC.mgChl-a^{-1}.m^{3}.hour^{-1}), ***PAR*** *is the* photosynthetically available radiation (Ein.m^{-2}.hour^{-1}), ***C*** *is the* chlorophyll-a concentration (mg.m^{-3}), ***T*** *is the water* temperature (deg-C) and ***t*** is the time for 24 hours. We proposed the carbon fixation rate, ***Pb***, as a function of PAR, temperature and depth from the in-situ measurement along the Equator and the middle latitude in the Pacific. The carbon fixation rate is given as follows;

$$Pb(z,PAR(z,t),T)=16\,[1-\exp\{-0.5a*PAR\%(z)*0.01\}]\,\exp\{-0.3b*PAR\%(z)*0.01\} \quad \text{.....(2)}$$

,and $a=0.1*s*PAR(0)+i$

$s=-0.00011T^{**}3+0.0039*T^{**}2-0.0007T+0.2557$

$a=0.000215T^{**}3-0.0106T^{**}2+0.0868T-0.1042$

$b=0.00048T^{**}3-0.018T^{**}2+0.1134T+3.1214$

We empirically defined a vertical distribution of photosynthetically available radiation along the depth in percentage, $PAR\%(z,C_0)$, as a function of a chlorophyll-a concentration in the surface as follows;

$$Log(PAR\%(z,C_0))=(aC_0+b)Z+2 \quad \ldots(3)$$

,where C_0 is a chlorophyll-a concentration in the surface, which could be replaced by a satellite observation, Z is the depth, and a and b is empirical constants.

A vertical distribution of chlorophyll-a concentration is proposed by the following function as a function of a vertical distribution of PAR and a chlorophyll-a concentration in the surface.

$$C(z)=[1-c\cdot exp\{-a\cdot PAR\%(z,C_0)\}]\cdot exp\{-b\cdot PAR\%(z,C_0)\}+C_0 \quad \ldots..(4)$$

,where a, b, and c are empirical constants.

2. Photosynthetically Available Radiation

A determination of the PAR on the surface is another key issue to estimate the primary productivity. Frouin et al. (.http://orca.gsfc.nasa.gov/seawifs/par/doc/seawifs_par_wfigs.pdf, 2000) proposed a research product for the PAR from SeaWiFS measurement. The PAR at the surface for the day, ***PARday***, is computed with a remote sensing reflectance ***R i(t)*** from SeaWiFS measurement as follows:

$$PAR_{day}=PAR_{ext}\iint f(Ri(t), Td, Tg, Sa)dt\,d\lambda \quad \ldots..(5)$$

,where ***PARext*** is the incoming solar flux at the top of the atmosphere, ***Td*** is the clear sky diffuse transmittance, ***Tg*** is the gaseous transmittance, ***Sa*** is the spherical albedo. They computed the PAR at the sea surface at the time for a single path from the top of the atmosphere to the sea surface without considering the total sky radiance.

In our study, ***PAR(t)*** at the sea surface is computed by MODTRAN-4.3 for the ideal atmospheric condition as a function of the time, ***t***, date of the year, and the latitude with considering the total sky radiance. In this computation, the aerosol model is selected for the maritime extinction with 23 km visibility under the model for the mid-latitude summer atmosphere. Then, a cloud distribution is estimated from the SeaWiFS chlorophyll-a distribution, where missing data is considered as the presence of cloud. The weekly composite data is selected to estimate a cloud distribution. Although there remains a possibility of the sun glint region in the missing data as discussed by Frouin et al.(2000), we took a lower possibility of the sun glint region than a daily composite chlorophyll-a distribution. The averaged ***PAR(t)*** for the hour and for one month is computed by MODTRAN-4.3. Fig.1 shows an example of ***PAR(t)*** distribution for Jun, where a higher irradiation is expected in the northern higher latitude. Then, the daily integrated ***PARday*** for one month is given as follows:

$$PAR_{day}=(0.9-0.05\,\Sigma Cloud)\int PAR(t)\,dt \quad \ldots..(6)$$

,where ***Cloud*** is given as 1.0 from the missing chlorophyll-a data. The cloud distribution is integrated four weeks

and the PAR is integrated for 24 hours.

Fig.2-a shows a monthly mean PAR determined in this study and Fig. 2-b shows a monthly mean PAR proposed by Frouin et al.(2000), indicated as GSFC. Fig.3 shows a comparison of the PAR along the date line in December 1997 between this research and GSFC.

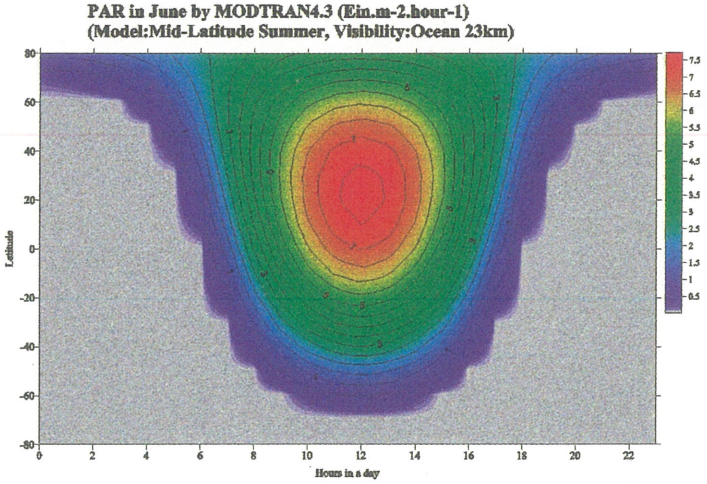

Fig. 1 Monthly mean PAR in June computed by MODTRAN4.3 in $Ein.m^{-2}.hour^{-1}$. X axis shows hours for the day and Y axis shows latitude.

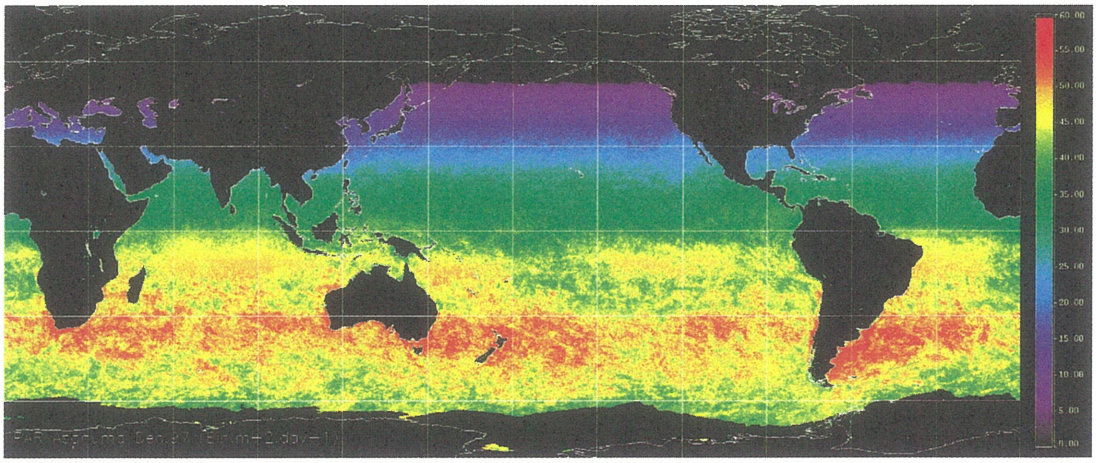

Fig. 2-a Monthly mean PAR for December 1997.

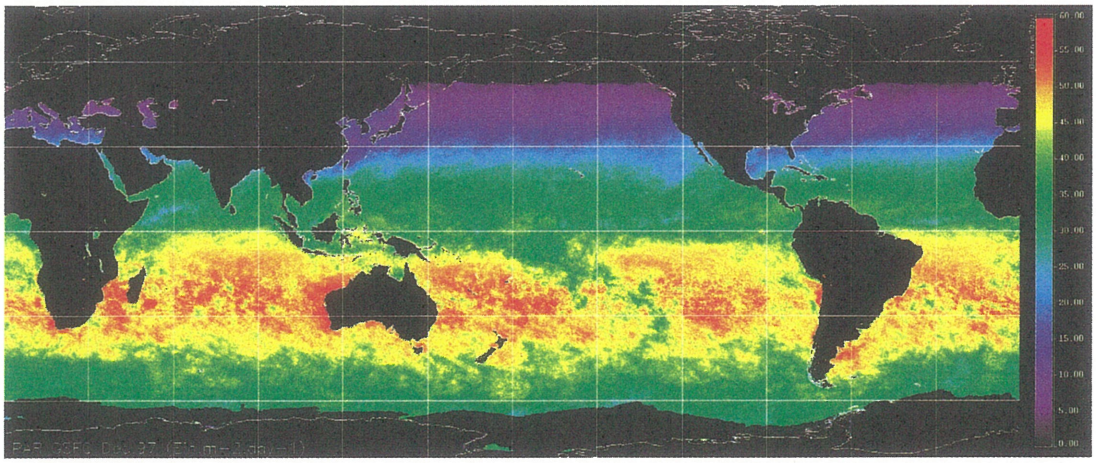

Fig. 2-b Monthly mean PAR for December 1997 by Frouin et al. (2000).

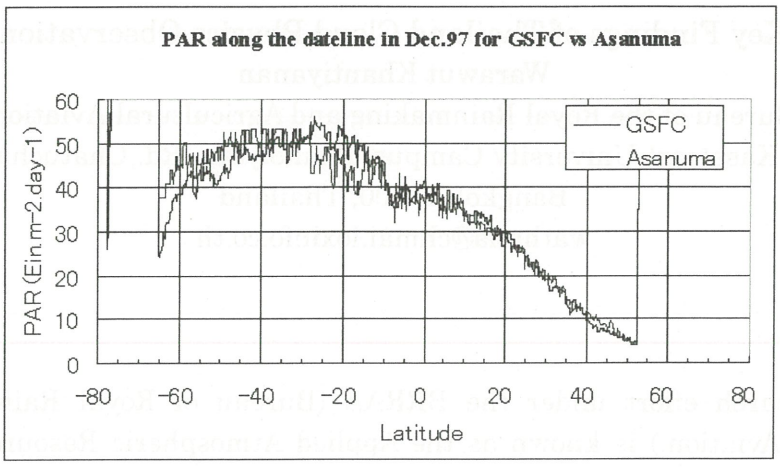

Fig.3 PAR along the dateline in December 1997 for GSFC and this research.

3. Discussion

This research and GSFC showed a different PAR in the southern higher latitude for December 1997 in Fig. 2-a and 2-b. According to the profile along the date line in Fig.3, two profiles show a good agreement for the northern sphere and to 10 deg-S. In contrast, GSFC showed a higher PAR around 20 deg-S and a lower PAR between 40 to 60 deg-S. Around 20 deg-S, the sun glint region, which was not eliminated through weekly composite and was recoginzed as a missing data, has a possibility to reduce the PAR in our research. The difference between this research and GSFC goes to 5 to 10 Ein.m^{-2}.day^{-1} around 20 deg-S. In 40 to 60 deg-S, the difference between two algorithms may go to the difference of definition of PAR. Frouin et al.(2000) computed the PAR on the surface as the transmitted ***PARext*** through the atmosphere. This research computed the PAR on the surface by MODTRAN4.3 with including all possible sky radiance to the sea surface. The difference may increase for the higher latitude, especially for the longer daytime. The maximum difference between two PARs is around 25 %, which may cause a significant difference in the primary productivity. Unfortunately, we are missing PAR data on the higher latitude and it will be an important target for the in-situ measurement.

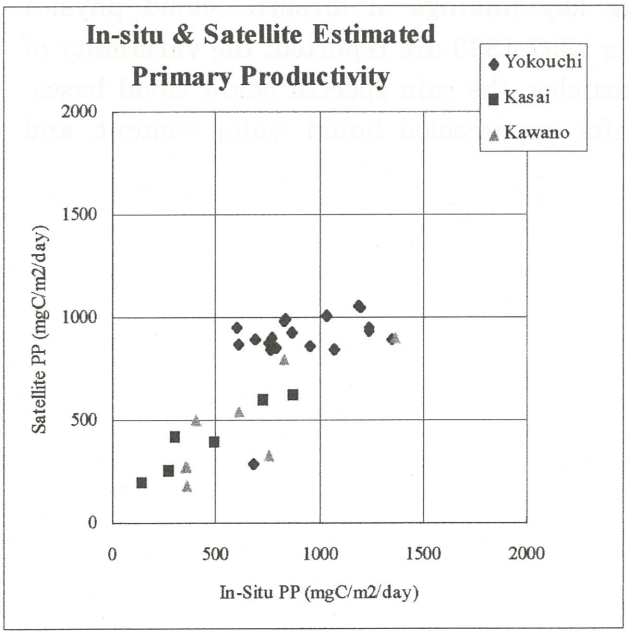

Fig. 4 In-situ and satellite estimated PP.

Currently, our primary productivity model is running very well. Fig.4 shows a scatter diagram between the computed primary productivity and in-situ measurements along the Equator and the mid-latitude around Japan. As described for the PAR in-situ measurement, the in-situ measurement in the higher latitude may keep a key for this study.

Key Findings of Thailand Cloud Physics Observation

Warawut Khantiyanan
Bureau of the Royal Rainmaking and Agricultural Aviation
In Kasetsart University Campus, Phaholyotin Rd.,Chatuchak,
Bangkok 10900, Thailand
wathana@chmai.loxinfo.co.th

The research effort under the BRRAA (Bureau of Royal Rainmaking and Agricultural Aviation.) is known as the Applied Atmospheric Resources Research Program (AARRP). The goal of the program is to upgrade the capability to conduct a scientifically sound demonstration project to quantify the water augmentation potential of rainmaking in Thailand.

During the 1997 field season, the BRRAA acquired two King Air B-350 cloud physics aircraft. The instrumentation on the King Air cloud physics aircraft included, among other things, FSSP, 2DC and 2DP probes for the measurement of cloud hydrometeors, a King hot-wire device for the measurement of cloud liquid water content, a Ball variometer for the estimation of cloud updrafts, temperature and dew point probes, and a GPS navigation system; all of which were recorded on a data acquisition system with real-time display capabilities. In addition, the aircraft was equipped with a forward-looking video camera. During 1997, one of the aircraft also contained a PCASP probe and University of Wyoming Cloud Condensation Nuclei (CCN) counter which NCAR provided on a short-term loan. During 1998, the BRRAA acquired University of Wyoming CCN counters for both aircraft.

In this presentation the following key findings of airborne cloud physics measurements under the AARRP during 1997-1999 are reported: the variability of the CCN measurements and aerosol particles, the rain spectra below cloud bases, and the cloud profiles including updrafts, supercooled liquid water content, and cloud droplet concentrations.

Statistical relationship between ISCCP cloud type and relative humidity observed by radiosonde

Toshiro Inoue and Hirotaka Kamahori
Meteorological Research Institute
1-1 Nagamine, Tsukuba Ibaraki 305-0051, Japan

Abstract

The statistical relationship between ISCCP (International Satellite Cloud Climatology Project) cloud type and relative humidity profile observed by radiosonde was studied during the period from July, 1992 to June, 1994. The ISCCP-DX data of GMS were used to compute the cloud amount for each cloud type over the 1.5 degree grid area centered at the radiosonde station. To obtain the reliable cloud type classification, the data at 00 UTC when the visible data were available were used. The radiosonde observations when the 1.5 degree grid area is covered by single cloud type were used to compare the relative humidity profile. Four cloud types of low-level, middle-level, cirrus- and cumulonimbus-type cloud were selected for the comparison.

As was expected, the relative humidity was highest at all levels when the cumulonimbus-type cloud existed and was lowest at all levels when no cloud existed. The relative humidity was higher than that of a cloud-free case at middle-level (low-level) when middle-cloud (low-cloud) existed. Cirrus clouds are difficult to identify objectively from single infrared measurement. In ISCCP, however, cirrus cloud can be identified with the use of visible and infrared measurements. When cirrus cloud existed, the high level relative humidity showed local maximum and was higher than that when low- and middle-cloud existed.

1. Introduction

The presence of clouds influences the energetics of the atmosphere in two ways, the atmospheric water cycle and the radiation budget. In numerical weather prediction models, cloud amount is one of the important quantities to determine radiative fluxes (Saito and Baba, 1988). The ascent of damp air can lead to condensation and cloud is formed. During the ascent, although the mixing ratio of water vapor remains constant, the relative humidity increases and may reach 100% and condensation occurs. While, cloud will disappear when the cloud goes into drier air. Therefore, cloud is closely related with relative humidity at the level of cloud exists.

The study of the relationship between cloud and relative humidity is important in two ways, to estimate the relative humidity from the cloud amount, and to estimate the cloud amount from the relative humidity. The vertical moisture profiles have been estimated from GMS cloud data and used in the moisture analysis at the numerical weather prediction model in the Japan Meteorological Agency. The algorithm was statistically derived from the comparison between cloud data and moisture field observed by radiosonde.

Baba (1987,1995) improved the algorithm using the cloud data by considering mean cloud top temperature, minimum cloud temperature and standard deviation of brightness temperature within the 1 degree latitude/longitude area.

The former studies were based on single infrared measurement, which tends to misclassify the thin cirrus cloud as middle- or low-level cloud. The ISCCP (International Satellite Climatology Project) provides nine cloud types according to cloud height and optical thickness. In the cloud analysis, radiances are converted into cloud parameters with the help of a radiative transfer model and auxiliary data like temperature profiles derived from TOVS (Tiros Operational Vertical Soundings) and ozone information etc

In this study, cloud types classified in the ISCCP and cloud amount are taken into consideration to study the statistical relationship between cloud information and the vertical relative humidity profile, using data obtained during the period from July, 1992 to June, 1994.

2. Data

a) ISCCP-DX data

The ISCCP was established in 1982 and provided cloud information analyzed by combining satellite-measured radiances with TOVS atmospheric temperature-humidity data. The first version of

ISCCP products is called the C-series and the revised version of products is called the D-series. The pixel by pixel analysis is performed for satellite radiance data set and the results are reported in the DX data product, which has a nominal resolution of 30km and 3 hours. Here we use the ISCCP-DX data of GMS.
In ISCCP, visible (day only) and infrared data are used to retrieve cloud parameters. During day-time, the optical thickness of cloud is determined from visible reflectance. In the ISCCP-DX data, ice crystals with 30 μm effective radius are used to compute the optical thickness of clouds which are colder than 260K. The cloud top temperature is corrected for transmitted radiation as a function of optical thickness for transparent cirrus clouds. The ISCCP-DX data of daytime provides reliable cloud parameters by combining visible and IR data.

Based on these cloud optical thicknesses and heights, each cloudy pixel is classified into one of nine cloud types according to three cloud top pressure categories (divided at 440 and 680 hPa) and three visible optical thickness categories (divided at 3.6 and 23). In this study, we select four cloud types for simplicity in the comparison between cloud and radiosonde, instead of nine cloud types which are classified in the ISCCP. High-level cloud is classified as cirrus-type cloud with an optical thickness smaller than 3.6, and cumulonimbus-type cloud with an optical thickness greater than 3.6. Middle- and low-level cloud is combined as one cloud type, instead of the three cloud types at each level in ISCCP. We also consider the cloud-free case as another category

Since the ISCCP-DX data have a spatial resolution of 5km with sampled every 30km, we construct the 0.5 degree latitude/longitude grid map of cloud parameters over the GMS coverage of 50N-50S, and 110E-180E. The 00UTC data are used for comparison between cloud and radiosonde observations because the visible data of GMS is available at 00UTC.Cloud amount is computed over 3 by 3 grids (1.5 degree latitude/longitude area) data centered at the grid of the radiosonde station. The radiosonde data where only single cloud type exists over the 3 by 3 grids are used to study the relative humidity profile.

b) Radiosonde

To compare with cloud information from GMS, we use the 00UTC TEMP data, which coincide with the cloud observation. We use the standard level data of moisture information at 1000, 925, 850, 700, 500, 400 and 300hPa for computation of the relative humidity. Therefore, some fine vertical structures of moisture profiles are neglected.

Fig.1. shows an example of the position of radiosonde stations used in this study during August, 1993. The radiosonde stations are selected considering the height of the station and the effectiveness of the visible image at 00UTC during winter time. The radiosonde stations are selected near coasts or islands because the main purpose of this study is to find better relationship between cloud and relative humidity over the ocean where conventional radiosonde observations are sparse.

3. Results

ISCCP-DX data of GMS which is sampled every 30km is mapped onto a 0.5 degree latitude/longitude grid map. Every grid has cloud information of its nearest neighbor's original data. Cloud type is determined from the visible optical thickness and corrected cloud height is determined from visible and infrared data. Cloud amount is computed over 3 by 3 grids (1.5 degree latitude/longitude area) data centered at the grid of the radiosonde station.

Figure 2. shows the vertical profiles of mean relative humidity for four cloud types (low-level, middle-level, cirrus-type and cumulonimbus-type cloud) derived from ISCCP analysis and cloud free. As is expected, the relative humidity is higher at the level where cloud exists. The relative humidity is lowest for all levels in the cloud-free case. There is a local maximum of relative humidity at 850hPa. The water vapor is concentrated at lower levels when it is clear.

When cumulonimbus-type cloud exists, the relative humidity indicates the largest value for all levels. When the low-level cloud exists, the relative humidity at lower than 850 hPa is higher than when other cloud types exist except for when cumulonimbus-type cloud exists. When the middle-level cloud exists, the relative humidity at the level higher than 700hPa shows a larger value than low-level cloud. When cirrus cloud exists, the relative humidity at higher than 400hPa indicates a larger value than that of when middle-level cloud exists. However the relative humidity at lower levels is not significantly smaller, although it is smaller at the 850 and 700 hPa levels.

Generally, the humidity over the tropics is higher than that over the subtropics. We compare the cloud information with the northern subtropics (25N-50N), tropics (25N-25S) and southern subtropics (25S-50S). Regional characteristics of relative humidity profile was studied for each cloud type. Figures are

shown only cloud-free (Fig.3.) and cirrus-type cloud (Fig.4) cases.

Cloud-free case

Figure 3. shows the vertical profile of relative humidity with standard deviation for the cloud-free case. The top shows the data computed from the area of the northern subtropics at a higher latitude than 25N, the middle shows the data over the tropics and the bottom shows the data over the southern subtropics higher than 25S. The salient features of high relative humidity at lower than 850hPa can be seen over the tropics. The northern subtropics tend to be drier at the level higher than 500hPa in comparison with other areas. Over the southern subtropics, the relative humidity is rather drier at all levels.

Low-level cloud

The vertical profile of relative humidity over the northern subtropics is similar to that over the tropics. Again, the relative humidity over the southern subtropics tends to be drier at the level lower than 500hPa. A significant difference in relative humidity at lower levels can be seen in comparison with low-level cloud and the cloud-free case over the mid-latitudes of both hemispheres. However, over the tropics the vertical profile of relative humidity is similar to the cloud-free case, although the relative humidity is much larger at low levels.

Midle-level cloud

The vertical profile of relative humidity over the northern subtropics is similar to that over the southern subtropics except for higher levels. The relative humidity at lower levels is moist over the tropics. A large difference of the vertical profile of relative humidity can be seen for the mid-level cloud case at all levels and for all regions in comparison with the cloud-free case.

Cirrus-type cloud

It is interesting to find a similar vertical profile of relative humidity and local maximum at 400 hPa for both subtropical regions when cirrus cloud exists (Fig.4.). Again, the relative humidity tends to be drier at all levels for the southern subtropics. We cannot see the local maximum of relative humidity at higher levels over the tropics, although the relative humidity is larger especially at higher levels in comparison with the cloud-free case.

Cumulonimbus-type case

The vertical profile of relative humidity over the northern subtropics is similar to that over the tropics, although with a slight difference at lower levels. The relative humidity is drier at all levels over the southern subtropics.

4. Concluding Remarks

Using the reliable cloud information derived from ISCCP-DX, we studied the statistical relationship between cloud type and relative humidity profile observed by radiosonde observation. The studied region is the GMS coverage area and the studied period is the two year period from July 1,1992 to August 31, 1994. The 00UTC radiosonde observations are compared with the cloud information from GMS visible and infrared data taken at 00UTC. The spatial resolution of ISCCP-DX data is 5km and sampled every 30km. The satellite data are mapped onto 0.5 latitude/longitude grids. The cloud information is retrieved over the 1.5 by 1.5 latitude/longitude (3 by 3 grid) area centered at the radiosonde station. The five cloud types (including the cloud-free case) are derived from optical thickness and cloud height by ISCCP-DX data. They are low-level cloud , middle-level cloud, cirrus-type cloud and cumulonimbus-type cloud. The low-level and middle-level clouds are defined as cloud lower than 600hPa, and cloud higher than 600hPa and lower than 440hPa, respectively. The cirrus-type cloud is defined as cloud higher than 440hPa with visible optical thickness smaller than 3.6. The cumulonimbus-type cloud is defined as cloud higher than 440hPa with visible optical thickness larger than 3.6. The reader should note that the cloud type classification is slightly different from the original cloud type name in ISCCP.

The radiosonde observation of relative humidity is used for comparison when the 1.5 by 1.5 latitude/longitude area is covered by a single cloud type. The characteristics of the vertical profile of relative humidity are statistically studied in terms of cloud type and regional difference.

As is expected, the vertical profile of relative humidity is highest at all levels when cumulonimbus

type cloud exists and is lowest at all levels when no cloud exists. The relative humidity is higher than that of the cloud-free case at middle-level (low-level) when middle-cloud (low-cloud) exists. In the cloud-free case, the tropics shows a very high relative humidity maximum at 850hPa, which is not seen in mid-latitudes.

When cirrus cloud exists, the high level relative humidity is higher than that when low- and middle-cloud exists. We expect the local maximum of relative humidity at higher levels for the cirrus cloud case, however, the feature is seen only mid-latitude and not in the tropics. The middle-level (low-level) relative humidity is also higher than that when low-level (middle-level) cloud exists. Cirrus cloud is often associated with lower level clouds. In this multi-layer cloud case the satellite cloud retrieval algorithm tends to retrieve only higher cloud. This is one reason for the relatively higher relative humidity at middle- and low-level than in the cloud-free case.

Generally, the relative humidity over the southern subtropics is smaller in comparison with the northern subtropics and tropics. The 'Vaisala' radiosonde is used in Australia. It is known that the 'Vaisala' radiosonde shows a dry bias. The relative humidity at high levels tends to be larger over the northern subtropics than other places.

Acknowledgment

ISCCP-DX data of GMS were obtained from the NASA Langley Research Center EOSDIS Distributed Active Archive Center.

References

Baba, A., 1987: Improvement of the estimation method of moisture data from satellite cloud soundings, JMA/NPD Technical Report, No.16

Baba, A., 1995: Estimation of vertical moisture profiles from GMS cloud data, Technical Rev. RSMC Tokyo Typhoon Center, Vol. 1, 9-18.

Saito, K. and A. Baba, 1988: A statistical relation between relative humidity and the GMS observed cloud amount, 61, 187-192.

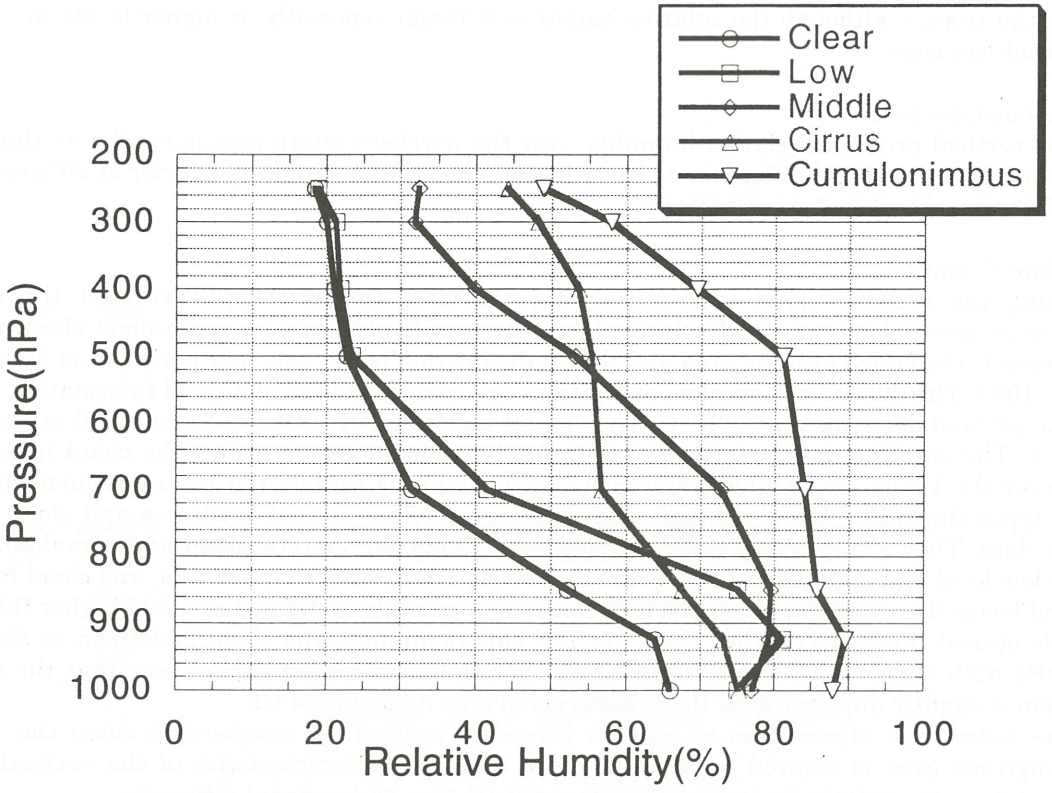

Fig.2. Mean vertical profile of relative humidity for each cloud-type.

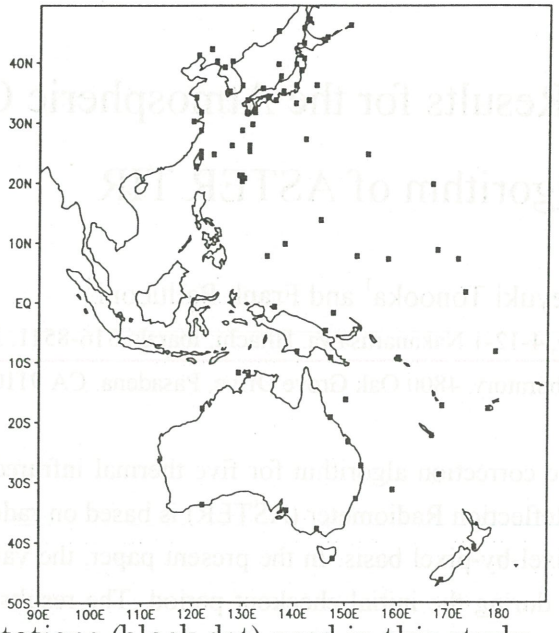

Fig.1. Radiosonde stations (black dot) used in this study.

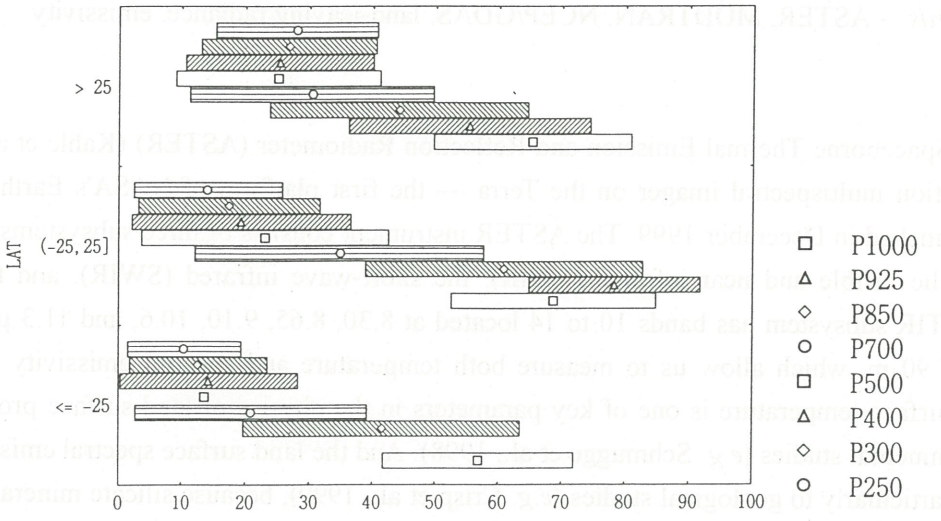

Fig.3. Regional difference of vertical profile of relative humidity for cloud-free case.

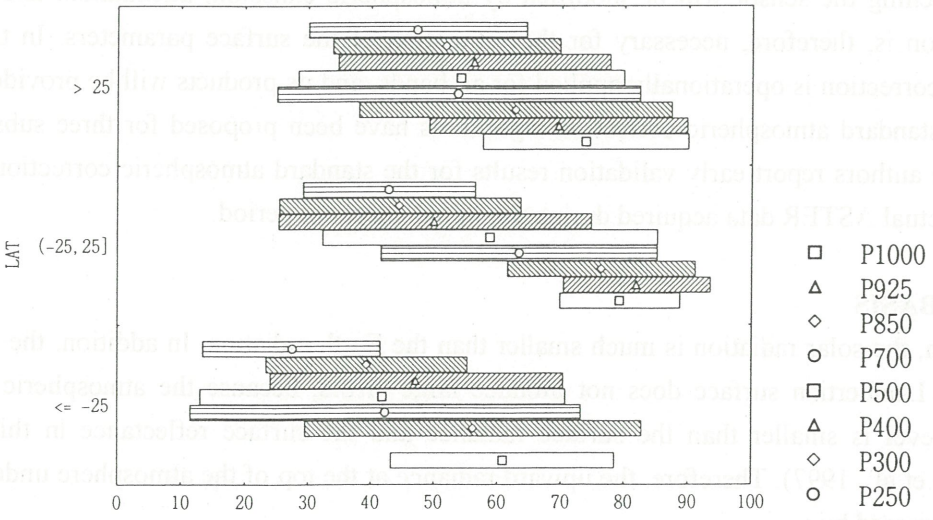

Fig. 4. Regional difference of vertical profile of relative humidity for cirrus-type cloud.

Early Validation Results for the Atmospheric Correction Algorithm of ASTER TIR

Hideyuki Tonooka[1] and Frank Palluconi[2]

1. Ibaraki University, 4-12-1 Nakanarusawa, Hitachi, Ibaraki 316-8511, Japan

2. Jet Propulsion Laboratory, 4800 Oak Grove Drive, Pasadena, CA 91109, USA

Abstract— The standard atmospheric correction algorithm for five thermal infrared bands of the Advanced Spaceborne Thermal Emission and Reflection Radiometer (ASTER) is based on radiative transfer calculation with global assimilation data on a pixel-by-pixel basis. In the present paper, the validity of this algorithm is studied using ASTER data acquired during the initial checkout period. The results show that the algorithm works well in dry conditions, but may fail in some humid conditions.

Keywords— ASTER, MODTRAN, NCEP/GDAS, land-leaving radiance, emissivity

INTRODUCTION

The Advanced Spaceborne Thermal Emission and Reflection Radiometer (ASTER) (Kahle et al., 1991) is a high-spatial-resolution multispectral imager on the Terra — the first platform of NASA's Earth Observing System (EOS) — launched in December 1999. The ASTER instrument consists of three subsystems divided by the spectral range: the visible and near infrared (VNIR), the short-wave infrared (SWIR), and the thermal infrared (TIR). The TIR subsystem has bands 10 to 14 located at 8.30, 8.65, 9.10, 10.6, and 11.3 μm with the spatial resolution of 90 m, which allow us to measure both temperature and spectral emissivity of the land surfaces. The land surface temperature is one of key parameters in the physics of land-surface processes, and used in many environmental studies (*e.g.* Schmugge et al., 1998). And the land surface spectral emissivity gives useful information particularly to geological studies (*e.g.* Crisp et al., 1990), because silicate minerals, included in many rocks and soils, have variety in emissivity (*e.g.* Salisbury et al., 1992).

The radiance reaching the sensor will be modified by atmospheric emission, attenuation, and scattering. Atmospheric correction is, therefore, necessary for the estimation of the surface parameters. In the ASTER project, atmospheric correction is operationally applied for all bands, and its products will be provided to users. For this processing, standard atmospheric correction algorithms have been proposed for three subsystems. In the present paper, the authors report early validation results for the standard atmospheric correction algorithm of TIR bands using actual ASTER data acquired during the initial checkout period.

THEORRETICAL BASIS

In the TIR region, the solar radiation is much smaller than the Earth radiation. In addition, the assumption that the surface is a Lambertian surface does not produce large errors, because the atmospheric downward radiance at ground level is smaller than the surface radiance and the surface reflectance in this region is generally small (Wan et al., 1997). Therefore, the upward radiance at the top of the atmosphere under clear-sky conditions can be expressed by

$$I(\lambda,\theta) = \tau(\lambda,\theta)\varepsilon(\lambda)B(\lambda,T_S) + I^{u}(\lambda,\theta) + \tau(\lambda,\theta)(1-\varepsilon(\lambda))I^{d}(\lambda) \quad (1)$$

where λ is the wavelength, θ is the view angle, $\varepsilon(\lambda)$ is the surface emissivity, T_S is the surface temperature, $B(\lambda,T_S)$ is the Planck function, $\tau(\lambda,\theta)$ is the atmospheric transmittance, $I^u(\lambda,\theta)$ is the path radiance, and $I^d(\theta)$ is the downward sky radiance (calculated by dividing the downward atmospheric irradiance at ground level by π). Equation (1) can be rewritten with a good approximation (Becker et al., 1990):

$$I_i(\theta) = \tau_i(\theta)\varepsilon_i B_i(T_S) + I_i^u(\theta) + \tau_i(\theta)(1-\varepsilon_i)I_i^d \quad (2)$$

where the index i means a weighted average in band i of each λ-dependent variable.

If the atmospheric effect parameters ($\tau_i(\theta)$, $I_i^u(\theta)$, and I_i^d) are known, the land-leaving radiance $I_i^L(\theta)$ is derived from Eq. (2):

$$I_i^L(\theta) = \varepsilon_i B_i(T_S) + (1-\varepsilon_i)I_i^d \quad (3)$$

where I_i^d is known. For each pixel, Eq. (3) is given for each band but unknowns are ε_i for each band and T_S — a typical underdetermined inverse problem. Many temperature/emissivity separation (TES) algorithms have been proposed for solving this problem (*e.g.*, Realmuto, 1990; Gillespie, 1998).

STANDARD ATMOSPHERIC CORRECTION ALGORITHM FOR ASTER TIR

The standard atmospheric correction algorithm of the TIR bands (Palluconi et al., 1996) is a method that estimates the atmospheric effect parameters on a pixel-by-pixel basis using MODTRAN (Kneizys et al., 1996) combined with atmospheric profiles and a digital elevation model (DEM). Water vapor and air temperature profiles given MODTRAN are derived from the products of MODIS, NCEP/GDAS (Global Data Assimilation System) or NASA/GEOS-1 (Goddard EOS) assimilation system. In these sources, the GDAS product (Kalnay et al., 1990) is currently used because the MODIS product has not been available yet for validation. The GDAS product is a data set for providing weather forecast systems with the initial values of various atmospheric parameters (humidity, temperature, wind speed etc.) at each 3-D grid-point (horizontally 1-degree spacing) every 6 hours. As for DEM, the GTOPO30 (USGS, 1997) is used.

VALIDATION OF THE ALGORITHM

As the first attempt for the validation of the above algorithm, we studied the algorithm performance based on the spectral emissivity of water targets retrieved from ASTER data. For this purpose, ten scenes acquired during the initial checkout period were used, and a rectangle target on lake or sea was selected from each scene.

Table 1: Test sites for the validation study.
(PWV: precipitable water vapor, RCC: radiometric calibration coefficient)

UTC date	Overpass	Site name (country or US state)	Elev. (m)	PWV (cm)	RCC ver.
12-Mar-00	Day	Lake Tahoe (CA)	1898	0.59	1.0
16-May-00	Day	Lake Kasumigaura (Japan)	1	2.02	1.0
16-May-00	Day	Tokyo Bay (Japan)	0	2.11	1.0
25-May-00	Night	Uchiura Bay (Japan)	0	2.90	0.4
4-Jun-00	Day	Salton Sea (CA)	-74	1.51	1.0
5-Jun-00	Day	Hawaii/Ocean (HI)	0	2.68	1.0
11-Jun-00	Day	Cold Springs Reservoir (NV)	1584	1.05	1.0*
7-Aug-00	Day	Salton Sea (CA)	-74	2.21	1.0
7-Nov-00	Day	Lake Tahoe (CA)	1898	0.58	1.0
8-Nov-00	Night	Lake Tahoe (CA)	1898	1.37	1.0

* Expedited Data Set (EDS). Default calibration coefficients (version 1.0) were used.

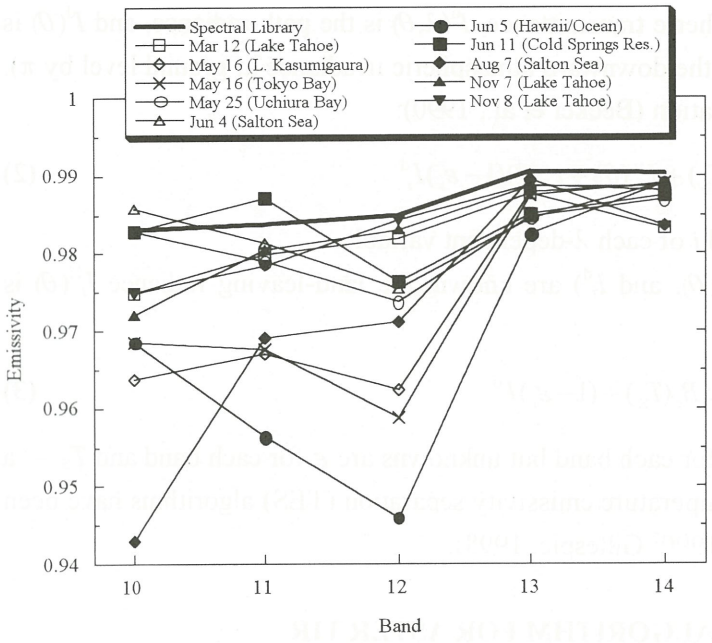

Figure 1: Comparison between the mean emissivity retrieved from each water target and the water emissivity included in the spectral library.

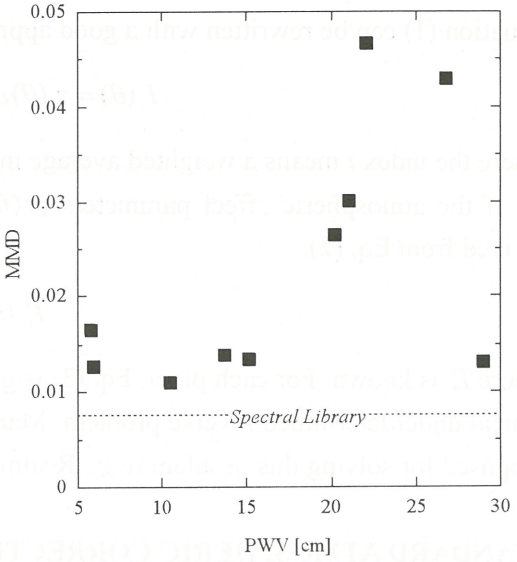

Figure 2: Plot of the precipitable water vapor (PWV) versus the minimum–maximum difference (MMD) in emissivity.

Table 1 gives some information on each scene and target. The size of each target is 30x30 pixels except for the June 11 data (4x4 pixels) and the November 8 data (20x20 pixels). For each pixel of each target, we made the following processing.

First, the digital number for each band was converted to the radiance measured. For nine sites except for the May 25 data, the latest radiometric calibration coefficients (version 1.0) were used. Next, the atmospheric effect parameters for each band were calculated using MODTRAN 3.7 combined with NCEP/GDAS products, TOMS total-ozone products, and GTOPO30. Then, the land-leaving radiance at each band was derived from the radiance measured, the transmittance, and the path radiance. Finally, the spectral emissivity for each band was retrieved from the land-leaving radiance and the sky radiance by the spectral normalization method (Realmuto, 1990) — one of TES algorithms — with the maximum emissivity of 0.99, and compared with the spectral emissivity of water included in a spectral library (Salisbury et al., 1992).

Thus, if the atmospheric correction applied includes an error, it will be detected in most cases as an abnormal spectral pattern on the retrieved emissivity.

RESULTS AND DISCUSSIONS

Figure 1 gives the comparison result between the mean emissivity retrieved from each site and the water emissivity included in the spectral library. The result shows that the atmospheric correction worked well for the six sites that the minimum emissivity is greater than 0.97, but not for the other four sites since the emissivity at bands 10 to 12 is smaller than expected. In particular, the emissivity retrieved from the June 5 and August 7 data is not acceptable (the difference of 0.03 in emissivity is almost corresponding to that of 1.8 K in temperature).

Figure 2 is the plot of the precipitable water vapor (PWV) versus the minimum–maximum difference (MMD) in emissivity for each site, which shows that the MMD increases with increasing PWV. As the result,

we can estimate that the atmospheric correction errors shown in Fig. 1 were caused mainly from the water vapor profile errors — the standard atmospheric correction algorithm works well in dry conditions but may fail in some humid conditions. However, the number of the data sets used in this study is not enough for us to suggest the algorithm performance in various conditions. We will continue the validation study for this purpose.

CONCLUSIONS

We studied the validity of the standard atmospheric correction algorithm of ASTER TIR using ten scenes acquired during the initial checkout period. As the result, the algorithm worked well in dry conditions, but failed in some humid conditions. However, more case studies are necessary for reliable validation. We will continue the validation study for this algorithm.

ACKNOWLEDGMENTS

The authors would like to thank MITI and ERSDAC for supplying original ASTER data.

REFERENCES

Becker, F., and Z.-L. Li, "Temperature-independent spectral indices in thermal infrared bands", *Remote Sens. Environ.*, vol. 32, pp. 17-33, 1990.

Crisp, J., A. B. Kahle, E. A. Abbott, "Thermal infrared spectral character of Hawaiian basaltic glasses", J. *Geophys. Res.*, vol. 95, no. B13, pp. 21657-21669, 1990.

Gillespie, A., S. Rokugawa, T. Matsunaga, J. S. Cothern, S. Hook, and A. B. Kahle, "A temperature and emissivity separation algorithm for Advanced Spaceborne Thermal Emission and Reflection Radiometer (ASTER) Images", *IEEE Trans. Geosci. Remote Sens.*, vol. 36, no. 4, pp. 1113-1126, 1998.

Kahle, A. B., F. D. Palluconi, S. J. Hook, V. J. Realmuto, and G. Bothwell, "The Advanced Spaceborne Thermal Emission and Reflectance Radiometer (ASTER)", Int. *J. Imag. Sys. Tech.*, vol. 3, pp. 144-156, 1991.

Kalnay, E., M. Kanamitsu, and W. E. Baker, "Global numerical weather prediction at the National Meteorological Center", *Amer. Meteor. Soc.*, vol. 71, no. 10, pp. 1410-1428, 1990.

Kneizys, F. X., L. W. Abreu, G. P. Anderson, J. H. Chetwynd, E. P. Shettle, A. Berk, L. S. Bernstein, D. C. Robertson, P. Acharya, L. S. Rothman, J. E. A. Selby, W. O. Gallery, and S. A. Clough, "The MODTRAN 2/3 report and LOWTRAN 7 model", F19628-91-C-0132, Phillips Laboratory, 1996.

Palluconi, F., G. Hoover, R. Alley, M. J. Nilsen, and T. Thompson, "An atmospheric correction method for ASTER thermal radiometry over land", ASTER Algorithm Theoretical Basis Document (ATBD), revision 2, 1996.

Realmuto, V. J., "Separating the effects of temperature and emissivity: Emissivity spectrum normalization", *in Proc. of the Second Thermal Infrared Multispectral Scanner (TIMS) Workshop*, JPL Publication 90-55, pp. 31-35, 1990.

Salisbury, J. W., and D. M. D'Aria, "Emissivity of terrestrial materials in the 8-14 μm atmospheric window", *Remote Sens. Environ.*, vol. 42, no. 2, pp. 83-106, 1992.

Schmugge, T. J., W. P. Kustas, and K. S. Humes, "Monitoring land surface fluxes using ASTER observations", *IEEE Trans. Geosci. Remote Sens.*, vol. 36, no. 5, pp. 1421-1430, 1998.

USGS, "GTOPO30 Documentation", http://edcwww.cr.usgs.gov/landdaac/gtopo30/README.html, 1997.

Wan, Z., and Z.-L. Li, "Physics-based algorithm for retrieving land-surface emissivity and temperature from EOS/MODIS data", *IEEE Trans. Geosci. Remote Sens.*, vol. 35, no. 4, pp. 980-996, 1997.

Validation of Satellite Aerosol Retrievals from AERONET Ground-based Measurements

Brent Holben[1], Lorraine Remer[2], Omar Torres[3] and Tom Zhao[4]
[1]NASA/GSFC, Code 923, Greenbelt, MD, USA
[2]NASA/GSFC, Code 913, Greenbelt, MD, USA
[3]Joint Center for Earth Systems Technology, UMD Baltimore Co, Baltimore, MD21250
[4]CIRA Visiting Scientist, NOAA/NESDIS/ORA, Camp Springs, MD 20746

Accurate and comprehensive assessment of the parameters that control key atmospheric and biospheric processes including assessment of anthropogenic effects on climate change is a fundamental measurement objective of NASA's EOS program (King and Greenstone, 1999). Satellite assessment programs and associated global climate models require validation and additional parameterization with frequent reliable ground-based observations. A critical and highly uncertain element of the measurement program is characterization of tropospheric aerosols requiring basic observations of aerosols optical and microphysical properties. Unfortunately as yet we do not know the aerosol burden man is contributing to the atmosphere and thus we will have no definitive measure of change for the future. This lack of aerosol assessment is the impetus for some of the EOS measurement activities (Kaufman et al., 1997; King et al., 1999) and the formation of the AERONET program (Holben et al., 1998). The goals of the AERONET program are to develop long term monitoring at globally distributed sites providing critical data for multi-annual trend changes in aerosol loading and optical properties with the specific goal of providing a data base for validation of satellite derived aerosol optical properties.

The AERONET program has evolved into an international federated network of approximately 100 ground-based remote sensing monitoring stations to characterize the optical and microphysical properties of aerosols. The recognized importance of these measurements to the international scientific community has likewise evolved. Initial requirements to provide improved characterization of the atmosphere for atmospheric correction of RS data was later augmented by the need to validate aerosol retrievals from satellites (Holben et al., 1998). Development of cloud cleared and quality assured data sets has anchored that effort (Smirnov et al., 1999). Recent growth and development of the program has further shifted emphasis to a complimentary system with satellite aerosol owing to the improved and new microphysical and optical properties retrieved from the globally distributed network of instruments (Dubovik and King, 2000). AERONET measurements characterize total column aerosol optical and microphysical properties in regions difficult for passive satellite systems, in particular over land where low aerosol loading and high surface reflectance presents only a weak noisy signal for satellite retrievals but is in the normal operating range for sun photometry. Furthermore, the diversity of geographic locations, aerosol types, and water vapor regimes dictates new opportunities for data collection, analysis of results and comparisons to satellite, airborne and in situ observational data sets. Clearly, progress in the earth sciences is driven by more and better measurements integrated with rigorous model development and analysis.

The AERONET program provides an array of aerosol optical and microphysical properties from inversion of direct sun and sky radiance measurements in the UV, visible and near-infrared wavelengths at approximately 100 globally distributed ground-based sites. The resulting temporal data-base of column integrated spectral aerosol optical thickness, spectral single scattering albedo, spectral phase function, particle size distribution among other parameters are quality assured and cloud screened. Accuracy assessments of field instruments have shown typical uncertainties of $\pm$ 0.01, $\pm$0.03 and $\pm$0.01 for AOD, single scattering albedo and effective radius respectively, well within the expected accuracy required for comparisons to and validation

of satellite retrievals. Validation is facilitated by development of a daily updated parameter specific spreadsheet of all AEROENT sites thus allowing direct temporal comparisons for all sites as needed for satellite retrievals and statistical assessment.

AERONET sites include most aerosol types such as biomass burning, urban/industrial sulfate, biogenic, marine and desert dust aerosols as well as various combinations of the above. These data have been compared to several satellite aerosol retrieval systems in an effort to provide an assessment of the processing algorithms and ultimately assist in a global aerosol assessment. TOMS, AVHRR, and MODIS represent a wide diversity of satellite system resolutions, spectral sensitivity and methods used to retrieve AEROSOL optical properties that have recently taken advantage of the AERONET data-base. Following is a brief summary of the results and approaches taken to assess satellite retrievals of aerosols.

TOMS

Total Ozone Mapping Spectrometer (TOMS) developed to assess ozone concentrations in the earth's atmosphere has been processed to detect and characterize global aerosol dynamics (Herman et al., 1997 and Torres et al., 1998). The approach uses space-measured radiances in the 330-380 nm range by the TOMS series of instruments and takes advantage of low and similar reflectances of water and land in the UV allowing characterization of aerosols. Two methods are used to characterize aerosol loading, based on absorbing aerosols (carbonaceous and mineral dust) and scattering aerosols sulfate based aerosols. In the former case, multiple Rayleigh scattering increases the photon path length and the opportunity of absorption by UV absorbing aerosols. Since this technique depends on molecular scattering, in addition to aerosol amount and microphysical properties, the measured radiances at the top of the atmosphere also depend on the height above the ground of the absorbing aerosol layer. The non–absorbing aerosol method depends on added singly scattered radiance to the background scattered radiances, thus is not dependent on the height of the aerosol layer (Torres et al., 1998). The great advantage of the UV-TOMS approaches is aerosol characterization over ice and snow free land and water surfaces, daily global coverage and long-term data archive but the disadvantage is sub pixel cloud contamination of the relatively large 40x40 km pixels. Clearly assessment of the retrieval success is needed.

The following analysis is reported by Torres et al., (2000). Six land-based AERONET sites were chosen for comparison to the EP-TOMS retrievals in the US representing three non-absorbing aerosol sites in the US upper midwest, lower great plains and eastern US; two mineral dust dominated (but some smoke) sites in West Africa and Mongu, Zambia affected by a long biomass burning season. EP-TOMS measurements were averaged over a 1°x1° box centered over the AERONET site and compared to quality assured (Smirnov et al., 1999) averaged AERONET observations within 30 minutes of satellite overpass. All AERONET AOT time comparisons clearly show a correspondence however large departures are noted. Analysis of scatter plots of EP-TOMS AOT vs AERONET for the non absorbing sites clearly illustrates that for low optical depths (τ_{380}<0.2) there is no significant correlation however when all points are considered R^2 of ~0.5 is obtained, correlations are improved when high values are included. For sun photometer AOT measurements exceeding 0.2 the level of agreement is within the predicted accuracy (±20%) of correct values (Torres et al., 1998 and Torres et al., 2000). Clearly over estimates by EP-TOMS may be attributed to optically thin clouds increasing the observed radiance with the TOMS FOV.

Comparison to absorbing aerosols shows a similar trend of low correspondence at low AOT however the R^2 is higher due to the larger optical depths observed at these sites driving the correlation. Most points do fall within the limits of uncerainty estimated by Torres et al., (1998)

that may be attributed to aerosol height, cloud contamination and prescribed surface reflectivity. It is postulated that some of the random uncertainty in the comparison is due to the variability is the aerosol distribution across the 1°x1° box which is not reflected in the AERONET point observation.

AVHRR

Zhao et al, (2000) addressed the issue of proper sampling of AERONET and satellite data for comprehensive validation of satellite aerosol retrievals. Their approach is to standardize the validation procedure by identifying through sensitivity studies optimal time/space match-up windows, the ensemble statistical analysis and the best selection of channels of sun-photometer observation and numerical scheme to interpolate/extrapolate sun photometer observations to satellite channels. The validation procedure was developed for and tested with NOAA-4/AVHRR and TRMM/CERES (VIRS) using oceanic AERONET sites with the added complication of extrapolation to 1.6 μm not measured by current AERONET instruments. Three aspects of validation were addressed, the calibration window size (100, 200, 300, 400 and 500 km radius), time from overpass window (1, 2, 3, and 4 hr), interpolation between bands to achieve the best spectral match up, and to determine the best method of selecting points within a time/space window.

A series of linear regressions are computed from aerosol optical depth and Angstrom exponent (τ_{st} vs τ_{sp} and α_{st} vs α_{sp}) scattergrams for a variety of daily time and space match-ups. The regression parameters (intercept, slope, standard deviation and R^2) may then be analyzed. A non zero intercept suggest the retrieval may be associated with system calibration error or improper assumption of ocean surface reflection. A non-unity slope indicates inconsistency between the aerosol microphysics model used in the retrieval algorithm and the true model. Seven oceanic and coastal sites were used both together and individually in the analysis.

Results from this investigation are absolutely clear. Zhao et al., (2000) report not unexpectedly that 1hr/100km proved to be the optimal time space match up and for AVHRR bands bracketed by the AERONET wavelengths, no significant difference was observed in channel combinations. They also determined that an ensemble of points falling within the 1hr/100km window is superior to specific selection criteria in part for improved statistics with the greater number of ensemble points. With the validation parameters clearly defined, Zhao et al., (2000) addressed questions on the global AVHRR retrieval set relating to retrieval model parameters, aerosol types, and viewing geometry.

MODIS

The MODerate resolution Imagining Spectroradiometer (MODIS) aboard NASA's Terra is the most advanced satellite system to retrieve aerosol optical properties including daily, global aerosol characterization (Tanré et al., 1997; Kaufman et al., 1997). Over cloud-free, glint free ocean scenes, the MODIS aerosol algorithm inverts the measured 500m resolution radiance from six MODIS bands (0.55-2.13 μm) to retrieve the aerosol information on a 10 km grid. Specific retrievals include aerosol optical thickness in seven wavelengths, the effective radius of the aerosol, the fraction of the total optical thickness contributed by the fine mode aerosol and various aerosol-related quantities derived from these primary retrievals (Tanré et al. 1997).

Remer et al., (2000) use a more restrictive time space window (30 min/50 km square) than Zhao to compare to the AERONET observations. Since August, 2000, eleven AERONET stations were included in the validation data set. These represent the Mediterranean (4 stations), the coastal western North Atlantic (2 stations), the Caribbean (2 stations) and a few island sites in the central North and South Atlantic (2 stations) and Indian oceans (1 station). The Pacific is not

represented. All MODIS data used in this study are derived with Version 2.6.1 of the algorithm (http://modis-atmos.gsfc.nasa.gov). All AERONET data is Level 1.5, which indicates preliminary cloud clearing, but no final calibration or Quality Assurance (Smirnov et al., 2000). MODIS derives two primary size parameters: the effective radius of the total aerosol size distribution and the fraction of optical thickness contributed by the fine mode aerosol. AERONET employs the Dubovik and King (2000) inversion on the sky radiance data to derive the aerosol size distribution and from the size distribution calculates the effective radius and the aerosol volume in each mode. The Dubovik and King (2000) effective radius is identical to the MODIS effective radius and directly comparable. The MODIS ratio of optical thickness should correlate to the AERONET ratio of volumes, but it is not the same quantity, and the two parameters are not expected to agree quantitatively.

The eleven site ensemble agreement, as represented by the linear fit (R^2= 0.88 at 660 nm), is exceptionally good and well within the expected uncertainty ($\Delta\tau = \pm 0.03 \pm 0.05\tau$) (Tanré et al., 1997; Tanré et al., 1999; King et al., 1999). The validation of the effective radius and the comparison of the ratio of modes are made for data with $\tau_{660} > 0.15$. For most of the range of sizes in this data set, MODIS retrievals fall within ±0.10 μm of the AERONET retrievals. The comparison of modal ratios indicate definite correlation, even though the values of the two parameters differ. This comparison with ground-based data gives us confidence that MODIS can differentiate between large mode and small mode aerosol, and begin to quantify the size of the aerosol particles.

These three examples of satellite aerosol validation represent very recent use of the AERONET data-base. As new AERONET data products are developed and micro and mega validation data-bases improved and made available on the AERONET website (http://aeronet.gsfc.nasa.gov:8080/), opportunities for multi satellite, ground-based and model comparisons and validations are expected to arise and improve our understanding of the global aerosol disposition.

References

Dubovik, O. and M. D. King, A flexible inversion algorithm for retrieval of aerosol optical properties from Sun and sky radiance measurements., *J. Geophys. Res.*, *105*, 20,673-20,696, 2000.

Herman, J.R., P.K. Bhartia, O.. Torres, C. Hsu, C. Seftor and E. Celarier, Global Distribuiton of UV-absorbing aerosols from Nimbus7/TOMS data, J. Geophys. Res., 102, 16911-16922, 1997.

Holben, B.N, T. F. Eck, I. Slutsker, D. Tanré, J. P. Buis, A. Setzer, E. Vermote, J. A. Reagan, Y. J. Kaufman, T. Nakajima, F. Lavenu, I. Jankowiak and A. Smirnov, AERONET--A federated instrument network and data archive for aerosol characterization, *Rem. Sens. Environ.*, *66*, 1-16, 1998.

Kaufman, Y.J., D. Tanré, L. A. Remer, E. Vermote, A. Chu and B. N. Holben, Operational remote sensing of tropospheric aerosol over land from EOS moderate resolution imaging spectroradiometer., *J. Geophys. Res.*, *102*, 17051-17067, 1997.

Kaufman, Y.J., D.Tanre, H.R.Gordon, T.Nakajima, J.Lenoble, R.Frouin, H.Grassl, B.M.Herman, M.D.King, and P.M.Teillet, Passive remote sensing of tropospheric aerosol and atmospheric correction for the aerosol effect, *J.Geophys.Res.*, *102*, 16,815-16,830, 1997.

King, M.D and Greenstone, 1999, EOS Reference Handbook, ed., NP-1999-08-134-GSFC, National Aeronautics and Space Administration.

King, M.D., Y. J. Kaufman, D. Tanré and T. Nakajima, Remote sensing of tropospheric aerosols from space: Past, present, and future, *B. Am. Meteor. Soc.*, *80*, 2229-2259, 1999.

L. A. Remer, Y. J. Kaufman, D. Tanré, C. Ichoku, S. Mattoo, R. Levy, D. A. Chu, B. N. Holben, J. Vanderlei Martins, R-R Li, Validation of MODIS Aerosol Retrieval Over Ocean, in preparation, 2000.

Tanré, D., Y. J. Kaufman, M. Herman and S. Mattoo, Remote sensing of aerosol properties over oceans using the MODIS/EOS spectral radiances., *J. Geophys. Res.*, *102*, 16971-16988, 1997.

Torres, O., P.K. Bhartia, J.R. Herman, Z Ahmad and J. Gleason, Derivation of aerosol properties from satellite measurements of backscattered ultraviolet radiation, Theoretical Basis, J. Geophys. Res., 103, 17099-17110, 1998.

Torres, O. P.K. Bhartia, J.R. Heerman, A. Sinyuk, Paul Ginoux and B. Holben, A long-term record of aerosol optical depth from TOMS observations and comparison to AERONET measurements, submitted to J. Atmos. Sci., 2000.

Zhao, T.X.-P., L.L. Stowe, A.B. Smirnov, A.M. Ignatov, D. Cosby, Development of a global validation package for satellite oceanic aerosol retrieval based on AERONET sun-photometer observations and its application to the NOAA/NESDIS operational aerosol retrieval algorithm, submitted, J. Atmos. Sci., 2000.

Derivation of aerosol optical properties from multi-wavelength lidar observations

H. Kinjo*, M. Yabuki, H. Kuze, and N. Takeuchi*
Center for Environmental Remote Sensing, Chiba University
1-33 Yayoi-cho, Inage-ku, 263-8522 Japan
*E-mail: wood@ceres.cr.chiba-u.ac.jp

ABSTRACT

A multi-wavelength Mie lidar is a powerful tool to investigate the optical properties of aerosol particles along with their vertical profile information. In the usual analysis with the Fernald method, however, it is required to assume both the extinction-to-backscattering ratio (lidar ratio, S_1) and the extinction coefficients at the far end boundary. For a multi-wavelength lidar, appropriate choices of these parameters are indispensable to derive consistent profiles from the actual data. In this work, we propose two algorithms for the analysis of four-wavelength lidar data. The first approach is a pragmatic one, and it relies on the sun photometer data simultaneously measured with the lidar data. By assuming a constant S_1 value for each wavelength in the lower troposphere, a consistent set of S_1 is determined by fitting the observed profiles to reference profiles that are relevant to the aerosol optical thicknesses from the sun photometer measurement. The second algorithm is more comprehensive in that it adopts the direct fitting of the lidar A-scopes to the theoretical curves that are based on a look-up table: the table is pre-calculated for various combinations of the extinction coefficient, S_1 parameter, complex refractive index, and aerosol size distribution. As a result, the vertical profiles of these parameters are determined along with the extinction profile.

1. INTRODUCTION

Mie-scattering lidars provide extinction profiles of atmospheric aerosols. For the inversion of the lidar data to give the aerosol extinction, Fernald[1] methods are commonly employed. In this method, it is necessary to postulate a lidar ratio, also known as the S_1 parameter. For particle size distributions and refractive indices of tropospheric aerosols, Mie calculations show that the values of the S_1 parameter can vary in a range of 10 to 100 sr. This wide range implies uncertainty of more than a factor of 10 in the retrieved optical thickness, obviously too large to provide reliable information on aerosol extinction profiles for many practical purposes. Knowledge of the lidar ratio is essential for the interpretation of the lidar data. Since it is by no means possible to determine the lidar ratio only from the elastic backscattering lidar measurements, practical calibration methods have to be contrived. In regard to this, two complementary, alternative approaches are available. First, the optical thickness data from a sun photometer can be used to calibrate the lidar data. Second, the Mie theory can be employed to calculate the aerosol optical properties beforehand.

In the first approach, a sun photometer is used to observe the aerosol optical thickness simultaneously with the lidar observation. Then, the S_1 parameter is specified by matching the optical thickness τ derived from the lidar measurement with that from the sun photometer[2] (hereafter we call this the "τ -matching method").

In the second approach, the aerosol optical properties (extinction coefficient, scattering coefficient, S_1 parameter, and so on) are calculated by the Mie theory[3], assuming a certain aerosol size distribution (ASD) and complex refractive index. So far, a number of attempts have been made to combine lidar measurements and Mie calculations. Sasano and Bowell[4] showed the capability of a multi-wavelength lidar for discriminating between several aerosol types using the wavelength dependence ofaerosol backscatter coefficients. Qing *et al.*[5] simulated numerically the derivation of the ASD from multi-wavelength lidar data, and discussed the errors in the derived size distribution. Rajeev and Parameswaran[6] retrieved the altitude profile of aerosol extinction and the shape of ASD using two iterative methods.

The atmospheric data collection lidar (ADCL)[7,8] at the Center for Environmental Remote Sensing, Chiba University, provides information on tropospheric aerosols at wavelengths of 355, 532, 756 and 1064 nm. The system is designed to monitor the aerosol in the lower troposphere, the contribution from which is essential for the atmospheric correction of satellite remote sensing data. In the present work, we propose two methods for the analysis of multi-wavelength lidar data employing the ADCL case for our simulation and demonstration. Nevertheless, it is emphasized that our approach could in principle be applied to any other multi-wavelength lidar systems.

The first algorithm[9] utilizes the sun photometer data simultaneously measured with the lidar data Since a sun photometer provides multi-wavelength optical thickness data, its use as a calibration tool in the multi-wavelength lidar

measurements might seem straightforward at first glance. Practically speaking, however, this is not always the case. Even when a sufficient range is covered for a wavelength near the center of the visible spectrum (e.g. at 532 nm), the situation becomes worse for longer wavelengths because of the degradation of the detector sensitivity. For shorter wavelength, on the other hand, larger extinction due to the molecular scattering and absorption tend to hinder sufficient range coverage. For these wavelengths it may happen that the range of lidar data is too limited to infer the optical thickness which is to be compared with the sun photometer data. To alleviate such difficulties associated with the wavelength, here we propose a "reference profile" method, which is based on the simultaneous measurement using a multi-wavelength lidar and a sun photometer. In the analysis, we postulate that for each wavelength, the value of the S_1 parameter is constant in the entire troposphere. The parameter at 532 nm is determined by comparing the data from the two instruments (the τ-matching method, as mentioned above). To obtain the reference profile, we assume that at each altitude, the aerosol extinction coefficients for the other wavelengths (355, 756, and 1064 nm) are proportional to the coefficient at 532 nm. The proportional factors are given by the ratio between the optical thickness at each wavelength and that at 532 nm. On the other hand, the lidar signals for the three wavelengths are separately analyzed with the Fernald method by changing S_1 in a plausible range. By minimizing the difference between this retrieved profile and the reference profile, it becomes possible to determine the S_1 parameter.

The second algorithm[10] utilizes a look-up table (LUT) to derive vertical distributions of aerosol optical parameters in the troposphere. The LUT is calculated by the Mie theory for 11 types of aerosol size distributions and 3000 values of the imaginary part of the complex refractive index. The analysis of multi-wavelength lidar signals is accomplished by directly fitting the lidar A-scopes to the theoretical curves that are based on the look-up table. At each altitude, not only the aerosol extinction coefficient but also the S_1 parameter, the imaginary part of the complex refractive index, and the ASD are derived from this procedure. These include most of the important information on the aerosol optical properties. In this respect, this algorithm exhibits quite a unique feature among the analysis methods of multi-wavelength lidar data. The resulting optical parameters, however, are dependent on the parameters that are used to pre-calculate the LUT. This infers that in order to attain reasonable results, it is indispensable to prepare a LUT which is representative of the actual aerosol properties. For this purpose conventional approaches such as the reference profile method are useful for the first-step analysis of multi-wavelength lidar data.

2. THEORY

2.1. Fernald Analysis

Here we briefly summarize the analysis of lidar signals utilizing the Fernald method.[1] This algorithm is mainly required for the implementation of the reference profile method (Sec. 2.2). The single scattering lidar equation is given by

$$P(z) = K\frac{G(z)}{z^2}[\beta_1(z)+\beta_2(z)]\times\exp\left[-2\int_{z_0}^{z}\alpha_1(z')dz' - 2\int_{z_0}^{z}\alpha_2(z')dz'\right], \tag{1}$$

where K is a system constant, $G(z)$ the geometric form factor, z the range from the lidar to the target, and β_j and α_j (j =1,2) are the backscattering and extinction coefficients, respectively: subscripts 1 and 2 refer to the aerosol particles and molecules, respectively. We assume a linear relation between β_j and α_j:

$$\alpha_j = S_j\beta_j, \tag{2}$$

where S_j is the extinction-to-backscattering ratio. The molecular coefficients (β_2 and α_2) can be obtained from standard atmospheric data. We define the range-corrected signal as $X(z) \equiv P(z)z^2$. The aerosol extinction coefficient can be derived as

$$\alpha_1(z) = -\frac{S_1(z)}{S_2}\alpha_2(z) + \frac{S_1(z)X(z)\exp[I(z)]}{\dfrac{X(z_f)}{\dfrac{\alpha_1(z_f)}{S_1(z_f)}+\dfrac{\alpha_2(z_f)}{S_2}} + J(z)}, \tag{3}$$

where the integrals $I(z)$ and $J(z)$ are defined as

$$I(z) = 2\int_{z}^{z_f}\left[\frac{S_1(z')}{S_2}-1\right]\alpha_2(z')dz', \tag{4}$$

and

$$J(z) = 2\int_{z}^{z_f} S_1(z')X(z')\exp\left[I(z')\right]dz' \cdot \tag{5}$$

In these equations, z_f refers to the far-end boundary altitude at which a value is assumed for the aerosol extinction $\alpha_1(z_f)$.

2.2. Reference profile method

The S_1 parameter at 532 nm is determined by adjusting it in the Fernald analysis of the lidar data at 532 nm so that the resultant optical thickness agrees with that from the simultaneously measured sun photometer data. The aerosol extinction profile $\alpha_1^{(\mathrm{Obs})}(\lambda_{532}, z)$ can also be determined in this manner.

The reference profile for each wavelength $\alpha_1^{(\mathrm{Obs})}(\lambda_{532}, z)$ (j = 355, 756, and 1064) is defined as follows:

$$\alpha_1^{(\mathrm{Ref})}(\lambda_j, z) = C_j \alpha_1^{(\mathrm{Obs})}(\lambda_{532}, z), \tag{6}$$

where $C_j = \tau(\lambda_j)/\tau(\lambda_{532})$ with $\tau(\lambda_{532})$ and $\tau(\lambda_j)$ representing the optical thickness at λ_{532} and at λ_j as derived from the sun photometer data. On the other hand, the Fernald analysis of the data at λ_j yields an "observed" profile of $\alpha_1^{(\mathrm{Obs})}(S_1, \lambda_j, z)$. When $\alpha_1^{(\mathrm{Obs})}(S_1, \lambda_j, z)$ is retrieved from the lidar signal, we employ the value of $\alpha_1^{(\mathrm{Ref})}(\lambda_j, z)$ at the far-end boundary. Then the difference between $\alpha_1^{(\mathrm{Obs})}(S_1, \lambda_j, z)$ and $\alpha_1^{(\mathrm{Ref})}(\lambda_j, z)$ is considered using a function

$$D_j(S_1) = \left\{\frac{1}{N}\sum_{l=m}^{n}\left[\alpha_1^{(\mathrm{Obs})}(S_1, \lambda_j, z_l) - \alpha_1^{(\mathrm{Ref})}(\lambda_j, z_l)\right]^2\right\}^{1/2} \times \left[\frac{1}{N}\sum_{l=m}^{n}\alpha_1^{(\mathrm{Ref})}(\lambda_j, z_l)\right]^{-1}, \tag{7}$$

where m and n denote the initial (the lowest altitude) and the final (the highest altitude) data number of the fitting, respectively, with N indicating $n - m + 1$. For each wavelength, the value of S_1 is determined by the condition that one obtains a minimum value of $D_j(S_1)$ in a plausible range of S_1.

2.3. LUT method

2.3.1. Construction of LUT

A look up table (LUT) is constructed by means of the Mie-scattering theory. Table 1 summarizes the parameters used to calculate the present LUT. For the ASD $n(r)$, we take the urban and maritime model[11] as two extreme cases, and nine intermediate cases are defined by logarithmically interpolating between the two. The real part of the aerosol refractive index (m') is fixed at 1.50, representing an average value usually obtained from the ground sampling. The imaginary part (m"), on the other hand, is allowed to vary between 0.0 and 0.03, with a step of 1.0×10^{-5}. This small step size is necessary to deal with the rapid changes in the wavelength dependence of the optical parameters derived from the LUT analysis. For simplicity, we neglect the wavelength dependence of the refractive index.

Using the Mie-scattering theory[3], we calculate the extinction coefficient α_1 and the S_1 parameter for each $n(r)$, m", and wavelengths λ (355, 532, 756, 1064 nm). A table consists of a set of α_1 and S_1 parameters for the four wavelengths calculated with the same size distribution and the refractive index. The values of α_1 are normalized to the value for 532 nm. In the following, we denote the (normalized) extinction coefficient and S_1 parameter of the table data as $e_1(\lambda(i), m(j), s(u))$ and $S_1(\lambda(i), m(j), s(u))$, respectively. Here $\alpha(i)$ indicates the wavelength (i =1 for 355, i =2 for 532 nm, i =3 for 756 nm, and i =4 for 1064 nm), $m(j)$ the refractive index (j =0, 1, ..., 3000), $s(u)$ the size distribution model (u = 0 for the urban, ... u = 10 for the maritime).

Table 1. Parameters used to calculate LUT.

*** Size distribution**

	i	N_0	r_g	σ
Urban aerosol model[11]	1	9.93×10^{4}	0.00651	0.245
	2	1.11×10^{3}	0.00714	0.666
	3	3.64×10^{4}	0.0248	0.337
Maritime aerosol model[11]	1	1.33×10^{2}	0.0039	0.657
	2	6.66×10^{1}	0.0133	0.210
	3	3.06×10^{0}	0.29	0.396

$$\frac{dN}{d\log r} = \sum_{i=1}^{3} \frac{N_{0i}}{\sqrt{2\pi}\sigma_i} \exp\left[-\frac{(\log r / r_{gi})^2}{2\sigma_i^2}\right]$$

Division of each model into 10 logarithmically (u=0 to 10).

s(0) : Urban model , ···, s(u), ···, s(10) : Matitime model

*** Complex refractive index**

Real part: 1.50

Imaginary part: 0.00000 to 0.03000 (step 0.00001)

*** Wavelength**

355, 532, 756 and 1064nm

2.3.2. LUT method

The altitude z is considered in a discrete way of $z(q)$ (q = 1,2,...,Q) with z_1=z (1) being the lowest altitude in the analysis. In order to avoid the effect of the lidar overlapping function, we assume that z_1 is taken at an altitude where $G(z)$ becomes unity. Moreover, we assume that for every wavelength, $\alpha_1(z_1)=\alpha_1(z_2)$ and $S_1(z_1)=S_1(z_2)$: for all the altitudes below z_2, α_1 and S_1 are postulated to be constant. Under these assumptions, the aerosol optical parameters are determined as described below. In the following, the extinction coefficient, S_1 parameter, refractive index, size distribution, and the signal power are written as $\alpha_1^*(z(q), \lambda(i))$, $S_1^*(z(q), \lambda(i))$, $n^*(z(q), \lambda(i))$, $P_{cal}^*(z(q), \lambda(j))$, respectively.

2.3.2.1. Determination of the initial parameters

First we determine the initial values of $\alpha_1^*(z_1, \lambda(i))=\alpha_1^*(z_2, \lambda(i))$ and $S_1^*(z_1, \lambda(i))=S_1^*(z_2, \lambda(i))$. Since the extinction coefficient in the LUT is normalized to the value of 532 nm, we apply a factor $C(t)$ to convert the value to the actual extinction coefficient. Here, $C(t)$ is varied between 5.0×10^{-6} to 1.0×10^{-3} (in units of m^{-1}) with a step of 5.0×10^{-6} (*i.e.* t = 0 ~200). Thus, the aerosol extinction is given by $C(t)\cdot e_1(\lambda(i), m(j), s(u))$. Combining this extinction coefficient with the S_1 parameter, $S_1(\lambda(i), m(j), s(u))$, the signal intensity at the altitudes z_1 and z_2 are calculated as

$$P_{cal.}(z(q),\lambda(i),m(j),s(u),C(t)) = \frac{K}{z(q)^2}\left[\frac{C(t)\cdot e_1(\lambda(i),m(j),s(u))}{S_1(\lambda(i),m(j),s(u))} + \frac{\alpha_2(z(q),\lambda(j))}{S_2}\right] \times \exp\left[-2\int_0^{z(q)} C(t)\cdot e_1(\lambda(i),m(j),s(u))dz' - 2\int_0^{z(q)} \alpha_2(z')dz'\right]_{q=1,2} \quad (8)$$

We define an error, *Err*, as the summation over the four wavelengths of the difference between the calculated ratio of the signal intensity and the observed ratio of the signal intensity.

$$\text{Err.} = \sum_{i=1}^{4}\left[\frac{P_{cal.}(z(2),\lambda(i),m(j),s(u),C(t))}{P_{cal.}(z(1),\lambda(i),m(j),s(u),C(t))} - \frac{P_{obs.}(z(2),\lambda(i))}{P_{obs.}(z(1),\lambda(i))}\right]^2. \quad (9)$$

Note that the system constant K in eq. (1) is eliminated owing to the form of eq. (9). The value of *Err* is calculated for all the possible combinations of j = 0~3000, u = 0~10, and t = 0~200. We determine the parameters at z_1 and z_2 from the

condition that *Err* takes a minimum value (j =J, u =U, and t =T). Therefore, we have

$$\begin{cases} \alpha_1^*(z(1,2), \lambda(i)) = C(T) \cdot e_1(\lambda(i), m(J), s(U)) \\ S_1^*(z(1,2), \lambda(i)) = S_1(\lambda(i), m(J), s(U)) \\ m^*(z(1,2)) = m(J) \\ s^*(z(1,2)) = s(U) \\ P_{\text{cal.}}^*(z(1,2), \lambda(j)) \\ \quad = P_{\text{cal.}}(z(1,2), \lambda(i), m(J), s(U), C(T)) \end{cases} . \tag{10}$$

2.3.2.2. Successive determination of the parameters

Second, we apply the method in a successive way to determine the aerosol parameters at altitudes $z(q)$ ($q \geq 3$). The signal power at $z(q)$ is calculated as

$$P_{\text{cal.}}(z(q), \lambda(i), m(j), s(u), C(t)) = \frac{K}{z(q)^2}\left[\frac{C(t) \cdot e_1(\lambda(i), m(j), s(u))}{S_1(\lambda(i), m(j), s(u))} + \frac{\alpha_2(z(q), \lambda(j))}{S_2}\right] \times \exp\left[-2\left(\int_0^{z(q-1)} \alpha_1^*(z', \lambda(j))dz' + \int_0^{z(q-1)} \alpha_2(z')dz'\right) - 2\left(\int_{z(q-1)}^{z(q)} C(t) \cdot e_1(\lambda(i), m(j), s(u))dz' + \int_{z(q-1)}^{z(q)} \alpha_2(z')dz'\right)\right]_{q \geq 3} . \tag{11}$$

Since the extinction α_1* is already known below the altitude of $z(q$ -1), it is only required to determine the parameters at $z(q)$. In this case, we introduce an error function defined as

$$\text{Err.} = \sum_{q'=1}^{q-1} \sum_{i=1}^{4} \left[\frac{P_{\text{cal.}}(z(q), \lambda(i), m(j), s(u), C(t))}{P_{\text{cal.}}^*(z(q'), \lambda(i))} - \frac{P_{\text{obs.}}(z(q), \lambda(i))}{P_{\text{obs.}}(z(q'), \lambda(i))}\right]^2 . \tag{12}$$

Namely, the squared difference between the ratio of the calculated signal intensities and the ratio of the observed signal intensities is summed over the altitudes below $z(q$ -1) and over the wavelengths. The reason we employ the altitude below $z(q$ -2) is to hold down the noise effects. The minimum of *Err* is sought by changing the indices j, u, and t, as in the case of eq. (8) (the values of indices are determined to be J, U, and T, respectively). In this manner, the aerosol parameters at the altitude $z(q)$ are obtained to be

$$\begin{cases} \alpha_1^*(z(q), \lambda(i)) = C(T) \cdot e_1(\lambda(i), m(J), s(U)) \\ S_1^*(z(q), \lambda(i)) = S_1(\lambda(i), m(J), s(U)) \\ m^*(z(q)) = m(J) \\ s^*(z(q)) = s(U) \\ P_{\text{cal.}}^*(z(q), \lambda(j)) \\ \quad = P_{\text{cal.}}(z(q), \lambda(i), m(J), s(U), C(T)) \end{cases} . \tag{13}$$

By use of the parameters in eqs. (10) and (13) and the size distribution function $ns(r)$ for the model distribution $s^*(z(q))$, the size distribution at an altitude $z(q)$ can be derived as

$$n^*(r, z(q)) = ns(r) \frac{\alpha_1^*(z(q), \lambda(j))}{\int_0^\infty ns(r) \cdot \sigma_{ext}(r, \lambda(j))dr} . \tag{14}$$

Thus, all the aerosol parameters have been determined at $z(q)$. A similar procedure is applied at a next altitude of $z(q$+1). The parameters are obtained in this manner at each altitude up to $z(Q)$.

3. RESULTS AND DISCUSSION

3.1. Reference method

3.1.1. Simulation of the reference profile method

In this section, we describe the result of a simulation in which the influence of atmospheric as well as operational parameters is examined for the reference profile method. As for the vertical distribution of aerosol extinction, we use model profile at 355 and 532 nm. The model extinction coefficient is assumed to be constant in the mixed boundary layer (MBL) up to 1500 m. In the free troposphere, the extinction coefficient is postulated to decrease exponentially with the altitude. For 532 nm, the extinction value in this layer is changed in five ways: $\alpha_1^{(\mathrm{Model})}(\lambda_{532}, \mathrm{MBL}) = 1.0\times10^{-4}$, 2.5×10^{-4}, 5.0×10^{-4}, 7.5×10^{-4}, and 1.0×10^{-3} m^{-1}. (Hereafter these are named as models 1-5.)

By using these model profiles (and the wavelength dependence of α_1 and S_1 parameters, as explained below), lidar signals are simulated and analyzed with the Fernald method to obtain $\alpha_1^{(\mathrm{Obs})}(\lambda_j, z)$. At the same time, the total optical thickness is derived for each wavelength, yielding the proportional constant C_j in eq. (6).

The wavelength dependence of the extinction and the value of S_1 parameter are calculated by means of the Mie scattering theory. In MBL, an aerosol refractive index of $1.5 - 0.05i$ is assumed for all the wavelengths with the size distribution of urban type[11]. In the free troposphere, on the other hand, we assume that the refractive index is $1.5 - 0.01i$ and the size distribution is of background type[11]. The vertical distribution of S_1 is common to all the models. Although we assume a constant S_1 parameter for the entire range of analysis in the reference profile method, we retain its altitude dependence in the calculation of these model profiles. Below, we derive the S_1 parameter in the MBL.

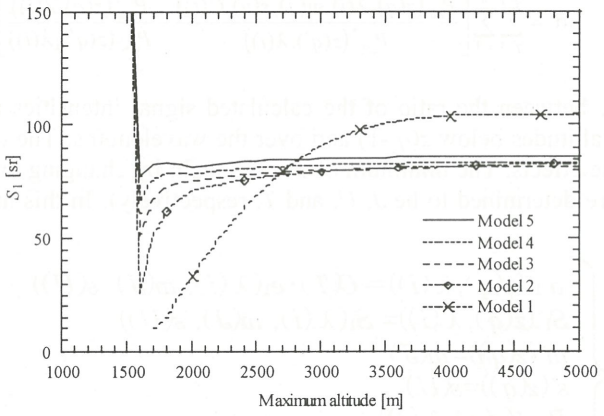

Figure 1. Effect of the fitting interval on the retrieval of the S_1 parameter. With a fixed initial altitude of 500 m, the variation of the resulting S_1 parameter is examined for 355 nm by changing the maximum altitude. For models 2-5, reasonable values are obtained for maximum altitudes above 2000 m.

In the reference profile method, the difference between $\alpha_1^{(\mathrm{Obs})}(S_1, \lambda_j, z)$ and $\alpha_1^{(\mathrm{Ref})}(\lambda_j, z) = C_j \alpha_1^{(\mathrm{Obs})}(\lambda_{532}, z)$ is considered using $D_j(S_1)$ in eq. (7). If the interval between the lowest altitude and the maximum altitude is too small, local inhomogeneity in $\alpha_1^{(\mathrm{Obs})}$ might lead to an error of S_1. On the contrary, if the maximum altitude is too high, the noise included in $\alpha_1^{(\mathrm{Obs})}$ (due to the degraded signal-to-noise ratio) may obscure the minimum of $D_j(S_1)$. Therefore, here we examine how the fitting of S_1 is influenced by the fitting interval. In the vertical measurement with the ADCL, the lowest altitude (determined by the overlap of the laser beam with the telescope field of view) is approximately 400 m with a telescope field-of-view angle of 3 mrad. Thus, fixing the initial altitude at 500 m, we have studied the variation of the resulting S_1 parameter for 355 nm by changing the maximum altitude. The result is summarized in Fig. 1 for the extinction profiles (models 1-5) mentioned above. As seen from this figure, the behavior for the case of model 2-5 is more or less similar, though it is obviously different for model 1, which has the smallest value of the extinction in the MBL. Since in this latter case the contribution above the MBL becomes more significant, the resultant value of S_1 exhibits noticeable

dependence on the maximum altitude. Although the value saturates above approximately 3500 m, this limiting value has no relation with the MBL value in the original assumption. For models 2-5, on the contrary, the derived values are found to be within $\pm 15\%$ of the originally assumed value in the MBL (S_1 = 74.8 sr) as long as the maximum altitude is placed above 2000 m.

3.1.2. Application of the reference profile method to ADCL data

Here the reference profile method is applied to the actual lidar data measured with the ADCL.

To obtain $\alpha_1^{(Obs)}(\lambda_j, z)$ using the Fernald method, we assume constant values of extinction coefficients for the altitude range lower than the full overlap altitude of the ADCL. Figure 2 depicts the results for signals observed on October 9, 1998.

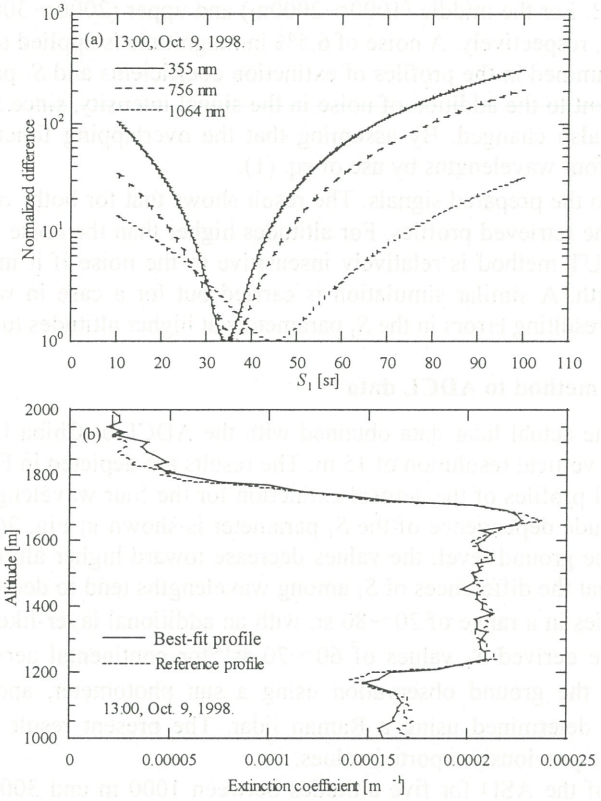

Figure 2. Analysis of an ADCL data observed on October 9, 1998. (a) Behavior of the normalized difference $D_j(S_1)$ as a function of S_1 (λ_j =355, 756, and 1064 nm). From the minimum positions of the curves, best-fit values of S_1 are determined. (b) Comparison between the reference profile $\alpha_1^{(Ref)}(\lambda_{355}, z)$ with the best-fit curve of $\alpha_1^{(Obs)}(\lambda_{355}, z)$ that minimizes $D_{355}(S_1)$.

Figure 2(a) shows the behavior of $D_j(S_1)$ as a function of $S_1(\lambda_j$=355, 756, and 1064 nm). The value of $D_j(S_1)$ is normalized so that its minimum value becomes unity. The initial and final altitudes of the fitting are set to be 1000 m and 2000 m, respectively. In Fig. 2(b) we plot $\alpha_1^{(Ref)}(\lambda_{355}, z)$ along with the best-fit profile of $\alpha_1^{(Obs)}(\lambda_{355}, z)$ that minimizes $D_{355}(S_1)$. For 532 nm, the value of the S_1 parameter is 43 sr, as derived from the τ-matching method. For the other wavelengths, the best-fit values from this analysis are 34 sr (355 nm), 36 sr (756 nm), and 44 sr (1064 nm). In the case of Fig. 2, the optical thickness at λ_{532} between the altitude of 0 m and 2000 m amounts to 84 % of the total optical thickness. Thus, in accordance with the result in Sec. 3.1.1, the error in the estimation of $\alpha_1^{(Ref)}$ is small. To check the S_1 values derived from the reference profile method, we derive S_1 by using the separate application of the τ-matching method to

each wavelength. The S_1 parameters are obtained to be 31 sr (355 nm), 29 sr (756 nm), and 37 sr (1064 nm), in reasonable agreement with the values from the present analysis.

3.2. LUT method

3.2.1. Simulation of the LUT method

Since the LUT method basically relies on the wavelength dependence of the signal intensity, it may happen that a noise superposed onto the signal at a particular wavelength at a particular range affects the entire result higher than that altitude. In order to evaluate such a noise effect, here we conduct a sensitivity-analysis simulation assuming a threefold layer. First we prepare the vertical distributions of the extinction coefficients and the S_1 parameters. For the ground layer from 0 to 1000m, we assume the size distribution of the urban aerosol model (s = 0) with a relatively large value of the imaginary part of the refractive index of m"=0.02. For the middle (1000～2000m) and upper (2000～3000m) layers, we assume s = 5 with m"=0.01, and s = 10 with m"=0.0, respectively. A noise of 6.5% in magnitude is applied to a data point at 1600 m of the 355 nm S_1 profile, and its effect is examined in the profiles of extinction coefficients and S_1 parameters, as retrieved by the LUT method. This situation is equivalent to the addition of noise in the signal intensity, since with the change in the S_1 the value of the aerosol backscattering is also changed. By assuming that the overlapping function $G(z)$ takes a value of 1, we calculate the lidar signals for the four wavelengths by use of eq. (1).

The LUT method is applied to the prepared signals. The result shows that for both α_1 and S_1, the errors at the location of 1600 m are less than 10% in the retrieved profiles. For altitudes higher than the noise location, the errors are found to be less than 1.2%. Therefore, the LUT method is relatively insensitive to the noise if it influences the lidar signal only at a location at a particular wavelength. A similar simulation is carried out for a case in which a 6.5% noise is added at an altitude to two wavelengths. The resulting errors in the S_1 parameters at higher altitudes turn out to be less than 6%.

3.2.2. Application of the LUT method to ADCL data

The LUT method is applied to the actual lidar data obtained with the ADCL at Chiba University. The data were taken on May 21, 1999 (JST 15:55) with a vertical resolution of 15 m. The results are depicted in Fig. 3.

Figure 3(a) shows the vertical profiles of the aerosol extinction for the four wavelengths. It is seen that the mixed layer height is about 2300 m. The altitude dependence of the S_1 parameter is shown in Fig. 3(b). For all the wavelengths, the S_1 values are relatively large near the ground level: the values decrease toward higher altitudes, becoming larger again in the free troposphere. It is also seen that the differences of S_1 among wavelengths tend to decrease as the altitude becomes higher. The S_1 parameter for 532 nm varies in a range of 20～80 sr, with an additional layer-like structure around 1500 m. For this wavelength, previous works have derived S_1 values of 60～70 sr[12]for continental aerosols using a 180° backscattering nephelometer, 20～70 sr[2] from the ground observation using a sun photometer, and 75 ±20 sr[13] from the vertical distribution of the S_1 parameter determined using a Raman lidar. The present result of 20～80 sr is considered to be reasonable as compared with these previously reported values.

Figure. 4 shows the curves of the ASD for five altitudes between 1000 m and 3000 m. Within the mixed layer, it is apparent that the fine (accumulation mode) particles are dominant, and the shape and magnitude of the curves exhibits little changes. In the free troposphere, on the other hand, the relative importance of the coarse mode particles increases, with notable decrease in particle concentrations

In the present method using a LUT, the analysis starts at the near-end boundary. This is in contrast with the case of the Fernald method, in which a far-end boundary value is assumed for the extinction coefficient. Obviously, the present method has the advantage that the signal at the near-end boundary is less likely to be influenced by the detection noise, and as a result, stable convergence of the solution is expected. In Fig. 5, we show the vertical distribution of the aerosol extinction coefficient obtained by applying the Fernald method to the same signals used in Fig. 3. In this case, the inversion is carried out using the S_1 parameters derived from the Mie-scattering calculation with a refractive index of 1.50-0.01i, a value usually assumed for the urban aerosol model.[11] From Fig. 5, it is seen that the variation of the extinction coefficient is smoother than the case of Fig. 3(a), exhibiting nearly constant values below ～1500 m. Whereas in Fig. 3(a) a layer-like feature is recognizable around 1500 m, no such feature is found in Fig. 5 except one around 3000 m. The extinction coefficients exhibit broad peaks around 2000 m in Fig. 5: the location and height of the peaks, however, are variable in accordance with the choice of the far-end boundary values and S_1 parameters.

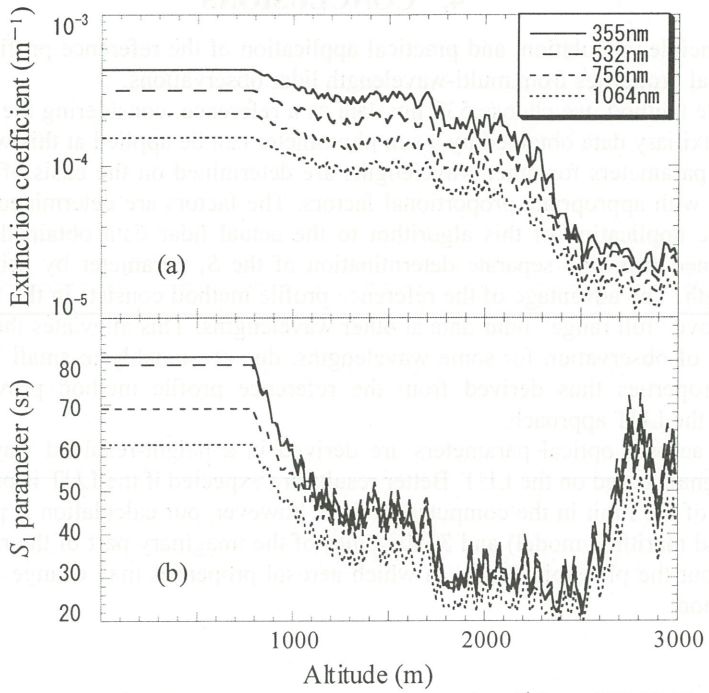

Figure 3. Results obtained with the LUT method for lidar data observed at Chiba at JST 15:55 on May 21, 1999: (a) aerosol extinction coefficient and (b) S_1 parameter.

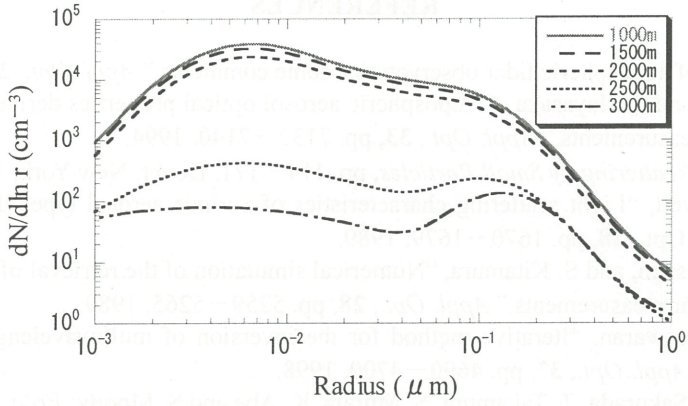

Figure 4. Altitude dependence of the number size distribution obtained for the data same as in Fig. 3.

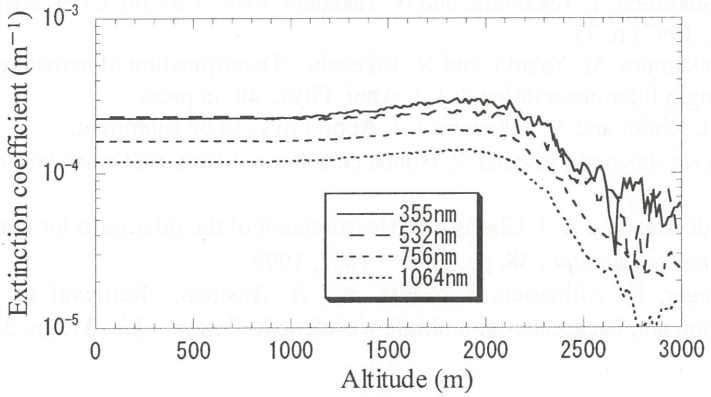

Figure 5. Aerosol extinction profile obtained with the Fernald method for the data same as in Fig. 3. The S_1 parameters are assumed to be 49.8, 47.9, 43.3, and 37.9 sr for 355, 532, 756, and 1064 nm, respectively.

4. CONCLUSIONS

We have described the principle, simulation, and practical application of the reference profile method and LUT method to determine the aerosol optical properties from multi-wavelength lidar observations.

In the reference profile method, we choose 532 nm data as a reference, considering the wavelength dependence of the lidar observation range. Auxiliary data obtained by a sun photometer can be applied at this wavelength to calibrate the lidar data. Subsequently, the S_1 parameters for other wavelengths are determined on the basis of reference profiles obtained by scaling the 532 nm profile with appropriate proportional factors. The factors are determined from the sun photometer data for other wavelengths. The application of this algorithm to the actual lidar data obtained with the ADCL gives results comparable to those obtained from the separate determination of the S_1 parameter by using the sun photometer optical thickness at each wavelength. The advantage of the reference profile method consists in the fact that apart from the 532 nm data, it is not required to have "full range" lidar data at other wavelengths. This alleviates the burden on the lidar hardware, allowing the limited range of observation for some wavelengths, due presumably to small laser power or limited detector efficiency. The aerosol properties thus derived from the reference profile method provide convenient bases for the construction of the table in the LUT approach.

In the LUT method, aerosol optical parameters are derived in a height-resolved way through fitting the observed signals to the calculated signals based on the LUT. Better results are expected if the LUT is prepared for parameter ranges as wide as possible. Because of the limit in the computation time, however, our calculation is performed for 11 types of ASD (varying between urban and maritime model) and 3000 values of the imaginary part of the refractive index (m"=0.0~0.03). Thus, good knowledge about the plausible ranges in which aerosol properties may change is prerequisite for the effective implementation of the method.

REFERENCES

1. F. G. Fernald, "Analysis of atmospheric lidar observations: some comments," *Appl. Opt.*, **23**, pp. 652−653, 1984.
2. T. Takamura, Y. Sasano, and T. Hayasaka, "Tropospheric aerosol optical properties derived from lidar, sun photometer, and optical particle counter measurements," *Appl. Opt.*, **33,** pp. 7132−7140, 1994.
3. H. C. van de Hulst, *Light scattering by Small Particles*, pp. 114−171, Dover, New York, 1957.
4. Y. Sasano and E.V. Browell, "Light scattering characteristics of various aerosol types derived from multiwavelength lidar observations," Appl. Opt., **28**, pp. 1670−1679, 1989.
5. P. Qing, H. Nakane, Y. Sasano, and S. Kitamura, "Numerical simulation of the retrieval of aerosol size distribution from multiwavelength laser radar measurements," *Appl. Opt.*, **28**, pp. 5259−5265, 1989.
6. K. Rajeev and K. Parameswaran, "Iterative method for the inversion of multiwavelength lidar signals to determine aerosol size distribution," *Appl. Opt.*, **37**, pp. 4690−4700, 1998.
7. N. Takeuchi, H. Kuze, Y. Sakurada, T. Takamura, S. Murata, K. Abe and S. Moody: *Proc. 18th Int. Conf. Laser Radar, Berlin, 1996* (Springer-Verlag, Berlin, 1997) p. 71.
8. H. Kuze, M. Qiang, Y. Sakurada, T. Takamura, and N. Takeuchi: *Proc. 18th Int. Conf. Laser Radar, Berlin, 1996* (Springer-Verlag, Berlin, 1997) p. 75.
9. H. Kinjo, H. Kuze, T. Takamura, M. Yabuki, and N. Takeuchi: "Determination of aerosol extinction-to-backscattering Ratio from Multiwavelength lidar observation,": J. J. Appl. Phys., **40**, in press.
10. M. Yabuki, H. Kuze, H. Kinjo, and N. Takeuchi: J. J. Appl. Phys., to be submitted.
11. R. Jaeniche, *Tropospheric Aerosols*, in Peter V. Hobbs ed., *Aerosol-Cloud-Climate Interactions*, pp. 1−31, Academic, 1983.
12. S. J. Doherty, T. L. Anderson, and R. J. Charison, "Measurement of the lidar ratio for atmospheric aerosols with 180° backscatter nephelometer," *Appl. Opt.*, **38**, pp. 1823−1832, 1999.
13. D. Muller, U. Wandinger, D. Aithausen, I. Mattis, and A. Ansman, "Retrieval of physical particles from lidar observations of extinction and backscatter at multiple wavelengths," *Appl. Opt.*, **37**, pp. 2260−2262, 1998.

Airborne observations of Arctic tropospheric aerosols (ASTAR 2000) for validation of satellite and ground-based remote sensing

Takashi Yamanouchi and Masataka Shiobara

National Institute of Polar Research, 9-10 Kaga 1-chome, Itabashi-ku, Tokyo 173-8515, JAPAN, yamanou@pmg.nipr.ac.jp

and

Andreas Herber

Alfred-Wegener Institute for Polar and Marine Research, Am Handelshafen 12, 27570 Bremerhaven, GERMANY, aherber@awi-bremerhaven.de

1. Introduction

The polar regions are receiving increased attention in climate change scenarios obtained from climate models. Recently, large variations in many climate parameters have been found in the "Changing Arctic" (Morison et al., 1998). Warming of the air temperature near the surface is clearly observed, especially over the continent (Chapman and Walsh, 1993; Walsh and Chapman, 1998; Serreze, 2000), and thinning of sea ice in the 1990s is reported for a wide area of the Arctic Ocean (Rothrock et al., 1999).

Aerosols, together with clouds, are believed to have a strong impact on climate through the radiative effect with a large spatial variability; however, their 3-D distribution and interactions are still uncertain, especially in the polar regions. In the Arctic, concentrations of normal background aerosols are very low and optical thickness in the 500 nm is in the range 0.03 to 0.05 (Herber, 1996). However, strong seasonal variations in aerosol optical depth are known and the large spring increase is due to high concentrated layered aerosols called "Arctic Haze" (Shaw, 1995; Herber, 1996; Heintzenberg, 1989). This large spring maximum of aerosol loading is originated from anthropogenic sources surrounding the Arctic, and trapped a long time in the strong inversion layer over the Arctic Ocean without any effective removal process (Shaw, 1995). Though this is only a seasonal phenomenon, its radiative effect is not negligible, because solar radiation becomes effective just in this season after the long polar night and a large influence might be expected related to the melting and decay of sea ice. Many observational studies have been devoted to the Arctic Haze (Bodhaine and Dutton, 1993; Jaeschke et al., 1999); however, not so much has been done concerning the radiative effect yet.

A new cooperative project on aerosols in the Arctic, ASTAR 2000 (Arctic Study of Tropospheric Aerosol and Radiation) was conducted for March and April 2000 in and around Svalbard to investigate the 3-D behavior and radiative effects of tropospheric aerosols in the Arctic and their impact on climate. Airborne observations using a Dornier 228 aircraft and coordinated remote sensing, in-situ measurements and sampling of aerosols were done at the international research site, Ny-Ålesund, Svalbard (Fig. 1). At this site, scientists from several countries including German and Japanese scientists have already conducted ground based atmospheric science observations for about 10 years (Gernandt et al., 2000; Yamanouchi et al. 1996). Satellite measurements of SAGE-II (Stratospheric Aerosol and Gas Experiment) were also included as part of the ASTAR 2000 campaign. Finally, data will be used as input for regional climate model studies (HIRHAM) to estimate radiative forcing and discuss the climatic impact of aerosols in the Arctic atmosphere.

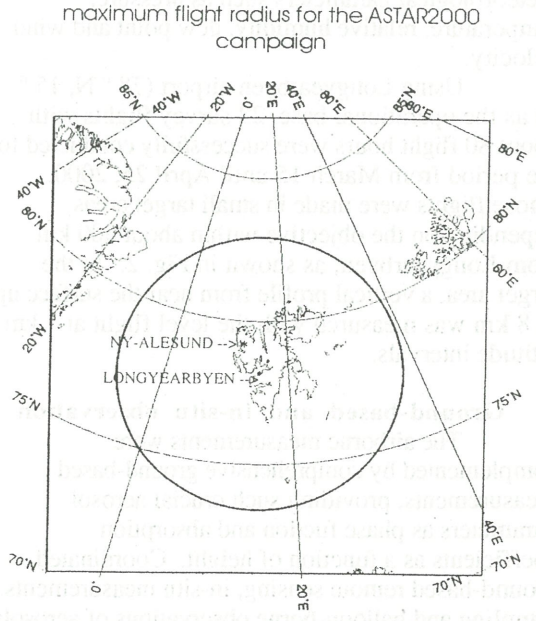

Fig. 1 Map showing the ground-based observation site, Ny-Ålesund, and base of airborne observation, Longyearbyen. Also shown is a circle with maximum flight radius.

2. Airborne observations

Airborne observations using Dornier 228 aircraft of Alfred-Wegener Institute for Polar and Marine Research (AWI) were the crucial experimental part of the project. A sunphotometer was used for the measurement of solar radiance to derive optical depth and extinction coefficients, and also for the measurement of sky brightness in the almucanter plane to derive the scattering phase function. The sunphotometer was installed in the plane on a solar tracker behind a quartz window, which was prepared specially for optical measurements. The sunphotometer was to be adjusted to the direction of the sun, 80 degrees apart from the plane heading and the solar height should be between 15 ° to 7 ° for the extinction measurement. By rotating the heading of the air plane 180 degrees, horizontal scan for brightness measurement in the same zenith angle was made. Downward and upward shortwave and longwave radiation fluxes was measured by broad band radiometers settled on the roof and bottom of the plane. In-situ measurements of aerosols were made; particle size distribution, absorption and scattering coefficients will be measured by optical particle counters (OPCs), a particle soot absorption photometer (PSAP) and an integrating nephelometer (IN), respectively. Aerosols were also sampled with a low volume filter sampler and aerosol impactor to conduct chemical analyses and electron microscope analyses.Air was introduced to the diffuser from the intake settled at the roof of the plane, and then guided to each instrument. Data from all the instruments were to be recorded in a central data recorder together with flight information and basic meteorological parameters such as pressure, temperature, relative humidity, dew point and wind velocity.

Using Longyearbyen airport (78 ° N, 15 ° S) as the operational base, 22 survey flights with about 80 flight hours were successfully conducted for the period from March 15 until April 25, 2000. Those flights were made in small target areas depending on the objective within about 500 km from Longyearbyen, as shown in Fig. 2. In the target area, a vertical profile from near the surface up to 8 km was measured with the level flight at 1 km altitude intervals.

3. Ground-based and in-situ observation

The airborne measurements were complemented by comprehensive ground-based measurements, providing such crucial aerosol parameters as phase fuction and absorption coefficients as a function of height. Coordinated ground-based remote sensing, in-situ measurements, sampling and balloon-borne observations of aerosols were performed at the surface, at the international research site, Ny-Ålesund (78.95 °N, 11.93 °E; Fig. 1).

In 1991, regular measurements of aerosols commenced at Ny-Ålesund. Since then observations have been improved and extended by newly developed instruments, such as sun and star photometers, to retrieve the aerosol optical depth and phase function in the visible and near infrared spectral range, the tropospheric Raman-lidar to measure extinction coefficients and depolarization as a function of altitude, and the Fourier transformed infrared spectrometer (FTIR) to calculate the aerosol optical depth in the IR spectral range by measuring emission spectra. Additional new systems are a micropulse lidar for backscatter measurement and sky radiometers for extinction and phase function measurements.

In-situ measurements were made by optical particle counters (OPCs), integrating nephelometer and particle mobility analyzer. Ground sampling of aerosols were done by high volume and low volume samplers and an aerosol impactor. Balloon-borne aerosol sonde with OPC was launched and a tethered balloon with OPC was used to obtain the vertical distribution of aerosol particle concentration in the atmosphere close to the surface. Supporting data included surface ozone measured by Dasibi ozone meter, precipitable water amount and liquid water content by microwave radiometer, precipitation by POSS, surface radiaitive fluxes by BSRN (Baseline Surface Radiation Network) radiometers and aerological soundings. At the Zepelin mountain station (470 m a. s. l.), in-situ measurements and samplings of aerosols were also made.

4. Results

Within ninteen profiles obtained by airborne observations, five was in a haze condition ($\tau > 0.1$) and another five was in a background condition ($\tau < 0.06$). Some profiles even without haze condition contained some layers with high concentration of aerosols. Fig. 2 is one of the extinction profile obtained in the haze condition with the largest total optical depth, $\tau = 0.18$, among the campaign. A high concentration layer between 3 km and 1 km was noticeable. In other 4 cases in a haze condition, the lower most layer was the extensive higest concentration layer.

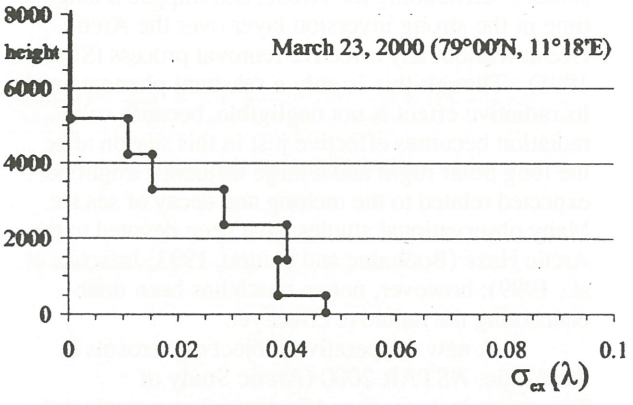

Fig. 2 Aerosol extinction (532 nm) profile obtained from airborne sunphotometer, March 23, 2000.

From the in-situ measurements on board airplane, scattering coefficients were measured by an integrating nepheloeter (IN), and absorption coefficients were measured by a particle soot absorption photometer (PSAP). Adding both coefficients, extinction coefficients were also estimated and the vertical profile was derived. Comparing both figures, similar extinction profiles are found qualitatively. However, quantitatively, extinction coefficients obtained from in-situ measurements are roughly half of those obtained from sunphotomter measurements. This discrepancy might partly be attributable to the correction factor of the in-situe instruments - air intake, diffuser, intake pipes and instruments theirselves, IN and PSAP. Anyway, we could obtain extinction profile using great differnt type of instruments within factor of two. From the electron microscope analysis of impacted samples, chemical constituents of aerosols were derived and found that aerosols in most of layers were made of sulpahate particles, but some upper layer were soot abundant for the profile of March 23.

From the ground-based in-situe measurements at Ny-Ålesund continuous record of aerosol parameters were obtained. The variation of scattering coefficients at three wavelength region during the campaign was examined. Roughly seen, there are three terms with high scattering coefficients, scattering coeficient (at 550 nm) > 0.01 km^{-1}. It was found that these high aerosol concentration at the surface occurred during northerly wind components, which corresponded to the typical meteorological condition with northery air flow from the Arctic airmass, looking at 500 hPa geopotential hight patterns of meteorological analysis, such as NCEP/NCAR.

Aerosol opticasl properties were retreived from the sky-radiometer measurements. Not only an optical depth, but also size distribution, complex refractive index and scattering phase function were obtained. Rather larger Ångstrom parameters were derived for the haze condition, which meant the higher abundunce of smaller particles. These results could also be estimated from physical parameters by in-situ measurents and compared.

Vertical distribution of aerosol extinction was estimated from ground-based lidar measurements. Using an lidar ratio estimated by fitting the total optical depth to the sunphotometer optical depth, an extinction profile was derived from backscatter coefficients measured by AWI lidar (Schumacher and Neuber, 2000). A good correspondence was seen with the airborne sunphotomter profile on March 23 (Fig. 3). Time height cross section of extinction coefficient were also estimated from micro-puls lidar, and growth and decay of thick aerosol layers were seen. However, some distortion of extinction profile was seen in noon time due to the contamination of solar radiation into the signal because of the inclined setting of the lidar. Some kind of correction needed to be made for these data.

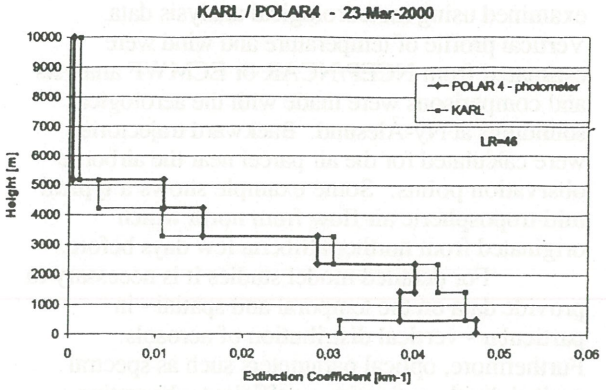

Fig. 3 Comparison of aerosol extinction profile measured by airborne sunphotometer (thick line) and by ground-based backscatter lidar (thin line) at Ny-Ålesund, Svalbard, March 23, 2000 (Schumacher and Neuber, 2000).

5. Satellite observations, meteorological analysis and model studies

SAGE-II (Stratospheric Aerosol and Gas Experiment) satellite observations of stratospheric aerosols are used to separate the tropospheric contribution from total atmospheric aerosol burden and provide information on spatial distributions in the Arctic region (McCormick, 1987). Also, satellite extinction measurement could be validated from airborne measurement data. A combination of all of these methods is recently used to obtain as much information as possible on temporal and vertical distributions of atmospheric aerosols and their optical properties. In the first comparison of extinction coefficients made for April 19, profiles between airborne measurments and satellite measurements provided an excelent correspondence (Fig. 4; Thomason and Burton, 2000).

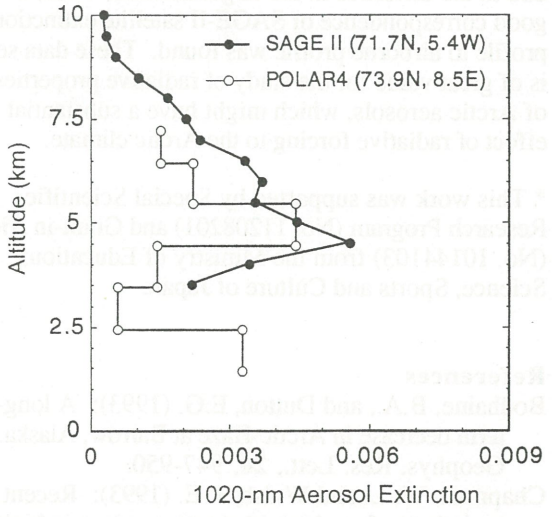

Fig. 4 Comparison of aerosol extinction profile (1020 nm) measured by airborne sunphotometer (white circle) and by SAGE-II measurement (black circle), near Svalbard, April 19, 2000 Thomason and Burton, 2000)

Atmospheric circulation patterns were examined using meteorological analysis data. Vertical profile of temperature and wind were estimated from NCEP/NCAR or ECMWF analysis and comparisons were made with the aerological soundings at Ny-Ålesund. Backward trajectories were calculated for the air parcel near the airborne obsrvation points. Some example shows a typical mid tropospheric air flow from north which originated from northern Siberia few days before.

For detailed model studies it is necessary to provide data on the temporal and spatial - in particular - vertical distribution of aerosols. Furthermore, optical parameters such as spectral optical depth, extinction coefficient, absorption coefficient, and phase function have to be measured. For all of these parameters a large number of different methods and instruments are used, including satellite information, like SAGE-II. There is not yet a clear understanding of the impact of tropospheric aerosols on radiative forcing processes in the Arctic. All these aerosol data will then be incorporated in to the HIRHAM Arctic regional climate model (Dethloff et al., 1996) for detailed model studies on the direct radiative forcing of Arctic tropospheric aerosols.

6. Concluding remarks

A five-week field capaign have provided a data set for the validation of satellite and ground-based remote sensing. Among 19 vertical profiles obtained by airborne measeurements, five profiles showed a haze condition ($\tau > 0.1$; 500 nm) with a layer of exetinction coefficient about 0.05 km^{-1} and another five showed a background condition ($\tau <$ 0.06). A good correlation was seen between the airborne measured extinction profile and ground-based lidar profile in several occasions; however, sometimes, it was dificult to compare both profiles due to the differnce in the target airmass. Also, a good correspondence of SAGE-II satellite extinction profile to airborne profile was found. These data set is of great value for the study of radiative properties of Arctic aerosols, which might have a substantial effect of radiative forcing to the Arctic climate.

* This work was supported by Special Scientific Research Program (No. 11208201) and Grant-in Aid (No. 10144103) from the Ministry of Education, Science, Sports and Culture of Japan.

References

Bodhaine, B.A., and Dutton, E.G. (1993): A long-term decrease in Arctic-Haze at Barrow, Alaska. Geophys. Res. Lett., **20**, 947-950.

Chapman, W. L. and Walsh, J. E. (1993): Recent variations of sea ice and air temperature in high latitudes. Bull. Amer. Meteorol. Soc., **74**, 33-47.

Dethloff, K., Rinke, A., Lehmann, R., Christensen, J.H., Botzet, M. and Machenhauer, B. (1996): Regional climate model of the Arctic atmoshere. J. Geophys. Res., **101**, 23401-23422, 1996.

Gernandt, H., Neuber, R. and von der Gathen, P. (2000): Recent contributions to long-term atmospheric studies at Koldewey Station. Mem. Natl Inst. Polar Res., Spec. Issue, **54**, "Environmental Research in the Arctic 2000", in press.

Herber, A., Thomason, L. W., Dethloff, K., Viterbo, P., Radionov, V. F. and Leiterer, U. (1996): Volcanic perturbation of the atmosphere in both polar regions: 1991-1994. J. Geophys. Res., **101**, 3921-3928.

Heintzenberg, J. (1989): Arctic Haze: Air pollution in the polar region. AMBIO, **18**, 50-55.

Jaeschke, W., Salkowski, T., Dierssen, J. P., Trumbach, J. V., Krischke, U. and Gunther, A. (1999): Measurements of trace substances in the Arctic troposphere as potential precursors and constituents of Arctic haze. J. Atmos. Chem., **34**, 291-319.

McCormick, M.P (1987): SAGE II: An overview. Adv. Space Rev., **7**, 319-326.

Morison, J., Aagaard, K. and Steele, M. (1998): Report on Study of the Arctic Change Workshop held November 10-12, 1997, University of Washington, Seattle, Washington. Report No. 8, Polar Science Center, Applied Physics Laboratory, University of Washington, 34p.

Rothrock, D. A., Yu, Y., and Maykut, G. A. (1999): Thinning of the Arctic sea-ice cover. Geophys. Res. Lett., **26**, 3469-3472.

Serreze, M. C., Walsh, J. E., Chapin III, F. S., Osterkamp, T., Dyurgerov, M., Romanovsky, V., Oechel, W. C., Morison, J., Zhang, T. and Barry, R. G. (2000): Observational evidence of recent change in the northern high-latitude environment. Climate Change, **46**, 159-207.

Shaw, G. E. (1988): Antarctic aerosols: A review. Rev. Geophys., **26**, 89-112.

Shaw, G. E. (1995): The Arctic haze phenomenon. Bull. Am. Meteor. Soc., **76**, 2403-2413.

Schumacher, R. and Neuber, R. (2000): Extinction profiles measured with the Koldwey aerosol Raman lidar (KARL) during ASTAR 2000. Paper presented at 4th ASTAR Workshop, 3-5 October 2000, Kawaguchiko, Japan.

Thomason, L. W. and Burton, S. P. (2000): SAGE-II observations of tropospheric aerosol. Paper presented at 4th ASTAR Workshop, 3-5 October 2000, Kawaguchiko, Japan.

Walsh, J. E. and Chapman, W. L. (1998): Arctic cloud-radiation-temperature associations in observational data and atmospheric reanalyses. J. Climate, **11**, 3030-3045.

Yamanouchi, T., Aoki, S., Morimoto, S. and Wada, M. (1996): Report of atmospheric science observations at Ny-Ålesund, Svalbard. Proc. Int. Symp. Environmental Research in the Arctic, 19-21 July 1995, NIPR, Tokyo. Mem. Natl Inst. Polar Res., Spec. Issue, **51**, 153-163.

Behavior of the tropospheric aerosols in the Arctic region measured by Micro Pulse Lidar and Sky-radiaometer at Ny-Alesund, Svalbard, during the ASTAR2000 campaign

M. Yabuki*[1], M. Shiobara[2], T. Yamanouchi[2],
T. Shibata[3], H.Kuze[1], and N. Takeuchi[1]

1) Center for Environmental Remote Sensing, Chiba University.
2) National Institute of Polar Research
3) Solar-Terrestrial Environment Laboratory, Nagoya University.
*E-mail: yabuki@ceres.cr.chiba-u.ac.jp

ABSTRACT

Arctic Study of Tropospheric Aerosol and Radiation (ASTAR2000) were conducted in March and April 2000. The principal objectives of ASTAR2000 were to observe and clarify the behavior of tropospheric aerosols, especially of the "Arctic haze", and their radiative effects. During the ASTAR2000, we carried out aerosol profile measurements with a Micro Pulse Lidar (MPL) and sky radiance measurements with a Sky-radiometer at Ny-Alesund (79 N,12 E), Svalbard.

The MPL is a useful tool to observe the temporal and spatial aerosol behavior, while the Sky-radiometer measures the sky radiance and can provide information on aerosol properties such as size distribution, scattering phase function, optical depth, Angstrom parameter, and refractive index. These instruments worked well during the campaign and we could observe representative features of the Arctic haze events. In the case of Arctic haze on the ground level, the height of the mixing layers was limited in the lower altitude with relatively small value of the Angstrom parameter. In contrast, when the haze layer was found in the higher atmosphere, the mixing layer height could not be distinguished clearly, and the Angstrom parameter exhibited larger values. This result is interpreted in relation to the aerosol transport.

1. INTRODUCTION

In this paper we report on observations conducted as part of the campaign of the Arctic Study of Tropospheric Aerosol and Radiation, in spring 2000 (ASTAR2000). The study was undertaken to examine the behavior of tropospheric aerosols, especially of the "Arctic haze", and the aerosol radiative effects. Here the term "Arctic haze" is used to indicated aerosol particles found during winter and spring, resulting from aerosol transportation in the planetary boundary layer from industrial areas in mid-latitudes into the Arctic area[1].

The haze aerosols are mainly sulfate and black carbon[2,3]. Since the haze contains light absorbing material such as black carbon, it appears dark when viewed from above over the highly reflecting ice cap and introduces some heating into the earth-atmosphere system[4]. For the transport routes for the haze, Eurasian emissions are much more important than those from North America, in part because the Eurasian sources are 5° to 10° further north than those in North America.

2. OBSERVATIONS

During the ASTAR2000 campaign, simultaneous measurements were carried out with a MPL (SESI MPL) and a sky-radiometer (Prede POM-01) at the Rabben Observatory, about 10 m above sea level, at Ny-Alesund, Svalbard (79 N, 12 E).

The MPL system, equipped with a 523nm Nd:YLF laser. Operated at 2.5 kHz, provides a vertical resolution of 30 m in the aerosol backscattering measurements. By means of the lidar equation[5], this measurement leads to the vertical profile of the aerosol extinction coefficient, and hence detection of the layer-like structures in the atmosphere. The sky-radiometer measures the direct solar radiance in eight spectral channels in a spectral range of 368 to 1020 nm, with ancillary sky radiance data in five spectral channels of 400, 500, 675, 870, and 1020 nm. We applied the sky-radiance inversion method[6,7] in order to retrieve the aerosol optical thickness, size distribution and single scattering albedo. As for the ground albedo needed in the inversion, we assumed a value of 0.5, an average usually encountered for the new and old snow.

In this paper, we focus on the difference between the days of Arctic haze events (HZ) and those of background cases (BG). The discrimination of these two cases is made on the basis of the optical thickness at 500nm, $\tau(500)$, with additional information about the ground visibility. The HZ cases were found for March 23, morning of March 25, April 13, and April 19, whereas the BG for March 22, afternoon of March 25, and April 17. For each case, a time bin of 10 minutes is defined to average the variations of the aerosol optical parameters after the cloud-covered data is excluded.

The observations on optically thick HZ days are categorized into two situations, namely with and without the presence of significant upper layers, In order to clarify the role of such layers for the generation of the Arctic haze events, here we examine whether the existence of upper layers affects the aerosol optical properties.

3. RESULTS

In Fig. 1 we compare the HZ and BG days by studying the occurrence frequency of (a) the aerosol optical thickness at 500nm $\tau(500)$, (b) Angstrom parameter, and (c) single scattering albedo. Figure 1(a) shows that for the most part, the two situations are well separated by $\tau(500)$, though the ground-level haze persisted in spite of the relatively smaller value of $\tau(500) < 0.1$. From Fig. 1 (b), it can be seen that the Angstrom parameter is somewhat larger for the HZ cases than for the BG cases. This suggests the increase in the number of smaller particles for the former. On the other hand, no clear distinction is found for the single scattering albedo, as seen from Fig. 1 (c).

Figure 2 shows, in terms of the observed distributions of the Angstrom parameter, a comparison between the situations with and without the layer-like structure under the haze conditions detected by the MPL measurements. These two cases do exhibit differences: when there exists the layer, the averaged value of the Angstrom parameter value is 1.86, whereas it is 1.52 for no layer situations. Note that this latter value is the same as the BG case depicted in Fig. 1(b). This result indicates that the aerosol particles with smaller size (hence, larger Angstrom parameter) are predominant not in the ground layer, but in the upper layer observed in an altitude range of 2−5 km. Previous works of the Arctic haze revealed that the polluted air mass, which is composed mainly of sulfate and black carbon[1], was transported from industrial regions. It is considered that this transportation takes place far above the mixed boundary layer. Such a picture is consistent with the present observation of the upper layers with enriched concentrations of smaller particles.

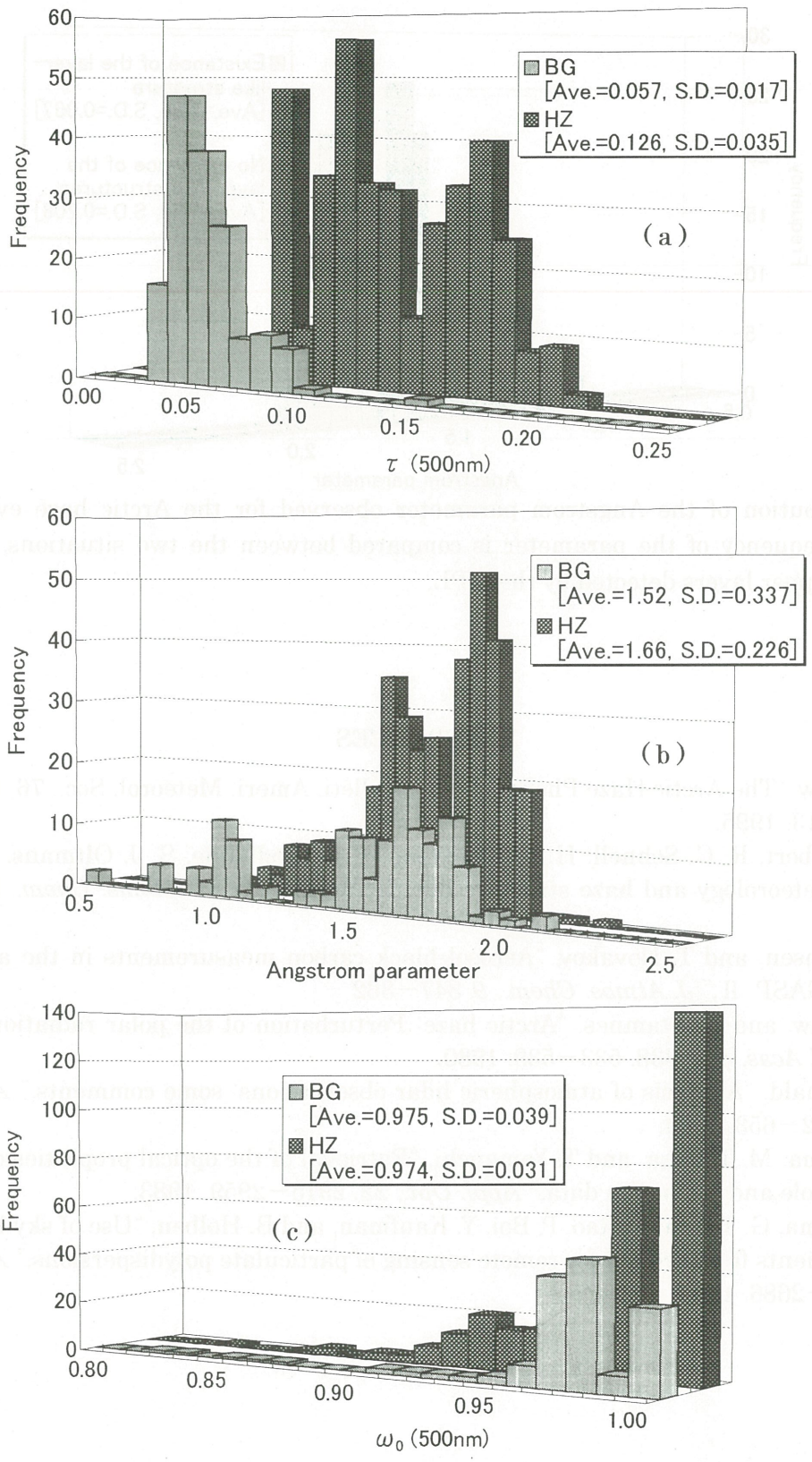

Fig. 1 Observed distributions of (a) the aerosol optical thickness at 500nm, (b) Angstrom parameter, and (c) single scattering albedo for the Arctic haze (HZ) events and the background (BG) cases.

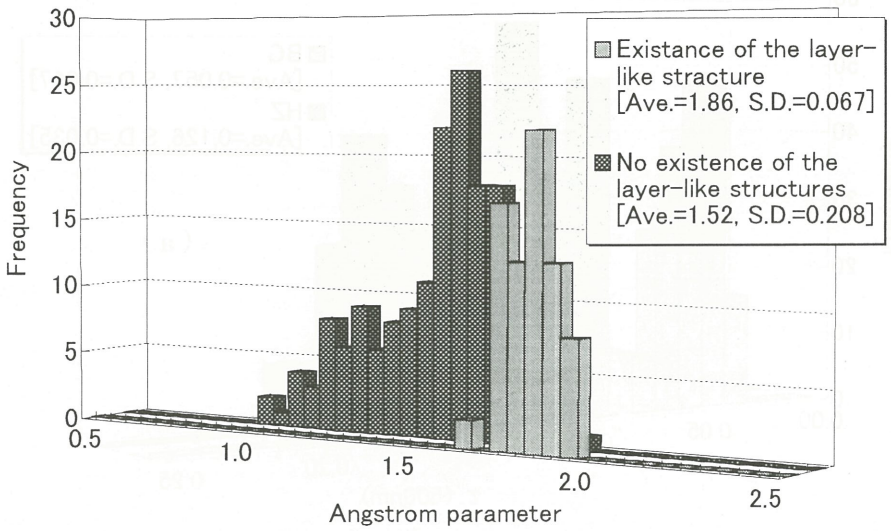

Fig.2 Distribution of the Angstrom parameter observed for the Arctic haze events. The occurrence frequency of the parameter is compared between the two situations, with and without the upper layers detected by the MPL.

REFERENCES

1. G. E. Shaw, "The Arctic Haze Phenomenon," Bulleti. Ameri. Meteorol. Soc., **76**, no. 12, pp. 2403−2413, 1995.
2. G. A. Herbert, R. C. Schnell, H. A. Bridgman, B. A. Bodhaine, S. J. Oltmans, and G. E. Shaw, "Meteorology and haze structure during AGASP Ⅱ," *J. Atoms. Chem.*, 9, 17−48, 1989.
3. A. D. Hansen, and T. Novakov, "Aerosol black carbon measurements in the arctic haze during AGASP Ⅱ," *J. Atmos. Chem.*, *9*, 347−362
4. G. E. Shaw, and K. Stamnes, "Arctic haze: Perturbation of the polar radiation budget," *Ann. N. Y. Acas. Sci.*, 338, 533−539, 1980.
5. F. G. Fernald, "Analysis of atmospheric lidar observations: some comments," *Appl. Opt.*, 23, pp. 652−653, 1984.
6. T Nakajima, M. Tanaka, and T. Yamauchi, "Retrieval of the optical properties of aerosols from aureole and extinction data," *Appl. Opt.*, 22, 2915−2959, 1983.
7. T. Nakajima, G. Tonna, R. Rao, P. Boi, Y. Kaufman, and B. Holben, "Use of sky brightness measurements from ground for remote sensing of particulate polydispersions," *Appl. Opt.*, 35, 2672−2686, 1996.

Retrieval of the optical thickness of inhomogeneous clouds from multispectral satellite measurements

Nobuyuki KIKUCHI, Hironobu IWABUCHI and Tadahiro HAYASAKA

Center for Atmospheric and Oceanic Studies, Graduate School of Science, Tohoku University, Aramaki Aza Aoba, Aoba-ku, Sendai, Japan

ABSTRACT

A method is presented for determining the optical thickness of horizontally inhomogeneous clouds from reflected solar radiation measurements. A new parameter of effective gradient is defined as an oblique angle of the plane parallel. Under the assumption that the effective particle radius of clouds is constant in the cloud layer, the optical thickness and effective gradient of clouds in the independent pixels of satellite scene can be determined from reflection function measurements at weak absorbing wavelength (0.86μm) and absorbing wavelength (2.16μm). Applying this method to Landsat TM measurements, we recognize that the effective gradient at 0.86μm is smaller than at 2.16μm and the effective gradient ratio is estimated to be 0.65 for nadir view with oblique sun ($\theta_0 = 60^\circ$). By applying the effective gradient ratio to the oblique plane parallel model, the analysis provides a good estimate of the optical thickness and effective gradient of cloud.

In addition to Landsat TM measurements, an analysis of the forward and backward scattered radiation field of a fractal cloud model is carried out using a Monte Carlo simulations. It is shown that a good agreement between estimates and originals of the optical thickness of cloud can be obtained and the effective gradient ratio is smaller in the backward view and larger in the forward view than in the nadir view.

1. Introduction

When the radiative properties of the clouds are measured by using the remote sensing, it cannot be disregard that the horizontally inhomogeneous of the cloud exerts the influence on the radiation characteristic of the cloud. The research of a qualitative character and a quantitative evaluation of the inhomogeneous cloud had developed in ten years recently (titov 1988, Galinsky and Ramanathan 1988 and Oreopoulos el al. 2000). However, because the parameter, which quantitatively evaluated inhomogeneous of the cloud by the remote sensing, did not exist, a plane parallel model of homogeneous cloud keeps being used at applied stage as for the cloud. In this study, the oblique plane parallel cloud model is adopted, and a new parameter effective gradient, which shows cloud inhomogeneity, is proposed. And, it was attempted to remove an influence of the cloud inhomogeneous and to presume optical thickness of the cloud by using two wavelengths, which are the wavelength without absorption by the cloud and with absorption. Two features of effective gradient are as follows. the first, effective gradient ties directly the inhomogeneity of the cloud to the optical effect , and the second effective gradient can be measured by the satellite

remote sensing.

Chapter 2 describes the oblique plane parallel cloud model, and effective gradient is defined. The plane parallel cloud model is applied to the measurements of the TM sensor of Landsat satellite, optical thickness and effective gradient are presumed in Chapter 3. In chapter 4, the radiation calculation, which uses the Monte Carlo method, is done. The presumption of optical thickness and effective gradient when the satellite sees the cloud from various angles is attempted. Chapter 5 describes the summary and consideration.

2. Oblique plane parallel cloud model

We decided the plane parallel cloud model to be used as a method of showing the radiation characteristics of an inhomogeneous cloud. However, when the calculation values were compared with the Landsat TM sensor measurement value, it was understood that bigger measurement than the calculation value was earned. In a word, combining plane parallel cloud models cannot show the actual radiation scene of inhomogeneous clouds.

Next, it was tried to incline the plane parallel cloud model in the direction of the sun. Figure 1 shows the result of doing the radiation calculation whose clouds models have solar zenith angle 60 degree, the satellite nadir viewing angle 0 degree, cloud optical thickness 16. When the plane parallel cloud inclines at 10 degree to the direction of sun, 50% of the amount of the radiation has increased. The strong reflected radiance, which cannot be shown by the calculation value of the plane parallel cloud model is expected to be able to be shown by inclining the plane parallel cloud model. The increase and decrease of the incidence sunlight is caused by the surface's of the cloud inclining. The first problem when the oblique plane parallel cloud model is applied to the actual cloud is that the inclining part does not continue infinitely in the actual cloud. Then, the both neighborhoods of the inclining cloud is assumed to be adjacent the level cloud, and the horizontal radiation budget in the inclining part is examined. When the inclination of the cloud is positive, the incidence sunlight increases and the horizontal transportation of the radiation increases more than an adjoining level cloud. Therefore, the horizontal divergence of the radiation is caused and the reflection light decreases. Similarly, when the inclination of the cloud is negative, the horizontal convergence of the radiation is caused and the reflection light increases. The reflection light increases because settling the radiation occurs horizontally in respect, which inclined similarly and negatively. It is possible to show the character of the divergence and convergence of the radiation of horizontal direction by reducing the inclination of the plane parallel cloud model more than an actual inclination.

The second problem is an effect of absorption by the cloud. The horizontal moved distance of photon becomes small in the wavelength with a strong absorption, and the transportation of the radiation of horizontal direction becomes small. Therefore, the divergence and convergence of radiation becomes small, increasing and decreasing the incidence sun light decide reflection light, and the correction of the inclination is smaller than the wavelength without absorption.

3. Landsat measurements

The oblique plane parallels cloud model described in Chapter 2 is applied to Landsat satellite data of a high resolution, and the presumption of optical thickness is attempted. The data used is a scene

in the western North Pacific Ocean on January 18, 1991, and the radiation and microphysical observation of WCRP were done at a simultaneous period. The aircraft measurements show the effective radius of cloud particles was 5μm. When the satellite passed sky, the solar azimuth angle is 60 degrees and the azimuth angle is 141 degrees. The sensor used is Channel 4 (0.86μm) and channel 7(2.2μm) of TM, and the resolution of the sensor is 30m. The area without the space of the cloud was cut out from one scene. Assuming effective radius to be 5.0μm did the radiation calculation for the entire the scene, and using the oblique plane parallel cloud model. Figure 1 shows Landsat satellite data and the result of the radiation calculation. Landsat satellite data has been installed almost completely in the lattice of the calculation result. The ratio of effective gradient of 0.86μmand 2.2μm has been calculated here as 0.65:1.0. Figure 2a is a picture of optical thickness, and, Figure 2b is a picture of effective gradient. Making it clear is from Figure 3 to the removal of the effect that the reflection light on the side where the sunlight is hit strengthens, and the good reproduction of optical thickness. It was confirmed that bias, which depended on the direction of the incidence of the sunlight, had disappeared as a result of two dimensions Fourier spectrum analysis.

4. Monte Carlo Simulation

Using the Monte Carlo method, the plane parallel cloud model which inclines at the radiation scene of an inhomogeneous cloud is applied, and the presumption result of optical thickness is verified, reproduces the radiation scene of a not homogeneous cloud. Moreover, only when the right under is seen in Landsat satellite data, the direction where scattering forward and a rear scattering are seen is verified in the Monte Carlo method simulation. Same resolution of 30m as Landsat satellite data was given to the Monte Carlo calculation, and the area of 256x256 pixels was calculated. Effective radius differed from the time of Landsat satellite, and assumed 10μm. 1,000,000,000 numbers of photons were turned on to adjust the calculation accuracy to 1%. The estimate of optical thickness by the oblique plane parallel cloud model can reproduce a direction of the nadir viewing, forward scattering viewing, and a backward scattering viewing very well. The ratio of effective gradient is 0.5:1.0 in nadir, 0.75: 1.0 in forward scattering and 0.4: 1.0 in backward scattering. The ratio of effective gradient is different depending on the viewing direction. The reason is that the scattered frequency increases in backward scattering, and the influence of absorption strengthens and the scattered frequency decreases in scattering forward, and the influence of absorption weakens.

5. Summary and Conclusions

A method is presented for determining the optical thickness of horizontally inhomogeneous clouds from reflected solar radiation measurements. An oblique plane parallel model whose normal is tilted in a vertical plane, including direction of solar incident, is used to represent the variation of incident solar radiation on the cloud surface and horizontally transported radiation in the cloud layer. A new parameter of effective gradient is defined as an oblique angle of the plane parallel model and the parameter is not just the gradient of real cloud surface but modified with horizontally convergence or divergence of radiation. A cloud pixel tilted to the solar direction receives more solar radiation on the surface than a level cloud pixel and this positive gradient cloud

enhances the reflected radiation but loses the radiation with the horizontally divergence in the oblique cloud layer. Under the assumption that the effective particle radius of clouds is constant in the cloud layer, the optical thickness and effective gradient of clouds in the independent pixels of satellite scene can be determined from reflection function measurements at weak absorbing wavelength (0.86μm) and absorbing wavelength (2.16μm). Horizontally convergence and divergence of radiation at weak absorbing wavelength is larger than that of absorbing wavelength so the effective gradients of 0.86μm wavelengths are smaller than that of 2.16μm. In order to reduce the unknown variables to two, this method assumes that the ratio of the effective gradient between the two wavelengths is uniform for variation of the optical thickness and effective gradient of clouds. Applying this method to Landsat TM measurements, we recognize that the effective gradient at 0.86μm is smaller than at 2.16μm and the effective gradient ratio is estimated to be 0.65 for nadir view with oblique sun ($\theta_0 = 60^\circ$). By applying the effective gradient ratio to the oblique plane parallel model, the analysis provides a good estimate of the optical thickness and effective gradient of cloud.

In addition to Landsat TM measurements, an analysis of the forward and backward scattered radiation field of a fractal cloud model is carried out using a Monte Carlo simulations. It is shown that a good agreement between estimates and originals of the optical thickness of cloud can be obtained and the effective gradient ratio is smaller in the backward view and larger in the forward view than in the nadir view.

REFERENCES

Galinsky, V. L. and V. Ramanathan, 1988: 3D Radiative transfer in weakly inhomogeneous medium. Part I: Diffusive approximation. *J. Atmos. Sci.*, 55, 2946-2959.

Oreopoulos, L., A. Marshak, R. F. Cahalan, and G. Wen, 2000: Cloud three-dimensional effects evidenced in Landsat spatial power spectra and autocorrelation functions. *J. Geophys. Res.*, 105, 14777-14788.

Titov, G. A., 1988: Radiative horizontal transport and absorption in stratocumulus clouds, J. *Atmos. Sci.*, 55, 2549-2560.

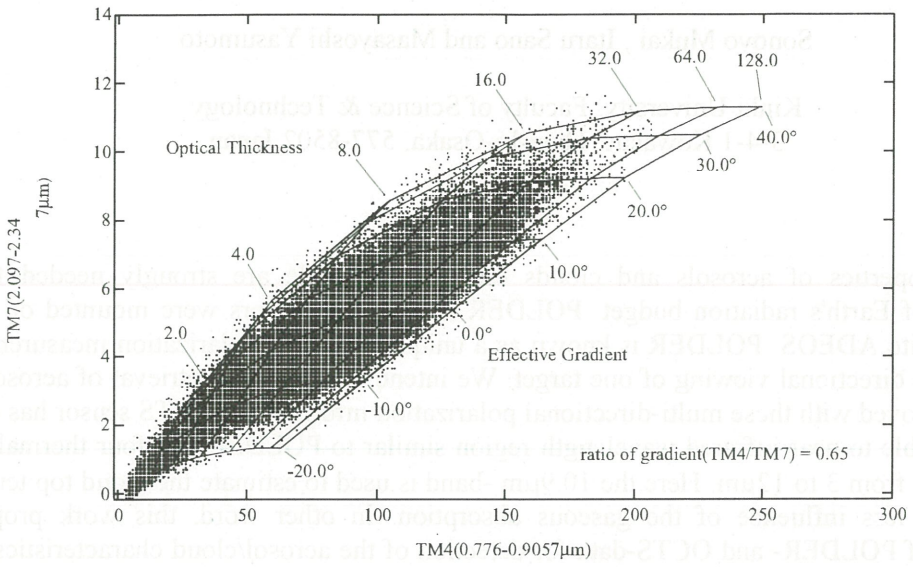

Figure 1. Theoretical relationships between the reflection function at 0.86 μm and 2.2 μm for various values of the cloud optical thickness and effective gradient. Data from Landsat TM sensor are superimposed on the figure (18 June 1991).

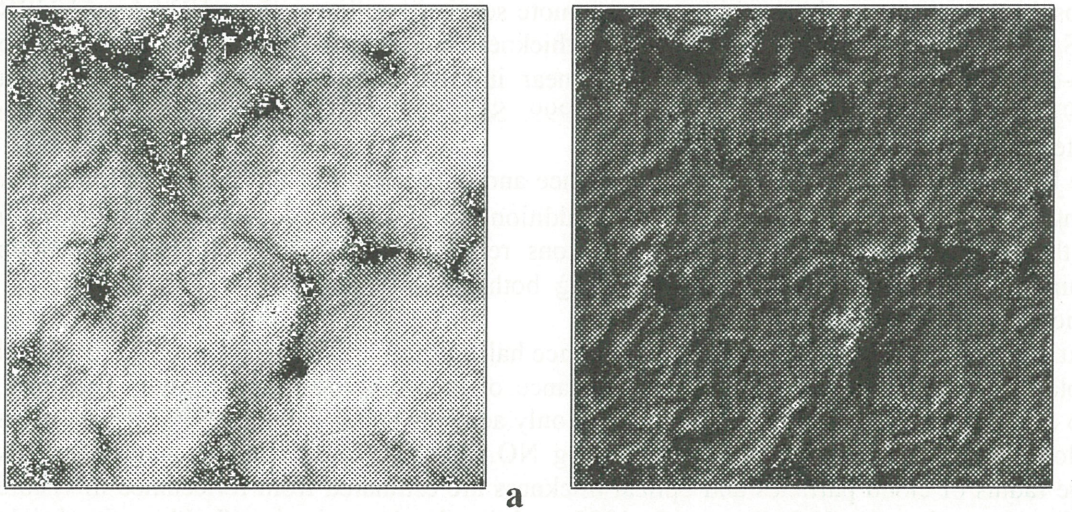

Figure 2. Images of optical thickness (a) and effective gradient (b) retrieved from a scene of Landsat TM sensor using the oblique plane parallel cloud model.

Retrieval of aerosols and clouds on a global scale

Sonoyo Mukai , Itaru Sano and Masayoshi Yasumoto

Kinki University, Faculty of Science & Technology
3-4-1 Kowakae, Higashi-Osaka, 577-8502 Japan

Abstract

Radiative properties of aerosols and clouds on a global scale are strongly needed for better understanding of Earth's radiation budget. POLDER and OCTS sensors were mounted on the earth observing satellite ADEOS. POLDER is known as a unique sensor as polarization measurements and multi-(up to 14) directional viewing of one target. We intend to show that retrieval of aerosols/clouds are greatly improved with these multi-directional polarization information. OCTS sensor has 8 spectral bands from visible to near-infrared wavelength region similar to POLDER and four thermal bands in the wavelengths from 3 to 12μm. Here the 10.9μm -band is used to estimate the cloud top temperature because of the less influence of the gaseous absorption. In other word, this work proposes the combined use of POLDER- and OCTS-data for detection of the aerosol/cloud characteristics over the ocean and over the land.

1. Introduction

Global distribution of aerosol/cloud properties are strongly needed for better understanding of Earth's climate (King et al.,1999). Therefore the aerosol properties such as optical thickness, Angstom Exponent, complex refractive index etc, and thermodynamic phase of cloud and optical and/or geometrical properties of cloud are the important parameters of the earth Global Circulation Model (GCM) simulations. Nakajima et al. (Higurashi and Nakajima,1999, Nakajima et al.,1999)have shown the aerosol properties over the world by using remote sensing satellite such as NOAA / AVHRR and ADEOS / OCTS. These works retrieved optical thickness and Angstrom exponent of aerosols based on two-channel relationship of visible and/or near infrared radiance measurements. Goloub et al.(1999) and Mukai et al.(Mukai and Sano, 1999, Sano and Mukai, 2000) also derived aerosol parameters from ADEOS / POLDER data.

The POLDER sensor measures both of radiance and polarization of the Earth's reflectance at the wavelengths of 0.443, 0.670 and 0.865 μm. In addition the POLDER sequentially obtains the frame image, therefore we get the light up to 14 directions reflected from one target. Here we describe an algorithm for retrieving aerosol properties using both radiance and polarization as well as their multi-viewing information given by POLDER.

Next cloud retrieval procedures are shown. Since half of the Earth's surface is covered with cloud, cloud plays an important role in the energy balance of atmosphere-surface system. Therefore, in order to estimate the Earth's radiation budget, not only aerosols but also cloud properties are necessary on a global scale. Recently cloud retrieval using NOAA/AVHRR data has been proposed, where effective radius of cloud particles and optical thickness are estimated from reflectance in visible and near infrared wavelengths (Nakajima et al., 1990) and the cloud type is classified by using brightness temperature based on the split window method (Inoue, 1987). This work proposes the combined use of polarization data by POLDER and thermal data by OCTS for detection of the cloud coverage and its thermodynamic phase. Combination of multi-sensor data as well as the multi-spectral data looks promising to estimate the optical properties of the cloud. In addition, multi-directional polarization information provided by POLDER sensor has a capability to improve the cloud retrieval.

2. Aerosol Retrieval

First of all aerosol sample should be prepared. Model aerosols take the typical values of refractive index (m) , e.g. 1.33-i0.0 for clean aerosols, 1.50-i0.005 for water soluble type and dust aerosols, and 1.40-i0.0 for mixed case of both types. Aerosol size distribution takes a single-mode log-normal distribution. The modal radius are set up as 0.03, 0.07, 0.14 and 0.27 μm. The width of log-normal

curve is fixed to 2.37 μm. The range of Angstrom exponent (α) varies from 0.0 to 1.7 for the present parameters, because the value of α relates to the aerosol size distribution and complex refractive index. The optical thickness of aerosols is represented by τ.

Aerosol characteristics is estimated based on comparison of measurements by POLDER with the calculated values stored in look up table (LUT) compiled from multiple scattering simulations in an atmosphere-sea surface model. The comparison is made from pixel to pixel of the satellite image. Namely viewing angles of sun and satellite on each pixel of the image correspond to angles of incident and scattered light at a scattering process. In other word, each pixel of the image gives each scattering angle. Thus a scattering angle correlates radiance/polarization of a pixel of POLDER image with a simulated value in the LUT. Therefore in our aerosol retrieval, the interpolation process with respect to angles is necessary in order to estimate a proper simulated value corresponding to an observational geometry. As a result an optimized aerosol model is retrieved to minimize the relative error between the measurements and the simulations at each pixel. Once τ and α have been set up at each pixel of satellite image, the optimized value of *m* can be determined. At every step mentioned above, POLDER directional data are effectively used.

3. Cloud Retrieval

First, a procedure for detection of the cloud is described. In general, cloud coverage map is made from both of reflectance and brightness temperature (Rossow et al., 1991). Therefore reflectance at 0.865μm given by POLDER and brightness temperature at 10.9 μm by OCTS are used for our cloud detection. Furthermore polarization tendency with scattering angle is available for our present study, because it in a case of clear sky is very different from that under the cloudy condition. Thus polarized reflectance given by POLDER is expected to be useful for cloud detection (Buriez et al., 1997). Our cloud detection algorithm is based on an idea that a pixel is labeled as cloudy if one of the following three tests proves positive; (1) the reflectance at 0.865μm by POLDER is significantly larger than its clear-sky estimate, (2) brightness temperature at 10.9μm by OCTS is lower enough than its clear-sky estimate, (3) polarized reflectance at 0.865μm by POLDER is larger enough than its clear-sky estimate. If all of the above tests prove negative, the pixel is labeled as clear.

Next, distinction of thermodynamic phase of the top cloud is examined using POLDER and OCTS data. The single scattering simulations of polarized reflectance are compared with the polarized reflectance data at a wavelength of 0.865 μm given by POLDER in order to distinguish the water cloud from the ice cloud (Parol et al., 1999). Because angular tendency of polarized reflectance of the water droplet is clearly different from that of the ice crystal. This fact suggests a capability to distinguish the thermodynamic phase of the top of the cloud. Here the values of polarized reflectance are calculated from Mie scattering and the geometrical optics for water and ice, respectively. Because ice particles are assumed to be hexagonal crystal which is described by the ray-tracing technique (Macke,1993).

On the other hand, it is well known that thermal temperature is available to distinct the thermodynamic phase of water. The airborne data by King et al. (1992) suggests a value of 250K for the boundary temperature to distinguish liquid water from ice. Therefore brightness temperature derived from OCTS data at a wavelength of 10.9μm is also used to estimate the thermodynamic phase of cloud top. Finally it is of interest to mention that the polarized reflectance at 0.865μm can be used not only the distinction of the water/ice cloud but also retrieval of the size and shape of cloud particles based on light scattering simulations (Yasumoto et al).

4. Results

Global distributions of aerosol/cloud parameters are obtained by averaging all of the retrieved results throughout one-month over the whole world including both land and ocean. Fig.1 shows the distributions of aerosol optical thickness at wavelength of 0.865 μm (τ) and Angstrom exponent (α) in November 1996. It is of interest to mention that the aerosols over the coastal zone show the natural feature.

When thermodynamic phase of water cloud top and that of ice one are represented by black and white, respectively, relative occurrence of water cloud and ice cloud during one month is represented by gray scale. Fig.2 shows global map of cloud phase frequency in November, 1996. This map is compiled by combination of polarization information by POLDER and thermal data by OCTS.

POLDER and OCTS data were provided by CNES in France and NASDA in Japan, respectively.

References

1. King, M.D., Y.J. Kaufman, D. Tnaré, and T. Nakajima, "Remote Sensing of Tropospheric Aerosols from Space: Past, Present, and Future", *Bull. Americ. Meteo. Soc.*, **80**, 2229-2258, 1999.
2. Higurashi, A., and T. Nakajima, "Development of a Two Channel Aerosol Retrieval Algorithm on Global Scale using NOAA / AVHRR", *J. Atmos. Sci.*, **56**, 924-941 1999.
3. Nakajima, T., A. Higurashi, K. Aoki, T. Endoh, H. Fukushima, M. Toratani, Y. Mitomi, B.G. Mitchell, and R. Frouin, "Early Phase Analysis of OCTS Radiance Data for Aerosol Remote Sensing, *IEEE Trans. Geosci. Remote Sensing*, **37**, 1575-1585, 1999.
4. Goloub, P., D. Tanré, J.L. Deuzé, M. Herman, A. Marchand, and F.M. Bréon, "Validation of the First Algorithm Applied for Deriving the Aerosol Properties Over the Ocean using the POLDER / ADEOS Measurements", *IEEE Trans. Geosci. Remote Sensing*, **37**, 1586-1596, 1999.
5. Mukai, S., and I. Sano, "Retrieval Algorithm for Atmospheric Aerosols based on Multi-angle Viewing of ADEOS/POLDER", *Earth, Planets, Space*, **51**, 1247-1254, 1999.
6. Sano, I. , and S. Mukai, "Algorithm description of system flow for global aerosol distribution", *Appl. Math. & Comp.*, **116**, 79-91, 2000.
7. Inoue., T, "A cloud type classification with NOAA-7 split window measurements", *J. Geophys. Res.*, **92**, 3991-4000, 1987.
8. Nakajima, T., and M. D. King, "Determination of the Optical Thickness and Effective Particle Radius of Clouds from Reflected Solar Radiation Measurements. Part I : Theory", *J. Atmos. Sci.*, **47**, 1878-1893, 1990.
9. Rossow, W. B., and R. A. Schiffer, "ISCCP Cloud Data Products", *Bull. Amer. Meteor. Soc.*, **72**, 2-20, 1991.
10. Buriez, J.-C., C. Vanbauce, F. Parol, P. Goloub, M. Herman, B. Bonnel, Y. Fouquart, P. Couvert and G. Seze, "Cloud Detection and Derivation of Cloud Properties from POLDER", *Int. J. Remore Sens.*, **18**, 2785-2813, 1997.
11. Parol, F., J.-C. Buriez, C. Vanbauce, P. Couvert, G. Sezè, P. Goloub, and S. Cheinet, "First Results of the POLDER "Earth Radiation Budget and Clouds" Operational Algorithm", *IEEE Trans. Geosci. Remote Sensing*, **37**, 1597-1612, 1999.
12. Macke, A., "Scattering of Light by Polyhedral Ice Crystals", *Appl. Opt.*, **32**, 2780-2788, 1993.
13. King, M. D., Y, J. Kaufman, W. P. Menzel and D. Tanré, "Remote Sensing of Cloud, Aerosol, and Water Vapor Properties from the Moderate Resolution Imaging Spectrometer (MODIS), *IEEE Trans. Geosci. Remote Sensing*, **30**, 2-27, 1992.
14. Yasumoto, M., I. Sano and S. Mukai, "Combined Use of OCTS and POLDER for Cloud Retrieval", *Adv. Space Res.*, (submit to).

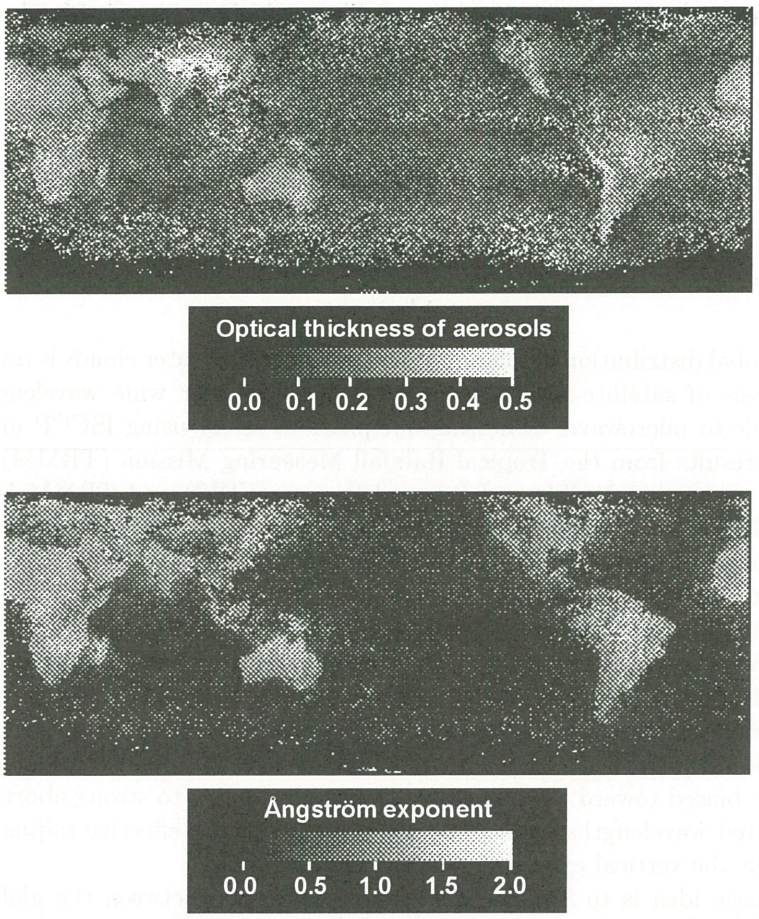

Fig. 1 Global distribution of aerosol optical thickness (upper) and Angstrom exponent (lower) in November, 1996.

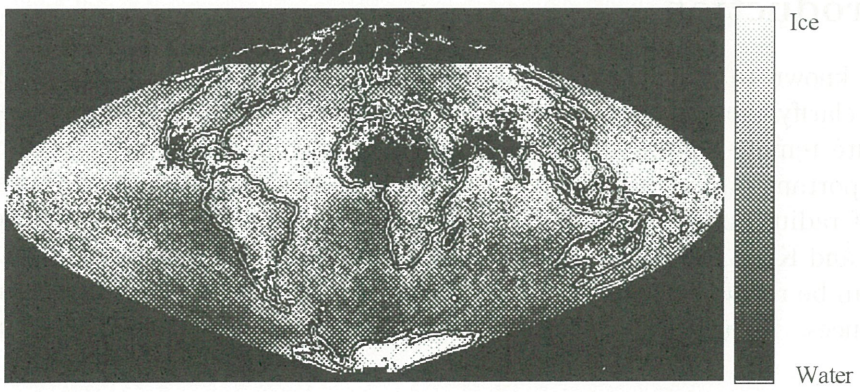

Fig. 2 global map of cloud phase frequency in November, 1996.

Cloud Observation by Visible/Infrared Imager and Microwave Radiometer

Hirohiko Masunaga[1], Takashi Y. Nakajima[1], Teruyuki Nakajima[2], Misako Kachi[1], Riko Oki[1], Shunsuke Kuroda[2,3]

[1] *Earth Observation Research Center, 1-9-9 Roppongi, Minato-ku, Tokyo 106-0032, Japan*

[2] *Center for Climate System Research, University of Tokyo, 4-6-1 Komaba, Meguro-ku, Tokyo 153-8904, Japan*

[3] *Present affiliation : Sun Microsystems, Inc.*

Abstract

The global distribution of microphysical properties of water clouds is investigated on the basis of satellite-retrieved spectral radiances over wide wavelength range from visible to microwave. Following our previous study using ISCCP and SSM/I data, the results from the Tropical Rainfall Measuring Mission (TRMM) data are presented employing Visible and Infrared Scanner(VIRS) and TRMM Microwave Imager(TMI). Use of the TRMM sensors has the advantage that highly simultaneous observation is possible in comparison with analysis of combined data from sensors on different platforms such as ISCCP and SSM/I.

Combination of visible and near-infrared radiances, denote by Vis-NIR method, can retrieve cloud microphysical parameters such as the cloud optical thickness and effective droplet radius. The effective droplet radius can be obtained also from visible and microwave radiances (Vis-Mic method) by combining the optical thickness and the liquid water path. The effective radius retrieved by Vis-NIR method may tend to be biased toward the value near the cloud top due to strong abortion in the near-infrared wavelengths, while Vis-Mic would yield the effective radius averaged throughout the vertical extent of clouds.

The basic idea is to find a characteristic difference between the global distributions of effective cloud droplet radii from Vis-NIR and Vis-Mic methods. The difference would be caused in part by vertical inhomogeneity of droplet size within clouds, and therefore is expected to be a possible indicator of occurrence of drizzle.

1 Introduction

Clouds are known to play significant roles in the earth's radiation budget, and it is inevitable to clarify the global distribution of cloud characteristics for climate system studies. Satellite remote sensing of the microphysical and optical properties of clouds has been an important subject in the last decade. An established scheme to retrieve the effective droplet radius and optical thickness of clouds employs a pair of shortwave channels (Nakajima and King 1990; Han, Rossow, and Lacis 1994; and references therein).

LWP can be retrieved from microwave brightness temperatures as well as from shortwave radiances. A large number of algorithms have been developed to obtain LWP by

microwave radiometers over oceanic environment (e.g., Wilheit and Chang 1980; Petty 1990; Greenwald et al. 1993; Lin, Wielicki et al. 1998). Comparison of the microwave-retrieved LWP with the shortwave-retrieved LWP obtained by spaceborne sensors has been done by some authors (Greenwald et al. 1993; Lojou, Frouin, and Bernard 1991; Lin and Rossow 1994; Lin, Minnis et al. 1998). However, it is important to reexamine the difference between the microwave and shortwave LWPs in terms of variation of the effective droplet radius since the effective radius was assumed to be constant in the past studies.

We describe in section 2 the data and retrieval algorithm adopted in this study, and show the results in section 3.

2 Data and Retrieval Algorithm

Following our preceding study using visible and infrared radiances from International Satellite Cloud Climatology Project (ISCCP) data and microwave brightness temperature from Special Sensor Microwave/Imager (SSM/I) data (Kuroda 1999), we employ Visible and Infrared Scanner (VIRS) and TRMM Microwave Imager (TMI) as counterparts of ISCCP and SSM/I respectively, where the both sensors are boarded on Tropical Rainfall Measuring Mission (TRMM) Satellite. There are some advantages to use the TRMM sensors for our purpose: (1) Use of imagers on the same platform enables us highly isochronous observation, and (2) The global distribution of rain rate retrieved by Precipitation Radar (PR) aboard on TRMM is available for direct comparison with our results. On the other hand, TRMM data require us longer term average to obtain a global map of clouds than other satellites' data such as ISCCP and SSM/I data, because VIRS and TMI have narrow swath due to a low altitude (~350km) of the TRMM orbit. Variable solar angles, since TRMM is sun asynchronous, also cause difficulty in retrieval of the cloud properties by VIRS.

VIRS and TMI data are assigned on the common $0.25^\circ \times 0.25^\circ$ grid. Present analysis is concentrated on water clouds ($T_c \geq 273$K) over marine environment. We retrieve the effective droplet radius, cloud optical thickness, and clout top temperature from VIRS radiances of ch.1(0.63μm), ch.3(3.75μm), and ch.4(10.8μm) by a modified version of the algorithm developed by Nakajima and Nakajima(1995). TMI brightness temperatures at 19.35, 21.3, and 37.0GHz yield the column water vapor (CWV) and liquid water path(LWP). In order to construct a look-up table for retrieving CWV and LWP, we have performed microwave radiative transfer calculations.

We present the ratio of effective droplet radii retrieved in two independent methods. One of them (Vis-NIR method) employs shortwave radiances of ch.1 and ch.3 of VIRS to obtain the effective radius by the Nakajima and Nakajima(1995) algorithm. Another scheme (Vis-Mic method) yields the effective radius, R_e, from the cloud optical thickness

at an optical wavelength, τ_c, and the microwave LWP according to the well-known formula,

$$R_e = \frac{3}{2}\mathrm{LWP}/\tau_c. \quad (1)$$

The results are shown in the next section.

3 Results and Discussion

We present here the retrieved values averaged over three months from January to March in 2000. Fig. 1 illustrates the ratio of R_e retrieved in Vis-Mic method and Vis-NIR method. One can see that areas where the ratio is less than unity corresponds to the regions with low precipitation rates, and vice versa. A possible interpretation is that the ratio R_e(Vis-Mic)/R_e(Vis-NIR) correlates with occurrence of drizzle. The effective droplet radius given by Vis-NIR method tends to represent the microphysical condition near the cloud top because of large extinction in an absorption channel in the near-infrared, while R_e by Vis-Mic method is considered to be an average value in the whole cloud. The ratio R_e(Vis-Mic)/R_e(Vis-NIR) therefore would depend on inhomogeneity in the vertical distribution of the effective droplet radius. This presumption leads us to an idea that the R_e ratio is an indicator of drizzling clouds, for which R_e(Vis-Mic)/R_e(Vis-NIR) is expected to be larger than unity because of large drizzle droplets accumulated near the cloud base.

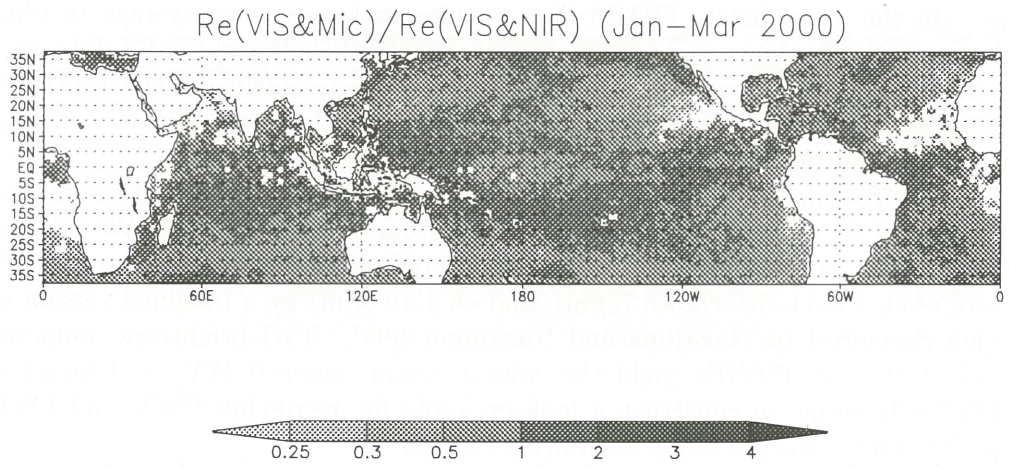

Figure 1: Global map of ratio of the effective droplet radii R_e(Vis-Mic)/R_e(Vis-NIR) during Jan-Mar, 2000.

References

Greenwald, T. J., G. L. Stephens, T. H. Vonder Haar, and D. L. Jackson, 1993, A physical retrieval of cloud liquid water over the global oceans using Special Sensor Microwave/Image(SSM/I) observations *J. Geophys. Res.*, **98**, 18471-18488

Han, Q., W. B. Rossow, and A. A. Lacis 1994, Near-global survey of effective droplet radii in liquid water cloud using ISCCP data, *J. Clim.*, **7**, 465-497

Kuroda, S. 1999, Master Thesis, Univ. of Tokyo (written in Japanese)

Lin, B. and W. B. Rossow 1994, Observations of cloud liquid water path over oceans: Optical and microwave remote sensing methods *J. Geophys. Res.*, **99**, 20907-20927

Lin, B., B. Wielicki, P. Minnis, et al. 1998, Estimation of water cloud properties from satellite microwave, infrared and visible measurements in oceanic environments 1. Microwave brightness temperature simulations, *J. Geophys. Res.*, **103**, 3873-3886

Lin, B., P. Minnis, B. Wielicki, et al. 1998, Estimation of water cloud properties from satellite microwave, infrared and visible measurements in oceanic environments 2. Results *J. Geophys. Res.*, **103**, 3887-3905

Nakajima, T. and M. D. King 1990, Determination of the optical thickness and effective particle radius of clouds reflected solar radiation measurements. Part I: Theory, *J. Atmos. Sci.*. **47**, 1878-1893

Lojou, J.-Y., R. Frouin, and R. Bernard 1991, Comparison of Nimbus-7 SMMR and GOES-1 VISSR atmospheric liquid water content, *J. Appl. Meteor.*. **30**, 187-198

Nakajima, T. Y. and T. Nakajima 1995, Wide-Area Determination of Cloud Microphysical Properties from NOAA AVHRR Measurement for FIRE and ASTEX Regions, *J. Atmos. Sci.*. **52**, 4043-4059

Petty, G. W., 1990, On the response of the Special Sensor Microwave/Imager(SSM/I) to the marine environment - Implications for atmospheric parameter retrievals, Ph.D. dissertation, 291 pp., Univ. of Washington, Seattle

Wilheit, T. T. and A. T. C. Chang 1980, An algorithm for retrieval of ocean surface and atmospheric parameters from the observations of the scanning multichannel microwave radiometer, *Radio Sci.*. **15**, 525-544

SKYNET validation network and its activities

T. TAKAMURA[(1)], S. KANETA[(1)], I. OKADA[(2)], N. TAKEUCHI[(1)],
G-Y Shi[(3)] and T. NAKAJIMA[(4)]

(1) CEReS, Chiba University, (2) Japan Science and Technology Corporation,
(3) Institute of Atmospheric Physics, Chinese Academy of Sciences,
(4) CCSR, University of Tokyo

The impact factors on estimation of the global warming are uncertainties of cloud, aerosol and its interaction in the global model. Increase in cloud amount can suppress global warming by carbon dioxide increasing from fossil fuels consumption and other warming gases, but its responsibility is not clear as shown in IPCC report. In order to estimate the global impact of these factors, highly accurate analysis of satellite data is required combined with ground-based observations, i.e. validation.

SKYNET is a network spread out in East Asia to accomplish these objectives. The SKYNET sites have several instruments mainly composed of sky radiometer, pyranometer and pyrgeometer. In several sites, intensive observations have been done by support of other projects, such as GAME project(Sri Samrong in Thailand and Hefei in China). These sites are operated in cooperation with the local institutes or observatories. Data observed are sent and analyzed at the data center, CEReS, Chiba University and CCSR, University of Tokyo. These data are shared openly with research groups and communities attended to this program.

The SKYNET data can give aerosol parameters deduced by sky radiance and radiation amounts in the East Asia. Then some typical size distribution of aerosols around the sites can be compiled and also downward solar radiation at the surface estimated from GMS-5 data is validated with SKYNET radiation data. The downward solar radiation depends strongly upon characteristics of aerosol and cloud, therefore the difference between the observed and estimated radiation gives some suggestion on observation and analysis system.

While the more accurate results from the satellite data are required for overall mapping of radiation budget, the SKYNET can play an important role in the research of the global warming and climate change.

1. Introduction

The important factors in the global climate change are uncertainties of cloud, aerosol and its interaction in the global model. Increase in cloud amount can suppress global warming by carbon dioxide increasing and other warming gases, but its responsibility is not clear as shown in IPCC report. The direct effect of aerosol is concerned with its amount(optical thickness) and its complex refractive index(absorptive or reflective), and these parameters have been observed and estimated for many years. On the other hand, an indirect effect has much more uncertainties in the climate system. The modification of cloud system due to aerosols can give an effect to the climate system , especially near the urbanized region.

The radiation budget is one of key parameters in the global climate change as well as water cycle, and the surface radiation is also basic. The global map of radiation should require satellite data, especially geo-stationary satellite data, such as a GMS. The SRB program has been performed for the surface radiation budget which used the ISCCP data basically. In this study GMS-5 data is used for estimation of downward solar radiation. In order to estimate the global impact of the climate change, highly accurate analysis of satellite data is required with a validation of ground-based observations.

The SKYNET observation network has been constructed to accomplish these purposes, aerosol detection and validation of solar radiation estimated from satellite data. The sites in the network are mainly located in the East Asia, because the AERONET operated by NASA has covered the wide areas over the world except for the Asian region.

2. SKYNET

The SKYNET is an observation network with several objectives such as validation for satellite products, supplies of basic data for atmospheric collection of satellite data, typical modeling of regional aerosol and so on. These network sites have been located mainly in the East Asia from Mongolia to Thailand, as shown in Fig.1. These sites can cover typical climate conditions from tropical to arid/semi-arid and grassland areas including an industrial area(Chiba).

There are three sites in China to observe a yellow sand event(Kosa) along one of major air flow lines from the west to the east in cooperation with sites in Japan. Another features of the SKYNET are to get the longitudinal data in the west Pacific Ocean using research vessels and commercial ships. These ships with a sky radiometer are continuously operated.

The basic observation system consists of sky radiometer for aerosol derivation, pyranometer (CM21 by Kipp & Zonen) and pyrgeometer(PIR by Eppley Lab.) for the global solar and terrestrial radiation. Also environmental temperature and humidity are observed continuously. In the sites, Si-Samrong in Thailand and Hefei in China are intensive field sites for the GAME project so both sites have special features such as net radiation instruments, microwave radiometer for water vapor and cloud liquid content and so on.

Observation itself can be done automatically, but several instruments should be taken care of, e.g., to wipe a dome glass of pyranometer and pyrgeometer. Therefore, each site is operated by

local people who is with his institute or laboratory collaborated with our research center.

Collected data are stored in the CEReS, Chiba University and CCSR, the University of Tokyo, independently. These data is basically open to all community people after checking data. Quality control has been done carefully, because the clock of the computer at the observation site is sometimes unreliable. Recently, GPS receiver was introduced to the observation system of the Mandalgovi, Mongolia in order to adjust the system clock everyday. This modification could greatly improve the reliability of time stamp.

3. Asian Aerosol and its characteristics

Sky radiometer can give a size distribution and an optical thickness of aerosols which are derived from sky brightness of wavelength, 400, 500, 675, 870, and 1020nm(Nakajima et al., 1983,1996). An example of mean volume size distribution is shown in Fig.2.

The site of Minami-Torishima is more than 1800km southeast from Tokyo, and affected on a very low level by polluted air mass from the Asian continent. The pattern of size distribution can approximate a power law type roughly, such as Junge type, but in detail they have two or three mode depending on their source. The features of these distributions are that the density in an accumulation mode ranging around 0.1 to 0.2 um is lower than that of a giant particle mode over 1 um. This may be reasonable because the remote ocean area cannot have many sources of natural origin. The coarse mode might be made by natural sources, such as sea salt particles.

The third mode centered at 0.5 to 0.7um is found. After Pinatubo eruption, stratospheric aerosols were increasing temporarily and abruptly. This showed a similar mode(Remer and Kaufman, 1998), but the mode in our case may be not the stratospheric aerosols because three modes in the figure are increasing simultaneously.

Chiba and Tokyo Bay area have been industrialized and merchandized widely up to now. There are many manufacturers which consume huge energy, such as iron industries, oil plant, power plant and so on. Figure 3 shows mean volume size distributions observed at CEReS, Chiba Univ. Typical distribution shows a bi-modal distribution, accumulation and coarse mode. The mode centered around 1 um is not clear for lower density, but distinguished for relatively heavier cases. The source of this mode has been not identified and may be different from the remote maritime type. Accumulation mode is very clear and has a wide variety for seasons. As well-known, the mode has main part of second particles through a gas-to- particles process, such as sulfate particles, and can reflect the atmospheric pollution.

The seasonal variation of the size distribution is not so clear, but each season shows a little different distribution and density. The optical thickness in winter is relatively lower than that in other seasons, as shown in Table 1. This table shows also other related parameters for seasons. It should be noted the complex refractive index of aerosols are assumed to be 1.50-0.01i for all. The single scattering albedo(SSA) is strongly dependent upon it, so the SSA has almost similar value for all cases.

4. Surface radiation

4.1 Estimate of downward solar radiation at the surface

Surface solar radiation is the most sensitive to cloud amount as well as its optical thickness. Therefore, these are key parameters for retrieval of

surface solar radiation from the satellite data. GMS-5 is a Japanese meteorological satellite which is one of geo-stationary network satellites in the world, and has four channels, wide visible, water vapor channel and split window channels. This can observe the Earth facing to the satellite every hour. It is the biggest advantage over the orbital satellite and is suitable for radiation study.

In this study, the analyzing area for estimation covers from 60° N, 80° E to 20° S, 160° E wide. The minimum basic unit in the analysis is 0.5 x 0.5 degree in Lat. and Lon. ECMWF(European Centre for Medium-range Weather Forecasts) objective analysis data is adopted for profiles of temperature, water vapor, and atmospheric pressure.

Cirrus which is detected by a split window technique was classified into the cases over 253 K and under 253 K. Optical thickness is assumed to be 2.2 and 7.4, respectively in warmer and colder case(Inoue, 1987). Water clouds are classified into 3 layers according to ISCCP category (Rossow and Garder, 1993). Cloud type, convective or stratus, is also checked by using auto-correlation technique. Cloud overlapping model is introduced such that maximum overlapping is used for convective cloud and random overlapping for stratus. Optical thickness of cloud can be retrieved by a reflection method of solar radiance, which was described in detail in Nakajima and Nakajima(1995).

Figure 4 shows an example of monthly averaged total cloud fraction in the northern summer (July, '97) and the northern winter (January, '97). In summer, a rain band from the Bay of Bengal to the Okhotsk Sea is shown apparently. Cloud due to the ITCZ is also seen from Philippine islands to the equator in the Central Pacific. Clouds found in the Japan sea in winter are convective due to heating from the warm sea covered by the Siberian clod air blow-off.

For computation of surface solar radiation, RSTAR5 code, developed by Nakajima et al.(1983, 1986 and 1988), is used. Lookup table for surface solar flux is composed of parameters of optical thickness of cloud, ratio of water cloud to ice cloud, optical thickness of aerosol, effective water vapor, solar zenith angle, and surface reflectance. Global Aerosol Data Set (GADS, Kopke et al., 1997) developed by the Max Planck Institute is adopted for aerosol data because of no information over land.

Figure 5 shows an example of a daily mean map of surface downward solar flux in summer and winter. The mean solar flux which is derived by integration of hourly incoming solar radiation can reflect the variation of cloud and aerosol amounts. Cloud forcing for solar radiation at the surface is shown in Fig. 6, which is defined by the daily mean flux (Fig.5) minus daily mean cloud free flux. In July, large negative values are shown from the Bay of Bengal to the Okhotsk Sea and around the Philippine islands, corresponding to the cloud amount described before. There are also large negative value in South of the equatorial and small value in the Bengal Sea in January. Small values are shown over the part of Australia.

4.2 Comparison between estimated and observed radiation

The estimated surface solar flux can be compared with that observed at sites of the SKYNET. The comparison is performed using a daily mean solar flux, because an hourly data is not so good accordance with each other due to brokenness of cloud in space and time(or locality in cloud).

Figure 7 shows the comparison of the

estimated flux in daily mean with the observed one. Figure 7a shows the cases under clear sky condition which is classified by surface observed data using pyranometer output. The data at Si-samrong in October 1997 shows the small difference between them, but in January 1998 the estimation is under the observation. The satellite solar flux under clear sky condition has a variation due to water vapor and aerosol amount. The observed flux is widely changeable in time and space rather than the estimated flux, because the latter one is used with a representative aerosol model and water vapor from ECMWF data. So, these parameters should be discussed to be appropriate or not. Further analyses using aerosol characteristics derived from the SKYNET data will solve the distinction between the satellite estimate and the observed solar flux.

Figure 7b is the same as Fig. 7a except for cloudy condition. The surface observed data at Shouxian in July, 1998 show wide variation from 46 to 312 W/m2, while the satellite solar flux varies from 162 to 301 W/m2. The figure shows the overestimation of satellite solar flux as a whole. In other words, the cloud amount and/or optical thickness may be under-estimated. The difference between the observed and estimated flux is relatively small for more than 250W/m2 while for less than around this value the difference become bigger when the observed value is smaller, i.e. cloud is heavier. This means that the cloud estimation including overlapping effect has some problems.

In the algorithm to infer the surface solar radiation, an optical thickness of cloud has been decided by choosing the median pixel which is the center of the histogram of the brightness temperature by thermal infrared channel in the unit area (0.5 x 0.5 deg in Lat and Lon.). This selection of the pixel for retrieving the optical thickness has no physical reason, but the pixel can represent the typical cloud brightness temperature, i.e., cloud height. The statistics in optical thickness in the unit area should be considered as well as the brightness temperature histogram. Another possibility of underestimation of cloud optical thickness is inhomogeneity. The rough surface of cloud top can make shadow to a neighboring cloud and can affect the estimation of optical thickness of cloud to be smaller. This effect will be estimated by highly resolved cloud images such as airborne data.

5. Summary

The SKYNET data can give information of aerosol at various sites in the east Asia. Typical aerosol models are compiled from these observations, and will be introduced into radiative process in the solar radiation estimation.

These are also used for validation of the downward solar radiation estimated from GMS-5 data. The comparison with ground-based observed data shows the relatively good accordance for clear sky days, but for the cloudy condition, the difference is much bigger than that for clear days. This suggests that the cloud estimation has some defects in the algorithm or data analysis processes.

References

Kopke, P., M. Hess, I. Schult, and E.P. Shettle, 1997: Max Planck Institut fur Meteorologie, No. 243, Hamburg.

Inoue, T., 1987: A cloud type classification with NOAA-7 split window measurements, *J. Geophys. Res.*, **92**, 3991 - 4000.

Nakajima, T. and M. Tanaka, 1983: Effect of wind-generated waves on the transfer of solar

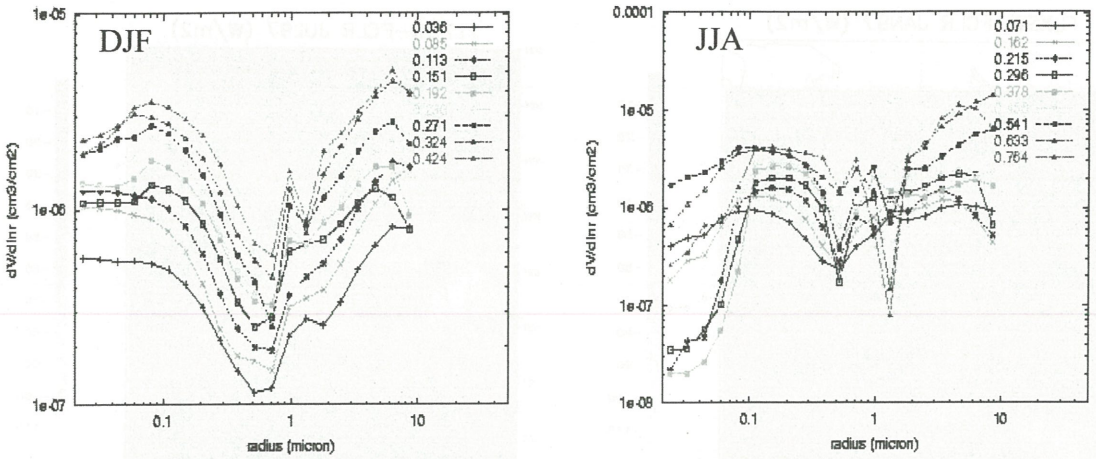

Figure 3 Same as Figure 2 but for Chiba. (Left: DJF, Right: JJA)

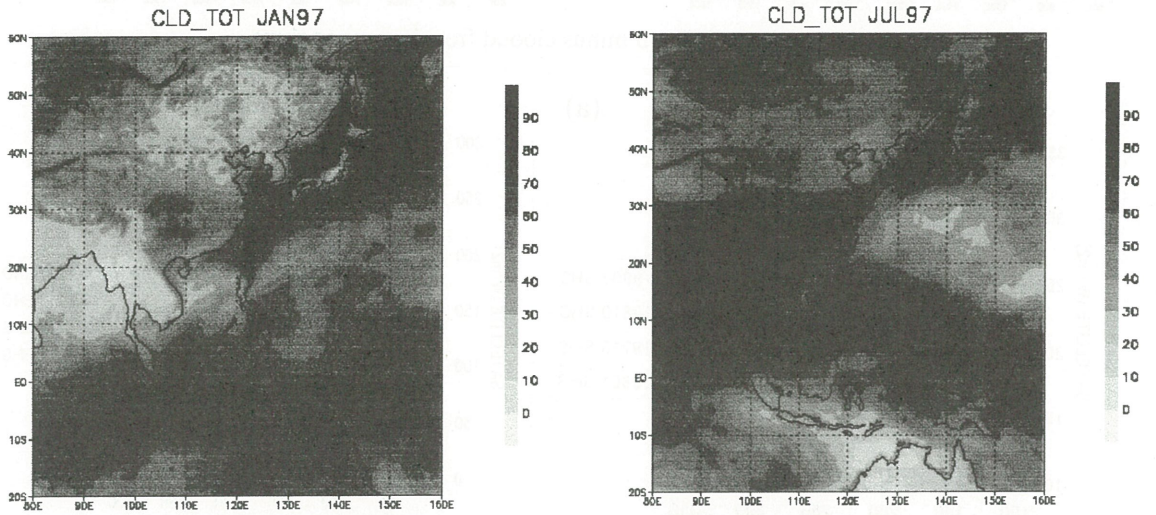

Figure 4. Total cloud amount for Jan.(Left) and for Jul.(Right)

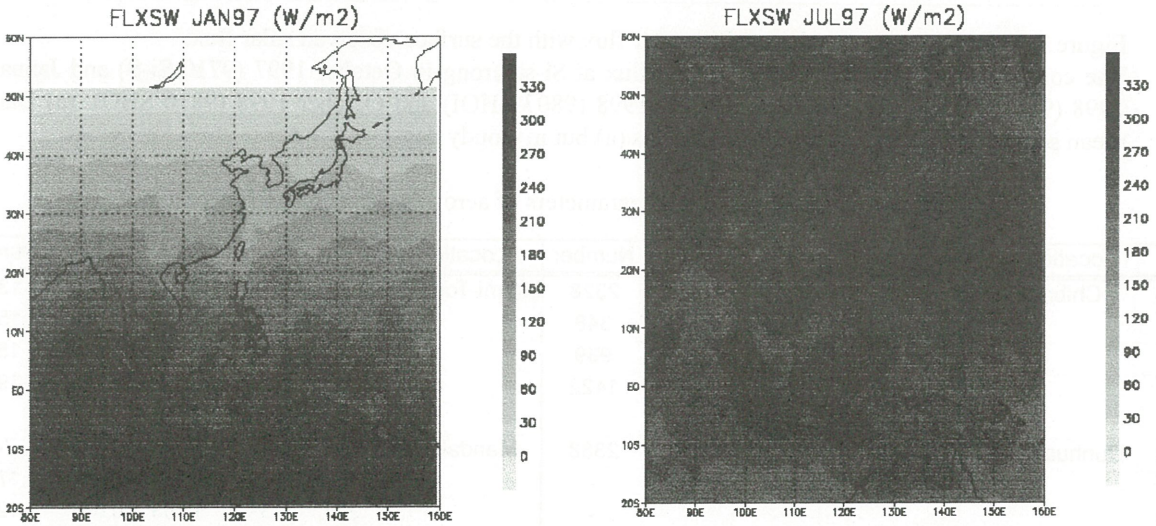

Figure 5. Daily mean downward surface solar radiation(Left:Jan.1997, Right: Jul. 1997)

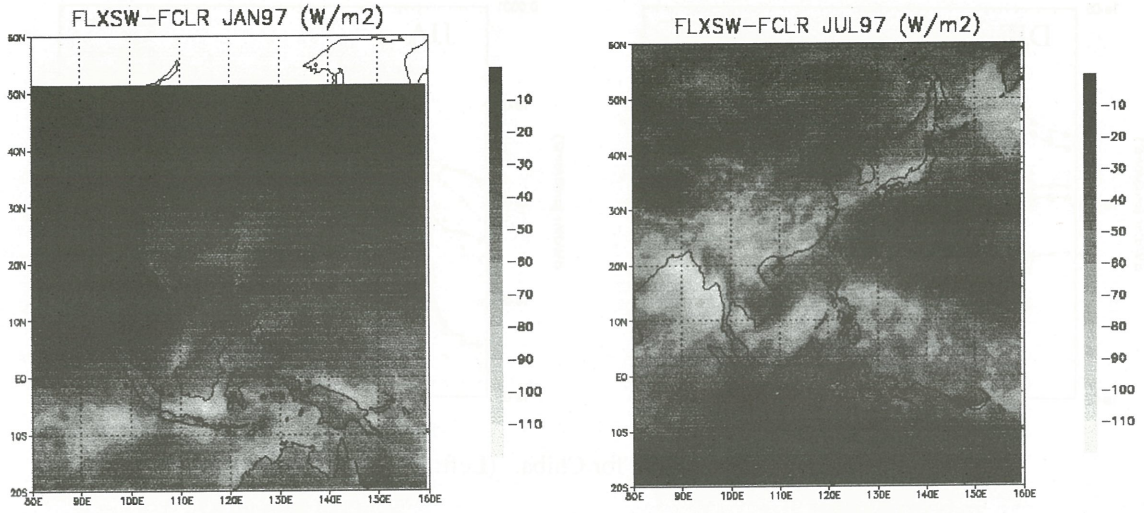

Figure 6. Radiative forcing(Fig. 5 minus clooud free downward flux)

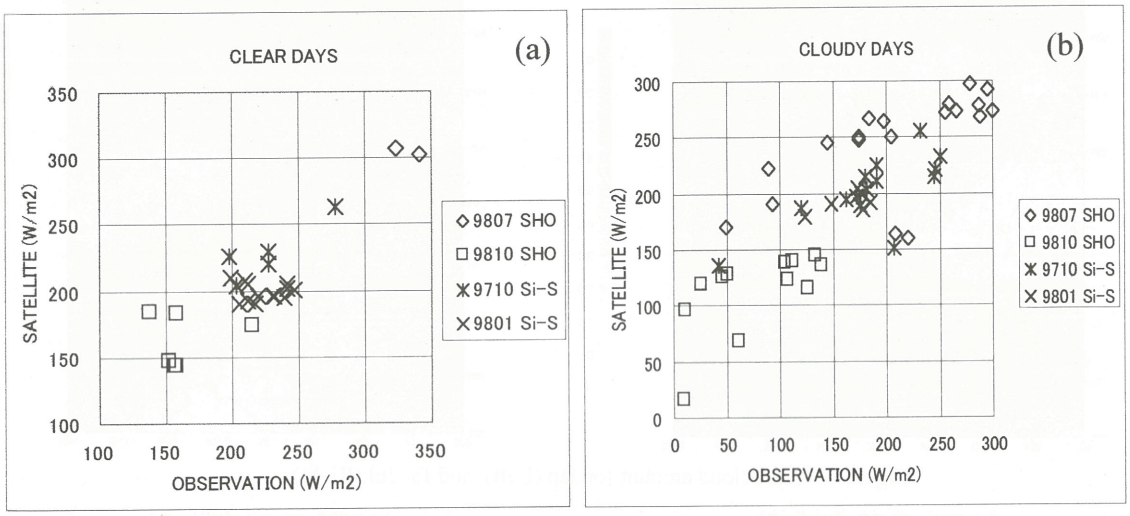

Figure 7. The comparison of the satellite solar flux with the surface observed solar flux.
The comparison is available in daily mean flux at Si-samrong in October 1997 (9710 Si-S) and January 1998 (9801 Si-S), and at Shouxian in July 1998 (9807 SHOI) and October 1998 (9810 SHO). (a) Daily mean solar flux in clear sky days. (b) Same as (a) but in cloudy days.

Table 1. Summary of optical parameters of aerosols. M=1.50-0.01i is assumed.

Location		Tau	SSA	G	Number	Location		Tau	SSA	G	Number
Chiba	DJF	0.251	0.873	0.636	2328	Minami-Torishim	DJF	0.127	0.821	0.742	1397
	MAM	0.470	0.888	0.678	348		MAM	0.122	0.814	0.734	1544
	JJA	0.485	0.875	0.683	939		JJA	0.188	0.841	0.722	1505
	SON	0.284	0.886	0.673	1422		SON	0.100	0.816	0.737	1973
	Yr	0.319					Yr	0.132			
Dunhuang	DJF	0.318	0.819	0.754	2388	Mandalgovi	DJF	0.231	0.850	0.616	742
	-	-	-	-	-		MAM	0.242	0.876	0.650	1753
	-	-	-	-	-		JJA	0.393	0.853	0.667	1293
	SON	0.202	0.814	0.767	1767		SON	0.175	0.855	0.646	3125
	Yr	0.269					Yr	0.239			
Si-Samrong	DJF	0.469	0.879	0.661	1032	Yinchuan	DJF	0.323	0.821	0.754	8708
	MAM	0.330	0.824	0.702	417		MAM	0.298	0.827	0.749	4024
	JJA	0.534	0.885	0.639	345		JJA	0.524	0.820	0.763	4771
	SON	0.329	0.869	0.717	705		SON	0.290	0.811	0.760	1679
	Yr	0.415					Yr	0.365			

Estimation of Methane Emission from Wetland with Sub-pixel Level Land Cover Characterization of Remotely Sensed Data

Yoshifumi Yasuoka*, Wataru Takeuchi*, Masayuki Tamura**

* Institute of Industrial Science, University of Tokyo
4-6-1 Komaba, Meguro, Tokyo 153-8505, Japan
E-mail: yyasuoka@iis.u-tokyo.a.jp, Phone: +81-3-5452-6409, Fax: +81-3-5452-6409

** National Institute for Environmental Studies
16-2 Onogawa, Tsukuba, Ibaraki 305, Japan
Phone +81-298-51-2543, Fax +81-298-51-4732

Abstract

Methane has high global warming potential and its increase may give a serious impact to our future climate and environment. Since wetland is one of the major emission sources of methane estimation of methane emission requires precise characterization of wetland conditions in global or continental scale. This study examined a remote sensing method to estimate methane emission from extensive wetland areas. A scaling method between high spatial resolution data (SPOT HRV) and coarse resolution but wide coverage data (NOAA AVHRR) was investigated to extrapolate local information on land cover mixture condition in wetland from HRV to more extensive area through AVHRR, and to estimate wetland coverage area more precisely. First, in SPOT data, land cover types of the area was classified into four categories including vegetation, water, and two types of bogs which are sources of methane, and next AVHRR image density was statistically regressed with category mixture ratio derived from HRV pixels in each AVHRR pixel. This scaling model from regression analysis provides wetland coverage ratio in sub-pixel level only from AVHRR data. The method was applied to western Siberian wetland, and total emission of methane was calculated by multiplying estimated bog areas with unit emission rate of methane in each bog types.

1. Introduction

Methane is one of the major green house gases. Since its global warming potential is very high estimation of methane from different sources is now one of the urgent tasks in tackling with global warming. Wetland is known as a major emission source of methane, and estimation of methane emission requires precise assessment of wetlands in global or continental scale. It is, however, not easy to investigate wetland area only with ground observation because it is usually extensive and difficult to get in. Remote sensing of wetland from satellite may provide an efficient tool to monitor wetland conditions and to delineate wetland from other land cover categories.

There have been several studies to produce land cover maps of individual wetlands by using high spatial resolution data from LANDSAT MSS, TM, SPOT HRV or JERS-1 SAR (e.g., Federal Geographic Data Committee 1992). High spatial resolution data is effective to monitor wetland environment in local or regional scale, however, it may not cover an extensive area because of its narrow coverage. Extending the area would require to use wide coverage data from NOAA AVHRR or TERRA MODIS. Normalized Difference Vegetation Index (NDVI) from AVHRR, for example, has

been successfully utilized to monitor vegetation conditions in continental or global scale (e.g., Tucker et al. 1995; Defries et al. 1995). However, on the other hand, AVHRR data may not detect fine spatial structures in mixtures of vegetation, water and soil in wetland areas because of its coarse resolution (1.1km). For example, when we simply classify vegetated wetland with AVHRR data pixels tend to be classified into forest even though wetland (water surface) covers 30% of the area in a pixel.

In this study a scaling technique between high spatial resolution (narrow coverage) data and low spatial (wide coverage) data is investigated to unmix each pixel in low spatial resolution data into different land cover categories including wetland (bog), forest and soil, and to estimate the area cover ratio of wetland in each pixel. A scaling model relates high spatial resolution data with coarse resolution data, and to extrapolate the local knowledge derived from high spatial resolution data to global scale (Iverson et al. 1989; Hlavka et al. 1995; Yasuoka et al. 1996).

Western Siberian wetland was selected as a test site since it is one of the biggest wetland in the world, and is recognized as a high potential area for methane emission due to global warming. Here, NOAA AVHRR and SPOT HRV around Plotnikovo were used to formulate a scaling model between them, and total methane emission from AVHRR area was calculated from the methane emission rates for two different types of bogs observed on the ground and from the estimated area ratio of two bog types.

2. Scaling between AVHRR and HRV

Synchronously observed data from SPOT/HRV and NOAA/AVHRR of July 7th, 1995 over Plotnikovo in western Siberian were geometrically corrected and overlayed so that one pixel of AVHRR covers a set of HRV pixels in a rectangular block of 50x124. Here, spatial resolution of one pixel of AVHRR is around 1.1km and that of HRV is around 20m. Figure 1 shows AVHRR (Fig.1 (a)) and HRV (Fig.1 (b)) images over the common area after registration. In Figure 1 image density of each pixel presents the Normalized Difference Vegetation Index (NDVI) whose value is calculated from Channel 1 and 2 for AVHRR and from Channel 2 and 3 for HRV respectively. The regression analysis shows high correlation between NDVI values for each AVHRR pixel and average NDVI values for corresponding HRV block pixels in 50x124 (r=0.93) and indicated good registration between them.

(a) NDVI image from NOAA AVHRR (b) NDVI image from SPOT HRV

Fig.1 Image overlay between NOAA AVHRR and SPOT HRV over Plotnikovo (1995/7/7).

Scaling model between NOAA AVHRR and SPOT HRV was investigated to unmix each pixel of AVHRR and to estimate the wetland coverage ratio among other land cover categories. First, each pixel of SPOT HRV was classified into four categories including bog1, bog2, forest and soil by using

supervised classification (Fig. 2). Here bog1 and2 represent wetland and are subject to the estimation of methane emission. The average emission rates of methane for bog1 and bog2 were provided based on ground observation (Tamura, et al., 1995). The difference between two types of bogs is mainly characterized by water depth. Then image density of AVHRR channel 1, 2 and 3 were correlated with the coverage ratios for each category mixing ratio of bog1, bog2, forest and soil using least squares method. The linear equations obtained with high correlation are Eqs. 3, 4 and 5 as follows.

$$AV\_1 = 34.7\,F + 60.0\,S + 23.8\,B1 + 29.2\,B2, \quad r^2 = 0.63 \qquad (1)$$
$$AV\_2 = 111\,F + 132\,S + 145\,B1 + 173\,B2, \quad r^2 = 0.87 \qquad (2)$$
$$AV\_3 = 87.0\,F + 96.7\,S + 42.3\,B1 + 55.7\,B2, \quad r^2 = 0.62 \qquad (3)$$

where F, S, B1 and B2 represent the area coverage ratio (percentage) for forest, soil, bog1 and bog2 and they satisfy the next equation.

$$F + S + B1 + B2 = 1 \qquad (4)$$

These relations indicate that the category mixing ratio (F, S, B1, B2) can be solved inversely from Eqs. (1) – (4) only from the AVHRR image density for the area where no SPOT data covers. The scaling model enables us to extrapolate the local information (category mixing ratio) from SPOT HRV to more extensive area by using NOAA AVHRR data once the equations are obtained over the common areas for AVHRR and HRV.

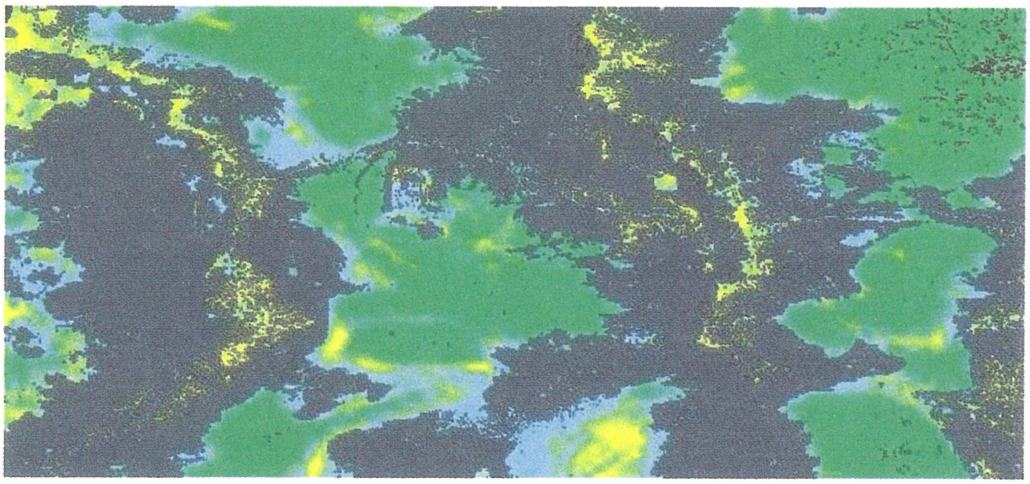

Fig. 2 Land cover classification from SPOT HRV data
(Forest: green, Soil: grey, Bog1: blue, Bog2: yellow)

3. Estimation of Methane Emission from West Siberian Wetland

Each category mixing ratio F, S, B1 and B2 for forest, soil, bog1 and bog2 was estimated over a whole target area by applying equations (1) – (4) to AVHRR data. Figure 3 demonstrate each category mixing ratio (area percentage) image for forest (a), soil (b), bog1 (c) and bog2 (d) where the brighter color shows the higher percentage of category cover.

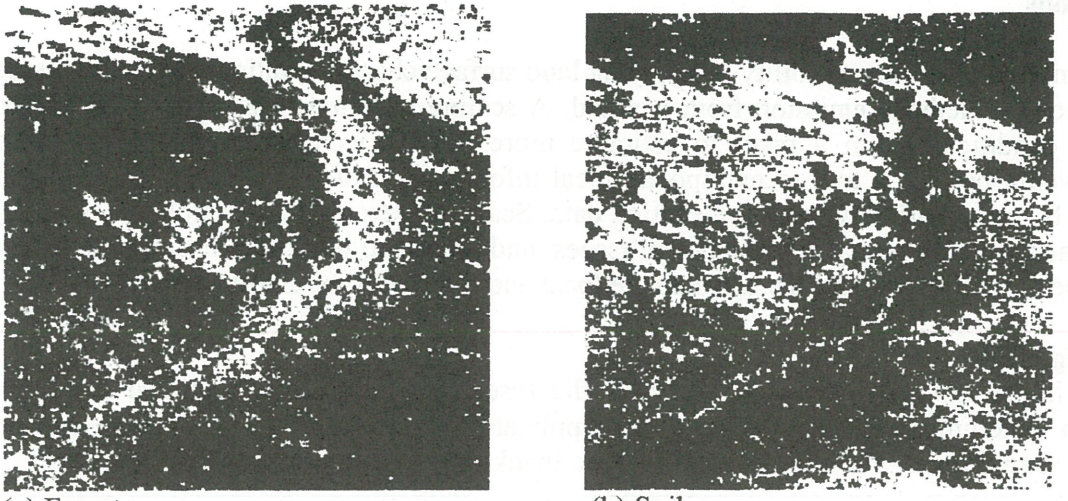

(a) Forest (b) Soil

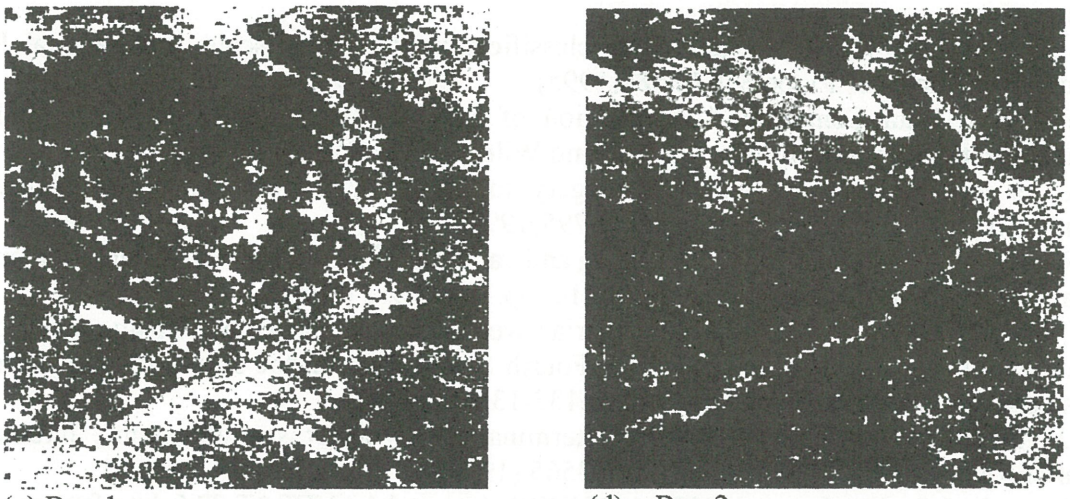

(c) Bog 1 (d) Bog 2

Fig. 3 Estimated category mixing ratio image for each category.

Finally the methane emission from the area was estimated by multiplying the average methane emission rate observed at ground and the area percentage of Bog1 and Bog2 in each pixel. Table 1 summarizes the emission of methane from the wetland.

Table 1 Estimated methane emission from western Siberian wetland around Plotonikovo.

Land cover	Area (10^3km^2)	Emission rate (mg/m^3/day)	Methane flux (10^9g/day)
Forest	113.0	0	0
Soil	75.2	0	0
Bog1	79.2	118	93.5
Bog2	35.1	166	58.3
Total	302.5		151.8

4. Conclusions

This study investigated the possibility of applying land surface characterization with remote sensing to the estimation of methane emission from wetland. A scaling technique was applied to unmixing of land cover condition within a pixel to estimate more precise wetland area coverage. A scaling technique would provide a tool to extrapolate local information from high spatial resolution data to larger scale by using with low spatial resolution data. Scaling up from local to global is one of the key aspects in tackling with global environmental issues, and a method proposed in this study is expected to play a role in realizing the bridge between the local and the global in remote sensing.

Acknowledgement
This study is partially carried out as a part of the research project "An integrated study on Earth Observation Satellite Data Network and its Application" sponsored by the Japan Science and Technology Corporation. The authors would like to thank the JST for their support.

References

Defries,R.S., et al.," NDVI-derived land cover classification at a global scale. International Journal of Remote Sensing", vol.15, pp.3567-3586(1995).

Federal Geographic Data Committee," Application of satellite data for mapping and monitoring wetlands", Wetland Subcommittee. US.Fish and Wild Service (1992).

Hlavka,C.A., et al., " Unmixing AVHRR imagery to assess clear cuts and forest regrowth in Oregon", IEEE Trans. GRS. vol.33, pp788-795(1995).

Iverson, L.R., et al.," A technique for extrapolating and validating forest cover across large regions", International Journal of Remote Sensing, vol.10, pp.1805-1812 (1989).

Tamura, M,. et al., " Observation of western Siberian wetlands by using remote sensing technique for estimating methane emission", Proc. of the Fourth Symposium on the Joint Siberian Permafrost studies between Japan and Russia in 1995, pp133-138.

Tucker, C.J., et al.," AVHRR data sets for determination of desert spatial extent", International Journal of Remote Sensing, vol.15, pp.3547-3565 (1995).

Yasuoka, Y., et al., " Scaling between NOAA AVHRR data and LANDSAT TM data for monitoring and mapping wetland", International Symposium on Vegetation Monitoring, pp.131-136 (1995).

Yasuoka, Y., et al, " Application of Remote Sensing to Environmental Monitoring - Wetland Monitoring", Optical Methods in Biomedical and Environmental Sciences (H. Ohzu and S. Komatsu eds.), Elsevier, pp269-272 (1994).

Relationship between NOAA/AVHRR-derived NDVI, Rainfall and Air Temperature for Diverse Vegetation Types in East Asia: I. NDVI vs. Rainfall

Eleonora Runtunuwu*, Akihiko Kondoh, Agung Budi Harto*, Teguh Prayogo*, and Shen Yanjun***
***Graduate School of Science and Technology, Chiba University**
****Center for Environmental Remote Sensing, Chiba Unive1rsity**
1-33 Yayoi Inage Chiba 263-8522, JAPAN
nora@ceres.cr.chiba-u.ac.jp

Abstract

This paper attempts to investigate the relationship between satellite phenology of NOAA/AVHRR-derived Normalized Difference Vegetation Index (NDVI) and rainfall based on vegetation types with study case in East Asia for a specified time period of January 1986 to December 1993. The study examines the relationships of these variables on annual and time series monthly data using both linear and non-linear regression and correlation analysis. The NDVI and rainfall associations are analyzed for twelve vegetations types: deciduous broadleaf forest, evergreen coniferous forest, evergreen broadleaf forest, mixed forest, forest and field, farmland, irrigated crop, grassland, savanna, shrub, semi desert and desert. Based on the relationship between annual integrated NDVI and mean annual rainfall, it seemed there is a marked similarity in regional or spatial structure between the both variables for whole region, but a number of important differences are apparent in the time series analyses. The range of integrated NDVI value, mean annual rainfall, timing of the NDVI response to rainfall, regression slope, and rain-green ratio are clearly demonstrated the differences among the vegetation types.
Keywords: NOAA/AVHRR, NDVI, rainfall, vegetation, and East Asia.

INTRODUCTION

The study of relationship between vegetation and rainfall is very important, especially in research of land cover and climate change, since changes that occur on ground surface, such in vegetation, could be associated with changes of climatic parameter including rainfall. An alternative way to obtain the existing vegetation distributions is by means of NDVI, which is generated from red and near-infrared (NIR) reflectances of satellite sensor by the following equation: (NIR-red)/(NIR+red). Thus, high values of this index are obtained for areas covered by green vegetation and low values for unvegetated and cloud covered areas. Recently, the NDVI has been related to many aspects of environment, for example, seasonal and annual evapotranspiration (Kondoh, 1995), radiation energy budget (Ackerman and Inoue, 1994), air temperature (Gallo, et al. 1993), simulated photosynthesis and transpiration of forests (Running and Nemani, 1988), and so on.

There were many studies on relationship between rainfall to NDVI such as in East Africa (Davenport and Nicholson, 1993), Bostwana (Nicholson and Farrar, 1994), Sahel (Milich and Weiss, 2000), Amazon and Northeastern Brazil (Santos and Negri, 1997), China (Lu, et al. 2000), and also in global scale (Schultz and Halpert, 1995). From those studies, the relation of precipitation and NDVI is complex, such as reported by Kerr, et al. (1989) that its relationship was linear in Senegal, while by Lu et al. (2000) the relationship was quadratics in China. Additionally, Milich and Weiss (2000) found that the relationship was inconsistent from year to year in Sahel, Africa. However, the NDVI and rainfall relationship has not yet been investigated in East Asia, which has extremely different characteristics of environmental variables. For an example, Kondoh (1995) found out that China was distributed not only by subtropical crops but also by tropical one.

The purpose of this paper is to investigate the relationship between NDVI, rainfall, and air temperature for various vegetations in East Asia that covers Japan, Korea, Taiwan, China, and Mongolia. Present study is concerning response NDVI to rainfall in both annual and monthly time series data. A similar study for NDVI versus air temperature has been carried out following this study, which presented in part II.

METHODS AND DATA

This study analyzed NDVI versus rainfall for various vegetation types in East Asia region within the specified eight-year period (January 1986 - December 1993). Both linear and non-linear regression models were utilized for annual and monthly time series data.

To achieve the goal of this study, three main input data were required, namely NDVI, rainfall, and vegetation data with the same punctual and temporal scale. Therefore, the latitude and longitude

coordinates of the climatic stations derived from Global Surface Summary of Day database (http://www.ncdc.noaa.gov) as shown in **Figure 1** has been correlated with nearest pixels of the land cover/vegetation maps, as well as the monthly time series of NDVI and rainfall maps in order to obtain their values of each climatic station. To be consistent with the whole datasets, all of the image data have been resampled to 0.5x0.5° spatial resolution covering East Asia region and re-projected on a linear latitude longitude grid.

The monthly NDVI data was derived from Time Series of 0.144° Global Monthly Vegetation Cover from NOAA/AVHRR CD-ROM Ver. 1.0. These data were provided and processed by NOAA/NCDC, which have been collected by the AVHRR onboard the NOAA-9 (April 1985-November 1988), NOAA-11 (November 1988-September 1994), and NOAA-14 satellites (February 1995-December 1997). Detail information of this data set is available on http://perigee.ncdc.noaa.gov.

The monthly rainfall data were obtained from The Climatic Research Unit, University of East Anglia, namely CRU05 0.5 Degree Monthly Climate Time-Series (1901-1995) CD-ROM, Ver.1. April 1999. Beside the rainfall data, the dataset consists of other climatic data such as air temperature (that was used in Part II), cloudiness, wind speed, vapor pressure, etc. Further information of these dataset can be found from http://ipcc-ddc.cru.uea.ac.uk.

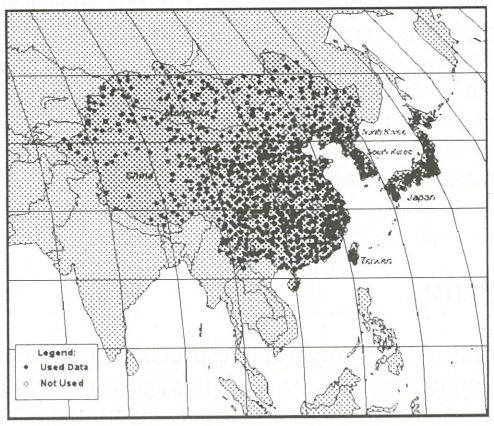

Figure 1.
The 1064 climatic stations distributed in East Asia (referred to Global Summary of Day database).

Three well-known one kilometer global land cover maps were used to identify the vegetation types of all the climatic stations. They are Olson Global Ecosystems (1994a, 1994b), United States Geological Survey (USGS) Land Use/Land Cover System (Anderson, et al. 1976), and Biosphere Atmosphere Transfer (BAT) Scheme (Dickinson, et. al.1986). These maps are accessible on the following site: http://edcwww.cr.usgs.gov. There is a slight different distribution of plant formations among these maps; therefore, this study used only several selected vegetation types in which all of the three maps above agree that a given vegetation type is present. The twelve selected vegetation types are deciduous broadleaf forest (16 stations), evergreen coniferous forest (22 stations), evergreen broadleaf forest (11 stations), mixed forest (50 stations), forest and field (15 stations), farmland (217 stations), irrigated crop (198 stations), grassland (183 stations), savanna (33 stations), shrub (26 stations), semi desert (54 stations) and desert (25 stations). These vegetation types could be clustered into five major phytomes of Olson's classification (Olson, 1989) namely, forests, woods, crops, grasses, and desert. From all 1064 distributed climatic stations in area study, 850 stations were found for further NDVI-rainfall analysis. The urban (18 stations) and wetland/inland water (78 stations) were excluded because the NDVI value are more representative to vegetated rather than unvegetated area. Additionally, the 118 remains stations were not used since there is no agreement of the vegetation type among the three land cover maps above.

RESULTS AND DISCUSSION

General Relationship between NDVI and Rainfall

Figure 2 (a, b, and c) shows the annual integrated NDVI (defined as the total of the twelve monthly values), the mean annual rainfall, and the vegetation distribution, respectively. The high rainfall (more than 1000 mm/year) distributes in Japan, east part of Korea, east and south part of China, and Taiwan, and it noticeably corresponds to high NDVI values more than 3.0. This is also consistent with the **Figure 2c,** which shows that the main vegetation of this area is forests and woods. The lower NDVI (around 2.0 – 3.0) are distributed in north Mongolia, west Korea, a little part in Japan (Kanto area), Taiwan and middle part of China. Not surprisingly, since crops and grasses dominates those areas, with mean annual rainfall

around 500-1000 mm/year. The lowest NDVI of less than 1.5 is concentrated in west China and south Mongolia, with rainfall less than 300 mm/year. Clearly, semi desert and desert are fairly dominated those area. Some places like Taiwan and west Korea have a high rainfall every year but the NDVI is lower; it matches with the vegetation of this area that is cropland (**Figure 2c**).

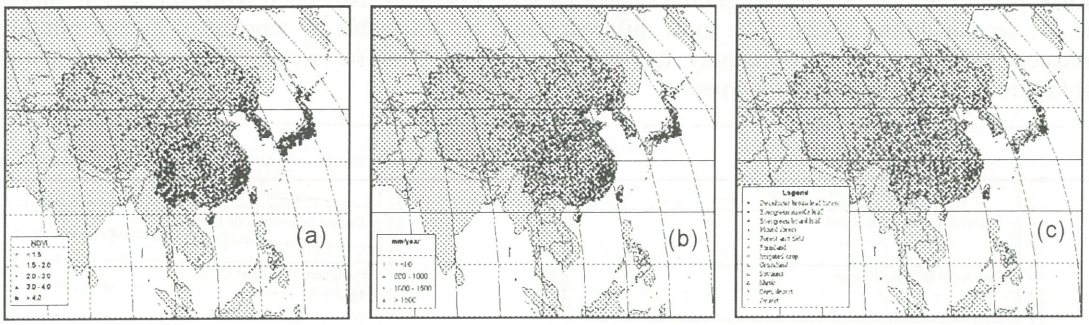

Figure 2.
Distribution of (a) annual integrated NDVI, (b) mean annual rainfall, and (c) vegetation types.

The correlation between the annual integrated NDVI and mean annual rainfall is illustrated in **Figure 3** that shows the relationship based on all 850 stations. The relationship characteristic is exponential with r is 0.74. In areas with annual rainfall less than 1000 mm per year or 80 mm per month, the integrated NDVI and mean annual rainfall is linearly correlated, although the variance is large. In contrast, in areas with annual rainfall greater than 1000 mm per year or 80 mm per month, NDVI saturates and there was no relationship between both variables. This result points out the NDVI relates to changing patterns of rainfall in dry climates, while it is not in wet region. Therefore, the NDVI might be a sensitive indicator of rainfall only in drier climates. In other explanation, when the rainfall increases, the canopy becomes dense, and NDVI values increase until the threshold value is reached. On that time, the NDVI remains constant although increasing rainfall. It means, rainfall is no longer as the limiting factor in plant growth that is other experimental variables become increasingly important.

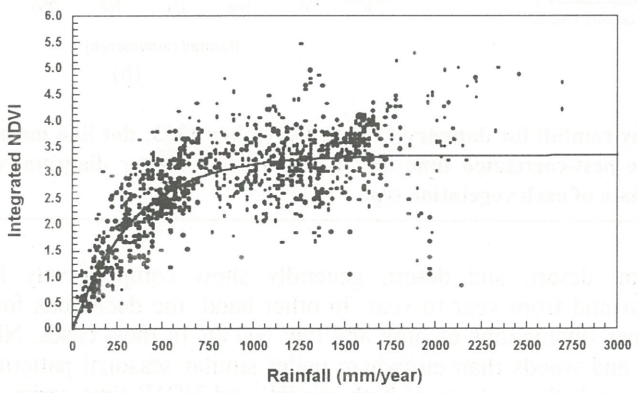

Figure 3.
Scatter plots of annual integrated NDVI versus mean annual rainfall; the solid line is approximate best fit of dataset.

Vegetation Types, Monthly NDVI and Rainfall

Differences in the timing of the NDVI response to rainfall could be used to understand the NDVI-rainfall relationship among the various types of vegetation. Thus, for each of the twelve vegetation types, the linear correlation has been computed between time series monthly NDVI versus rainfall in various averaging periods. The correlations were utilized between concurrent monthly values of NDVI with the rainfall data for the same month (0), previous month (1), two previous month (2), average concurrent and previous month (0+1), average one and two previous month (1+2), and average concurrent plus two preceding months (0+1+2). As shown in **Table 1,** the correlation generally is highest in concurrent and previous month (0+1), and low with the one (1) or two previous months (2) alone. This is slightly different with the results of Nicholson and colleagues, which noted the correlation is highest with three-months average rainfall (0+1+2), although they are not directly comparable, since both areas have a

contrasting different type of environmental parameters. In addition, for dense canopy like forests and woods, the time lag is varied from 0 to 0+1+2, while for cropland, grasses, and semi desert is immediate (0+1). It suggests the NDVI appears to respond rapidly in rare canopy rather than the dense one.

The relationship between NDVI and seasonal cycle of rainfall is examined in **Figure 4a**; comparing time series plots of monthly NDVI and rainfall from 1986 to 1993 of each vegetation type. In general, the rainfall pattern is same for all vegetation types that have one peak associated with wet season, and also one dry season during a year. The most different could be noticeable by amount of annual rainfall as indicated in **Table 1**. Not surprisingly, that the dense canopy (forests, woods) show higher amount of rainfall from the other vegetation types.

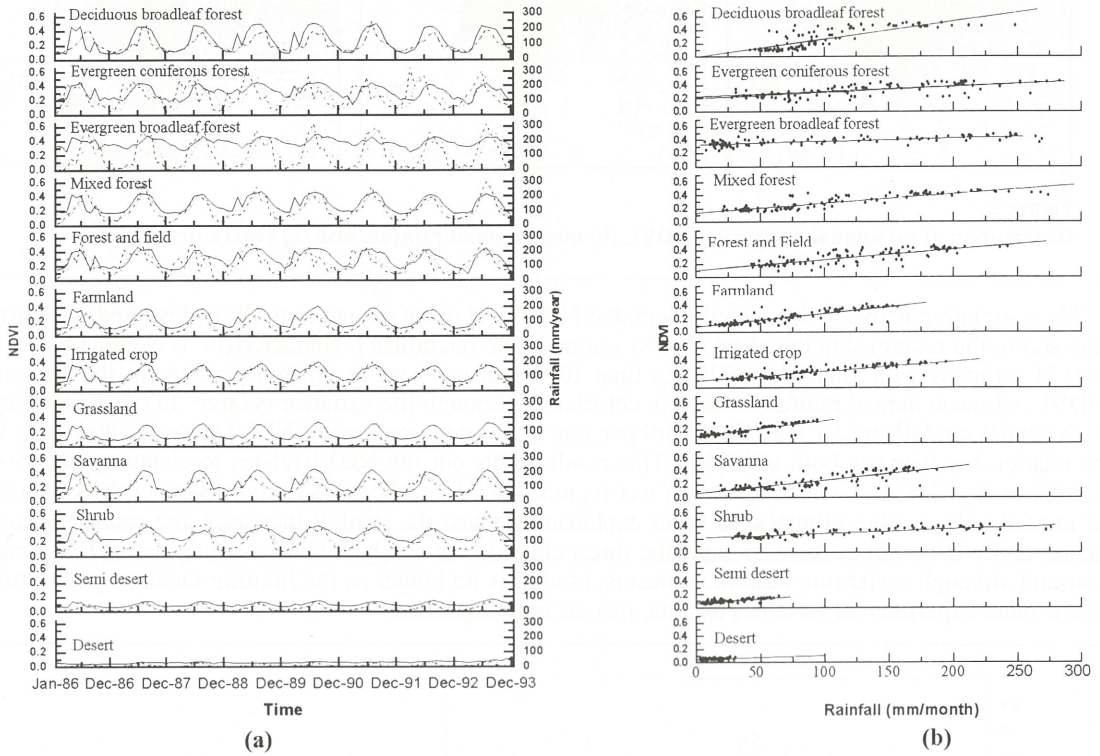

Figure 4.
(a) Time series of monthly NDVI versus rainfall for January 1986 to December 1993; dot line means mean rainfall and dash line means the best-correlated time lag of rainfall. (b) Scatter diagrams of monthly NDVI and Rainfall for whole data of each vegetation type.

Evergreen broadleaf forest, shrub, semi desert, and desert, generally show comparatively little interannual NDVI variability during a year and from year to year. In other hand, the deciduous forest, crops, and grasses exhibit large year to year fluctuations of high and low NDVI. In most cases, NDVI appears to be somewhat higher in forests and woods than elsewhere under similar seasonal patterns of rainfall. In deciduous broadleaf forest, the peak fluctuations of both rainfall and NDVI time series data are well correlated, showing no lag response of NDVI to rainfall; whereas, in other vegetations, such as evergreen coniferous forest, evergreen broadleaf forest, etc., the vegetations show lag response to rainfall. It seemed consistent with the time lag analyses as given in previous paragraph or in **Table 1**.

Scatter diagrams of NDVI versus rainfall **(Figure 4b)**, using the best-correlated rainfall parameter as indicated in **Table 1**, illustrated the relationship more detail**.** The ranges of rainfall as well as NDVI in forests, woods, and shrub, are quite large compared to crops, and other grasses. Desert groups show the narrowest one. Owing to a highly relationship, polynomial order-1 to -4 and exponential analysis were fitted to NDVI and rainfall data for each vegetation type as a whole. It appeared the polynomial order-1 (linear), -2 (quadratic), -3, and exponential analysis gave significant (correlation coefficient was more than 0.65; except desert was 0.38) and approximately same correlations, while polynomial-4 fit gave a marginal improvement over other curves. It seemed that the statistics analysis was unrevealable the diverse natural trend of the vegetations, as reported by Gupta, et al. (2000). Thus, the relationship between NDVI and rainfall of each vegetation type is adequately shown by linear regression, even though they have considerably different regression slopes among those vegetations as presents in **Figure 4b** and

Table 1.

A simple `rain-green ratio` parameter (defined as the rate of primary productivity per unit rainfall or the amount of above-ground phytomass produced per hectare per year per millimeter of rain) has been computed in this study. This parameter is analogues to rain use efficiency, which noted as ratio of mean annual integrated NDVI to mean annual rainfall. The low value indicates wetter regions, while the high one indicates dry land. As shown in **Table 1**, the lowest ratio is in dense canopy, such as deciduous broadleaf, evergreen coniferous, evergreen broadleaf forest, mixed forest, and forest and field. Irrigated crop, savanna and shrub are also relatively low, while it is high in dry land vegetation such as semi desert, desert, and grassland.

Table 1.
Summerized of the differences among vegetation types

Vegetation	NDVI	Rainfall	Time-lag	r	Slope (x1000)	NDVI/ Rainfall
Forests						
Deciduous broadleaf	3.27	1235	0, 0+1	0.8016	2.6	2.65
Evergreen coniferous	3.86	1587	1+2	0.6436	0.9	2.43
Evergreen broadleaf	4.63	1249	0+1+2	0.6930	0.5	3.70
Woods						
Mixed forest	3.56	1323	0+1	0.8757	1.4	2.69
Forest and field	3.63	1472	0+1+2	0.7858	1.6	2.47
Crops						
Farmland	2.73	853	0+1	0.8444	1.9	3.20
Irrigated crop	2.86	1120	0+1	0.8353	1.4	2.55
Grasses						
Grassland	2.19	401	0+1	0.8588	2.3	5.48
Savanna	3.04	1115	0+1	0.8104	2.0	2.73
Shrub	3.64	1352	0+1	0.7265	0.7	2.70
Desert						
Semi desert	1.24	293	0+1	0.7878	1.3	4.22
Desert	0.74	130	1, 0+1+2	0.3831	0.5	5.72

r is based on linear regression analyses.

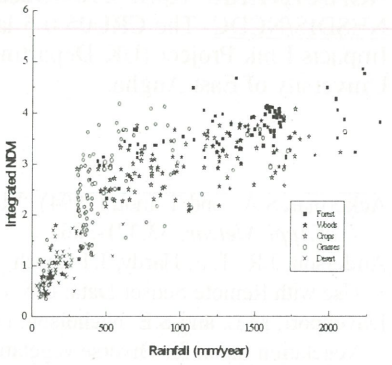

Figure 5.
Relationship between integrated NDVI and rainfall corresponding to five major phytomes for several representative stations.

CONCLUSION

Several analyses were carried out in order to illustrate the relationship between NDVI and rainfall for East Asia. Firstly, determination of the regional relationship between annual integrated NDVI and mean annual rainfall to understand the general relationship for this region as a whole, and then investigation their temporal relationship based on monthly time series data for January 1986 to December 1993 for twelve diverse vegetation types in East Asia. Based on mean annual data, the relationship characteristic is exponential with r is 0.74. In areas with annual rainfall less than 1000 mm per year or 80 mm per month, the integrated NDVI and mean annual rainfall is linearly correlated, although the variance is large. In contrast, in areas with annual rainfall greater than 1000 mm per year or 80 mm per month, NDVI saturates and there was no relationship between both variables. This result points out the NDVI relates to changing patterns of rainfall in dry climates, while it is not in wet region. From this result, it seemed there is a marked similarity in regional or spatial structure between the both variables for whole region, however, a number of important differences are apparent in time series analyses of each vegetation type.

The integrated NDVI value is more than 3.27 for forests and woods; around 2.73 to 2.86 for crops, around 2.19 to 3.0 for grasses; and the lowest is less than 1.24 for desert. The rainfall for forests and woods is the highest, with more than 1400 mm/year. For crops and grasses, the rainfall is ranging from 400 to 1100 mm/year, while for desert zone has the least with less than 300 mm/year. It is generally about the same of rain green ratio in forests and woods, ranging from 2.43 to 2.69. The exception is evergreen broadleaf forest with exceedingly high NDVI; the ratio is 3.70. Crops have relatively low ratio, ranging from 2.55 to 3.20, as well for savanna and shrub is about 2.7. The highest ratio is in semi desert, desert, and grassland which has value more than 4.2.

The relationship between NDVI and rainfall of each vegetation type is adequately shown by linear regression, even though they have considerably different time lag and regression slopes. For dense canopy like forests and woods, the time lag is varied from 0 to 0+1+2, while for cropland, grasses, and semi desert is immediate (0+1). It suggests the NDVI appears to respond rapidly in rare canopy rather than the dense one. The high slope correlated to the vegetations that have similar fluctuations between

NDVI and rainfall within a year (i.e. deciduous broadleaf forest, grassland, and savanna). On the other hand, evergreen coniferous forest, evergreen broadleaf forest, shrub, and desert exhibited large different fluctuations between both variables that match with the low value of slope.

Considering the strong correlation between NDVI and rainfall as yielded in this study, the long-term relationship between both variables might be useful to monitor the land cover or vegetation change, and also could provide valuable inputs in a land cover classification of East Asia region.

ACKNOWLEDGMENTS

The authors deeply appreciate the producers of Time series of Global Monthly Vegetation Cover from NOAA/AVHRR: April 1985-December 1997. NOAA/NCDC. Published on CD-ROM by NOAA/NESDIS/NCDC. The CRU05 0.5 lat/lon gridded monthly climate data has been supplied by the Climate Impacts Link Project (UK Department of the Environment Contract EPG 1/1/16) on behalf of the CRU, University of East Anglia.

REFERENCES

Ackerman S.A., and T. Inou (1994). "Radiation Energy Budged using Collocated AVHRR and ERBE Observations", *J. of Appl. Meteor.,* 33,371-386.

Anderson, J.R., E.E. Hardy, J.T.Roach, R.E. Witmer. (1976). "A Land Use and Land Cover Classification System for Use with Remote Sensor Data: *U.S. Geological Survey Professional Paper 964*, 28 pages.

Davenport, M.L. and S.E. Nicholson. (1993). "On the Relationship between Rainfall and the Normalized Difference Vegetation Index for Diverse vegetation Types of east Africa," *Inter. J. of Remote Sensing*, Vol.14, pp.2369-2389.

Dickinson, R.E., A.H. Sellers, P.J. Kennedy, and M.F. Wilson. (1986). "Biosphere-Atmosphere Transfer Scheme (BATS) for the NCAR Community Climate Model": *NCAR Techn. Note NCAR/TN275+STR, Boulder, CO.* 69pages.

Gallo, K.P., A.L. McNab, T.R. Karl, Brown, J.F., Hood, Tarpley, J.D. (1993). "The use of NOAA AVHRR Data for Assessment of the Urban Heat Island Effect", *J. of Appl. Meteor.* ,32,899-908.

Gupta, R.K., T.S.Prasad, and D. Vijayan. (2000). "Relationship between LAI and NDVI for IRS LISS and LANDSAT TM Bands", *Adv.Space Res.* Vol. 26, No.7, pp.1047-1050.

Kerr, Y.H., I. Imbernon, G. Dedieu, O. Hautecoeur, J.P. Lagouarde, and B. Seguin. (1989). "NOAA AVHRR and Its Uses for rainfall and Evapotranspiration Monitoring", *Int. J. Remote Sensing,* vol.10, NOS. 4 and 5, pp.847-854.

Kondoh A. (1995). "Relationship Between the Global Vegetation Index and the Evapotranspirations derived from Climatological Estimation Methods", *J. of Japan Society of Photogrammetry and Remote Sensing*, 34,2,14p.

Lu, X.X. and D.L. Higgitt. (2000). "NDVI and Its Relationships with Hydrological regimes in the Upper Yangtze," *Canadian Journal of remote Sensing*, Vol.26, No.5, pp.418-427.

Milich, L. and E. Weiss. (2000). "GAC NDVI images: relationship to rainfall and potential evaporation in the grazing lands of The Gourma (northern sahel) and in the croplands of the Niger-Nigeria border (southern sahel)", *International Journal of Remote Sensing*, Vol. 21, No.2, pp.261-280.

Nicholson, S.E. and T.J.Farrar. (1994). "The Influence of Soil Type on the Relations between NDVI, Rainfall, and Soil-Moisture in the Semiarid Botswana: 1, NDVI response to Rainfall, *Remote Sens. Env.*, 50, No2, pp. 107-120.

Olson, J.S. (1989). "World Ecosystems (WE1.4) Digital Data", *NOAA/NGDC/WDC-A*, Colorado. 17 pages.

Olson, J.S. (1994a). "Global ecosystem Framework-definitions: USGS EROS Data Center International report", *Sioux Falls, SD*, 37 pages.

Olson, J.S. (1994b). "Global Ecosystem Framework-Translation Strategy: USGS EROS Data Center International Report", *Sioux Falls, SD*, 39 pages.

Santos, P. and A. Negri (1997). "A Comparison of the Normalized Difference Vegetation Index and Rainfall for the Amazon and Northeastern Brazil", *Journal of Applied Meteorology*, Vol. 36, pp.958-965.

Running, S.W., and R.R.Nemani. (1988), "Relating Seasonal Patterns of the AHRR Vegetation Index to Simulated Photosynthesis and Transpiration of Forests in Different Climates", *Remote sensing of Environ.*, 24, 347-367.

Schultz, P.A., and M.S. Halpert. (1995), "Global Analysis of the Relationships among a Vegetation Index, Precipitation, and Land Surface Temperature", *International Journal of Remote Sensing*", Vol 16, 15, 2755-2777.

Relationship between NOAA/AVHRR-derived NDVI, Rainfall and Air Temperature for Diverse Vegetation Types in East Asia: II. NDVI vs. Air Temperature

Eleonora Runtunuwu*, Akihiko Kondoh, Agung Budi Harto*, Teguh Prayogo*, and Shen Yanjun***
***Graduate School of Science and Technology, Chiba University**
****Center for Environmental Remote Sensing, Chiba University**
1-33 Yayoi Inage, Chiba 263-8522, JAPAN
nora@ceres.cr.chiba-u.ac.jp

Abstract

This paper is the continuation of the study of the relationship between satellite phenology of NOAA/AVHRR-derived Normalized Difference Vegetation Index (NDVI) and rainfall in East Asia. That study noted significant differences in NDVI-rainfall relationship for the diverse vegetation types. The current paper examined these differences whether can be explained by relationship between NDVI and air temperature. Therefore, the NDVI and air temperature associations were carried out with several regression analyses: (a) the relationship was analyzed by using a mean annual integrated NDVI and a mean annual air temperature for all 850 stations. It seemed the linear relationship is relatively weak ($r = 0.40$). However, when separated analyses were used with the monthly time series data of each station, their correlation coefficients were significant for a given stations, which varied from –0.80 to 0.87. (b) Based on mean time series NDVI and air temperature data of each vegetation type in period January 1986 to December 1993, the correlations were linearly significant ($r > 0.70$), except for desert area, r was only 0.49. In addition, when investigating the characteristics of the mean annual air temperature and time lag, we realized the vegetation types did not strongly differ with respect to air temperature analyses.
Keywords: NDVI, air temperature, vegetation, and East Asia.

INTRODUCTION

We expected the relationships between NDVI and air temperature could explore the differences of the vegetation types, since temperature variable has been common used as one potency input to classify the vegetation distribution over a given area (Leeman, 1990; Kira, 1945; Box's, 1981, etc), and also as one determinant variable of crop production especially in sub tropics (Malingreau, 1986).

Recently, the relationship between remotely sensed NDVI and temperature has been widely observed (e.g. Smith and Choudhury, 1990; Lambin and Ehrlich, 1996; Schultz and Halpert, 1995). Smith and Choudhury (1990) found out that in agricultural land use had significant inverse relationship between estimated radiant surface temperature and NDVI but no such relationships were evident for forests over Southeastern Australia. Lambin and Ehrlich (1996) noted that at broad spatial scales the existence of a negative land surface temperature (Ts) and NDVI relationship in water limited environments. In other hand, for vegetated surfaces (evergreen forests) the slope of the Ts-NDVI relationship is positive. Schultz and Halpert (1995) have shown that the relationship is high in the Northern hemisphere middle and high latitudes, because plant growth is significantly reduced in the winter months, due to decreased temperatures, shorter days, etc. The lower correlation exists in the sub tropics and tropics, partly since the minimum temperature for vegetative growth are exceeded for a greater portion of the year. Negative correlations occur in far eastern Brazil, the Sahel, India, Australia, and parts of Southeastern Asia. Goward et al (1985), Nemani and Running (1989), Hope and McDowell (1992), and Choudhury (1994) also showed the negative relationship between both variables.

Following those research evidences, the purpose of this paper is to investigate the relationship between NDVI and air temperature for diverse vegetation types in East Asia region. The vegetation considered are as in Part I: deciduous broadleaf forest, evergreen coniferous forest, evergreen broadleaf forest, mixed forest, forest and field, farmland, irrigated crop, grassland, savanna, shrub, semi desert and desert.

METHODS AND DATA

This study utilizes 850 stations for the eight years period January 1986 to December 1993 as described in Part I. The statistical analyses were applied to obtain the relationships between NDVI and air temperature based on the annual and monthly time series data.

The NDVI data was derived from Time Series of 0.144° Global Monthly Vegetation Cover from NOAA/AVHRR CD-ROM Ver. 1.0, which provided by NOAA/NESDIS/NCDC (http://perigee.ncdc.noaa.gov.).

The vegetation types were derived from three global land cover maps are Olson Global Ecosystems (Olson, 1994a, 1994b), United States Geological Survey (USGS) Land Use/Land Cover System (Anderson, et al. 1976), and Biosphere Atmosphere Transfer (BAT) Scheme (Dickinson, et. al.1986). Details of these maps are accessible in http://edcwww.cr.usgs.gov.

The Climatic Research Unit at University of East Anglia provides the monthly air temperature data in CRU05 0.5 Degree Monthly Climate Time-Series (1901-1995) CD-ROM, Ver.1. April 1999.

For consistent, we resampled the monthly temperature, rainfall, vegetation and NDVI images, for ten minutes spatial resolution, and then corresponded with coordinates of each climatic station from Global Surface Summary of Day database (http://www.ncdc.noaa.gov) over East Asia region.

RESULTS AND DISCUSSION

General Relationship between NDVI and Air Temperature

Figure 1 shows the eight years mean annual integrated NDVI, mean annual air temperature, and the distribution of vegetation types for all 850 climatic stations in East Asia. Glance at these figures, there is a good corresponding between the NDVI and vegetation maps as noted in Part I; but it is relatively not with air temperature map. As an example, the desert area from the **Figure 1c** is discretely distributed in west China and south Mongolia, with specific NDVI is less than 1.5 **(Figure 1a)**. From the **Figure 1b**, the mean annual temperature of this region is ranging from 0-15°C that in fact could be found in other vegetation types and places such as in crops areas (northern part of China) or in forests area (northern part of Japan). We realized that the air temperature maps was more influenced by latitudinal effect, rather than by vegetation distributions.

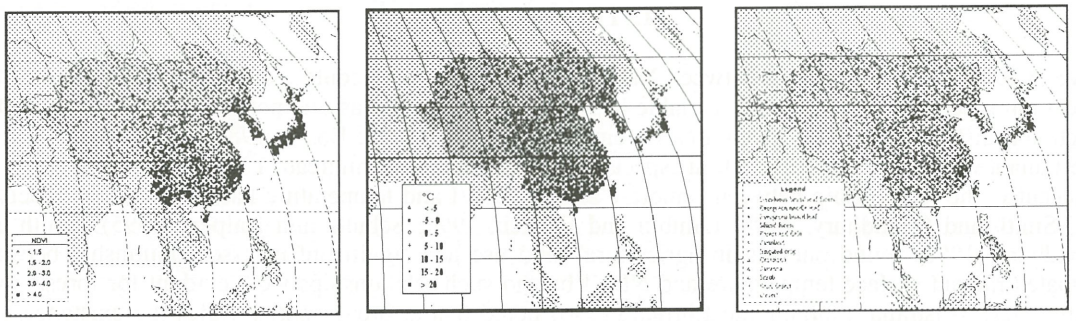

Figure 1.
Distribution of (a) annual integrated NDVI, (b) mean annual air temperature, and (c) vegetation types in East Asia.

Figure 2 illustrates the relationship between the annual integrated NDVI and mean annual air temperature for all 850 climatic stations. There is no apparent relationship between both variables; the correlation coefficient was 0.40. To further verify this result, the relationship between NDVI and air temperature were analyzed based on monthly time series data of each station (not shown). Negative correlation coefficients were merely distributed in deserts area of China. It matches with the result of Lambin and Ehrlich (1996) that the area in water limited environments has a negative correlation. The positive lower correlations (less than 0.40) occur in surrounding arid area, and tend to be a higher positive in the vegetated area of forests, woods, and crops in north Mongolia, east China, Korea and Japan. It was interesting that a vegetated part of China (Mengla, Mengwang, Ruili, etc.) has positive correlations less than 0.40. We realized that this area is boundary with the tropics, which perhaps has low NDVI-temperature relationship.

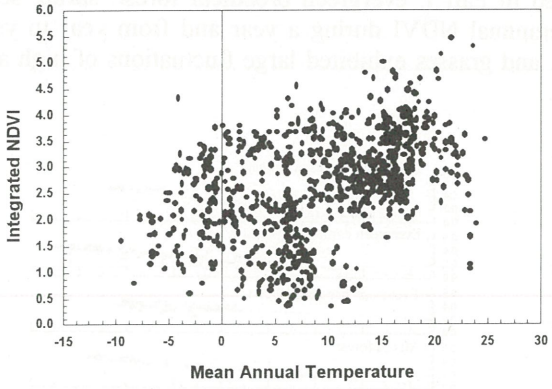

Figure 2. Scatter plots between integrated NDVI versus mean annual temperature (°C) for 850 stations in the study area.

Vegetation Types, Monthly NDVI and Air Temperature

The NDVI responded to air temperature based on differences of time lag has been demonstrated by analyzing the correlations between concurrent monthly NDVI and air temperature for the same month (0), previous month (1), two previous month (2), average concurrent and previous month (0+1), average one and two previous month (1+2), and average concurrent plus two preceding months (0+1+2), as shown in **Table 1**. In general, the NDVI responds to air temperature in time lag of 0. It means the NDVI of a given month is very influenced by air temperature of the same month. The exception is evergreen broadleaf forest with time lag of 2. The time lag of grassland and semi desert is 0+1, even though its r-value is no significantly different with time lag of 0. However, a precise lag cannot be determined since the data used here were monthly, and it may be happened within less than one month.

Table 1.
Linear correlation between monthly NDVI and air temperature for each vegetation type in various time lags. The underline value denotes the r coefficient for one type vegetation as a whole, while the bold value indicates the highest one for the representative station.

Vegetation type	0	1	2	0+1	1+2	0+1+2
Forests						
Deciduous broadleaf forest	0.87	0.75	0.43	0.84	0.61	0.75
- Pungsan, Korea	**0.84**	0.77	0.49	0.83	0.65	0.77
Evergreen coniferous forest	0.75	0.69	0.45	0.75	0.59	0.70
- Tai Ning, China	**0.75**	0.63	0.36	0.72	0.51	0.64
Evergreen broadleaf forest	0.42	0.65	0.73	0.55	0.72	0.66
- Jiangchen, China	0.24	0.53	**0.71**	0.41	0.65	0.55
Woods						
Mixed forest	0.85	0.72	0.39	0.82	0.58	0.72
- Jiuhailai, China	**0.79**	0.68	0.40	0.77	0.56	0.69
Forest and field	0.83	0.68	0.35	0.78	0.53	0.68
- Kuocangs, China	**0.81**	0.66	0.36	0.76	0.53	0.67
Cropland						
Farmland	0.87	0.76	0.44	0.84	0.62	0.76
- Iwamizawa, Japan	**0.85**	0.71	0.38	0.81	0.57	0.71
Irrigated crop	0.87	0.73	0.38	0.83	0.57	0.72
- Kuang Yua	**0.85**	0.69	0.36	0.80	0.54	0.70
Grasses						
Grassland	0.80	0.78	0.56	0.82	0.69	0.78
- Nangqen, China	0.75	0.77	0.59	**0.79**	0.71	0.78
Savanna	0.85	0.74	0.45	0.82	0.62	0.75
- Sanchenfa, Mongolia	**0.83**	0.76	0.49	0.82	0.65	0.76
Shrub	0.78	0.74	0.50	0.79	0.64	0.74
- Karuizawa, Japan	**0.81**	0.71	0.39	0.79	0.57	0.70
Desert						
Semi desert	0.74	0.75	0.56	0.77	0.68	0.75
- Ulangom, Mongolia	0.76	0.73	0.49	**0.77**	0.64	0.73
Desert	0.00	0.15	0.26	0.08	0.21	0.15
- Shiquanhe, China	0.13	0.34	**0.46**	0.24	0.41	0.34

Figure 3a shows the relationship between NDVI and the seasonal cycle of air temperature data from 1986 to 1993 for twelve vegetation types. As noted in Part I, evergreen broadleaf forest, shrub, semi desert, and desert comparatively showed little interannual NDVI during a year and from year to year variability, while deciduous broadleaf forest, crops, and grasses exhibited large fluctuations of high and low NDVI within a year.

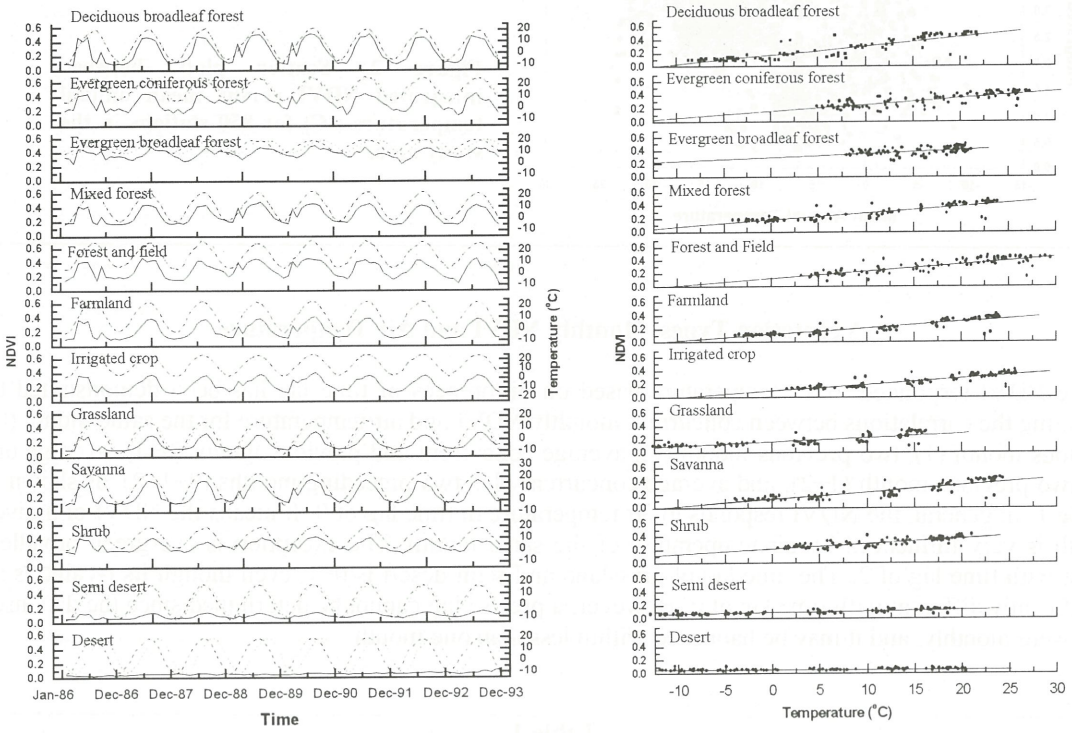

(a) (b)

Figure 3.
(a) Time series of monthly NDVI versus temperature for January 1986 to December 1993; dot line means mean temperature and dash line means the best correlated of time lag. (b) Scatter diagrams of monthly NDVI and temperature for whole data of each vegetation type.

As a characteristic of subtropics, the seasonal cycle of air temperature data showed apparent large interannual variability during a year for all vegetation types, except the evergreen broadleaf forest. As we expected, this vegetation is distributed in tropics boundary of south China (Mengla, Meng Wang, Ruili, etc), which has a little air temperature variability in a year.

Table 2.
Correlation coefficient (r) between monthly NDVI and air temperature computed using various analysis

Vegetation type	Linear	Quadratic	Polynomial-3	Polynomial-4	Exponential
Deciduous broadleaf	0.8669	0.8698	0.8732	0.8746	0.8659
Evergreen coniferous	0.7475	0.7490	0.7580	0.7580	0.7459
Evergreen broadleaf	0.7243	0.7246	0.7248	0.7312	0.7246
Mixed forest	0.8538	0.8592	0.8626	0.8634	0.8517
Forest and field	0.8253	0.8285	0.8340	0.8347	0.8280
Farmland	0.8644	0.8756	0.8756	0.8757	0.8620
Irrigated crop	0.8670	0.8686	0.8690	0.8690	0.8657
Grassland	0.8191	0.8560	0.8611	0.8621	0.8164
Savanna	0.8434	0.8667	0.8668	0.8676	0.8406
Shrub	0.7785	0.7862	0.7862	0.7863	0.7747
Semi desert	0.7769	0.7940	0.7941	0.7992	0.7720
Desert	0.4910	0.4915	0.4961	0.4971	0.4906

Figure 3b illustrates scatter diagrams of NDVI versus air temperature using the best-correlated time lag as shown in **Table 1**. For all vegetation types, the polynomial order-1, -2, -3, -4 and exponential analyses gave significant (r were more than 0.70, except desert, it was less than 0.50) and approximately the same correlation coefficients (**Table 2**). Therefore, the relationships were adequately shown by linear regression; however, they have considerably different slopes among those vegetations (**Table 3**). The high regression slope correlated to the vegetations that have similar fluctuations between NDVI and air temperature within a year (deciduous broadleaf forest, grassland, savanna, etc.) as shown in **Figure 3a**. On the other hand, evergreen broadleaf forest, semi desert, and desert exhibited large different fluctuations between both variables that match with the low value of slope.

Table 3.
Mean annual integrated NDVI value, annual air temperature (T), time lag, correlation coefficient (r), regression slope (S, x1000), and ratio of T-NDVI.

Vegetation types	NDVI	T °C	Time lag	r	S	T/ NDVI
Forests						
Deciduous broadleaf	3.27	7.38	0	0.8669	13.65	2.26
Evergreen coniferous	3.86	16.55	0+1	0.7475	9.75	4.29
Evergreen broadleaf	4.63	15.40	2	0.7243	5.69	3.33
Woods						
Mixed forest	3.56	10.88	0	0.8538	10.24	3.06
Forest and field	3.63	16.16	0	0.8253	10.82	4.45
Crops						
Farmland	2.73	11.19	0	0.8644	9.58	4.10
Irrigated crop	2.86	14.46	0	0.8670	9.53	5.06
Grasses						
Grassland	2.19	2.48	0+1	0.8191	13.65	1.13
Savanna	3.04	11.27	0	0.8434	10.54	3.71
Shrub	3.64	10.98	0, 0+1	0.7785	7.81	3.02
Desert						
Semi desert	1.24	4.17	0+1	0.7769	2.01	3.36
Desert	0.74	5.11	2	0.4910	0.018	6.91

r is based on linear regression analysis.

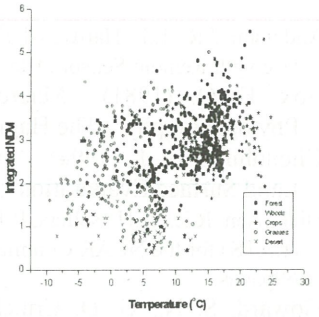

Figure 4.
Relationship between mean annual integrated NDVI and mean annual air temperature corresponding to the five major phytomes.

No surprisingly, the dense canopies of forests and woods had high value of integrated NDVI value (more than 3.27), while crops and grasses had lower ranging from 2.19 to 3.0. Desert area had the lowest one (less than 1.24) (**Table 3**). From this table, the mean annual air temperature shows no clearly differences among the twelve vegetation types, as also illustrated in **Figure 4**. Nevertheless, the range of the monthly air temperature was differed significantly among the vegetation types. For example, the evergreen broadleaf forest is only distributed in the region of 10-25°C, while the deserts is –15- 20°C per year. The surface temperature-NDVI ratio of Nemani and Running (1989) has been also computed in this study. As exposed in **Table 3**, the low ratio was in forests, while it was high in dry land vegetation of desert.

CONCLUSION

In conclusion, the relationship between mean annual integrated NDVI and mean annual air temperature in East Asia as a whole is relatively insignificant (r = 0.40). It seems the mean annual air temperature data is inadequately to describe the vegetation distribution in this area. This contrasts with the mean annual integrated NDVI and mean annual rainfall relationship that we described in Part I. The exception to this was appeared when the relationships were analyzed based on each vegetation type. All vegetation types, excluding desert, show a significant linear correlated between NDVI and air temperature (r > 0.70). In general, the NDVI responds to air temperature in time lag of 0. It means the NDVI of a given month is very influenced by air temperature of the same month. The high regression slope correlated to the vegetations that have similar fluctuations between NDVI and air temperature within a year (deciduous broadleaf forest, mixed forest, farmland, grassland, etc.) On the other hand, evergreen coniferous forest, evergreen broadleaf forest, shrub, and desert exhibited large different fluctuations between both variables that match with the low value of slope.

This study suggests that the vegetation types do differ with respect to mean annual integrated NDVI, regression slope, and ratio of air temperature-NDVI, but relatively same to mean annual air temperature and time lag. Therefore, for the purpose of land cover classification, it will be useful to add other environmental parameter such as day length and rainfall beside air temperature.

ACKNOWLEDGMENT

The authors deeply appreciate the producers of Time series of Global Monthly Vegetation Cover from NOAA/AVHRR: April 1985-December 1997. NOAA/NCDC. Published on CD-ROM by NOAA/NESDIS/NCDC. The CRU05 0.5 lat/lon gridded monthly climate data has been supplied by the Climate Impacts Link Project (UK Department of the Environment Contract EPG 1/1/16) on behalf of the CRU, University of East Anglia.

REFERENCES

Anderson, J.R., E.E. Hardy, J.T.Roach, R.E. Witmer. (1976). "A Land Use and Land Cover Classification System for Use with Remote Sensor Data: *U.S. Geological Survey Professional Paper 964*, 28 pages.

Box, E. O. (1981). "Macroclimate and Plant Forms: an Introduction to Predictive Modeling in Phytogeography". The Hague: Dr. W. Junk Publishers.

Choudhury, B. J. (1994). "Synergism of Multispectral Satellite Observations for Estimating Regional Land Surface Evaporation", *Remote Sens. Environ.*, 49, 264-274.

Dickinson, R.E., A.H. Sellers, P.J. Kennedy, and M.F. Wilson. (1986). "Biosphere-Atmosphere Transfer Scheme (BATS) for the NCAR Community Climate Model": *NCAR Techn. Note NCAR/TN275+STR, Boulder, CO.* 69pages.

Goward, S. N., G. D. Cruickshanks, and A. S. Hope. (1985). "Observed Relation between Thermal Emission and Reflected Spectral Radiance of a Complex vegetated Landscape", *Remote Sensing of Environment,* 18, 137-146.

Hope, A. S., and McDowell, T.P. (1992). "The relationship between Surface Temperature and a Spectral Vegetation Index of a Tallgrass Prairie: Effects of Burning and Other Landscape Controls". *International Journal of Remote Sensing,* 13, 2849-2863.

Kira, T. (1945). "New Climatic Zonation in Eastern Asia as a Basis of Agricultural Geography", *Kyoto Imperial University* (in Japanese).

Lambin E. F., D. Ehrlich. (1996). "The Surface Temperature-Vegetation Index Space for Land Cover and Land Cover Change Analysis". *International Journal of remote Sensing*, Vol 17, 3, 463-487.

Leeman, R. (1990). Global Holdrige Life Zones. Digital Data. *IIASA*, Laxenberg, Austria

Malingrau, J. P. (1986). "Global Vegetation Dynamics: Satellite Observations over Asia", *International Journal of Remote Sensing,* Vol. 7, No 9, 1121-1146.

Nemani, R. R., and S.W. Running. (1989). "Estimation of Regional Resistance to Evapotranspiration from NDVI and Thermal-IR AVHRR data". *Journal of Applied Meteorology,* 28, 276-284.

Olson, J.S. (1994a). "Global ecosystem Framework-definitions: USGS EROS Data Center International report", *Sioux Falls, SD*, 37 pages.

Olson, J.S. (1994b). "Global Ecosystem Framework-Translation Strategy: USGS EROS Data Center International Report", *Sioux Falls, SD*, 39 pages.

Schultz, P.A., and M.S. Halpert. (1995), "Global Analysis of the Relationships among a Vegetation Index, Precipitation, and Land Surface Temperature", *International Journal of Remote Sensing*, Vol 16, 15, 2755-2777.

Retrieval of precipitable water in a continental scale using split window data.

MAKOTO KUJI
Nara Women's University, Nara 630-8506, Japan

ITARU OKADA
Japan Science and Technology Corporation (JST), Saitama 332-0012, Japan

AKIHIRO UCHIYAMA
Meteorological Research Institute (MRI), Ibaraki 305-0051, Japan

TAMIO TAKAMURA
Center for Environmental Remote Sensing (CEReS), Chiba University, Chiba 263-8522, Japan

1. Introduction

Water vapor is one of the most dominant greenhouse effect gases as well as the most influential atmospheric components in remote sensing studies targeting at land and ocean. It is important to understand water vapor behavior in a global scale consequently. Water vapor also has great variability in spatial and temporal domain, and then it is optimal to retrieve globally the water vapor amount using satellite data, such as polar orbiters and geostationary satellites at frequent observational intervals. Several sensors, such as optical and microwave radiometers, have been used to retrieve the precipitable water (i.e., vertically integrated water vapor amount). It is said that microwave radiometer data are useful to retrieve precipitable water only over ocean because they are not well available over land due to the complexity of land surface emissivity.

Jedlovec (1990) illustrated the Split Window Variance Ratio (SWVR) method is applicable to the airborne Multispectral Atmospheric Mapping Sensor (MAMS) data. He suggested that the Visible and Infrared Spin Scan Radiometer (VISSR) Atmospheric Sounder (VAS) suffers in its lager spatial resolution and limited dynamic range.

Kleespies and McMillin (1990) analyzed Advanced Very High Resolution Radiometer (AVHRR) and VAS to retrieve the precipitable water. They addressed that the optimal instrumentation was the geostationary satellite with the quality of error reduced as much as AVHRR instrument aboard National Oceanic and Atmospheric Administration (NOAA) satellite. They also suggested that the subpixel cloudiness was critical factor for the VAS application.

Iwasaki (1994) has developed the retrieval algorithm for mesoscale water vapor variation using AVHRR / NOAA data. In the method, air temperature effect was corrected with atmospheric model calculations.

In this study, an algorithm has been under development to retrieve precipitable water in a continental scale using split window data (11 and 12 μm spectral bands) based upon Iwasaki (1994). The algorithm was applied to the VISSR aboard Geostationary Meteorological Satellite - 5 (GMS-5). The retrieved results were compared to the in situ radiosonde observation.

2. Data description

The three types of data were used in this study: One is VISSR / GMS-5 data and others are radiosonde and Automated Meteorological Data Acquisition System (AMeDAS) data as references for precipitable water and surface air temperature around Japan, respectively.

As to the VISSR data, the analyzed region ranges from 70 °N to 20 °S in latitude and from 70 °E to 160 °E in longitude. The spatial resolution is around 5 ° by 5 °, and then there exist 1800 by 1800 pixels in total. The analyzed scene number is 228 for 00 and 12 UTC, which extends from January, April, July, and October in 1997 in particular.

As for the reference data, on the other hand, both radiosonde and AMeDAS data from 1988 to 1997 around a calibration site of Japan in this study, were collected to estimate precipitable water and surface air temperature, respectively.

The algorithm under development utilizes the split window channels (11 and 12 μm spectral bands). In general, these spectral channels contains information in lower tro-

posphere (i.e., boundary layer) where almost all water vapor exists. A 6.7 μm spectral band (so to speak, a water vapor channel), is also available in VISSR / GMS-5 data, which is sensitive to the relative humidity around 200 to 500 hPa (middle troposphere to tropopause) (Soden and Bretherton 1993). The water vapor channel is expected to add some information on a water vapor profile which is not inferred only from split window channels. It is also interested to compare the water vapor distribution pattern of the upper troposphere in a global scale to that of the lower troposphere using aboard the same sensor / satellite.

3. Analysis and results

The algorithm utilizes a transmittance ratio of two split window bands, rather than difference of those brightness temperatures, based upon AVHRR analysis over land by Iwasaki (1994). In the first step of the algorithm, a calibration curve with statistical regression is made between precipitable water and the transmittance ratio parameter, so as to simply retrieve initial precipitable water with split window data. In the second step, air temperature effect is corrected and then apparent surface temperature (i.e., surface air temperature in the model atmosphere in this study) is derived as a by-product.

The algorithm has several new features such as 1) both 11 and 12 μm channels response function are taken into account, 2) not only water vapor continuum absorption but also line absorption with water vapor and other absorbing gases, are taken into consideration and 3) apparent surface temperature is also retrieved and compared to in situ observation such as surface air temperature.

The retrieval algorithm was preliminarily applied to VISSR / GMS-5 data on 00 UTC, October 19, 1997 in particular of all data described in previous section.

a. Retrieval with regressive curve (first step)

In the first step of the algorithm, SWVR method is utilized (Jedlovec 1990). At first, an unit, which contains 32 x 32 pixels around Cape Shionomisaki (33.45 °N, 135.77 °E), was set to make segment analysis. And then, available pixels, judged as least cloud-contaminated, were picked up among the 228 scenes, and then, the statistical value (SWVR) was calculated to retrieve precipitable water for the unit. Fig. 1 illustrates the relationship between the SWVR and precipitable water estimated from the radiosonde data (00 and 12 UTC) at the Cape Shionomisaki.

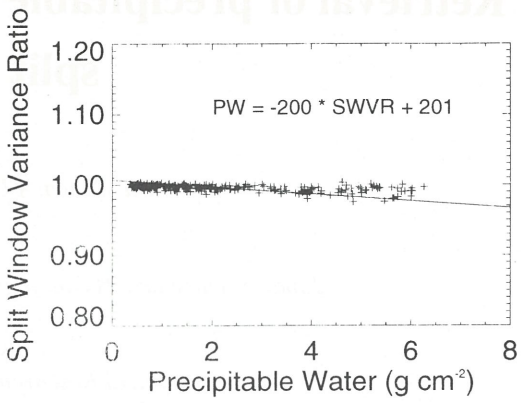

Fig. 1 The relationship between SWVR calculated from VISSR and precipitable water estimated from radiosonde data at Cape Shionomisaki. Dots are the actual data and regressive line is overlaid.

Fig. 1 indicates that linear relationship exists between SWVR and precipitable water. A regressive line was then determined with a least square fitting method:

$$PW = -200 * SWVR + 201. \quad (1)$$

And then, precipitable water is expected to be retrieved from SWVR for all units of the all scenes. For example, precipitable water, retrieved using Eq. (1), is shown in Fig. 2 for the case of 00 UTC October 19, 1997 around Japan.

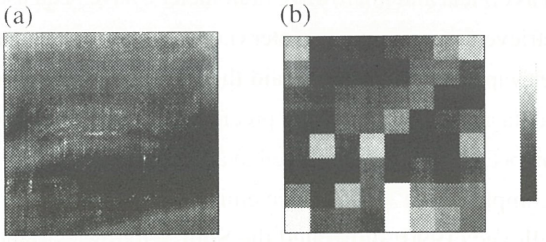

Fig. 2 (a) Water vapor channel (6.7 μm) imagery VISSR / GMS-5 and (b) retrieved precipitable water on 00 UTC (09 JST) October 19, 1997. Displayed region of these panels covers from the left top corner (42.8 °N, 129.2 °E) to the right bottom one (30.0 °N, 142.0 °E) in a uniform interval coordinate in latitudinal and longitudinal directions, and then there exist 256 x 256 pixels in total. A level slice is normalized from white to black with which corresponds from maximum to minimum value for panel (b) and vice versa for panel (a).

Precipitable water is retrieved for one unit which consists of 32 x 32 pixels, then it is found that in Fig. 2 the retrieved precipitable water distribution (panel b) is coarser than the spatial variation of water vapor channel image (panel a). Comparing them, tendency of overall distribu-

tion is not very different. But the precipitable water retrieved at the units, which contain mountain region, is smaller than that of their surroundings. The precipitable water retrieved at the units, which seems to contain cirrus, has also the same tendency

Precipitable water estimated from radiosonde data around Japan and that retrieved from the units corresponding to the radiosonde observation sites, are compared to validate the retrieved results on the same scene in Fig. 2. The comparison is illustrated in Fig. 3.

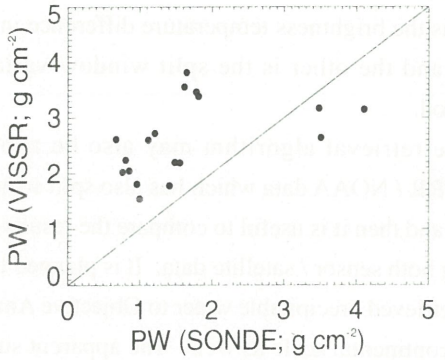

Fig. 3 The comparison of precipitable water (PW) on 00 UTC (09 JST) October 19, 1997 for the same scene in Fig. 2. The abscissa shows the precipitable water estimated from radiosonde data and the ordinate does the one retrieved using split window channels on VISSR. The one-to-one line is drawn as reference.

From Fig. 3, it is found that the retrieved precipitable water using VISSR data overestimates (underestimates) for small (large) precipitable water by about 2 (1) g cm^{-2} around 18 radiosonde observational sites in Japan.

Fig. 4 illustrates the result that the same retrieval method was applied to the VISSR data in a continental scale.

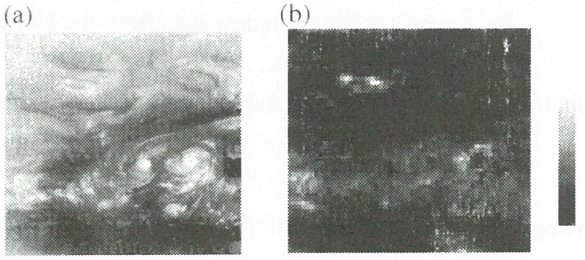

Fig. 4 (a) Water vapor channel (6.7 μm) imagery VISSR / GMS-5 and (b) retrieved precipitable water on 00 UTC (09 JST) October 19, 1997 for the same scene in Fig. 2. Displayed region of these panels covers from the left top corner (70 °N, 70 °E) to the right bottom one (20 °S, 160 °E) in a uniform interval coordinate in latitudinal and longitudinal directions and then, there exist 224 x 224 pixels in total. A level slice is normalized from white to black with which corresponds from maximum to minimum value for panel (b) and vice versa for panel (a).

In Fig. 4, displayed region is as follows: The left panel a (water vapor channel) consists of 224 x 224 pixels whose one pixel is made from average of 8 x 8 original pixels. The right panel b (retrieved precipitable water) also consists of 224 x 224 pixels after each retrieved unit is magnified by factor 4 for each direction, and then 56 x 56 units result in 224 x 224 pixels.

Comparison between Fig. 4a and Fig. 4b, the spatial variation pattern is well consistent at a glance. But there are several regions where variation pattern in each panel is inconsistent: One is the region at the Himalayas and Tibet plateau where topographic effect is not negligible and the other is where high-level clouds exist with typhoons and deep convective cloud system in tropical region.

b. Correction of air temperature (second step)

In the second step of the algorithm, sensitivity of SWVR to precipitable water was examined with model atmosphere. In the model atmosphere, water vapor and other gaseous absorption were taken into consideration as well as water vapor continuum absorption. Response functions of VISSR split window was weighted in the radiance simulation. Fig. 5 illustrates a simulation result.

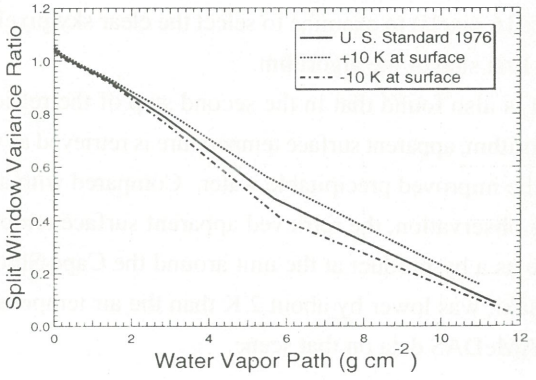

Fig. 5 The relationship between SWVR (ordinate) and Water Vapor Path (abscissa). The U. S. Standard atmosphere 1976 (hereafter USS76), incorporated into the LOWTRAN-7, was assumed as a atmospheric model. It was also assumed that surface radiative temperature in the model ranges from 285 to 295 K uniformly. Solid line is the case for USS76. Dashed line (dotted-dashed) line is the case for which air temperature profile is scaled as the surface air temperature is higher (lower) than USS76 by 10 K.

From Fig. 5, it is found that SWVR estimated using

VISSR data is sensitive to precipitable water in a simply decreasing manner. It is also found that the relationship between SWVR and precipitable water is remarkably affected by air temperature when precipitable water is greater than 2 g cm^{-2}.

As a result, it is desirable to correct air temperature effect and then improve accuracy of the retrieval of precipitable water. The correction method is also based upon Iwasaki (1994) in principle, but a few devices are added: Precipitable water is modified in iterative procedure as air temperature changes under the condition that water vapor volume mixing ratio is constant. A profile of air temperature is also multiplied for all level by the factor of the variation of surface air temperature in the iterative procedure.

As a result of the correction, retrieval accuracy was not improved at all and then the root mean square error was about 2 g cm^{-2}. This indicates that the exactness of regressive curve in the first step is more critical than the correction of air temperature when the retrieval method is applied to the VISSR / GMS-5 split window channel data.

It is now turned out that the regressive curves are different very much between from the actual VISSR data (Fig. 1) and from the simulation with a model atmosphere (Fig. 5). This discrepancy is attributed to the uncertainty of selection of clear sky (uncontaminated with cloud) pixel at this stage. It is then necessary to revise this portion of the algorithm: For example, the analysis unit size will be changed from current 32 x 32 pixels to smaller size (e.g., 16 x 16 pixels) to examine to select the clear sky pixels in the first step of the algorithm.

It is also found that in the second step of the retrieval algorithm, apparent surface temperature is retrieved as well as the improved precipitable water. Compared with an in situ observation, the retrieved apparent surface temperature as a by-product at the unit around the Cape Shionomisaki, was lower by about 2 K than the air temperature of AMeDAS data on that scene.

4. Summary and concluding remarks

To retrieve the precipitable water in a continental scale, a retrieval algorithm has been developed. The algorithm is going to be applicable in principle to the sensor which has the split window channel information such as VISSR / GMS-5 and AVHRR / NOAA. The retrieval algorithm was preliminary applied to the VISSR / GMS-5 data. The retrieved results were not well consistent with the precipitable water estimated from radiosonde observation around Japan. The inconsistency is attributed to the less exactness of regressive curve, rather than the influence of the atmospheric temperature at this stage. Further investigation is required to resolve this discrepancy.

Recently, Barton and Prata (1999) has showed that transmittance ratio method, which was identical to the SWVR method, did not work well and then they recommended to use the approach of split window brightness temperature difference.

The results in this study actually are consistent to their recommendation. It is, then, required the comparison with two retrieval method using the same VISSR / GMS-5 data: One is the brightness temperature difference in split window and the other is the split window variance ratio method.

The retrieval algorithm may also be applicable to AVHRR / NOAA data which has also split window channels, and then it is useful to compare the results each other using both sensor / satellite data. It is planned to compare the retrieved precipitable water to Objective Analysis Data in a continental scale as well. The apparent surface temperature, estimated as a by-product with the atmospheric temperature correction, will be compared with in-situ observational data in detail.

Acknowledgments. The authors would like to thank Professor T. Kikuchi of Kochi University for his kind provision of VISSR / GMS-5 data used in this study.

REFERENCES

Barton, I. J., and A. J. Prata, 1999: Difficulties associated with the application of covariance-variance techniques to satellite imagery. *Remote Sens. Environ.*, **69,** 76-83.

Iwasaki, H., 1994: Estimation of precipitable water over land using the split-window data from the NOAA satellite. *J. Meteor. Soc. Japan,* **72,** 223-233.

Jedlovec, G. J., 1990: Precipitable water estimation from high-resolution split window radiance measurements. *J. Appl. Meteor.,* **29,** 863-877.

Kleespies, T. J., and L. M. McMillin, 1990: Retrieval of precipitable water from observations in the split window over varying surface temperatures. *J. Appl. Meteor.,* **29,** 851-862.

Soden, B. J., and F. P. Bretherton, 1993: Upper troposphere relative humidity from the GOES 6.7 μm channel: Method and climatology for July 1987. *J. Geophys. Res.,* **98,** 16,669-16,688.

Cross and Vicarious Calibration Experiments for Terra ASTER and Landsat-7 ETM+ in the Thermal Infrared Region Using Hot Ground Targets

T. Matsunaga, T. Nonaka, Y. Sawabe (Tokyo Institute of Technology),
M. Moriyama (Nagasaki Univ.), H. Tonooka (Ibaraki Univ.), and H. Fukasawa (ERSDAC)

Abstract. For radiometric calibration of Terra ASTER TIR and Landsat-7 ETM+ thermal infrared band, vicarious calibration (VC) and cross calibration (CC) experiments were carried out in Lake Tahoe (Nevada), in Salton Sea (California), and Railroad Valley (Nevada) in 2000. For Salton Sea and Railroad Valley, ground temperature measurements were conducted in large playas during the overpasses of these satellites. For Lake Tahoe, airborne MASTER data were acquired. Atmospheric profile data were obtained with radisonde during experiments. These calibration results show that the radiant temperature of ASTER TIR, based on the on-board blackbody, is lower than those of VC/CC at high temperature. While the difference between ASTER/ ETM+ and CC is 0.5~1.4℃/ 3.9~4.2℃ in Lake Tahoe, the difference between ASTER and VC is 0.5~1.2℃ (except band 12) in Salton Sea, and 0.3~1.0℃ in Railroad Valley. Cross calibration accuracy of ASTER TIR and ETM+ in Lake Tahoe is 0.5~0.7℃, and 0.9℃, respectively.

1. Introduction

1.1 Background and Purpose

As the concern for the changes of the earth environments has been grown recently, the role of the remote sensing is changing from mapping to monitoring. To extract quantitative information from remote sensing data, more accurate calibration has been asked for. Though the importance of calibration of the satellite sensor has been increasing, the study for the radiometric calibration of satellite thermal infrared sensor is rare (except TM band6[1], and SST studies using AVHRR-type sensors[2]). The calibration at high temperature (about 20℃ higher than air temperature) is especially needed to estimate the daytime land surface temperature and surface heat balance accurately. However, thermal infrared sensors such as ASTER TIR, which carries only one blackbody, cannot always check its radiometric characteristics at high temperature[3][4]. So for these sensors, it is very important to examine its radiometric characteristics at high temperature by vicarious calibration (VC) and cross calibration (CC). The observation targets for the calibration in previous studies, however, are often water[3][5] because water has spatially homogeneous temperature and emissivity. In this study, we discuss the methodologies for accurate radiometric calibration of the satellite thermal infrared sensors using hot ground targets. Applying the methods to the experimental data, we also discuss the radiometric calibration accuracy of Terra ASTER TIR and Landsat-7 ETM+ band6 (thermal infrared band). Calibration results of ETM+ are reported only in Lake Tahoe.

1.2 Study Areas

CC experiment was conducted around Lake Tahoe (1.9km above sea level), NV in March 2000. VC experiments were around Salton Sea (-0.1km), CA, and Railroad Valley (1.4km), NV in June 2000 (Fig. 1). Table 1 shows the ground-level meteorological conditions at each experimental site.

Fig. 1. Map of study areas.

Table 1. Ground-level meteorological conditions.

Site	Date	Time	Temperature	Humidity
Lake Tahoe	00.3.12	11:09	4℃	75%
Salton Sea	00.6.4	10:34	32℃	52%
Railroad Vallety	00.6.11	11:30	28℃	9%

2. Instruments for Radiometric Calibration of Satellite Sensors

2.1 MASTER

MASTER[6] (MODIS/ASTER airborne simulator) was developed by NASA JPL (Jet Propulsion Laboratory). It includes ten bands from 7μm to 14μm, and band 42, 43, 44, 47, and 48 corresponds to ASTER TIR band 10, 11, 12, 13, and 14, respectively. It has two internal blackbodies, and its radiometric calibration is done for each scan. Table 2 shows the specifications of MASTER. The spectral coverage of Landsat-7 ETM+ band6 correspond MASTER band 47, 48, and 49.

Table 2. Specifications of MASTER.

Wavelength Range	0.4 ~ 13 μm
Number of Channels	50
Number of Pixels	716
Instantaneous Field of View	2.5 mrad
Digitization	16 bit

2.2 Multispectral Thermal Infrared Radiometer Used for Ground Observation

A multispectral thermal infrared radiometer, manufactured by CIMEL Electronique, has six bands (one broad band and five narrow bands) in the TIR region. Five narrow bands correspond to five ASTER TIR bands. Table 3 shows its specifications.

Table 3. Specifications of the multispectral radiometer.

Sensed Temperature Range	-80 ~ 50℃
Field of View	10°
Temperature Resolution	0.05 ~ 0.1K
Detector	Thermopile
Weight	Less than 5kg

3. Methods

In this section, CC/VC methods are described. CC is a calibration method in which satellite/ airborne sensor observes the same targets at the same time as the satellite sensor does. VC in this study is that ground instruments observe the ground targets when the satellite passes. Though CC is easy to grasp the temperature variation of observation targets, there are two problems. One is the calibration accuracy of the satellite/ airborne sensor is not so good, and the other is the difference of the spectral coverage between sensors. So MASTER is used because it's calibration accuracy is well established through experiments at Lake Tahoe (S. Hook, private communications). In case of VC, the accuracy of ground instruments is good, but it is difficult to grasp the spatial temperature variation within ground targets. So CC and VC is used complementarily. The goal of our study is, using CC and VC, to achieve 1℃ radiometric accuracy, which is calibration requirement of ASTER TIR.

3.1 Cross Calibration

Table 4 summarizes the observation around Lake Tahoe by ASTER, ETM+, and MASTER. Line 1 data were used for CC with ETM+, and Line 3 data with ASTER. Satellite and airborne radiance data were extracted from five or six ground targets (snow, grass, and desert) and three water bodies with spatially uniform radiance. Figure 2 is ASTER image, showing MASTER's flight line and data points. Atmospheric measurements were conducted with radiosonde. Figure 3 shows the transmittances and path radiance from ground to satellite altitude (705km) calculated by MODTRAN4 with radiosonde data. Transmittance drops around 9.6μm because ozone absorbs the electromagnetic wave around this wavelength. MASTER data was recalibrated at lake surface temperature and 30℃ (lower internal blackbody temperature). TOA (top of the atmosphere) radiance was calculated from recalibrated

MASTER data at each flight line (I_{AIR}). I_{AIR} is the average radiance of several pixels, correspond to the size of one pixel of ASTER or ETM+.

Table 4. Remote sensing observations around Lake Tahoe.

Sensor (Line)	Altitude	Time	Pixel Size	Data
ASTER TIR	705km	11:12	90m	Level 1B Ver 0.4
Landsat-7 ETM+ Band6	705km	10:32	60m	Level 1R
MASTER (1)	4.0km	10:30-10:34	5-10m	
MASTER (3)	8.6km	11:10-11:15	17–31m	

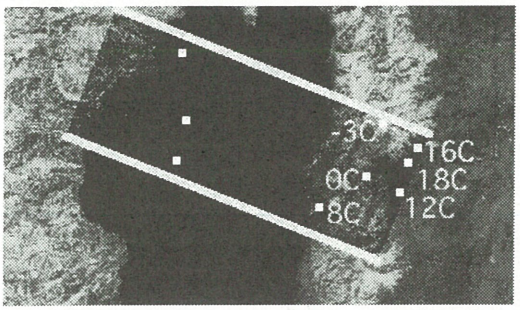

Fig. 2. Spatial extent of MASTER image line and data points in ASTER image.

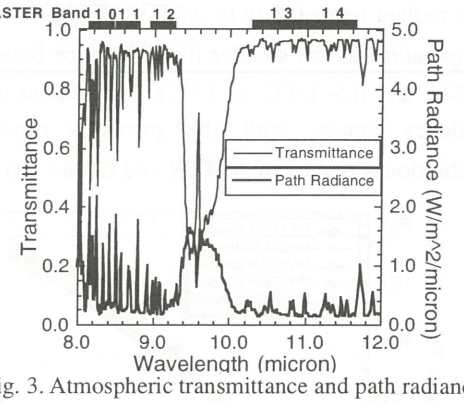

Fig. 3. Atmospheric transmittance and path radiance around Lake Tahoe from ground to satellite altitude.

3.2 Vicarious Calibration

The ground measurements were conducted by two broadband radiometers and one multispectral thermal infrared radiometer in Salton Sea and Railroad Valley. These areas are large playas having homogeneous temperature and emissivity. Using the multispectral thermal infrared radiometer with same spectral bands as ASTER TIR, radiance-based calibration was done. Figure 4 shows the schematic view of surface temperature measurement, and Figure 5 is experiments in Salton Sea. Playa surface brightness temperature was measured every 10m along the 90m square (90m is pixel size of ASTER TIR) shown in Figure 4 using broadband radiometers carried by an observer who walk around square. These radiometers were calibrated with portable blackbodies every 20 minutes. The multispectral radiometer was fixed at the height of 3.0m (FOV: 50cm). The brightness temperature measurements with it were automatically done every 150 seconds. Areal mean surface temperatures were estimated by adding temperature difference between two broadband radiometers and the broad band data of the multispectral radiometer to the temperature of the multispectral radiometer at each band. Atmospheric measurements were conducted with radiosonde, and TOA radiance from VC and surface radiant temperature from ASTER were calculated.

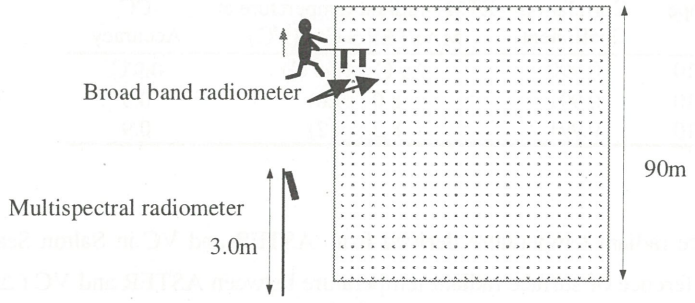

Fig. 4. Schematic view of surface temperature measurement.

Fig. 5. Experiment in Salton Sea.

4. Results

4.1 Cross Calibration

Figure 6/ 7 show the relationships between TOA radiant temperature of ASTER/ ETM+(Y) and that of MASTER data (X). Error bars indicate the standard deviation of MASTER data at the selected pixels. Three points around 6℃ are water, and the rest are ground targets. Table5/ 6 show the intercepts (a), slopes (b), and correlation coefficients of the linear regression between ASTER/ ETM+ and MASTER. Table 5/ 6 also show the radiant temperature of ASTER/ ETM+ when that of MASTER is 5℃ and 15℃, and cross calibration accuracy (α) of ASTER/ ETM+, defined by equation (1).

$$Y = a + bX +/-\alpha \qquad (1)$$

The radiant temperature of ASTER/ ETM+ is almost linear to that of MASTER. And the lower the radiant temperature is, the smaller the difference between ASTER and MASTER is (The difference is 0.1~0.3℃ at 5℃, and 0.5~1.4℃ at 15℃). The radiant temperature of ETM+ is 3~4℃ higher than MASTER. This tendency agrees with the previous report (URL: http://landsat7.usgs.gov/news/cali.html). Cross calibration accuracy of ASTER and ETM+ (α) is 0.5~ 0.7℃, and 0.9℃, respectively.

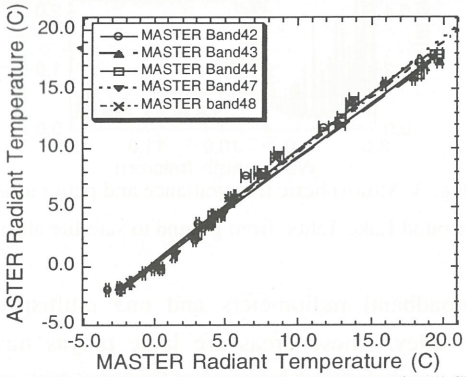

Fig. 6. TOA radiant temperature of ASTER and MASTER.

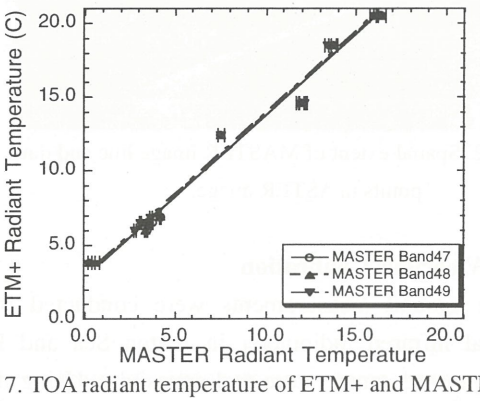

Fig. 7. TOA radiant temperature of ETM+ and MASTER.

Table 5. Linear regression coefficients between ASTER and MASTER, ASTER radiant temperature at MASTER 5℃, and 15℃, and cross calibration accuracy of ASTER.

ASTER Band	MASTER Band	Intercept (℃)	Slope	Correlation Coefficient	ASTER radiant temperature at MASTER 5℃(15℃)	CC Accuracy
10	42	0.42	0.94	0.995	5.1℃ (14.5℃)	0.7℃
11	43	0.26	0.89	0.997	4.7 (13.6)	0.5
12	44	0.12	0.91	0.997	4.7 (13.8)	0.6
13	47	0.14	0.96	0.997	4.9 (14.5)	0.6
14	48	0.34	0.94	0.996	5.0 (14.4)	0.7

Table 6. Linear regression coefficients between ETM+ and MASTER, ETM+ radiant temperature at MASTER 5℃, and 15℃, and cross calibration accuracy of ETM+.

ETM+ Band	MASTER Band	Intercept (℃)	Slope	Correlation Coefficient	ETM+ radiant temperature at MASTER 5℃ (15℃)	CC Accuracy
	47	2.43	1.10	0.990	7.9℃ (18.9℃)	0.9℃
6	48	2.51	1.10	0.991	8.0 (19.0)	0.9
	49	2.70	1.10	0.991	8.2 (19.2)	0.9

4.2 Vicarious Calibration

Table 7 shows TOA radiance and surface radiant temperature derived from ASTER and VC in Salton Sea and Railroad Valley. Figure 8 shows the difference of surface radiant temperature between ASTER and VC (ΔT). Except band12 in Salton Sea, ΔT is –1.2~ -0.5℃ in Salton Sea, and -1.0~ -0.3℃ in Railroad Valley. ΔT at band 12 in Salton Sea is larger (-1.8℃) than other bands. One of the reasons is that the ozone profile used in MODTRAN4 calculation was that of US standard model and did not reflect local variations of ozone amount. ΔT is different among bands. This is partly caused by the difference of atmospheric correction error

among bands. Both in Salton Sea and Railroad Valley, the areal mean surface temperature from VC is higher than ASTER. This tendency is not seen at the VC using water bodies[7]. We will clarify the reason why ASTER TIR shows the lower temperature than VC at high temperature targets.

Table 7. Difference of TOA radiance and surface radiant temperature between ASTER and VC in Salton Sea and Railroad Valley.

		Salton Sea					Railroad Valley				
	Band	B10	B11	B12	B13	B14	B10	B11	B12	B13	B14
TOA	L1B	12.47	13.01	13.06	13.36	12.63	11.20	11.84	11.97	12.20	11.66
Radiance	VC	12.67	13.11	13.39	13.47	12.82	11.43	11.89	12.12	12.31	11.83
(W/m2/μm/str)	Δ%	-1.6	-0.8	-2.5	-0.8	-1.5	-2.1	-0.5	-1.3	-0.9	-1.4
Surface	L1B	50.3	50.1	48.6	51.7	51.5	45.0	44.9	43.3	45.1	45.6
RT	VC	51.2	50.6	50.4	52.2	52.7	46.0	45.2	44.1	45.4	46.6
(℃)	Δ	-0.9	-0.5	-1.8	-0.5	-1.2	-1.0	-0.3	-0.8	-0.3	-1.0

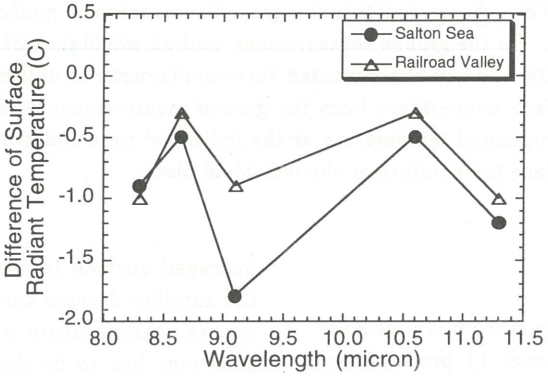

Fig. 8. Surface radiant temperature difference between ASTER and VC in Salton Sea and Railroad Valley.

5. Summary

Vicarious calibration and cross calibration experiments using ground targets for Terra ASTER TIR and Landsat-7 ETM+ thermal infrared band were carried out. Experiment results suggest that ASTER underestimate the surface radiant temperature 0.5~1.4℃ (around 15℃) in Lake Tahoe, 0.5~1.2℃ (50℃) except band 12 in Salton Sea, and 0.3~1.0℃ (45℃) in Railroad Valley. Cross calibration accuracy using an airborne sensor is about 0.5~0.7℃ for ASTER, and 0.9℃ for ETM+.

Acknowledgments

The authors are graceful to Dr. Simon J. Hook and Mr. Frank Palluconi of California Institute of Technology for providing ETM+, MASTER, and radiosonde data. We also thank the Ministry of International Trade and Industry for providing us ASTER data.

References

1) J. R. Schott and W. J. Volchok., 1985, Thermatic Mapper thermal infrared calibration. *Photogram. Eng. Remote Sens.* **51**, pp. 1351-1357.

2) H. Reutter, F. S. Olesen, and H. Fischer, 1994, Distribution of the brightness temperature of land surface determined from AVHRR data. *Int. J. Remote Sens.*, **15**, 1, pp. 95-104.

3) A. Ono, *et al*, 1996, Preflight and in-flight calibration plan for ASTER. *J Atoms. Oceanic Trch.*, **13**, 2, pp. 321-335.

4) H. Fujisada, *et al.*, 1996, Algorithm theoretical basis document for ASTER level-1 data processing (Ver. 3.0), *Earth Remote Sensing Data Analysis Center (ERSDAC) LEL/8-9.*

5) K. Thorne, *et al.*, 1998, ASTER preflight and inflight calibration and the validation of level 2 products. *IEEE Trans. Geosci. Remote Sens.*, **33**, 4, pp. 1161-1172.

6) MASTER team, MASTER-The MODIS/ASTER Airborne Simulator, URL: http://masterweb.jpl.nasa.gov/.

7) H. Tonooka, F. Palluconi, T. Matsunaga, M. Moriyama, H. Fukasawa, K. Arai, S. Tsutida, and Y. Yamaguchi, 2000, Early results from the inflight vicarious calibration of ASTER (thermal infrared radiometer), *Proc. of RSSJ*, **29**, pp.11-12.

The ground measurement and data processing method for the satellite derived land surface temperature validation

Masao Moriyama, Koji Yano and Yu Ito
Faculty of Engineering, Nagasaki University.
1 – 14 Bunkyo Nagasaki 8528521 JAPAN
matsu@rsirc.cis.nagasaki-u.ac.jp

Abstract : For the validation of the satellite derived surface temperature, the validation scheme is made. The scheme contains the ground measurement method and the data processing method. For the ground measurement method establishment, concave mirror equipped wide–IFOV and self–compensated thermoradiometer is designed. To get the area–averaged surface temperature from the ground measurement data, the time shift processing of the measured temperature at the individual time and the areal averaging method of the surface temperature at the individual place.

1 Introduction

Not a few present earth observation system will provide not only the satellite radiance (Level 1) product but also the physical variables (Higher order) product such as the surface reflectance, emissivity or temperature as the standard products. For such kinds of products, the establishment of the validation scheme will be important as well as the estimation algorithm development. In this study, the validation scheme for the surface temperature product is established.

2 Brief description of the surface temperature validation

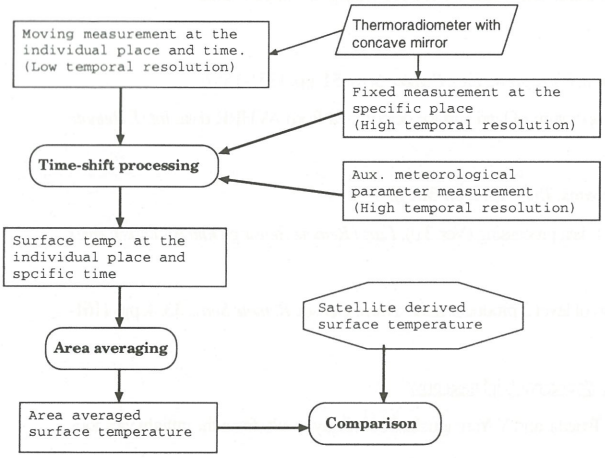

Figure 1: Flow of the surface temperature validation

Figure 1 shows the flow of the surface temperature validation scheme. The output of the scheme are the area averaged surface temperature and its error bar. While the satellite derived surface temperature is a kind of the average temperature over the IFOV, the ground measurement has to be done at the multiple points within the target area which area size is larger than the IFOV because of the poor geometric accuracy.

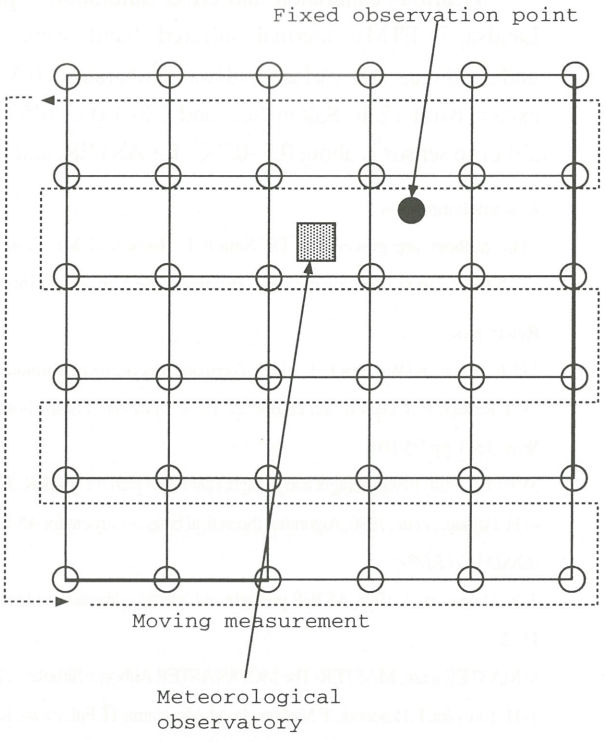

Figure 2: schematic of the measurement area layout

To increase the ground measurement points, by bringing the thermoradiometer, the observer measures the

surface temperature at the multiple points within the target area, these points are called "Moving observation points", also the surface temperature at the same point is measured with the short time intervals this is called "Fixed observation point". The measurement time at each Moving observation point are different from the satellite passing time, So the time shift processing of the each moving observation data to estimated the surface temperature of each moving observation point at the satellite passing time. From these surface temperature dataset, the areal averaged temperature is computed.

3 Thermoradiometer

3.1 Self–compensated thermoradiometer

The industrial thermoradiometer has the wide dynamic range so that it has poor accuracy. For the environmental measurement, the industrial thermoradiometer must be calibrated at the field. Also the industrial thermoradiometer has narrow FOV, so that the measured temperature often fluctuated with the measurement geometry. For the accurate surface temperature measurement and the convenience of the field measurement, the wide FOV and self compensated thermoradiometer had been designed [1].

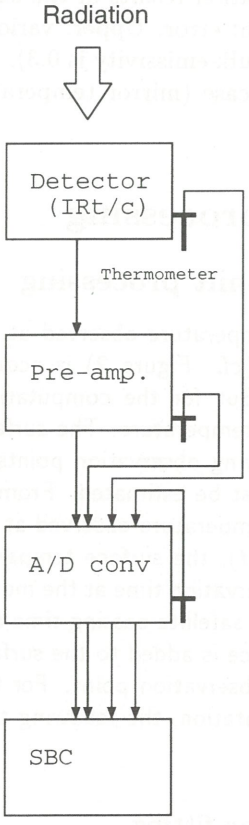

Figure 3: schematic of the self–compensated thermoradiometer

The main cause of the output drift of the thermoradiometer is the output drift of the analogue devices such as the detector, amplifier and A/D converter related to the device temperature fluctuation. The temperature of each analogue devices of the self–compensated thermoradiometer are measured and these temperature are used for the measured radiation temperature compensation. From the thermal test of the each analogue devices, the compensation formula is defined as follows.

$$T = c_{det}\theta_{det} + c_{amp}\theta_{amp} + c_{ad}\theta_{ad} + c_d T_d + c_0 \quad (1)$$

where T, c, θ and T_d are the compensated temperature, coefficient, analogue device temperature and detected radiation temperature, also the suffixes det, amp and ad show the detector, the amplifier and the A/D convertor. The latest accuracy of the self–compensated thermoradiometer is about 0.32 [deg. C].

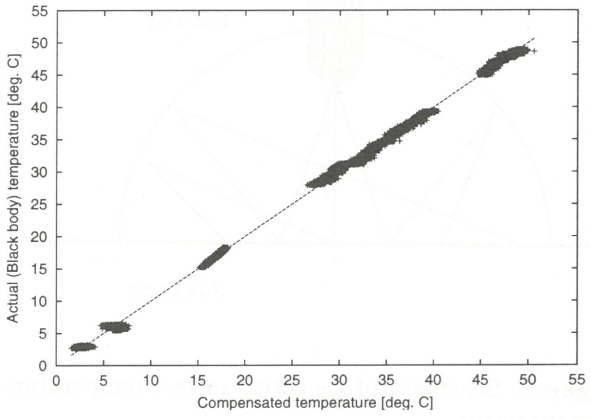

Figure 4: Comparison between the actual and compensated temperature of the self–compensated thermoradiometer.

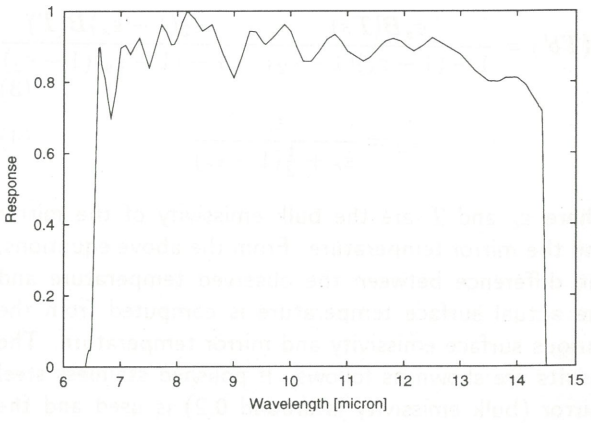

Figure 5: Relative response of the self–compensated thermoradiometer.

3.2 Actual surface temperature measurement using concave mirror

The thermoradiometer measures the brightness temperature expressed as follows.

$$B(Tb) = \varepsilon B(Ts) + (1-\varepsilon)\frac{F}{\pi} \qquad (2)$$

where B, Tb, Ts, ε and F are average Planck function, brightness temperature, surface temperature, average surface emissivity and downward atmospheric irradiance. To obtain the surface radiance from the brightness temperature, emissivity and atmospheric irradiance have to be measured or computed but these are costly and not so accurate.

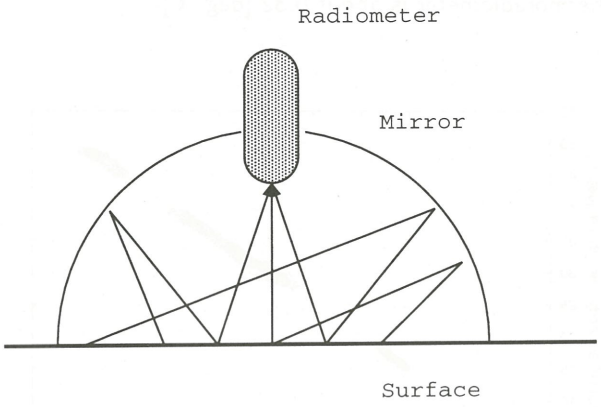

Figure 6: Schematic of the actual surface temperature measurement

By using the concave mirror, because of the multiple reflection the apparent surface emissivity becomes almost unity[8]. In the case that a semi–spherical mirror is used, the brightness temperature measured from the small hole at the top of the mirror Tb' can be expressed as follows[2],

$$B(Tb') = \frac{\varepsilon_s B(Ts)}{1-(1-\varepsilon_s)(1-\varepsilon_2)} + \frac{\varepsilon_2(1-\varepsilon_s)B(T)}{1-(1-\varepsilon_s)(1-\varepsilon_2)} \qquad (3)$$

$$\varepsilon_2 = \frac{\varepsilon_c}{\varepsilon_c + \frac{1}{2}(1-\varepsilon_c)} \qquad (4)$$

where ε_c and T are the bulk emissivity of the mirror and the mirror temperature. From the above equations, the difference between the observed temperature and the actual surface temperature is computed from the various surface emissivity and mirror temperature. The results are shown as follows. If polished stainless steel mirror (bulk emissivity is around 0.2) is used and the difference between the mirror temperature and the surface temperature is 5 [K], the measurement error is less than 0.1 [K] under the case which the surface emissivity is larger than about 0.9.

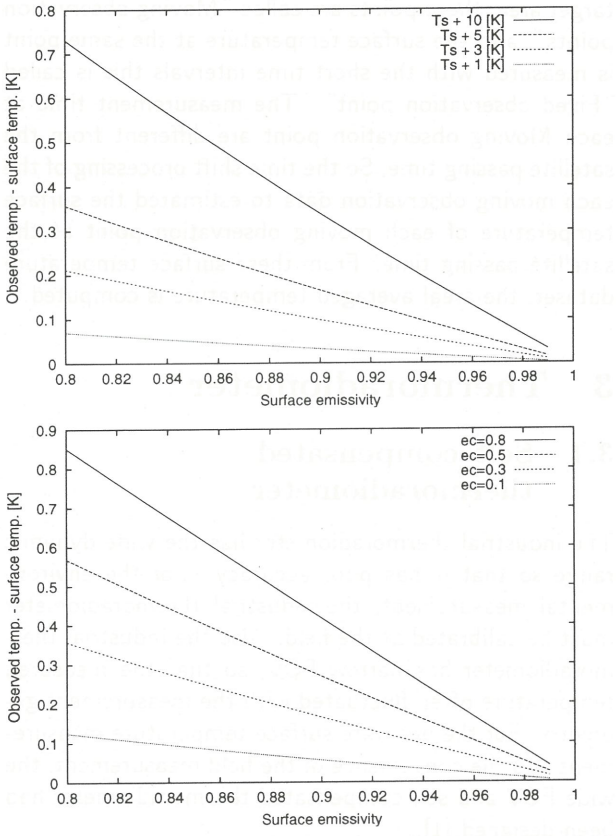

Figure 7: Simulation results of the surface temperature measurement error. Upper: various mirror temperature case (bulk emissivity is 0.3). Lower: various bulk emissivity case (mirror temperature is Ts + 5 [K]).

4 Data processing

4.1 Time shift processing

Each surface temperature observed at the moving observation point (*cf.* Figure 2) is acquired at the individual time. But for the computation of the areal average surface temperature, The surface temperature at the every moving observation points at the satellite passing time must be estimated. From the time series of the surface temperature observed at the fixed observation point $T_f(t)$, the surface temperature difference between the observation time at the moving observation point T' and the satellite passing time t'', and the temperature difference is added to the surface temperature at the moving observation point. For the temperature difference computation, the following two methods are considered[5].

4.1.1 Function fitting

If the time series of the surface temperature at the fixed observation point is approximated by an appropriate function, the fitting parameters can be defined by

least square method and the temperature difference between any time interval can be computed. Also the error variance of the time shift processing can be computed as the fitting error variance. For the most simple case, the linear fitting might be used. In this case, the gradient a and the intersect b are defined by least square method and the time shift processing becomes the multiplication a and the time interval.

$$T_f(t) \simeq a \cdot t + b \quad (5)$$

$$T_i(t'') = a \cdot (t'' - t') + T_i(t') \quad (6)$$

where $T_i(t)$ is the surface temperature at the i th. moving observation point.

4.1.2 Auto regression model

In the case which the $T_f(t)$ cannot be approximated by the any function, the other time series analysis method has to be used. In this study, the auto regression model described below is used. This model is the most simple and has the potential which extend to the multiple variable analysis.

$$T_f(t_i) \simeq \sum_{j=0}^{N} c_j \cdot T_f(t_{i-j}) \quad (7)$$

where t_i and c_j are the i th. observation time at the fixed observation point and the coefficient. These coefficients are defined from least square method. Also in this case, the error variance of the time shift processing can be computed as the regression error.

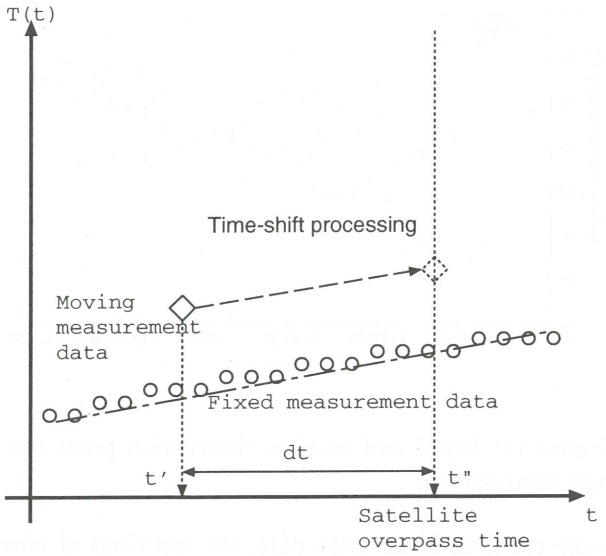

Figure 8: Schematic of the time shift processing.

4.1.3 Error propagation

Along with the both time shift processing, the surface temperature observation error propagates to the time shifted surface temperature as follows.

$$\sigma_{T_i}^2 = \sigma_l^2 + \sigma_I^2 \quad (8)$$

where $\sigma_{T_i}^2$, σ_l^2 and σ_I^2 are error variance of the time shifted surface temperature at i th. moving observation point, regression (fitting or auto regression model coefficient definition) error and measurement error of the thermoradiometer.

4.2 Area averaging of the surface temperature

4.2.1 Averaging scheme

From the time shift processing, the surface temperature at every moving observation point at the satellite passing time. From these data, the area averaged surface temperature is computed based on the radiance averaging[4].

$$\bar{T} = \left[\frac{1}{N \cdot \sigma} \sum_{i}^{N} \sigma T_i^4 \right]^{1/4} = \left[\frac{1}{N} \sum_{i}^{N} T_i^4 \right]^{1/4} \quad (9)$$

where T_i $\bar{T}$ and σ are the time–shifted surface temperature at point i, averaged surface temperature and Stefan–Boltzmann constant (5.67×10^{-8}[W/m ^{2}/K ^{4}]).

4.2.2 Error propagation

By averaging the surface temperature at every moving observation points, the surface temperature observation error propagates to the area averaged surface temperature as follows[7].

$$\sigma_{r_i} = 4T_i^3 \sigma_{T_i}$$

$$\sigma_R = \sqrt{\frac{1}{N^2} \sum_{i}^{N} \sigma_{r_i}^2}$$

$$\sigma_{\bar{T}} = \frac{\sigma_R}{4} \left[\frac{1}{N} \sum_{i}^{N} T_i^4 \right]^{-(3/4)} \quad (10)$$

$\sigma_{\bar{T}}^2$ is the error variance of the areal averaged surface temperature.

4.3 Spatial uncertainty

While the pointing accuracy of satellite data is about one tenth pixel order, the observation area must be larger than the pixel size. The area averaging made every pixel size window within the observation area, and the variance which computed from the all area averaged surface temperature computed from the every pixel size window is the spatial uncertainty of the area averaged surface temperature. So that the total error variance of the area averaged surface temperature is expressed as follows.

$$\sigma_T^2 = \sigma_{\bar{T}}^2 + \sigma_s^2 \quad (11)$$

where σ_T^2 and σ_s^2 are the total error variance and the spatial uncertainty variance.

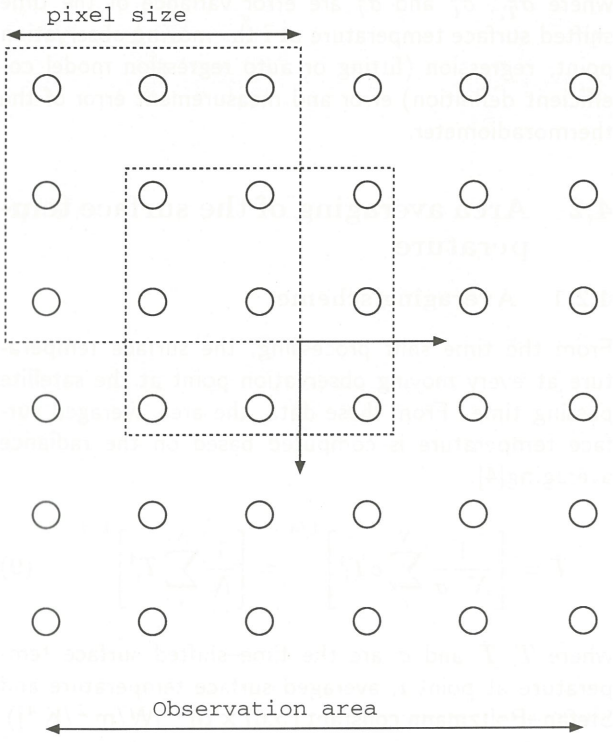

Figure 9: Schematic description of the spatial uncertainty.

5 Actual data processing of field measurement data

5.1 Description of the field and instruments

Site: Railroad playa (dry lake bed) NV

- Latitude: 38 ^{o} 27.7015"N
- Longitude: 115 ^{o} 41.4500"W

Date: 11 June 2000, 11:20 – 12:10 PDT

Target sensor: Terra/ASTER
(overpass time: 11:49 PDT)

Instruments:
thermoradiometer (with concave mirror)

- Self–compensated thermoradiometer × 2 for the moving observation. (Measurement error standard deviation: 0.3 [K])
- Horuba IT–340W for the fixed observation

JPL meteorological station (Wind speed, wind direction, air temperature and relative humidity)

Fixed point observation: Every 2 minutes with the single point calibration (using the portable blackbody) [3, 6]

Moving observation points:
Area: 200m × 200 m × 2 (25 m shifted)
Point distance: 50m
Number of points: 25 × 2

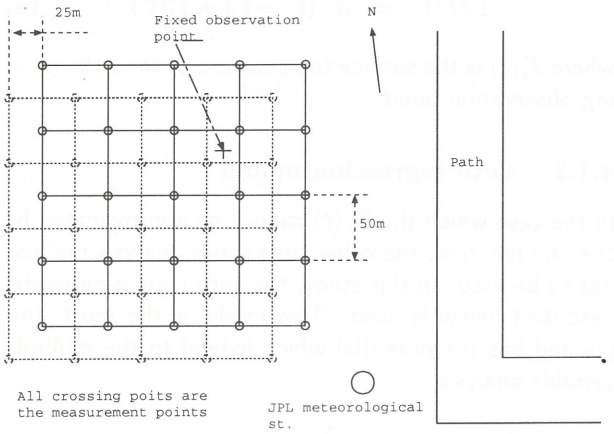

Figure 10: Observation site

5.2 Results

5.2.1 Surface temperature

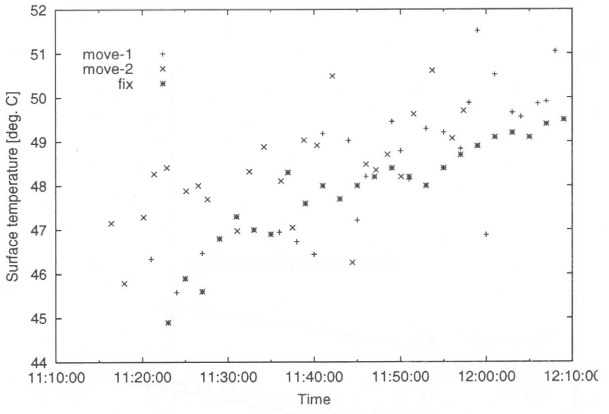

Figure 11: Fixed and moving observation point surface temperature

From the fixed observation data, the two kinds of time shift processing, linear fitting and 3rd. order auto regression model are made and the both results are almost the same so that the linear fitting is used. The time shift parameters are listed as follows.

```
Temperature gradient:  0.0740 [deg. C/min]
Error S.D. of fitting: 0.500 [deg. C]
Total error S.D.: 0.583 [deg. C]
```

Along with the above time shift parameters, the surface temperature at the satellite passing time is computed as follows.

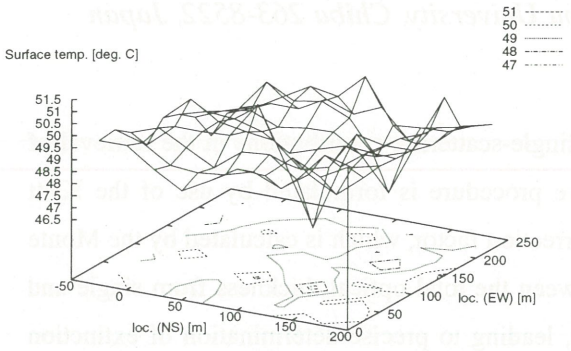

Figure 12: Surface temperature distribution at 11:49

There are 36 pixel size (100 m × 100 m) windows within the observation area, the next figure shows the averaged surface temperature at every window. The standard deviation of all of the area averaged surface temperature (spatial uncertainty) is 0.214 [deg. C]

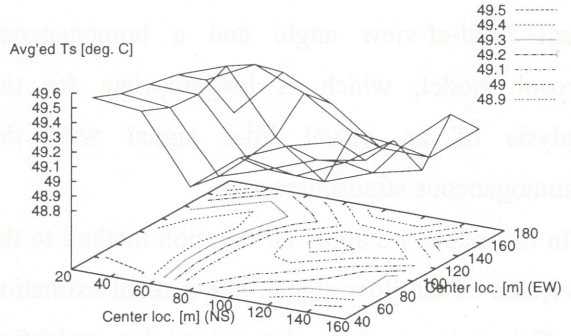

Figure 13: Averaged surface temperature distribution at 11:49

The averaged surface temperature from the all moving observation data is 49.26 [deg. C]. And the total surface temperature observation error standard deviation is 0.215 [deg. C].

6 Summaries

The previous discussion leads the following summaries. For the satellite derived surface temperature validation, the ground measurement method and data processing method are established. From this the systematic validation will be possible. For more precise and versatile validation, the following future works are considered.

- Stabilization of the self–compensated thermoradiometer.
- Bias error estimation of the mirrored surface temperature measurement on the basis of the mirror temperature measurement.
- Optimization of the auto regression based time shift processing (the order of the auto regression series and the extension to more precise time series analysis method).
- Establishment of the comparison between the satellite derived and ground measured surface temperature.

References

[1] Murayama and Moriyama, Development of the self–compensated thermoradiometer for the environmental temperature measurement, Proc. of 27th. conference Remote Sensing Society Japan, 1999.

[2] Moriyama and Murayama, Actual surface temperature measurement method using the thermoradiometer 27th. conference Remote Sensing Society Japan, 1999.

[3] Moriyama and Murayama, Accuracy validation of the portable blackbody, Proc. of 28th. conference Remote Sensing Society Japan, 2000.

[4] Moriyama, Sawabe and Murayama, The ground measurement data processing method for the validation of the satellite derived temperature and emissivity, Proc. of 28th. conference Remote Sensing Society Japan, 2000.

[5] Yano and Moriyama, Time shift processing of the ground measured surface temperature for the satellite derived surface temperature validation, Proc. of 29th. conference Remote Sensing Society Japan, 2000.

[6] Moriyama and Ito, Investigation of the calibration method for thermoradiometer, Proc. of 29th. conference Remote Sensing Society Japan, 2000.

[7] Iijima and Tsuzuki, Measurement theory, Kyoritsu Pub. Co., 1978.

[8] Nishikawa and Fujita, Heat transfer, Rikougakusya Pub. Co., 1982.

Iterative Correction of Multiple-Scattering Effects in Mie-Scattering Lidar Signals

Wahyu WIDADA, Mitsuo MINOMURA, Hiroaki KUZE and Nobuo TAKEUCHI
Center for Environmental Remote Sensing, Chiba University, Chiba 263-8522, Japan

Abstract

This paper describes an iterative method for extracting single-scattering contributions in the retrieval of aerosol extinction profiles from lidar signals. The iterative procedure is formulated by use of the Klett solution with introducing a multiple-scattering ratio as a correction factor, which is calculated by the Monte Carlo method. The numerical results of the difference between the total optical thickness from single and total scattering are used as a criterion of the convergence, leading to precise determination of extinction coefficient profiles. The iterative method is applied to an experimental signal observed by a multi-wavelength lidar

Key words: Mie-scattering lidar, lidar equation, multiple-scattering, optical thickness, Monte-Carlo method

1. Introduction

A backscattering lidar is considered to be one of the most valuable instruments for measuring vertical profiles of aerosol properties. The resulting data, however, occasionally suffer from large inaccuracies because of the inevitable assumptions about the target itself. The uncertainties consist in the relationship between backscattering and extinction coefficients, and a value of the aerosol extinction at a far-end boundary.[1] In addition, the multiple-scattering effects potentially hinder the simple application of the single-scattering lidar equation.[2-4]

A simple approximative way to account for multiple-scattering was proposed by Kunkel *et al*[2]: they introduced a so-called averaged multiple-scattering factor to reduce the extinction term in the lidar equation. Eloranta[3] developed an analytic model of doubly scattered lidar equation. Both approaches are useful for analysis of a large number of observed multiple-scattering data, but their accuracies are limited by truncation to the second scattering order and by the lack of suitable values of the factor. Bissonette[4] derived a multiple-scattering lidar equation from a phenomenological representation of the scattering process. However, this approach is limited for a small field-of-view angle and a homogeneous aerosol model, which is inappropriate for the analysis of an actual lidar signal with the inhomogeneous atmosphere.

In this paper we apply an iteration method to the inversion of the lidar signal. The aerosol extinction coefficient is precisely determined by evaluating and removing the effects of multiple-scattering. The method is based on single-scattering Klett[5] solution of the lidar equation with introducing a factor describing the multiple-to-single scattering ratio. A simulation is carried out to study the multiple scattering effect on lidar signals with and without the presence of cloud. It is shown numerically that the detection range in which the presence of a cloud influences the retrieved extinction coefficient extends beyond the geometrical thickness of the cloud. The iterative method is applied to a lidar data actually observed by a multi-wavelength lidar.

2. Theory and Simulation

2.1 Lidar Equation

The signal, $P_T(R)$, received by a lidar from the atmospheric backscattering contains two scattering components, namely single-scattering, $P_S(R)$, and multiple-scattering, $P_M(R)$. Assuming that pulse stretching due to the multiple-scattering is negligible, the signal from a range R is written as

$$P_T(R) = P_S(R) + P_M(R) . \quad (1)$$

Both $P_S(R)$ and $P_M(R)$ depend on the optical characteristics and spatial distribution of aerosols along the lidar detection path. The single-scattering signal can be written as follows:

$$P_S(R) = K\beta(R)T_S(R)/R^2 , \quad (2)$$

where K is a constant describing all the system parameters, $\beta(R)$ is the backscattering coefficient, $T_S(R) = \exp[-2\int_0^R \alpha_S(R)dR]$ is the transmittance, and $\alpha_S(R)$ is the extinction coefficient. Since both of $\beta(R)$ and $\alpha_S(R)$ are unknown, it is customary to adopt an assumption of $\alpha_S(R)/\beta(R) = S_1$ (constant). In the following numerical calculation, we assume the lidar wavelength at 532 nm and FOV of 3 and 6 mrad. The transmitted laser beam is assumed to be coaxial with the receiver telescope axis. The multiple-scattering lidar signal is considered by introducing a multiple-to-single scattering ratio, $MSS(R)$, in the single-scattering lidar equation. Subsequently, the multiple-scattering signal is expressed as:

$$P_M(R) = P_S(R)MSS(R) , \quad (3)$$

where $MSS(R)$ is calculated by means of the Monte Carlo method. The total scattering can be rewritten in terms of the single-scattering signal by substituting Eqs. (2) - (3) into Eq. (1) :

$$\begin{aligned} P_T(R) &= K\beta(R)T_T(R)/R^2 \\ &= K\beta(R)M(R)T_S(R)/R^2, \end{aligned} \quad (4)$$

where we have defined the multiple-scattering factor as $M(R) = [1 + MSS(R)] \geqq 1$. In the present simulation, for simplicity we assume that the signal is not affected by the experimental noise. Besides, the scattering is assumed to take place only from aerosol particles (Mie-scattering), and accordingly the Klett inversion method[5] is employed to calculate the extinction coefficient. A proportional relationship is postulated between the extinction and backscattering coefficients. The solution of the lidar equation, Eq. (4), with respect to the total scattering signal is

$$\alpha_T(R) = \frac{\exp[X_T(R) - X_T(R_c)]}{\alpha(R_c)^{-1} + 2\int_R^{Rc} \exp[X_T(R) - X_T(R_c)]dR} , \quad (5)$$

where $X_T(R) = \ln[R^2P_T(R)]$, the logarithmic range-squared power. The boundary value of the extinction coefficient, $\alpha(R_c)$, is obtained from a model profile adopted in the U.S. Standard atmosphere. The relevant backscattering coefficient is calculated by assuming $\beta(R) = \alpha_S(R)/S_1$. The extinction profile $\alpha_T(R)$ represents what is obtained by simply solving the lidar equation regardless of the multiple-scattering contribution. Thus, it is required to study the difference between $\alpha_T(R)$ and $\alpha_S(R)$, the extinction coefficient due only to the single-scattering. From Eq. (4), $\alpha_S(R)$ can be derived as:

$$\alpha_S(R) = \frac{\frac{M(R_c)}{M(R)}\exp[X_T(R) - X_T(R_c)]}{\alpha(Rc)^{-1} + 2\int_R^{Rc} \frac{M(R_c)}{M(R)}\exp[X_T(R) - X_T(R_c)]dR} . \quad (6)$$

Here we evaluate the difference between the two solutions by using the following parameter, ε_τ :

$$\varepsilon_\tau = \frac{|\tau_S - \tau_T|}{\tau_S} , \quad (7)$$

where $\tau_S = \int_{R_{min}}^{R_{max}} \alpha_S(R)dR$ and $\tau_T = \int_{R_{min}}^{R_{max}} \alpha_T(R)dR$ are the total optical thickness for the single and total-scattering signals, respectively. Here, R_{min} and R_{max} are the minimum and maximum range for the

lidar observation, respectively. In the iteration process described below, the errors ε_τ will be used for judging the convergence. Once an aerosol model (size distribution and refractive index) is specified, it is possible to prepare a lookup table (LUT) which describes the dependence of $M(R)$, τ_T, and ε_τ on various extinction coefficients.

In the present Monte Carlo calculation, the probability of nth order scattering $P_n(R)$ is considered for single photon ($n \leq 10$). For one calculation, we used five million photon trajectories using random variables. In order to reduce the $MSS(R)$ noise, we have also applied a least squares smoothing function.

2.2 Iterative Procedure to Evaluate the Multiple-scattering Effect

The iterative procedure is carried out according to the following three steps:

Step 1. To start with, a preliminary extinction coefficient profile, $\alpha_S^{(0)}(R)$, is determined from the observed signal $P_T(R)$:

$$\alpha_S^{(0)}(R) = \frac{\exp[X_T^{(0)}(R) - X_T^{(0)}(R_c)]}{\alpha(R_c)^{-1} + 2\int_R^{Rc} \exp[X_T^{(0)}(R) - X_T^{(0)}(R_c)]dR} . \quad (8)$$

This profiles is used to obtain a first guess of the optical thickness $\tau_S^{(0)}$, which is regarded as τ_T in Eq. (7).

Step 2. The extinction profiles $\alpha_S^{(0)}(R)$ is divided into several regions, each of which is characterized by a relatively homogeneous value of $\alpha_S^{(0)}(R)$. Then, the multiple-scattering ratio $M^{(0)}(R)$ of each region is calculated by means of the Monte Carlo method.

Step 3. The purpose of this step is to correct $\alpha_S^{(0)}(R)$ by means of $M^{(0)}(R)$. Using Eq. (6), one obtains:

$$\alpha_S^{(1)}(R) = \frac{\frac{M^{(0)}(Rc)}{M^{(0)}(R)} \exp[X_S^{(0)}(R) - X_S^{(0)}(Rc)]}{\alpha(Rc)^{-1} + 2\int_R^{Rc} \frac{M^{(0)}(Rc)}{M^{(0)}(R)} \exp[X_S^{(0)}(R) - X_S^{(0)}(Rc)]dR} , \quad (9)$$

where $\alpha_S^{(1)}(R)$ is the result of the first iteration. The error $\varepsilon_\tau^{(1)}$ is evaluated by comparing the retrieved single-scattering optical thickness $\tau_S^{(1)}$ with the total-scattering optical thickness $\tau_T = \tau_S^{(0)}$ ($\varepsilon_\tau^{(1)} = |\tau_S^{(1)} - \tau_S^{(0)}| / \tau_S^{(1)}$).

The operations in steps 1 - 3 can be formulated as:

$$\alpha_S^{(i)}(R) = I^{(i-1)}[P_T(R)], \quad (10)$$

where I denotes an inversion procedure using the Klett method with a multiple-scattering ratio $M^{(i-1)}(R)$ as a correction function, and i is the iteration order. The iteration procedure of Eq. (10) is repeated until a condition

$$\varepsilon_\tau^{(i)} \leq e, \ (i = 1,2,3,...), \quad (11)$$

is fulfilled. Here $\varepsilon_\tau^{(i)}$ is the error in the retrieved optical thickness of i-th iteration and e is a tolerance, for which we assume a value of 0.001 in the present simulation.

We have also successfully applied the Fernald method[6] in the iteration procedure to enable the analysis of a signal including aerosol and molecular scattering.

2.3 Atmospheric Parameters Used for the LUT

The aerosol and cloud types used in the present simulation are the urban aerosol and the C_1-cloud model. The size distribution of aerosol is described by the sum of two lognormal distributions.[8] The refractive index of aerosol particles is assumed to be 1.53 - 0.006i. For cloud particles, on the other hand, the size distribution is assumed to be a modified gamma distribution. The refractive index of cloud is assumed to be 1.33 - 0.00i, namely with the negligible contribution from the absorption. In accordance with these assumptions, the S_1 values of aerosol and cloud particles are assumed to be 30 and 18 sr, respectively.[7] We prepare the LUT for aerosol under clear sky conditions (without clouds) and a signal with presence of cloud. The ground

visibility is varied from 20 to 50 km.

3. Application to an Observed Signal

The iterative method is applied to a lidar signal observed using a multi-wavelength lidar system at Chiba University. The multi-wavelength lidar is operated at four wavelengths (355, 532, 756, and 1064 nm). As an example, Fig. 1(a) shows a 532 nm signal (April 3, 1998). A low cloud appeared at about 1.35 - 1.55 km with a geometrical thickness of about 0.2 km.

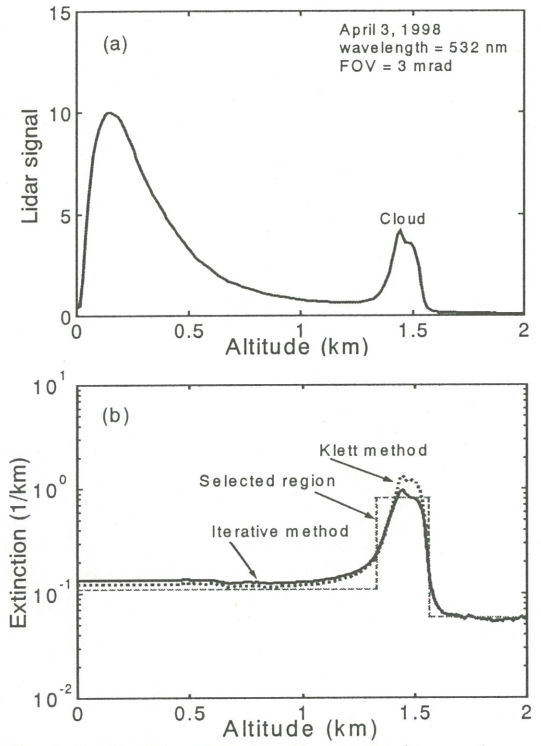

Fig. 1 Application of the iteration method to an observed signal. (a) Lidar signal observed on April 3, 1998. (b) Retrieved profiles of the extinction coefficient, $\alpha(R)$. Dotted and solid curves are the profiles calculated by means of the Klett method and iterative method, respectively.

As a first step in the iteration, a preliminary profile of the extinction coefficient is calculated by means of the Klett method as shown in Fig. 1(b). The complete overlap between the laser beam and the telescope FOV is achieved at a range of ~450 m for a FOV of 3 mrad. Below this altitude, the extinction coefficient is assumed to be the same as the value at the overlap altitude. The total optical thickness $\tau_S^{(0)} = \tau_T$ is about 0.532. The calculation of the multiple-scattering ratio, $M(R)$, is carried out for a simplified profile as indicated by a broken line in Fig. 1(b). The extinction coefficient profile illustrated with a solid line is the final result of the retrieval. The estimated value of the optical thickness due to the single-scattering is $\tau_S = 0.572$ ($\varepsilon_\tau = 7.5$ %). Above the cloud top, the error between the Klett profile and the final profile seems insignificant. Below the cloud base, on the other hand, the error increases as the distance increases downward from the cloud. Inside the cloud, the error is found to increase with the penetration depth of the laser beam.

4. Conclusions

We have introduced an iterative procedure for reducing the error in the extinction coefficient caused by the multiple-scattering. The method is based on the single scattering lidar inversion method with introducing a multiple-scattering factor. The iterative procedure is formulated by used of the Klett method for the cases where the aerosol scattering dominates the molecular scattering.

References

1. V. A. Kovalev: Appl. Opt. **32** (1993) 6,053.
2. K. E. Kunkel *et al.*: Atmos. Sci. **33** (1976) 1,772.
3. E. W. Eloranta: Appl. Opt. **37** (1998) 2464.
4. L. R. Bissonnette: Appl. Opt. **35** (1996) 6449.
5. J. D. Klett: Appl. Opt. **24** (1986) 1,638.
6. F. G. Fernald: Appl. Opt. **23** (1984) 652.
7. W. Widada *et al.*: Opt. Rev. **17** (2000) 95.
8. M. Hess *et al.*: Bull. Am. Met. Soc. **79** (1998) 831

AUTHOR INDEX

========

Chiba University

Chiba University was founded in 1949, unifying several regional former national colleges and schools such as Chiba Medical College and Chiba Normal School. Its fundamental mission since then has been, as encapsulated by the inscription on the University Bell, ad altiora semper (always toward the higher), to equip students with the ability to make mature and informed judgments while nurturing and guiding their creativity. Pursuing these goals of excellence has resulted in Chiba University becoming one of the leading academic research centers of Japan.

Currently, Chiba University consists of nine faculties, the university library system, the university hospital and other educational and research facilities. With 12,200 students in the undergraduate program, it has long been one of the largest universities in Japan. As for the graduate school, there are about 1,600 students in six master's programs and 900 in five doctoral programs.

The University's three campuses Nishi-Chiba, Inohana and Matsudo are ideally located in Chiba Prefecture, an area noted for its industrial, intellectual and international achievements. In recent decades Chiba has undergone rapid development which in many ways rivals the neighboring Tokyo Metropolis. Many national projects have been based in Chiba Prefecture, and now Chiba has one of the main international transport centers (New Tokyo International Airport Narita) and one of the largest business centers in Japan (Makuhari New Metropolitan Area and Nippon Convention Center). Many new academic and industrial complexes for the advanced sciences (The Kazusa DNA Research Institute) are located in Chiba Prefecture. The developments in Chiba today are representative of tomorrow's Japan. Matters occurring in the most progressive parts of Japan, or even in the world, will provide rich materials for research in various aspects of the human, social, industrial and natural sciences.

CEReS

Center for Environmental Remote Sensing (CEReS) was established in 1995 on the basis of an ordinance of the Ministry of Education, Science, Sports and Culture as utilization of the institute for nationwide collaboration of academic communities. The objectives of the CEReS are to develop remote sensing technology and conduct research on global and regional environment through remote sensing. CEReS consists of Department of Sensor and Atmospheric Radiation、Department of Geoinformation Analysis、Department of Data Base Research、and Department of Data Base Development. In the educational aspect, CEReS takes part in graduate school education, for both MS and Ph.D. CEReS is receiving images of NOAA and GMS, and offers the processed data to the scientific communities.

http://ceres.cr.chiba-u.ac.jp:8080

Department of Sensor and Atmospheric Radiation

This department studies the "Atmospheric Correction" of satellite remote sensing data on theoretical as well as observational bases. The precision of satellite data is limited to a large extent by the presence of the earth's atmosphere. Our target is to establish the algorithm of analyzing the satellite remote sensing data, and at the same time, the optical remote sensing data of atmosphere itself.

In the division for sensor development, basic researches are conducted on high-precision earth observing sensors, which are capable of effectively deriving physical quantities suitable for the observation purposes. The activity includes the routine observation using our Atmospheric Data Correction Lidar (multi-wavelength laser radar) synchronized with the flights of satellites, and simulation studies of the atmospheric correction with a variety of atmospheric models. The division is responsible also for the development of techniques of monitoring atmospheric trace gases using a differential absorption lidar or sun/lunar light sources, and the development of highly sensitive methods of detecting trace gases with a fiber laser and other optical sensors.

In the division for atmospheric radiation, studies are undertaken on the general and comprehensive techniques of analyzing satellite data, which, being based on the radiative transfer theory, incorporate the ground based observation data of clouds and other atmospheric constituents. This study leads to development of the atmospheric correction methods as well as to the better understanding of the atmosphere.

Published by Center for Environmental Remote Sensing (CEReS)
Chiba University, Chiba-shi 263-8522, Japan

Printed in Japan (2001)